UNIVERSITÉ DE STRASBOURG

ÉCOLE DOCTORALE des Sciences Chimiques

[UMR 7006]

THÈSE

présentée par :

Haijun PENG

soutenue le : **19 September 2022**

pour obtenir le grade de : **Docteur de l'université de Strasbourg**

Discipline/ Spécialité : Chimie

Cadre organique métallique/ Cadre organique covalent dans les applications de stockage d'énergie

---

THÈSE dirigée par :

M. SAMORI Paolo   Professeur, Université de Strasbourg, UMR 7006, Strasbourg ; France

M. CIESIELSKI Artur   Ingénieur de recherche (HDR), CNRS, UMR 7006, Strasbourg, France

RAPPORTEURS :

M. FENG Xinliang   Professeur, Technische Universität Dresden, Dresden, Germany

M. PALERMO Vincenzo   Professeur, Institute for the Organic Synthesis and Photoreactivity, Bologna, Italy

AUTRES MEMBRES DU JURY :

M. Mario Ruben   Professeur, Institut de Physique et Chimie des Matériaux de Strasbourg (IPCMS), CNRS UMR 7504, Université de Strasbourg, France

Résumé en Français

La demande croissante d'énergie a suscité des efforts de recherche à l'échelle mondiale en vue du développement de technologies liées aux énergies renouvelables.[1-2] Pour contrer la consommation croissante de combustibles fossiles et l'effet de serre, il est urgent de concevoir des dispositifs de stockage d'énergie efficaces et peu coûteux qui s'appuient sur des sources d'énergie renouvelables (p. ex. solaire, éolienne, houlomotrice).[3] Une quantité toujours plus grande d'énergie est nécessaire pour alimenter tous les outils numériques qui ont apporté et continueront d'apporter des changements remarquables à notre routine quotidienne à de nombreux niveaux. Dans ce cadre, il convient également d'examiner sérieusement la pénurie croissante de matières premières critiques (MPC) et les problèmes qui y sont associés. Cette tendance regrettable a déclenché la recherche de nouveaux systèmes de stockage d'énergie (SSE) hautement efficaces et durables. Les ESS tels que les supercondensateurs et les batteries, qui présentent des densités de puissance/énergie spécifiques élevées et une longue durée de vie, sont largement utilisés dans notre vie quotidienne en tant qu'électronique grand public (véhicules électriques, tablettes, smartphones et réseaux intelligents). Les progrès dans le domaine des ESS sont directement liés au développement de nouveaux matériaux pour les électrodes très poreux

présentant une capacité de stockage d'énergie accrue.[4]

       Les réseaux organométalliques (MOF) et les réseaux organiques covalents (COF) sont deux familles émergentes de matériaux fonctionnels poreux qui ont montré un grand potentiel dans les applications ESS.[5-6] Généralement, les MOF sont constitués d'ions ou de clusters métalliques liés à des ligands organiques par des liaisons de coordination fortes,[7-8] tandis que les COF sont fabriqués *via* la liaison covalente de blocs de construction organiques tels que les imines, les nitroborates, les boronyles et les liaisons C=C.[9-10] Les matériaux appartenant à ces deux classes présentent des propriétés uniques telles qu'une cristallinité élevée, des surfaces importantes, des porosités élevées et une abondance de sites fonctionnels redox-actifs, ce qui en fait des blocs de construction idéaux pour des applications en tant que matériaux constituant les électrodes pour les supercondensateurs et les batteries.[11-15] Cependant, les MOFs et COFs traditionnels souffrent de faibles conductivités électriques, en raison de la nature isolante des ligands organiques utilisés pour leur assemblage et du chevauchement des orbitales π-d entre les ligands organiques et les ions métalliques, ce qui limite leurs performances électrochimiques dans les applications de stockage d'énergie.[16] Par conséquent, le développement de nouvelles électrodes à base de MOFs/COFs et l'exploration de nouveaux sites redox-actifs dans les COFs sont nécessaires de toute urgence pour le

développement de dispositifs de stockage d'énergie à haute performance.

Dans le Chapitre 1, nous présenterons les matériaux poreux hybrides MOFs, COFs, et MOFs@COFs, les protocoles de synthèse, et leurs applications dans les supercondensateurs et les batteries zinc-ion aqueuses.

Le Chapitre 2 sera consacré à la discussion des méthodes et techniques expérimentales, notamment la synthèse des matériaux actifs MOFs@COFs et COF-TMT-BT, les méthodes de fabrication des supercondensateurs et des dispositifs de batterie zinc-ion, ainsi que les différentes techniques d'hybridation et de caractérisation utilisées dans cette thèse. Dans ce chapitre, nous expliquerons en détail les méthodes de synthèse hydrothermale des matériaux hybrides MOF-UIO-66, COF-TMT-BT, MOF@COF-LZU1, aza-MOF@COF, et MOF@COF-TCNQ. Parallèlement, une présentation complète des différentes méthodes de caractérisation, incluant les mesures électrochimiques, les caractérisations spectroscopiques (c'est-à-dire la diffraction des rayons X sur poudre, la spectroscopie infrarouge à transformée de Fourier, la spectroscopie photoélectronique à rayons X, les spectres de masse de désorption/ionisation par laser à temps de vol assisté par matrice, l'analyse thermogravimétrique, la calorimétrie différentielle à balayage) et les caractérisations de surface (c'est-à-dire la microscopie électronique à balayage et la microscopie électronique à

transmission) a été fournie afin d'obtenir la structure de tous les matériaux hybrides et leur composition.

Dans le Chapitre 3, nous discuterons d'un matériau hybride fonctionnel aza-MOF@COF avec une structure poreuse robuste construite avec le précurseur MOF@COF-LZU1 modifié par cycloaddition aza-Diels-Alder. L'hybride poreux aza-MOF@COF a été synthétisé en utilisant les trois étapes suivantes (Figure Ⅰ). (1) la modification de la surface du MOF-UIO-66-NH₂ avec du 1,3,5-benzenetricarboxaldéhyde pour obtenir le MOF-UIO-66(CHO), (2) la croissance in situ de la couche de COF sur le MOF-UIO-66(CHO) par condensation entre les aldéhydes sur le MOF-UIO-66(CHO) et la p-phénylènediamine, (3) les fragments de quinolone ont été introduits dans les hybrides MOF@COF-LZU1 liés à l'imine par un protocole de modification post-synthétique.
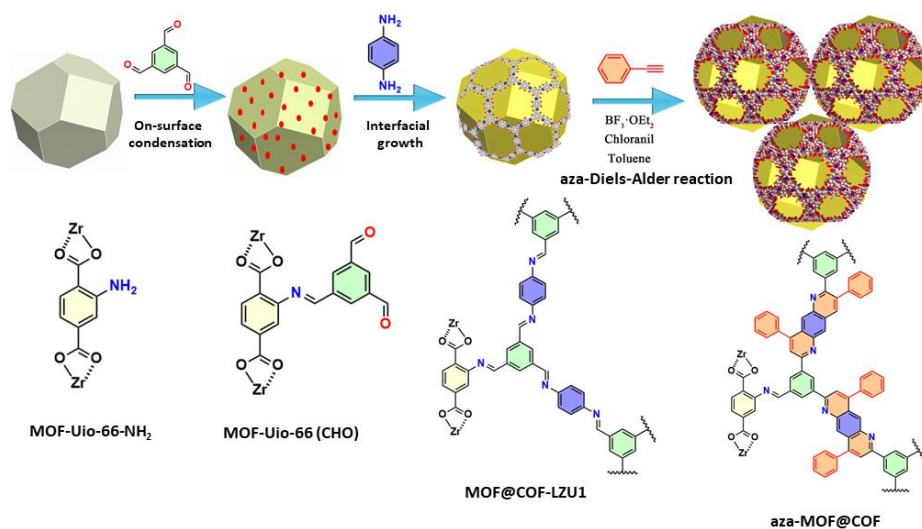

Figure Ⅰ. Illustration schématique de la voie de synthèse de la structure hybride aza-MOF@COF.

Résumé en Français

Dans le Chapitre 4, nous avons examiné un nouvel hybride MOF@COF-TCNQ formé par une infiltration en phase liquide de 7,7,8,8-tétracyanoquinodiméthane (TCNQ) redox actif dans les canaux de pores du MOF@COF. Le matériau hybride MOF@COF-TCNQ a été synthétisé en trois étapes (Figure II). La première étape repose sur la condensation en surface du MOF-UIO-66-NH$_2$ avec le 1,3,5-triformylphloroglucinol (Tp), ce qui donne le MOF-UIO-66-NH$_2$ (Tp). Dans la deuxième étape, la couche de COF a été développée sur le MOF-UIO-66-NH$_2$ en employant la condensation entre le Tp présent sur la surface du MOF-UIO-66-NH$_2$ (Tp) tel que préparé et la p-phénylènediamine. Dans la troisième et dernière étape, la modification post-synthétique du MOF@COF a été accomplie en utilisant l'infiltration en phase liquide d'accepteurs d'électrons TCNQ pour obtenir les matériaux hybrides MOF@COF-TCNQ.
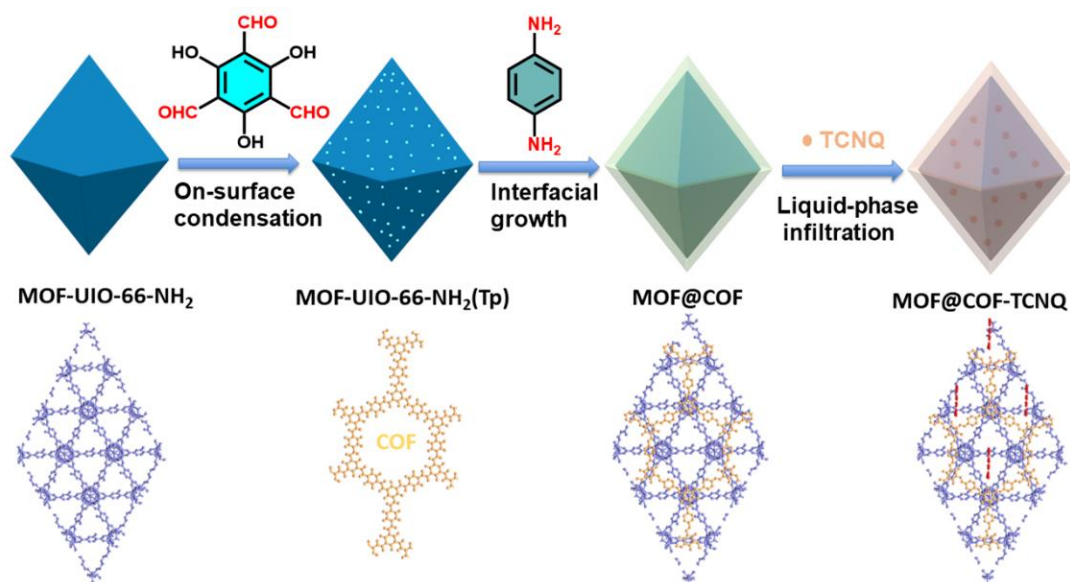
Figure II . Illustration schématique de la voie de synthèse de la structure hybride aza-MOF@COF.

Résumé en Français

Dans le Chapitre 5, nous avons examiné un nouveau COF-TMT-BT lié à une oléfine par condensation Aldol entre la 2,4,6-triméthyl-1,3,5-triazine (TMT) et le 4,4′-(benzothiadiazole-4,7-diyl)dibenzaldéhyde (BT), qui présente un nouveau site actif d'unités de benzothiadiazole pour les batteries zinc-ion aqueuses (ZIB). Les résultats expérimentaux et les calculs théoriques DFT indiquent que les dopants N pyridiniques/pyrroliques hautement électronégatifs dans le réseau COF-TMT-BT peuvent non seulement réduire considérablement l'énergie de liaison entre le groupe benzothiadiazole et Zn^{2+} en induisant une délocalisation de la charge du groupe benzothiadiazole, mais aussi favoriser l'adsorption de Zn^{2+} en se liant aux atomes S des unités benzothiadiazole pour former la liaison S-Zn-S des couches COF-TMT-BT successives. La substitution par le benzothiadiazole modifie la distribution des électrons du squelette du COF à proximité et augmente leur probabilité d'interagir avec Zn^{2+}, ce qui optimise les performances électrochimiques. En outre, les unités benzothiadiazole présentent également une activité électrochimique avec les ions Zn^{2+} dans le COF lié à l'imine.

Cette thèse se concentre sur la conception et la fabrication de nouvelles électrodes par la synthèse de nouveaux matériaux hybrides MOFs@COFs et par l'exploration de nouveaux COFs bidimensionnels (2D) liés à des oléfines (C=C) pour des dispositifs de supercondensateurs et de batteries zinc-ion, respectivement. Dans le Chapitre 3, L'hybride aza-MOF@COF formé a montré

d'excellentes propriétés lorsqu'il a été utilisé comme preuve de concept dans une électrode de supercondensateur à l'état solide, donnant une capacité spécifique de 20,35 µF cm^{-2} et une densité d'énergie volumétrique élevée de 1.16 F cm^{-3}. De plus, l'électrode à base d'aza-MOF@COF a montré une stabilité à long terme exceptionnelle et la capacité s'est maintenue à 89.3 % après 2000 cycles par rapport au MOF original et aux précurseurs MOF@COF-LZU1. Dans le Chapitre 4, L'hybride MOF@COF-TCNQ obtenu présente une capacité surfacique spécifique aussi élevée que 78.36 mFcm^{-2}, et une capacité de pile exceptionnelle de 4.46 Fcm^{-3}, qui dépasse la plupart des matériaux hybrides MOFs@COFs de pointe précédemment rapportée. De plus, en combinant les résultats expérimentaux avec des calculs de théorie fonctionnelle de la densité (DFT), nous introduisons le concept de capacité quantique aux hybrides MOF@COF. Les performances exceptionnelles du dispositif peuvent être attribuées aux raisons suivantes (i) la présence de pores uniformes qui facilitent la diffusion des ions et le comportement redox du COF lié à la β-céto-énamine dopée sur le MOF qui peut fournir une pseudo-capacité supplémentaire; (ii) la structure hautement cristalline et la structure poreuse bien définie formant des canaux, permettent un transport rapide des ions; (iii) l'infiltration de molécules de TCNQ dans les réseaux hybrides MOF@COF fournit une densité d'états électriques (DOS) et une capacité quantique (CQ) améliorées. Dans le Chapitre 5, Le COF-TMT-BT tel que synthétisé offre une capacité élevée de 283.5 mAh g^{-1} à une densité de courant de

Résumé en Français

0.1 A g^{-1}, une densité d'énergie maximale exceptionnelle de 219.6 Wh kg^{-1} et des densités de puissance de 23.2 kW kg^{-1}, ce qui est supérieur à la plupart des cathodes COFs rapportées et à d'autres matériaux constitutifs d'électrode organiques ou inorganiques. Enfin, le chapitre 6 décrira le résumé de l'ensemble des travaux présentés dans cette thèse. Les perspectives et les orientations futures pour la conception rationnelle de matériaux poreux hybrides MOFs@COFs pour des électrodes de supercondensateurs à haute performance et l'exploration de nouveaux actifs électrochimiques dans les matériaux à base de COFs pour les batteries zinc-ion aqueuses sont également présentées dans la dernière section de ce chapitre.

Summary in English

The growing energy demands have sparked worldwide research efforts towards the development of renewable energy technologies.[1-2] To counteract the growing consumption of fossil fuels as well as the adverse greenhouse effect, there is an urgent need to design efficient and low-cost energy storage devices that rely on renewable power sources (*e.g.*, solar, wind, wave).[3] An ever-increasing amount of energy is needed to power all digital tools that have brought and will keep bringing remarkable changes to our everyday routine on many levels. In this framework, it is worth also to seriously consider the increasing shortage of critical raw materials (CRM) and associated problems. Such an unfortunate trend has triggered the search for novel, highly efficient and sustainable energy storage systems (ESS). ESS such as supercapacitors and batteries, with high specific power/energy densities and long lifespan, are widely used in our daily life as consumer electronics (electric vehicles, tablets, smartphones, and smart grids). The progress in ESS is directly driven by the development of new highly porous electrode materials exhibiting enhanced energy storage capability.[4]

Summary in English

Metal-organic frameworks (MOFs) and covalent-organic frameworks (COFs) are two emerging families of porous functional materials which have shown great potential in ESS applications.[5-6] Typically, MOFs are comprised of metal ions or clusters tethered to organic ligands through strong coordination bonds,[7-8] whereas COFs are made *via* the covalent linkage of organic building blocks such as imines, nitroborates, boronyls, and C=C bonds.[9-10] Materials belonging to these two classes exhibit unique properties such as high crystallinity, high surface areas, high porosities, and abundance of functional redox-active sites which render them ideal building blocks for applications as electrode materials for supercapacitors and batteries.[11-15] However, traditional MOFs and COFs suffer from low electrical conductivities, as a result of the insulating nature of organic ligands used for their assembly and π-d orbital overlap between organic ligands and metal ions, which limits their electrochemical performance in energy storage applications.[16] Therefore, the development of novel MOFs/COFs-based electrodes and exploration of new redox-active sites in COFs is urgently needed for the development of high-performance energy storage devices.

In Chapter 1, I will introduce MOFs, COFs, and MOFs@COFs hybrid porous materials, the synthetic protocols, and their applications in supercapacitors and aqueous zinc-ion batteries.

Chapter 2 will be devoted to the discussion of the experimental methods and techniques including the synthesis of MOFs@COFs and COF-TMT-BT active materials, supercapacitors, and zinc-ion battery device fabrication methods, as well as various hybridization and characterization techniques used in this thesis. In this chapter, we will explain in details the hydrothermal synthesis methods for MOF-UIO-66, COF-TMT-BT, MOF@COF-LZU1, aza-MOF@COF, and MOF@COF-TCNQ hybrid materials. Meanwhile, a comprehensive introduction of various characterization methods including electrochemical measurements, spectroscopic characterizations (*i.e.,* powder-ray diffraction, Fourier transform infrared spectroscopy, X-ray photoelectron spectroscopy, matrix-assisted laser desorption/ionization time-of-flight mass spectra, thermogravimetric analysis, differential scanning calorimetry), and surface characterizations (*i.e.,* Scanning Electron Microscopy, Transmission Electron Microscopy) has been provided to acquire the structure of all hybrid materials and their composition.

In Chapter 3, we discuss a functional aza-MOF@COF hybrid material with a robust porous structure constructed with MOF@COF-LZU1 precursor modified *via* aza-Diels-Alder cycloaddition. The porous aza-MOF@COF hybrid was synthesized using the following three steps (Figure Ⅰ): (1) the surface modification of MOF-UIO-66-NH$_2$ with 1,3,5-benzenetricarboxaldehyde to obtain MOF-UIO-66(CHO), (2) the *in situ* growth of the COF layer on MOF-UIO-66(CHO) through

condensation between the aldehydes on MOF-UIO-66(CHO) and *p*-phenylenediamine, (3) the quinolone moieties were introduced into imine-linked MOF@COF-LZU1 hybrids by post-synthetic modification protocol.
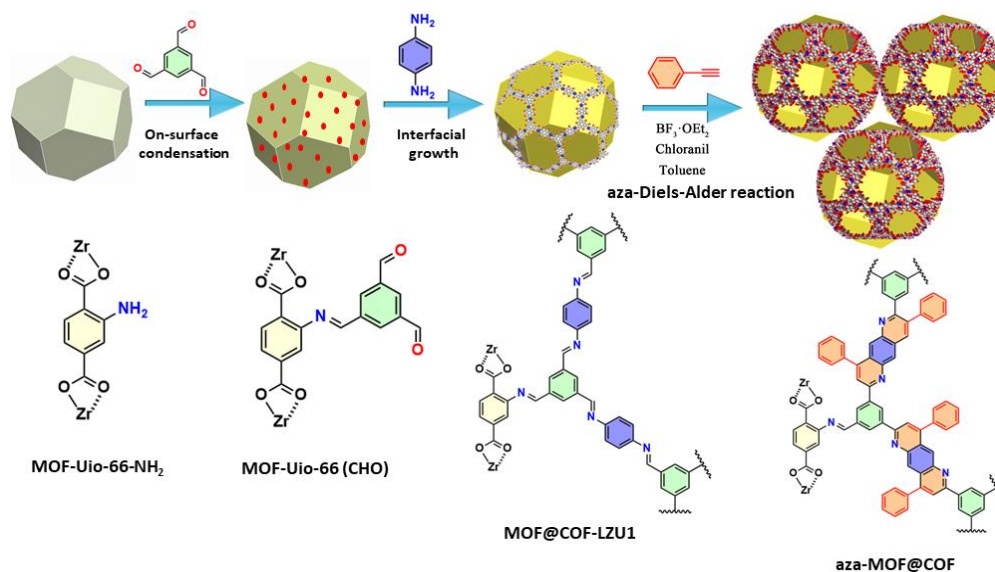

Figure Ⅰ. Illustration schématique de la voie de synthèse de la structure hybride aza-MOF@COF.

In Chapter 4, we have discussed a novel MOF@COF-TCNQ hybrid formed through a liquid-phase infiltration of redox-active 7,7,8,8-tetracyanoquinodimethane (TCNQ) into the MOF@COF pore channels. The MOF@COF-TCNQ hybrid material was synthesized in three steps. The first step relies on-surface condensation of the MOF-UIO-66-NH$_2$ with 1,3,5-triformylphloroglucinol (Tp) yielding MOF-UIO-66-NH$_2$ (Tp). In the second step, the COF layer has been grown on MOF-UIO-66-NH$_2$ by employing the condensation between the Tp present on the surface of the as-prepared MOF-UIO-66-NH$_2$ (Tp)

and *p*-phenylenediamine. In the third and final step, the post-synthetic modification of MOF@COF has been accomplished by using liquid-phase infiltration of electron acceptors TCNQ yielding the MOF@COF-TCNQ hybrid materials.
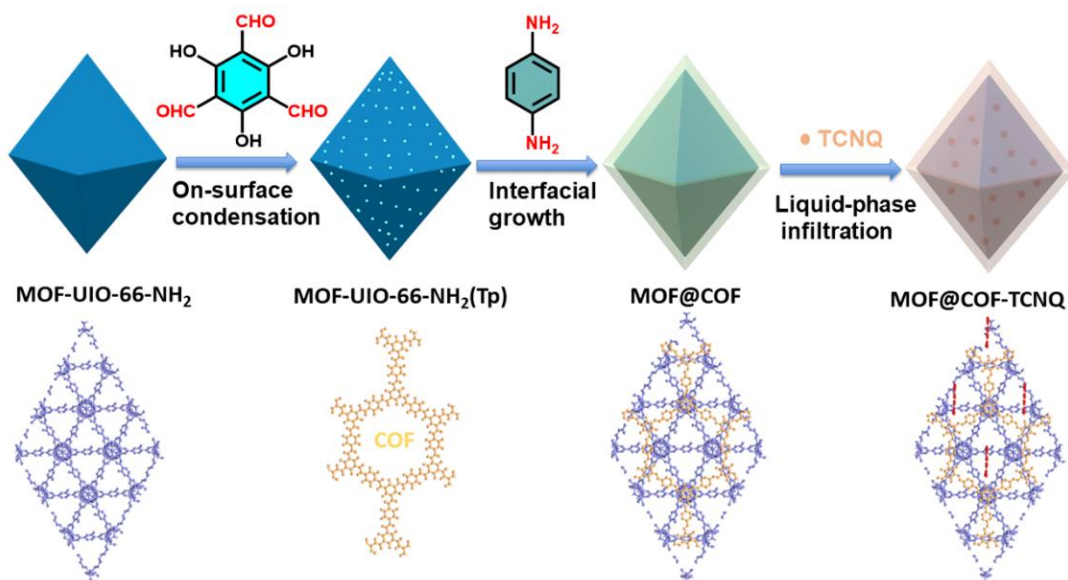

Figure Ⅱ. Illustration schématique de la voie de synthèse de la structure hybride aza-MOF@COF.

In Chapter 5, we have discussed a new olefin-linked COF-TMT-BT through Aldol condensation between 2,4,6-trimethyl-1,3,5-triazine (TMT) and 4,4′-(benzothiadiazole-4,7-diyl)dibenzaldehyde (BT), which exhibited a novel active site of benzothiadiazole units for aqueous zinc-ion batteries (ZIBs). The experimental results and theoretical DFT calculations indicate that the highly electronegative pyridinic/pyrrolic N dopants in the COF-TMT-BT framework can not only greatly reduce the binding energy between benzothiadiazole group and Zn^{2+} by inducing charge delocalization of the benzothiadiazole group, but also promote the adsorption of Zn^{2+} by bonding with the S atoms from the benzothiadiazole units to

form S-Zn-S bond of the successive COF-TMT-BT layers. The benzothiadiazole substitution changes the electron distribution of the COF backbone nearby and increases their likelihood to interact with Zn^{2+}, which optimizes the electrochemical performance. Furthermore, the benzothiadiazole units also display electrochemical activity with Zn^{2+} ions in imine-linked COF. We believe that our new benzothiadiazole functionalized 2D olefin-linked COF-TMT-BT not only open a new avenue for the further rational design and exploration of benzothiadiazole-based COF electrode but also broaden the COFs in aqueous ZIBs application.

This thesis is focused on the design and fabrication of novel electrodes *via* the synthesis of new MOFs@COFs hybrid materials and by exploring new olefin-linked (C=C) two-dimensional (2D) COFs for supercapacitor and zinc-ion battery devices, respectively. In Chapter 3, the formed aza-MOF@COF hybrid displayed excellent properties when employed as a proof-of-concept application in solid-state supercapacitor electrode, giving a specific capacitance of 20.35 μF cm^{-2} and high volumetric energy density of 1.16 F cm^{-3}. In addition, the aza-MOF@COF based electrode showed outstanding long-term stability and the capacitance maintained 89.3% after 2000 cycles compared with the original MOF and MOF@COF-LZU1 precursors. In Chapter 4, the obtained MOF@COF-TCNQ hybrid exhibits a specific areal capacitance as high as 78.36 mF cm^{-2}, and an exceptional stack capacitance of 4.46 F cm^{-3}, which exceeds most of the previously reported *state-of-the-art*

Summary in English

MOFs@COFs hybrid materials. Moreover, by combining the experimental results with density functional theory (DFT) calculations we introduce the concept of quantum capacitance to MOF@COF hybrids. The outstanding device performance can be attributed to the following reasons: (i) the presence of uniform pores that facilitate the diffusion of ions and the redox behavior of doped β-keto-enamine linked COF on MOF which can provide extra pseudocapacitance; (ii) the highly crystalline structure and well-defined porous structure forming channels, allow fast transport of ions; (iii) the infiltration of TCNQ molecules into MOF@COF hybrid frameworks provides an enhanced electrical density of states (DOS) and quantum capacitance (C_Q). In Chapter 5, the as-synthesized COF-TMT-BT delivers a high capacity of 283.5 mAh g^{-1} at a current density of 0.1 A g^{-1} and an outstanding maximum energy density of 219.6 Wh kg^{-1} and power densities of 23.2 kW kg^{-1}, which is superior to most of the reported COFs cathodes and another organic or inorganic electrode materials. Finally, Chapter 6 will describe the summary of the overall work presented in this thesis. Outlooks and future directions for the rational design MOFs@COFs hybrid porous materials for high-performance supercapacitor electrodes and exploring novel electrochemical active in COFs-based materials for aqueous zinc-ion batteries are also presented in the last section of this chapter.

References

1.   Gogotsi, Y.; Simon, P., True Performance Metrics in Electrochemical Energy Storage. *Science* **2011,** 334 (6058), 917-918.

2.   Simon, P.; Gogotsi, Y., Materials for electrochemical capacitors. *Nature Materials* **2008,** 7 (11), 845-854.

3.   Larcher, D.; Tarascon, J. M., Towards greener and more sustainable batteries for electrical energy storage. *Nature Chemistry* **2015,** 7 (1), 19-29.

4.   Wang, G.; Zhang, L.; Zhang, J., A review of electrode materials for electrochemical supercapacitors. *Chemical Society Reviews* **2012,** 41 (2), 797-828.

5.   Liang, Z.; Qu, C.; Guo, W.; Zou, R.; Xu, Q., Pristine Metal-Organic Frameworks and their Composites for Energy Storage and Conversion. *Advanced Materials* **2018,** 30 (37), 1702891.

6.   Li, J.; Jing, X.; Li, Q.; Li, S.; Gao, X.; Feng, X.; Wang, B., Bulk COFs and COF nanosheets for electrochemical energy storage and conversion. *Chemical Society Reviews* **2020,** 49 (11), 3565-3604.

7.   Zhu, L.; Meng, L.; Shi, J.; Li, J.; Zhang, X.; Feng, M., Metal-organic frameworks/carbon-based materials for environmental remediation: A state-of-the-art mini-review. *Journal of Environmental Management* **2019,** 232, 964-977.

8.   Baumann, A. E.; Burns, D. A.; Liu, B.; Thoi, V. S., Metal-organic framework functionalization and design strategies for advanced electrochemical energy storage devices. *Communications Chemistry* **2019,** 2 (1), 86.

9.   Geng, K.; He, T.; Liu, R.; Dalapati, S.; Tan, K. T.; Li, Z.; Tao, S.; Gong, Y.; Jiang, Q.; Jiang, D., Covalent Organic Frameworks: Design, Synthesis, and Functions. *Chemical Reviews* **2020,** 120 (16), 8814-8933.

10. Lohse, M. S.; Bein, T., Covalent Organic Frameworks: Structures, Synthesis, and Applications. *Advanced Functional Materials* **2018,** 28 (33), 1705553.

References

11. Zhou, L.; Jo, S.; Park, M.; Fang, L.; Zhang, K.; Fan, Y.; Hao, Z.; Kang, Y.-M., Structural Engineering of Covalent Organic Frameworks for Rechargeable Batteries. *Advanced Energy Materials* **2021,** 11 (27), 2003054.

12. Du, R.; Wu, Y.; Yang, Y.; Zhai, T.; Zhou, T.; Shang, Q.; Zhu, L.; Shang, C.; Guo, Z., Porosity Engineering of MOF-Based Materials for Electrochemical Energy Storage. *Advanced Energy Materials* **2021,** 11 (20), 2100154.

13. Cui, B.; Fu, G., Process of metal-organic framework (MOF)/covalent-organic framework (COF) hybrids-based derivatives and their applications on energy transfer and storage. *Nanoscale* **2022,** 14 (5), 1679-1699.

14. Liu, J.; Song, X.; Zhang, T.; Liu, S.; Wen, H.; Chen, L., 2D Conductive Metal-Organic Frameworks: An Emerging Platform for Electrochemical Energy Storage. *Angewandte Chemie International Edition* **2021,** 60 (11), 5612-5624.

15. Yan, R.; Ma, T.; Cheng, M.; Tao, X.; Yang, Z.; Ran, F.; Li, S.; Yin, B.; Cheng, C.; Yang, W., Metal-Organic-Framework-Derived Nanostructures as Multifaceted Electrodes in Metal-Sulfur Batteries. *Advanced Materials* **2021,** 33 (27), 2008784.

16. Talin, A. A.; Centrone, A.; Ford Alexandra, C.; Foster Michael, E.; Stavila, V.; Haney, P.; Kinney, R. A.; Szalai, V.; El Gabaly, F.; Yoon Heayoung, P.; Léonard, F.; Allendorf Mark, D., Tunable Electrical Conductivity in Metal-Organic Framework Thin-Film Devices. *Science* **2014,** 343 (6166), 66-69.

List of abbreviations

● Symbols

Symbols	English
°C	Celsius degree
T	Temperature
K	Kelvin degree
(h k l)	Miller indices
σ	Conductivity
C	Current rate
E_F	Fermi energy
λ	Wavelength
mA	Milliampere
h	Hour
g	Gram
T	absolute temperature
cm	Centimeter
mm	Millimeter
μm	Micrometer
nm	Nanometer
Li^+	Lithium ions
Zn^{2+}	Zinc ions
ΔG	Gibbs free energy
E_g	Bandgap energy
N_2	Nitrogen
NO	Nitrogen monoxyde
NO_2	Nitrogen dioxide

● Abbreviations

Abbrevitions	Full name
BET	Brunauer-Emmett-Teller
BE	binding energies
CVs	cyclic voltammograms
CE	coulombic efficiency
CVD	chemical vapor deposition
COFs	covalent organic frameworks
CP-MAS	cross-polarization magic angle spinning
DFT	density functional theory
DoS	Density of States
DSC	differential scanning calorimetry
EDS	energy-dispersive X-ray spectroscopy
EIS	electrochemical impedance spectroscopy
E_v	valence band
FTIR	Fourier transform infrared spectroscopy
FE-SEM	field emission scanning electron microscopy
GCD	galvanostatic charge-discharge
MOFs	Metal-organic frameworks
NMR	nuclear magnetic resonance
PSM	post-synthetic modification
PTFE	Poly(tetrafluoroethylene)
PVB	Polyvinyl butyral

PXRD	powder X-ray diffraction
SEI	Solid electrolyte interphase
SHE	Standard hydrogen electrode
SEM	Scanning electron microscopy
STEM	scanning transmission electron microscopy
SNW	Schiff base network
TEM	transmission electron microscope
TGA	thermogravimetric analysis
TpPa	triformylphloroglucinol phenylenediamine
TCNQ	7,7,8,8-tetracyanoquinodimethane
TFPT	1,3,5- tris-(4-formyl-phenyl) triazine
UV	Ultraviolet
Vis	visible light
UIO	University of Oslo
ZIB	zinc-ion battery

Table of contents

Chapter 1 Introduction

This Chapter introduces metal-organic frameworks (MOFs), covalent organic frameworks (COFs), and the formation of their hybridized structures, referred to as MOFs@COFs hybrid porous materials. Various fundamental aspects (*e.g.*, definition, classification, application, *etc*.) as well as their physical-chemical properties will be discussed.

1.1 Metal-organic frameworks (MOFs)

1.1.1 Definition of MOFs.

Metal-organic frameworks (MOFs), also known as metal-organic skeletal materials, are a class of crystalline materials with a periodic network structure resulting from the molecular self-assembly of metal ions or clusters and organic ligands as depicted in Figure 1.1. Because of their porous nature, they are also known as porous coordination polymers.[1]

Metal ions or clusters   **Organic linkers**   **Metal-organic framework**
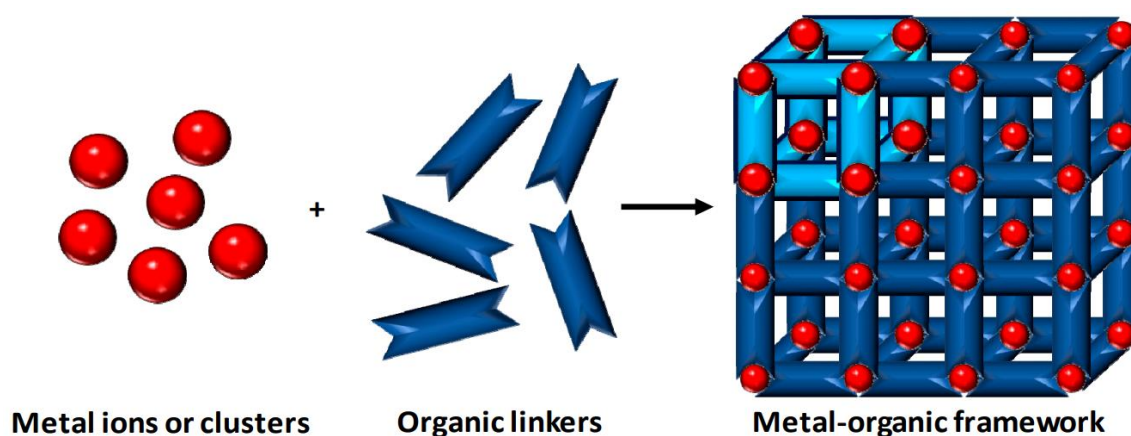
Figure 1-1 Schematic representation of a MOF synthesis. Adapted from Ref.[2]

In the last two decades, the term MOFs has become increasingly common due to the proliferation of organic ligands and their coordination with metal ions (*e.g.*, Zn^{2+}, Co^{2+}, Cu^{2+}, Mg^{2+}, Ni^{2+}, Al^{3+}, Zr^{4+}) to form novel structural complexes, which is one of the fastest-growing directions in the field of coordination chemistry in the last decade and is a new research topic encompassing organic, inorganic and coordination chemistry.

1.1.2 Classification of MOFs

Plethora of MOFs have been discovered by researchers since Yaghi's group (University of California, USA) reported the first MOF structure in 1999. MOF-5 with the formula $Zn_4O(BDC)_3$, where BDC^{2-} = 1,4-benzodicarboxylate was found to exhibit specific area as high as 2900 cm^2g^{-1}. The discovery of the MOF-5 is therefore considered a milestone in the study of MOF compounds.[3] Since then, various types of MOFs have been synthesized from molecular building blocks and the classification of MOFs based on dimensionality can be divided into 1D coordination polymers, 2D and 3D MOFs as depicted in Figure 1-2.
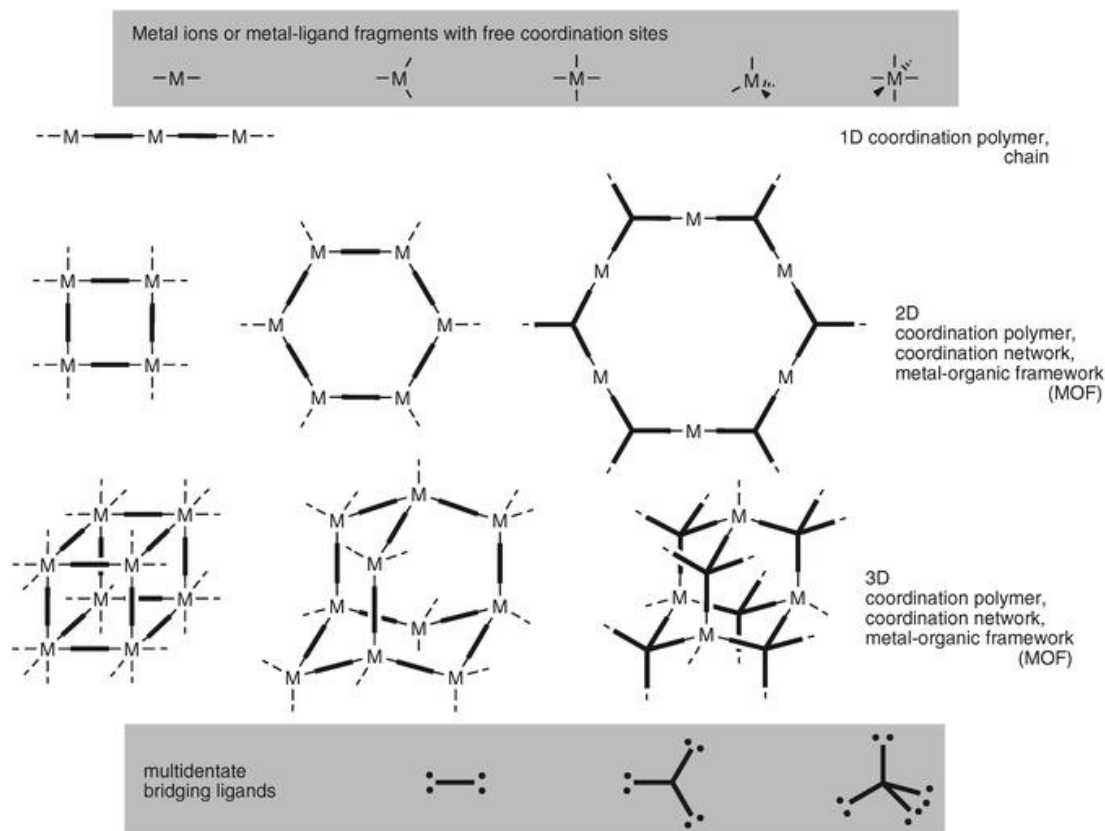
Figure 1-2 Classification of MOF, Adapted from Ref. [4]

The molecular building blocks are also termed as secondary building units (SBUs), including inorganic and organic SBUs. The design and synthesis of MOFs depend on reticular chemistry, which allows the design of specific structures through the selection of organic and inorganic SBUs. The inorganic SBUs determine the node connectivity and the organic linker indicates the number of nodes that will be interconnected. Figure 1-3 shows several representative examples of MOFs and their respective SBUs. One of the most representative examples are the families of UIO (University of Oslo, Norway) MOFs.
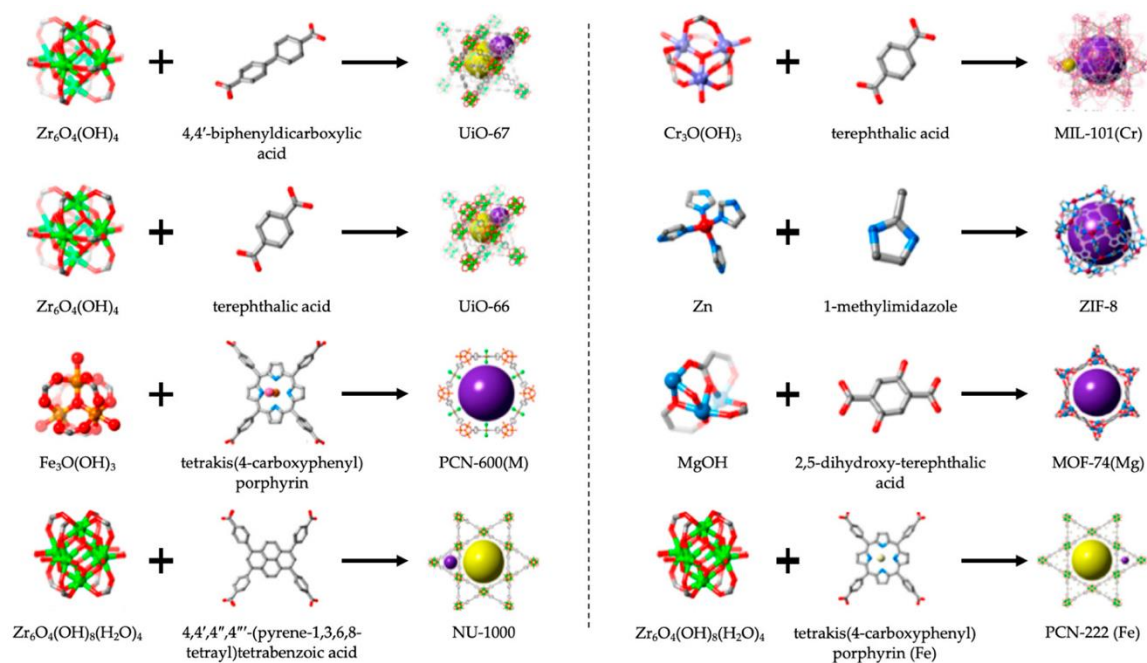
Figure 1-3 Examples of different MOFs structures with their corresponding SBUs. Adapted from Ref.[6]

This group of MOFs is characterized by the same topology and skeleton but different functionalization and pore dimensions due to changes introduced in the organic linker, such as increasing its length or the incorporation of different functional groups.[5]

1.1.3 General synthetic approaches towards MOFs

The preparation of MOFs follows common strategies to obtain crystalline structures such as conventional liquid-phase synthesis, diffusion approaches, solvothermal synthesis, sonochemical synthesis, microwave synthesis, and electrochemical synthesis methods. As illustrated in Figure 1-4a, the sonochemical synthesis process explores ultrasounds as source of heat driving the reaction and generation of MOFs, and a mixture of substrate solution for the required MOFs structure is introduced into a horn-type Pyrex reactor with a sonicator bar along with adjustable power output without any external cooling. As shown in Figure 1-4b, the conventional solution method relies on the use of organic ligands, metal elements, and other raw materials mixed in a solvent by stirring for a specified period at a fixed temperature. The diffusion method includes liquid phase diffusion and gas-phase diffusion. The liquid phase diffusion method uses an 'incompatible' solvent in which organic ligands and metal ions are dissolved to form MOF crystals because metal ions

and organic ligands contact surface reactions. Whereas in the gel diffusion method, the MOFs crystals are obtained in the gel phase as two branches of solution with center metal ions and gel substance dispersed with organic ligands. In the gas phase diffusion method, MOFs are generated by volatile organic ligands solution when there is a sufficient reaction by mixing between center metal ion solution and organic ligands solution (Figure 1-4c). The microwave synthesis methods employ microwaves, which cause the interaction between mobile electric charge and electromagnetic radiation *via* the energy obtained through irradiation of a solid or liquid state mixture with microwaves. (Figure 1-4g). The electrochemical synthesis of MOFs comprises a battery cell and cathode plates, in which the anode and cathode are immersed in an electrochemical medium (bath), including organic ligands and a metal salt, as shown in Figure 1-4f. The solvothermal synthesis method is also referred to as the hydrothermal synthesis method, in which water is used as a solvent, and organic ligands, metal ions, and reaction solvent with regulators at a certain ratio are mixed continuously in polytetrafluoroethylene liner for a definite time at a specified temperature as shown in Figure 1-4g.
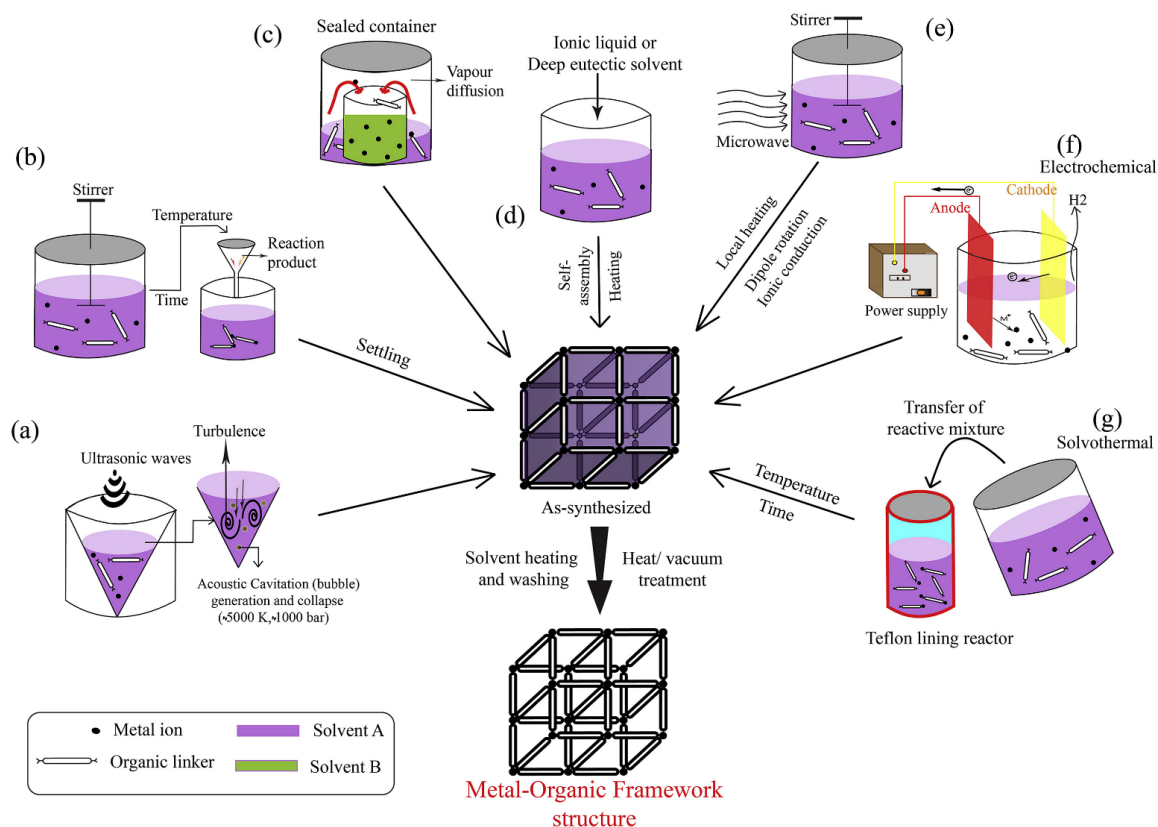
Figure 1-4 Different synthetic approaches towards MOFs, (a) Sono-chemical synthesis method, (b) Conventional solution method, (c) Diffusion synthesis method, (d) Iono-thermal process method, (e) Microwave synthesis method, (f) Electrochemical synthesis method, and (g) Solvothermal synthesis method. Adapted from Ref.[7]

1.1.4 Properties of MOFs

The MOF properties can be varied by selecting appropriate starting components. Noteworthy, not only the selection of structure constituents is important but also the manner, in which they are connected. Studying the formation of a framework from building units has revealed some regularities that can be used to predict the properties of synthesized MOFs.[8] Some MOFs

have been reported expressing more than one unique characteristics, with the most common ones being illustrated in Figures 1-5. It includes structural diversity, high chemical stability/thermal stability/surface area, and tunable pore sizes.
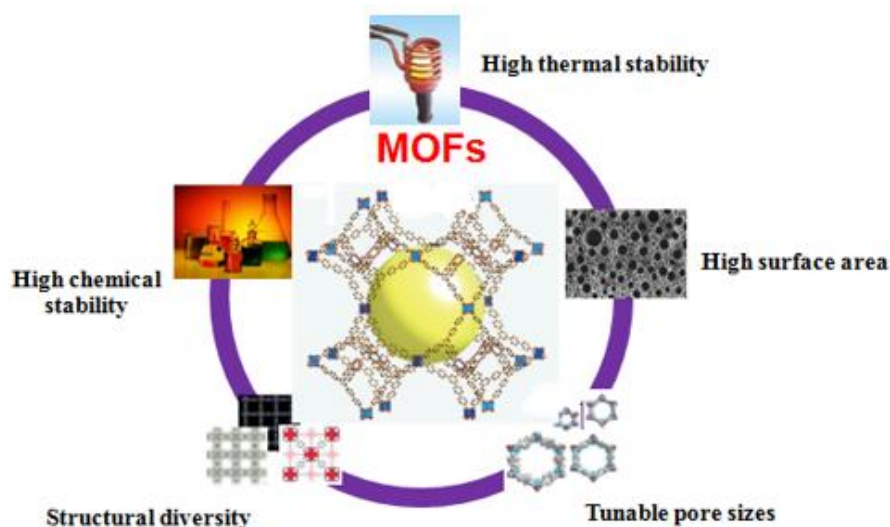
Figure 1-5 Illustration of common properties of MOFs in literature.

The structural diversity of the MOFs is mainly affected by the large number of coordination geometries adopted by the metal ions and the use of SBUs, the geometrical characteristics, the flexibility of the organic ligands, the role of the counterions, and the reaction solvent.[9] The network topology and dimensionality of the MOFs are strictly related to the different coordination geometries that can be adopted by the metal nodes, which vary depending on the electronic structure of the metal ions. Transition metal ions, especially those of the first row, lanthanides, and alkaline earth metals have been used because they display a wide variety of coordination numbers,

geometries, and oxidation states, thus, offering structural diversity.[10]

The chemical stability of MOFs refers to their ability to maintain their long-ranged ordered structure in a certain chemical environment. The strength of coordinate bonds is believed to be responsible for the thermodynamic stability of MOFs.[11] Thus, the stronger the coordinate bonds are, the more stable framework is expected to be formed.

Concerning the high surface area of MOFs, it is worth pointing out that MOFs are a class of ultra-porous materials with an exceptionally high accessible surface area due to the framework produced by the inorganic nodes coordinated by organic bridging ligands.[12] These surface areas can range from 1000 to 10 000 m^2 g^{-1}, thus exceeding other porous materials such as mesoporous-based oxides, zeolites, and carbons.[13]

1.2 Covalent-organic frameworks (COFs)

1.2.1 Definition of COFs

Covalent organic frameworks (COFs) are a class of crystalline porous organic polymers with permanent porosity and high-ordered structures that form two- or three-dimensional structures through reactions between organic precursors.[14] With an appropriate selection of COF secondary building units (SBUs), or precursors, the final structure could be predetermined, and

9

modified with exceptional control enabling fine-tuning of emergent properties.[15]

1.2.2 Classification of COFs.

In terms of the classification of COFs, depending on the dimensions of the building blocks, the resulting COFs can be divided into 2D and 3D COFs as shown in Figure 1-6.
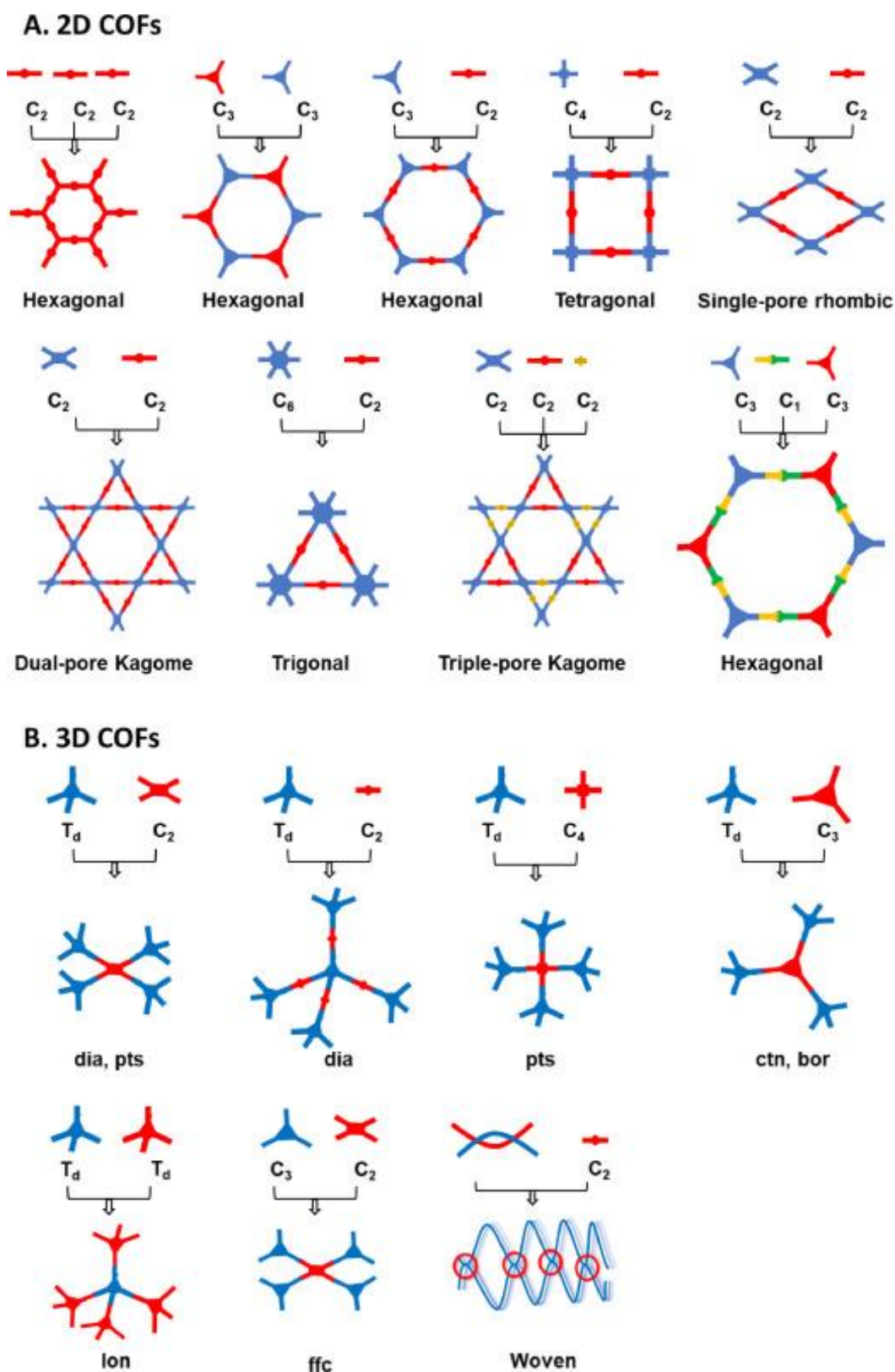
Figure 1-6 The basic topological diagrams for the design of A 2D COFs, and B 3D COFs. Adapted from Ref.[16]

In 2D COFs, the monomers usually need to be rigid and planar, and their reactive building sites should be located at a concerned geometry in order to assure the right orientation of each linkage bond in the resulting COFs. Therefore, the combination of planar monomers restricts the linkage of covalent bond formation to be in a plane with specific topologies.[17] Moreover, in 2D COFs the correlative position of adjacent layers is frequently π-π stacking controlled and directed by interlayer interactions.[18] In this sense, the monomer units in each layered 2D COFs are overlapped, maximizing the attractive energy.

In 3D COFs, the formation of the polymer backbone can be grown in all directions compared with 2D COFs, but the design of these 3D structures requires at least one of the monomers to own a Td or orthogonal geometry to allow the formation of all covalent bonds. However, the synthesis of appropriate organic molecules with 3D symmetries is rather difficult, which hampers the development of novel 3D networks. What's more, controlling multifold folding and interpenetration in these structures remains a challenge during the synthesis, which makes 3D COFs barely predesign able and limited structural diversity.

1.2.3 General synthetic approaches towards COFs

Since Yaghi and co-workers firstly introduced COFs in 2005, COFs have been formed by reversible reactions such as condensation of two-dimensional (2D) and three-dimensional (3D) organic building precursors.[14, 19] They usually comprised light elements (such as H, B, C, N, O) and are linked by robust covalent bonds *via* reticular chemistry. The most commonly used organic reaction and linkages for the synthesis of COFs is shown in Figure 1-7, yielding the production of stable COFs by making use of reversible or irreversible bonds through different condensation. Yaghi *et al.* pioneered the study of COFs through the co-condensation of boronic acids and catechol to form the five-membered boronic esters as connectors between the building units, as well as through the self-condensation of boronic esters to form boroxine (Figure 1-7 a, b).[20] Since then, various types of condensation reactions have been employed to synthesize COFs. Among them, stable COFs have been produced by introducing imine bonds, through the condensation of aldehydes and amines (Figure 1-7 c), After the full exploitation of the imine-based COFs, different linkages based on the formation of C-N bonds were explored. This includes the hydrazone linkage which is formed by the reaction of aldehydes with hydrazides in the presence of a catalytic amount of AcOH and azine linkages formed *via* condensation of hydrazine with ketones and aldehydes enabled the formation of highly stable COFs (Figure 1-7 d, e).[21, 22]

Moreover, the chemical stability has been improved with the synthesis of β-ketoenamines and primary amines, through irreversible enol-keto tautomerization, creating robust networks that resist strong acids and bases (Figure 1-7 f, g).[23] When the linkage is less reversible, high reaction temperatures are needed for the formation of the structure. In order to enhance the π-conjugation and chemical stability of the COFs framework, one of the methods is to develop C=C linked fully π-conjugated COFs (Figure 1-7 k). The first example was achieved *via* the Knoevenagel condensation of aldehydes and cyanides catalyzed, affording a cyanovinylene-based COF.[24] Furthermore, in 2019 a series of olefin-linked COFs were successfully synthesized by the reversible aldol condensation of aldehydes and s-triazine derivatives (Figure 1-7m).[25] Due to their robust skeleton and π-extended conjugation, olefin-linked COFs present outstanding thermal and chemical stabilities, even in the presence of strong acids or bases.[26] Besides the previously discussed linkages employed in the synthesis of COFs, some types of squarine-linked COF enable the formation of a zwitteronic structures within the pores of a COF,[27] and phenazine linkage with the fused planar structure of π-conjugated and stable COFs,[28] as well as the double-stage linkage approach with a bifunctional building block that can allow the formation of two different linkages for the synthesis of one COF.[29]
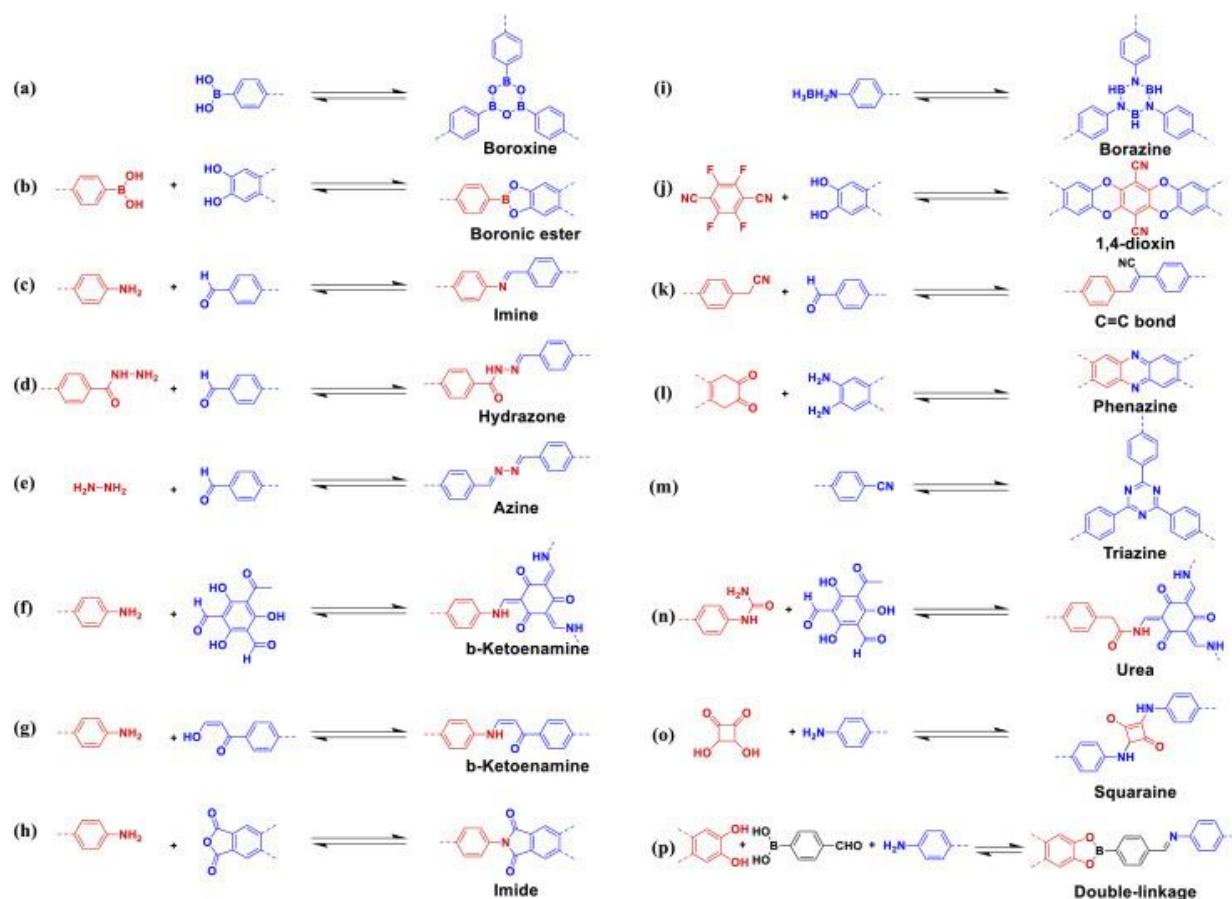
Figure 1-7 The condensations of widely used types of linkages in synthesis COFs: (a) boroxine, (b) boronic ester, (c) imine, (d) hydrazone, (e) azine, (f, g) β-ketoenamine, (h) imide, (i) borazine, (j) 1,4-dioxin, (k) C = C bond, (l) phenazine, (m) triazine, (n) urea, (o) squaraine, and (p) double-linkage. Adapted from Ref.[30]

Noteworthy, the rapid progress in the field of COFs is mainly due to their self-healing abilities and thermodynamically controlled dynamic covalent chemistry concerned in their assembly which leads to a long-range ordered crystalline structure.[31] Different from MOFs, the densities of COFs are usually lower and thus they exhibited excellent stability in organic solvents, and even under varying basic; acidic; reductive, and oxidative conditions. In

addition, COFs can be stable in harsh conditions and can retain their ordered structure and crystallinity. This is because of the metal-free skeletal structure connected *via* strong covalent bonds rather than coordination bonds that hold together the mooieties forming MOFs. Until now, the reported methods for synthesis COFs mainly include mechanochemical, solvothermal, ionothermal, sonochemical, microwave, and light-promoted methods, along with the properties and advantages of each synthetic method exhibited in Figure 1-8. Typically, the olefin-linked COFs are obtained by solvothermal methods, which is similar to classical protocols employed for the synthesis of inorganic zeolites in autoclaves. This contains the mixing of monomers in a specific organic solvent in a Pyrex tube with degassing sealing and heating at a specific temperature for a given reaction time. After that, the obtained products were washed and dried to produce solid powdered COFs. Therefore, we employed this method to synthesize olefin-linked COF-TMT-BT, and the related synthesis details are discussed in experimental Chapter 2.
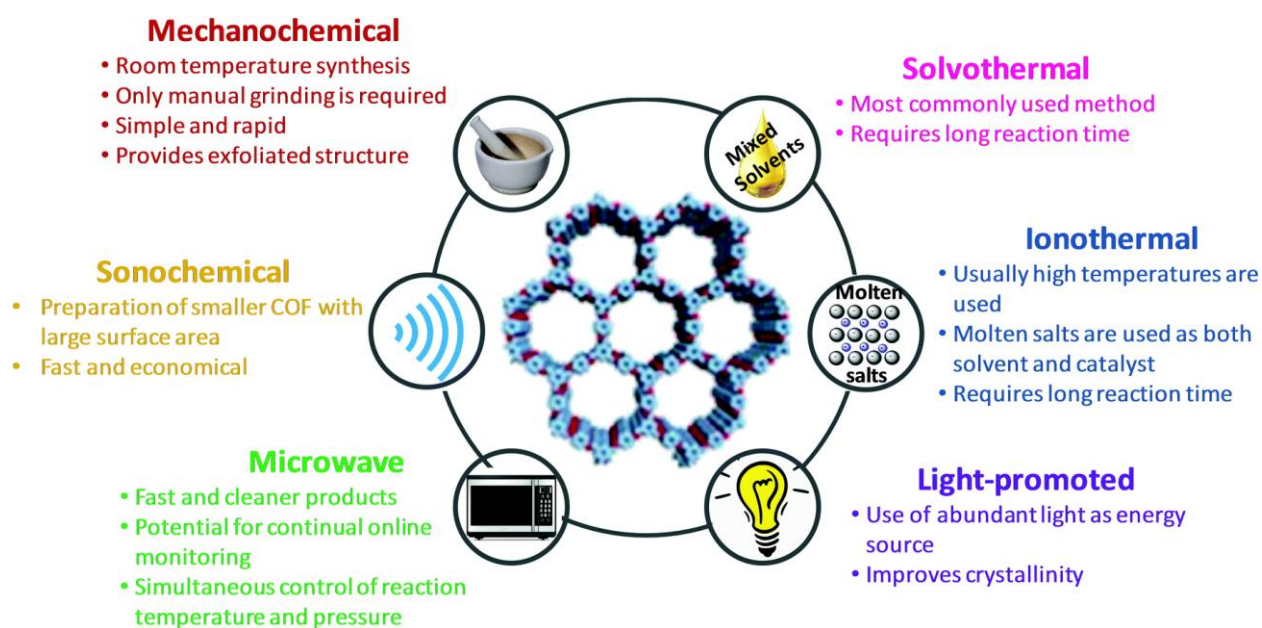
Figure 1-8 The properties and advantages of various synthetic methods of COFs.
Adapted from Ref.[32]

1.2.4 Properties of COFs

The most important property of COFs is their high porosity. The porosity is an intrinsic property of COFs, the molecular structure of building blocks governs the porosity of COFs, the length of building blocks determines the pore size of COFs, and the geometrical shape determines the topological structures of COFs through the assembly of building blocks in 2D or 3D frameworks as shown in Figure 1-9, which can constitute periodic and uniform voids that can be designed to meet specific requirements of shape, size, and functionality. Therefore, the concrete pore size can be tuned ranging from micropore to mesopore (0.64-5.3 nm) and they can be used as platform with

different functional groups to successfully interact with different guest.[33]
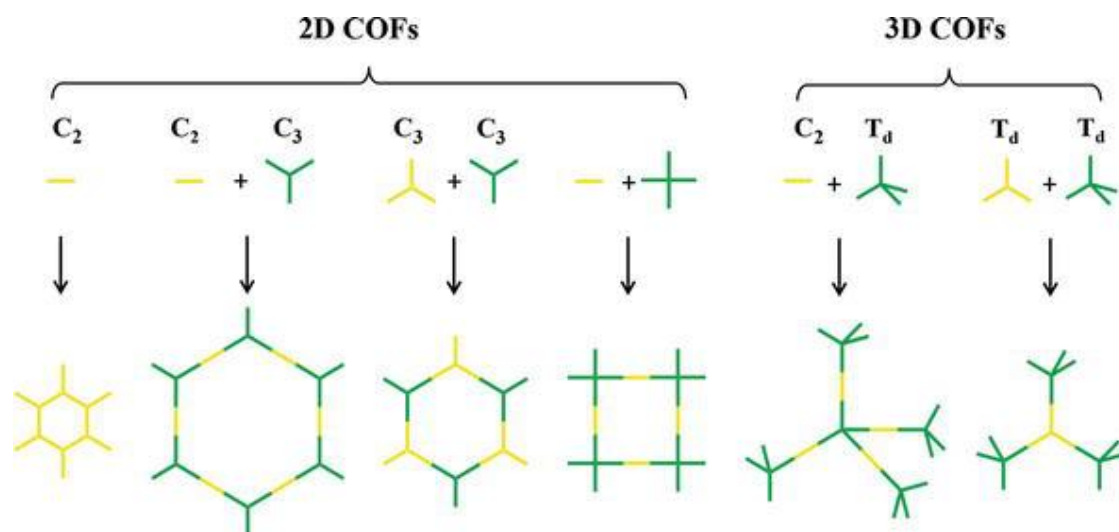
Figure 1-9 The combination of building blocks with different geometries to design COFs, Adapted from Ref.[30]

The porosity of COFs not only strongly relies on the size and molecular weight of the building units but also on the crystallinity of the network. It is of big interest to explore the full potential of porosity in COFs since enhanced surface area and large pore volume can be thus achieved. Even though some COFs display an exceptional porosity, with outstanding theoretical surface areas of 5070 $m^2\ g^{-1}$, in some cases the dense π clouds from monomers forming the COF skeleton in 2D COFs hinder the development of high porosity. Something similar happens to 3D COFs, whose porosity can be partially inhibited by the folded structures. For these reasons, activation of COFs, commonly referred to as the elimination of trapped volatile molecules from the pores, is a crucial step that can strongly influence the final porosity and

surface area of the material, and therefore its performance. The most widely spread strategies for COF activation include solvent exchange and evacuation at high temperatures under reduced pressure and drying with supercritical carbon dioxide.

Crystallinity is another key property that makes COFs different from other organic polymers, whose monomers are randomly placed within an amorphous structure. Furthermore, many of the unique properties of COFs arise from their structural order. However, understanding and rationalizing the factors that control the long-range order in these materials remains a challenge, especially due to the huge variety of linkages and building blocks described in the literature. Several reported studies indicate the evident and basic principle that crystallinity requires the reversible formation of covalent bonds,[34] since this allows the correction of wrongly formed linkages during the polymerization process. The possibility of removing these defects in the framework successfully leads to a crystalline structure. Other important parameters affecting the crystallinity of the framework are related to the selected building blocks: their solubility, their geometry, and their functionalization. A great example is the functionalization of aldehydes with -OH groups in imine COFs.[35, 36] The hydroxy group can readily establish a hydrogen bond with the vicinal imine linkage, granting not only superior stability to the resulting COF but also higher crystallinity in comparison to the

-OMe functionalized structures. These hydrogen bond interactions favor the planarization of the COF skeleton, minimizing the interlayer repulsion of the stacked COF layers and stabilizing interlayer adhesion.

Stability is another key property that also makes COFs different from other organic polymers due to the strong covalently bonded skeleton, COFs are thermally and chemically very stable compared to conventional polymers or their counterparts MOFs. Under an inert atmosphere, most COFs are thermally stable between 300 and 450 ℃. This makes them interesting materials for carbonization processes, which render new properties to the COFs while their skeleton is preserved. Robust chemical bonds enhance the chemical stability of COFs. However, they also affect the reversibility of the COF polymerization reaction, which can result in a lower crystallinity. For instance, boroxine linkage has a higher degree of reversibility compared to the imine bond. Therefore, boroxine-based COFs are generally more crystalline than imine-linked COFs, while they display much lower chemical stability and are easily hydrolyzed under humid or protic conditions.[37] Among nitrogen-based linkages, covalent triazine frameworks (CTFs) have shown outstanding chemical stability towards hydrolysis, extreme pHs, and oxidative conditions due to the formation of the triazine units.[38] Knoevenagel condensation or benzoxazole formation can be also considered when designing highly stable COFs. The chemical stability of COFs can be further improved by

strengthening the interlayer non-covalent interactions, like intralayer hydrogen-bonding or interlayer complementary π-interactions.[39] In addition, inducing the tautomerization of some linkages to a more stable bond, like the enol-keto tautomerization in some imine COFs, can also increase the stability of the resulting network.

1.3 MOFs@COFs hybrid materials

1.3.1 Definition of MOF@COF heterostructures.

Recently, a new class of hybrid architectures which combine the unique features of the individual MOF and COF components have attracted enormous attention. Hybridization of MOFs with COFs (and *vice versa*) enables generation of materials displaying novel physicochemical properties. For example, the MOF@COF heterostructures were synthesized by growing guest COFs on already existing host MOFs in an anisotropic/isotropic manner or through core-shell hybrid approaches.[40] The generated MOF@COF-based hybrids have shown synergistic performances between each component because they inherit the native properties of both MOFs and COFs, which makes them multi-functional materials and demonstrates improved properties and renders them applicable in wider spectrum of applications.[41] Moreover, new properties can be introduced through the hybridization of MOFs with

COFs including the electrochemical characteristics, which can be increased by the rapid electron transport enabled by the presence of the COF layer. At the same time, the obtained quasi-microscaled pores at the interface between COFs and MOFs provide a large specific surface area and large pore volume for the MOF@COF hybrids, accompanied by increased electrochemically active sites, which can be explored for improving electrochemical activity of the material. Therefore, the MOF/COF hybrids have been intensively explored to boost the performances in various devices, with the timeline of representative works of reported MOF/COF -based heterostructures being portrayed in Figure 1-10.
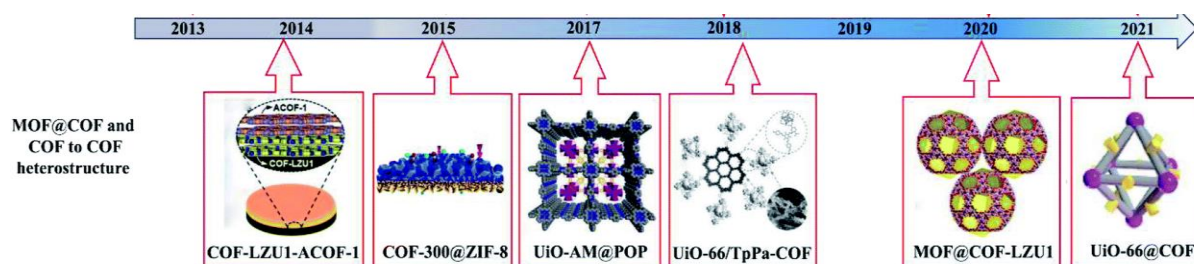

Figure 1-10 The timeline of representative works reported on MOF/COF-based heterostructure hybrids.

1.3.2 Classification of MOF@COF heterostructures.

Although many individual COFs and MOFs have been successfully synthesized and applied in different fields, their exploration and applications are still less than satisfactory because of the limited types and monomer structures. The obtained MOF@COF heterostructures can be obtained by combining different types of COFs and MOFs. Hitherto, the growth of MOF@COF porous hybrids mainly focuses on the formation of an imine bond (-C=N-) between the doped -NH$_2$ groups on the MOFs and the aldehydes (-CHO) monomer in COF through a condensation reaction.[42] In particular, the series of UIO-MOFs and MIL-MOFs are commonly used for the fabrication of MOF@COF heterostructures because of their high chemical stability, flexible synthetic strategies, and good crystallization.[43] Therefore, the classification of the current reported MOF@COF hybrids can be summarized according to their MOF type.

UIO-based MOF@COF

Different types of UIO-66 and UIO-related MOFs have been combined with various nanomaterials to enhance their potential applications.[44] A series of UIO-66-based MOF@COF hybrids were synthesized through the imine covalent binding of the functional groups of COF on MOFs.[45] For example, Zheng and co-authors synthesized a nanoscale UIO-AM@COF by using UIO-

type nanoscale MOFs as self-template as shown in Figure 1-11 (a).[46] In particular, the authors used an amine-based porphyrin molecule as a core and various functional-substituted tetraphthaladehydes as shell and obtained various MOF/COF hybrids with 2D networks. In 2018, Zhang, Cheng and co-authors synthesized NH_2-UIO-66/TpPa-1-COF nano-particles by covalently linking COF-TpPa-1 on the surface of MOF-NH_2-UIO-66 as shown in Figure 1-11(b).[47] Recently, Qi and co-authors reported a novel MOF@POP composite (UIO-66@SNW-1) through a Lewis acid site of Zr^{4+} clusters in UIO-66 and Brønsted base sites with amino groups in SNW-1 as exhibited in Figure 1-11(c).[48] More recently, Yao and co-workers reported a UIO-66@COF-2 hybrid porous material for eliminating aggregation-caused quenching and enhancing the emission of COFs as shown in Figure 1-11 (d),[49] in which the UIO-66-NH_2 crystals were selected as the MOF core, while the -NH_2 group on UIO-66-NH_2 could be used as active sites for synthesis of a COF-2 layer *via* a Schiff base reaction. Consequently, the UIO-66 core not only improves the bulky COFs formation but also boosts the sensing selectivity for adenosine triphosphate (ATP) owing to the high electron affinity of Zr^{4+} with the phosphate group.

More recently, Chen and co-authors reported a novel core-shell NH_2-UIO-66@TFPT-DETH as photocatalyst.[50] Herein, the TFPT-DETH COF was researched as the shell layer because of its high stability. For the preparation of the core-shell hybrids, the TFPT monomer was anchored on the surface of

MOF-NH$_2$-UIO-66, forming NH$_2$-UIO-66@TFPT through the Schiff-base reaction between the aldehyde group and amino group on NH$_2$-UIO-66 and the pre-coated TFPT molecules.
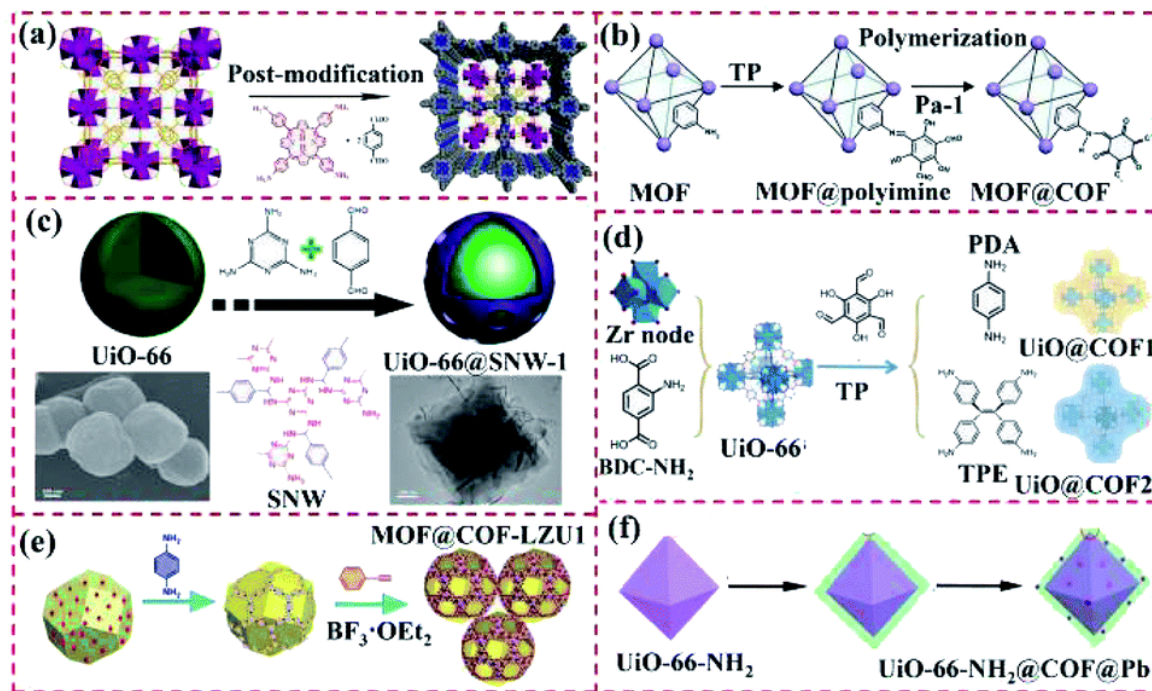
Figure 1-11 Structure of UIO-based MOF@COF heterostructures. (a) Adapted from Ref.[46] (b) Adapted from Ref.[47] (c) Adapted from Ref.[48] (d) Adapted from Ref.[49] (e) Adapted from Ref.[42] (f) Adapted from Ref.[51]

In 2020, our group reported a functional aza-MOF@COF hybrid material with a robust porous structure from MOF@COF-LZU1 precursor by aza-Diels-Alder cycloaddition, the details can be found in this thesis Chapter 4. Typically, the porous aza-MOF@COF hybrid was synthesized using the following three steps (Figure 1-11e): (1) the surface modification of MOF-UIO-66-NH$_2$ with 1,3,5-benzenetricarboxaldehyde to obtain MOF-UIO-

66(CHO), (2) the *in-situ* growth of the COF layer on MOF-UIO-66(CHO) through condensation between the aldehydes on MOF-UIO-66(CHO) and *p*-phenylenediamine, (3) the quinolone moieties were introduced into imine-linked MOF@COF-LZU1 hybrids by post-synthetic modification protocol. The formed aza-MOF@COF hybrid displayed excellent properties when employed as a proof-of-concept application in solid-state supercapacitor electrode, giving a specific capacitance of 20.35 $\mu F\ cm^{-2}$ and high volumetric energy density of 1.16 F cm^{-3}. In addition, the aza-MOF@COF based electrode showed outstanding long-term stability and the capacitance maintained 89.3% after 2000 cycles compared with the original MOF and MOF@COF-LZU1 precursors. For MOF@COF hybrid materials, the MOF component can usefully modulate their surface morphology, optical performance, and catalytic properties. Therefore, the N heteroatoms located in COFs endow them with a high ability for binding Pd or Pt atoms. For example, Zhu and co-authors provided a new UIO-66-NH_2@COF@Pd hybrid using UIO-66-NH_2 as the core and the covalently linked COF as the shell. As shown in Figure 1-11f, the synthesized UIO-66-NH_2@COF@Pd hybrids had a hierarchical porous structure with abundant Pd nanoclusters exhibiting excellent catalytic performances.[51]

MIL-based MOF@COF.

Some MOFs' crystals such those developed in MIL (Materials Institute Lavoisier, France) bear a functional amino group (such as NH_2-MI-68, NH_2-MIL125(Ti) MOF, and NH_2-MIL-101(Fe)), which can further covalently link with the aldehyde or carboxyl groups in the building shell of COFs, thus leading to the tight binding of MOFs and COFs (Figure 1-12 a). Hence, exploring the series of NH_2-MIL-MOF@COF hybrids could extend their potential applications. For example, Zhang's group synthesized NH_2-MIL-8@TPA-COF and explored it as an effective photodegradation catalyst as shown in Figure 1-12b. After the MOF NH_2-MIL-68 was post-modification with tris(4-formylphenyl) amine (TFPA), the TPA-COF was formed around the NH_2-MIL-68(CHO) surface by connecting TFPA and tris(4-aminophenyl)amine (TAPA) *via* an easy condensation synthesis method to obtain the NH_2-MIL-68@TPA-COF hybrid material. In addition, the Ti-based MOFs could always exhibit superior photocatalytic ability because of their redox ability and photocatalytic performances. For example, Sun and co-authors reported a Pd-doped core-shell MOF@COF hybrid by using Ti-ATA and the imine-based COF-LZU1 as the core and shell, respectively.[52]
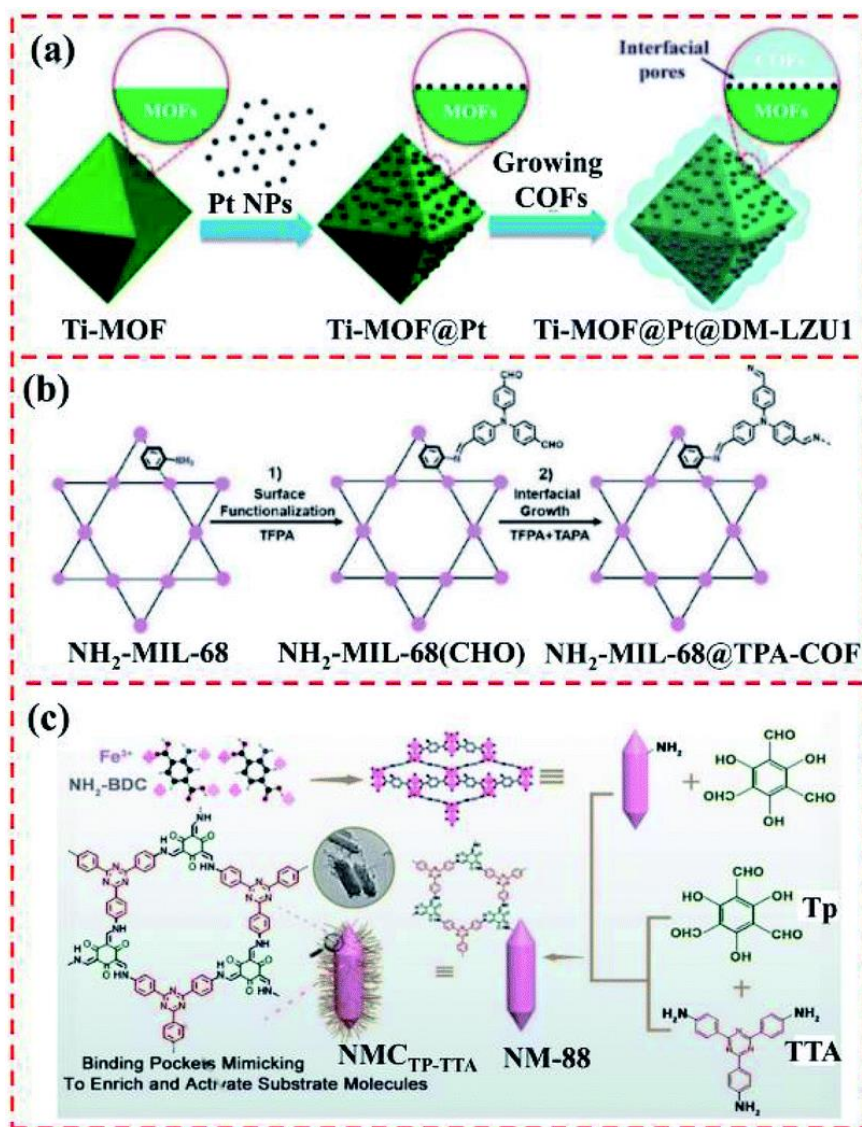
Figure 1-12 Structure of MIL-MOF-based MOF@COF heterostructures. (a) Adapted from Ref.[53] (b) Adapted from Ref.[54] (c) Adapted from Ref.[55]

In 2020, Zhang and co-workers reported a nature-inspired MOF@COF nanozyme named NMCTP-TTA by using NH_2-MIL-88 (Fe) as a model nanozyme, and the COF-TP-TTA layers were grown around NH_2-MIL-88B (Fe) as shown in Figure 2-9 c.[55]

Other types of MOF@COF hybrids

To date, except for the covalent linkages at the interface between amino-functionalized MOFs and aldehyde groups of COFs for the synthesis of core-shell nanostructured MOF@COF hybrids, other types of MOF@COF hybrids have also been prepared through hydrogen bonds or π-π stacking. For example, Fu and co-authors developed a ZIF-8@COF-300 hybrid composite membrane, as exhibited in Figure 1-13a, the hydrogen bonds were formed between terephthalic acid and the amine groups on the COF-300 layer, thus boosting the integration of the ZIF-8 top layer.[56] In Guo and co-authors' work,[57] their first prepared a Co-MOF *via* $Co(NO_3)_2 \cdot 6H_2O$ and 2-methylimidazole and then prepared a Co-MOF@TPN-COF through the polymerization of TPN-COF on the Co-MOF surface (Figure 1-13b). Gao and co-workers synthesized core-shell PCN-222-Co@TpPa-1 hybrid materials through strong π-π stacking which afforded multifunctional properties (Figure 1-13c).[58] Recently, a Ce-MOF@MCA nanohybrid was synthesized *via* the COF-on-MOF strategy, where MCA was prepared by reacting melamine and cyanuric acid as shown in Figure 1-13d.[59]
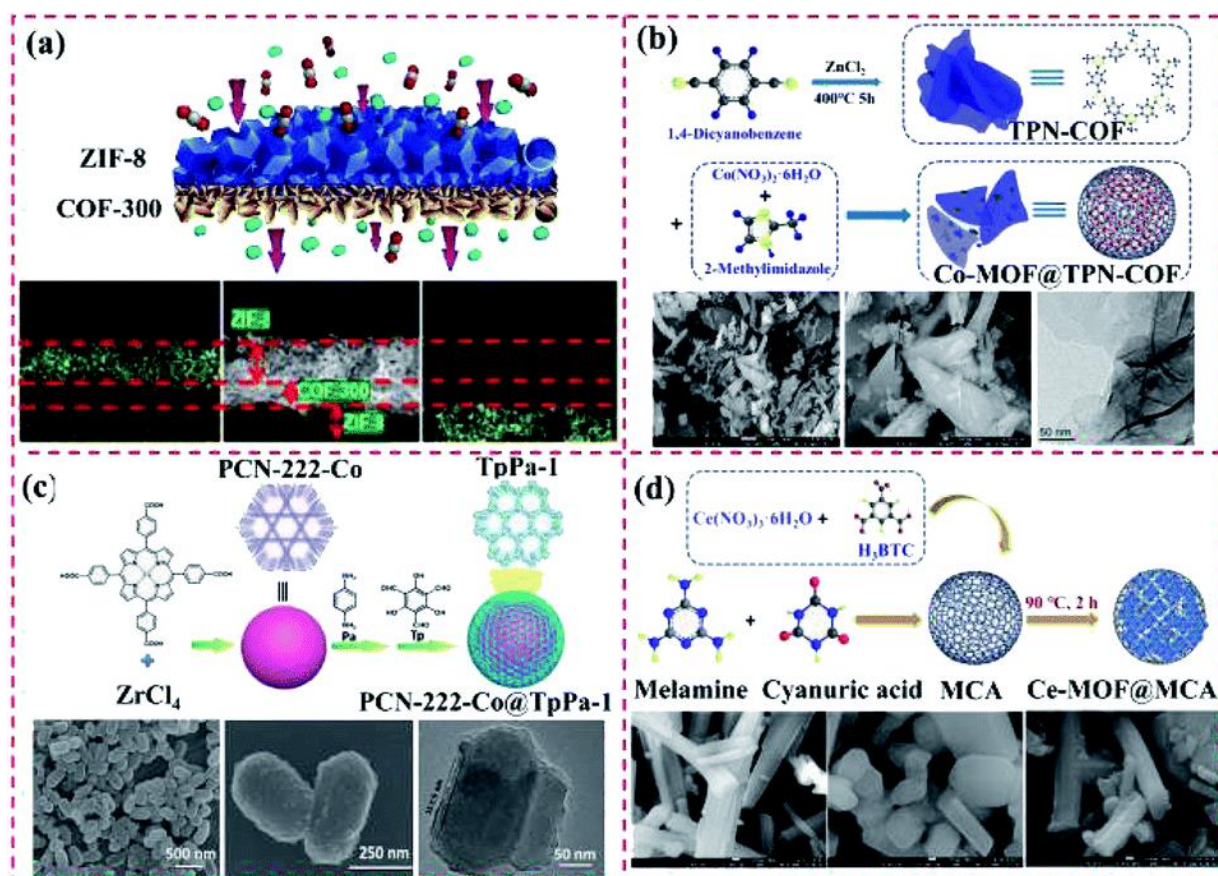
Figure 1-13 Structure of other types of MOF@COF. (a) Adapted from Ref.[56] (b) Adapted from Ref.[57] (c) Adapted from Ref.[58] (d) Adapted from Ref.[59]

1.3.3 General synthetic approaches towards MOF@COF

MOF@COF are generated *via* the condensation of amine-functionalized MOFs and amine-based COFs, yielding imine formation at the interface between the two components. However, high surface energy is commonly generated at the interfaces between different MOFs or COFs because of their various morphologies. The methods to prepare MOF@COF hybrids mainly include the interfacial design strategy, one-step synthesis

method, modular synthesis strategy, and coordination-induced approaches as shown in Figure 1-14. The interfacial design strategy involves coating specific COF layers on size-selective MOF cores to construct MOF@COF hybrids,[47] which is the most suitable method for synthesis MOFs@COFs hybrids, because the amino-functional MOFs afforded an efficient interface for binding the COF layer to fabricate excellent MOF@COF heterostructures. Therefore, we employed this method to synthesize aza-MOF@COF and MOF@COF-TCNQ (Chapter 3 and Chapter 4). The related synthesis details are discussed in experimental techniques chapter 2.

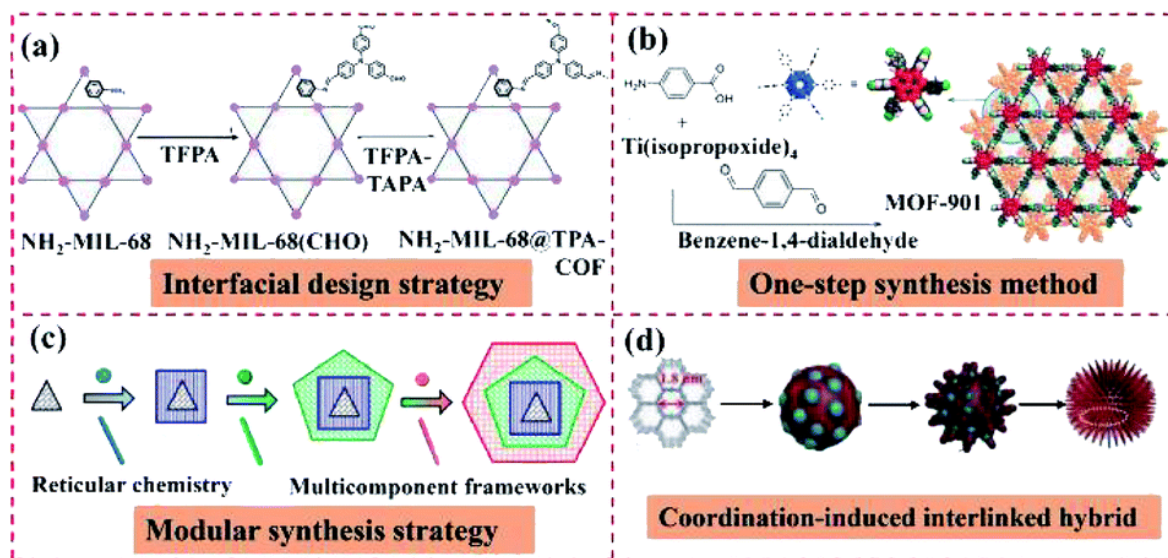**Figure 1-14** The schematic illustration of the synthesis methods of MOF@COF heterostructures. (a) Adapted from Ref.[54] (b) Adapted from Ref.[60] (c) Adapted from Ref.[61] (d) Adapted from Ref.[62]

1.3.4 Properties of MOF@COF

MOFs@COFs hybrid structures containing traits of both MOFs and COFs exhibit excellent crystal and structural performances, including tunable skeletons of both MOFs and COFs, large specific surface area and high electrochemical activity, typically superior to those of individual components. Therefore, the MOF@COF-based heterostructures have been proposed as a new type of multifunctional porous materials exhibiting advantages of individual components, to enable harvest the performance in (photo)catalysis,[52, 63] gas separation,[56] sensors,[59] bacterial inhibition[55], and lithium-ion batteries.[62] For example, because of the tunable skeleton features of both MOFs and COFs, the chemical interaction between them can be tailored, aand explored for specific applications such as diverse photocatalysis. For example, Lan's group presented an integrated porous NH_2-UIO-66/TpPa-1-COF hybrid with superior photocatalytic H_2 evolution under visible light. After modulation of its basic performances, the NH_2-UIO-66/TpPa-1-COF (4: 6) hybrid displayed a high photocatalytic H_2 evolution rate of 23.41 mmol g^{-1} h^{-1}, 20-times higher than that of TpPa-1-COF.[63] In addition, because of its large surface area, the MOF@COF heterostructure demonstrates a synergistic enhancement in gas adsorption. Maspoch's group reported a UIO-66-NH_2@COF-TAPB-BTCA nanohybrid (Figure1-15) displaying higher adsorption ability for water at the same P/P_0 than that of the pristine COF pores,

with enhanced water uptake. The N_2 and H_2O adsorption isotherms of the UIO-66-NH$_2$@COF-TAPB-BTCA cores both exhibited around 3-fold higher SBET and 2-fold higher adsorption (q_{max}) values due to the additional pores at the MOF/COF interface (Figure1-15 a and b).[64]
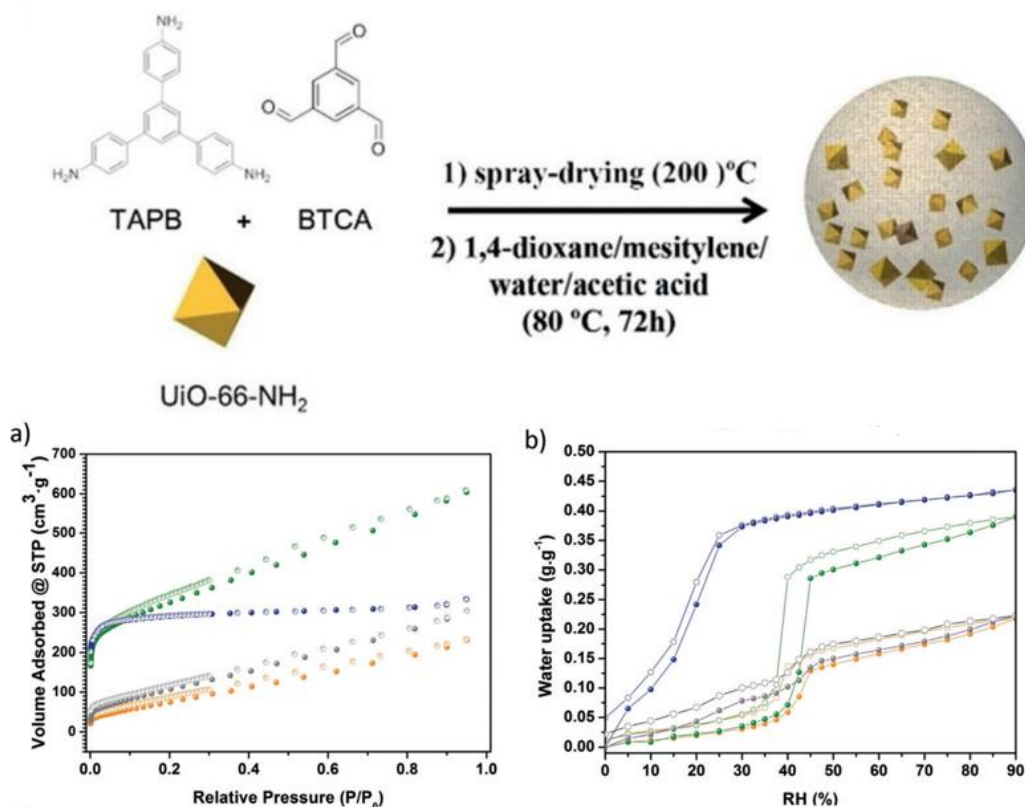
Figure 1-15 a) N_2 adsorption isotherms for UIO-66-NH$_2$ (blue), COFTAPB-BTCA beads (orange), the physical mixture of these two components (grey), and UIO-66-NH$_2$@COF-TAPB-BTCA beads (green). b) Water adsorption isotherms for UIO-66-NH$_2$ (blue), COF-TAPBBTCA beads (orange), the physical mixture of these two components (grey), and UIO-66-NH$_2$@COF-TAPB-BTCA (green).

As for the superior electrochemical properties of MOF@COF heterostructures, Wang *et al*.[62] reported a coordination-induced interlinked

hybrid of imine-based COFs and Mn-based MOFs (COF/Mn-MOF), which exhibit superior lithium storage properties compared with pure Mn-MOF and COF because of the adjustable morphology and microstructure for the COF/Mn-MOF. (Figure 1-16)
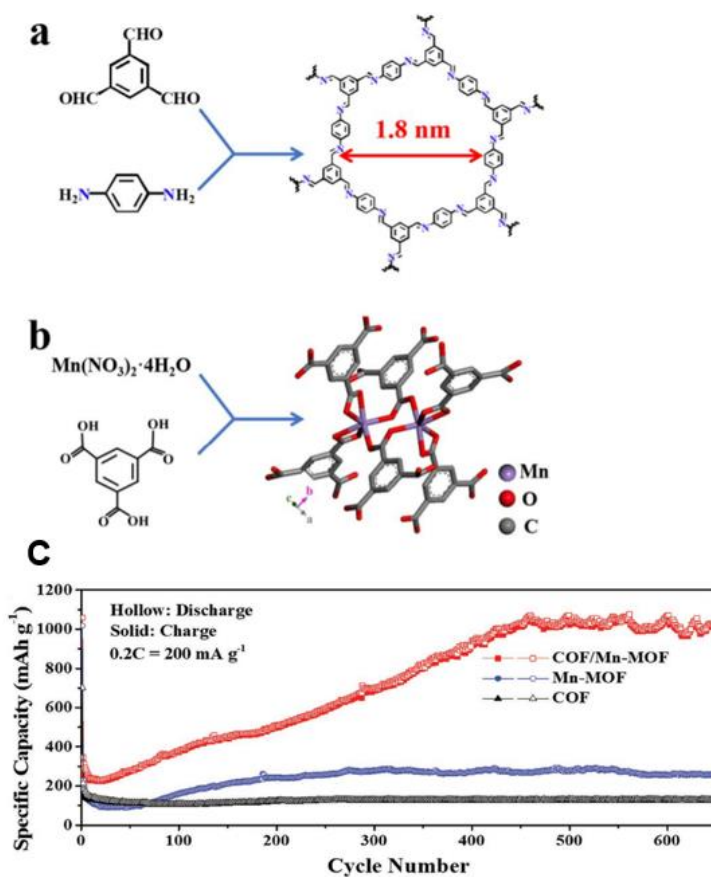
Figure 1-16 Schematic diagram showing the growth process of a) pristine COF, b) pristine Mn-MOF. c) Cycling performances of COF, Mn-MOF, and COF/Mn-MOF

1.4 Supercapacitors and aqueous Zinc-ion batteries: fundamental principles

1.4.1 Supercapacitor *vs.* Capacitor

The classical capacitor is a passive device that stores energy in an electrostatic field rather than in chemical form; it usually consists of two conducting electrodes and is separated by an insulating dielectric material as shown in Figure 1-17. The supercapacitors (SCs), also known as electrochemical double-layer capacitors (EDLCs), are a special type of capacitors which operate through charging and discharging at the electrode-electrolyte interface of the high surface area of materials. They are dominated by the same basic principles as conventional capacitors and are ideally suited to the rapid storage and release of energy. However, they incorporated electrodes with much higher effective surface areas and thinner dielectrics which result in an increase in both capacitance and energy of about 10,000 than those achieved by capacitors. [65]
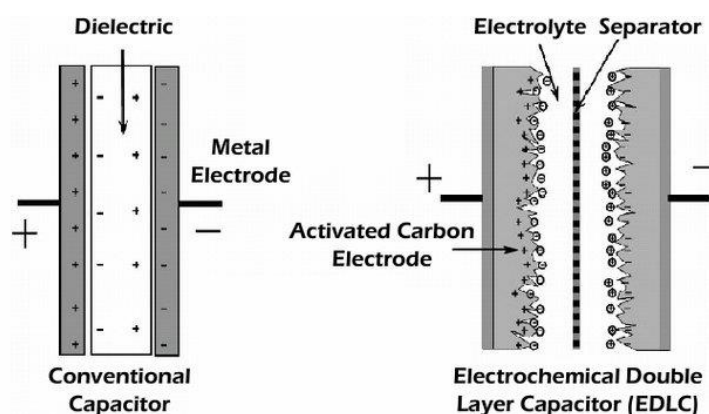
Figure 1-17 Schematic representative of capacitor and supercapacitor.

1.4.2 Types of supercapacitors

According to the nature of electrodes and the energy storage mechanism, electrochemical supercapacitors can be classified as electrochemical double layer capacitors (EDLC),[66] pseudo-capacitors[67], and quantum capacitors.[68]

Electrochemical Double Layer Capacitors (EDLCs)

In EDLCs, the charge storage by electrostatic interactions at the interface between the electrode surface and electrolyte as shown in Figure 1-18. In particular, the extra electric charges accumulate on the positive or negative electrode surfaces, while electrolyte ions with compensating charges aggregate in the electrolyte solution to maintain electrical neutrality. When the system is charged, the cations in the electrolyte shift to the negative electrode and the anions migrate to the positive electrode, and the electrons move through the external circuit from the negative to the positive electrode. In this

way, the double layer is formed at the interfaces with the electrodes. During the process of discharge, the reverse processes happen. The mechanism of electric charge generation on the surface of the electrode indicates the concentration of electrolyte remains constant regardless of the process of charging/discharging. As a result, energy accumulates in the double-layer interface.[69]
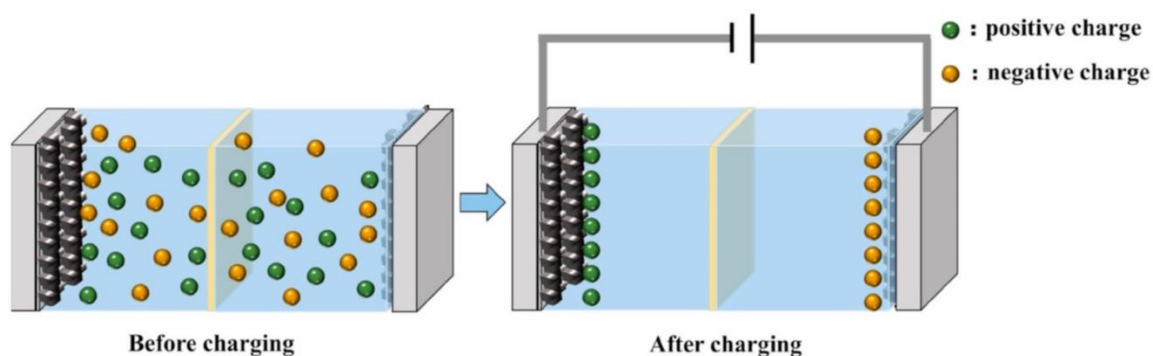
Figure 1-18 Schematic operating principle of EDLCs, Adapted from Ref [70]

Pseudocapacitors

Pseudocapacitors, also known as faradaic supercapacitors, in which energy storage relies on reversible redox reaction (faradaic process) occurring at or near the surface of electrode material and are different from EDLCs as shown in Figure 1-19. The faradaic electrochemical redox process is so fast that the device's electrochemical charge across the double layer and passes through the supercapacitor cell. These processes occurring in the supercapacitor improve the energy density and increase the specific capacitance.
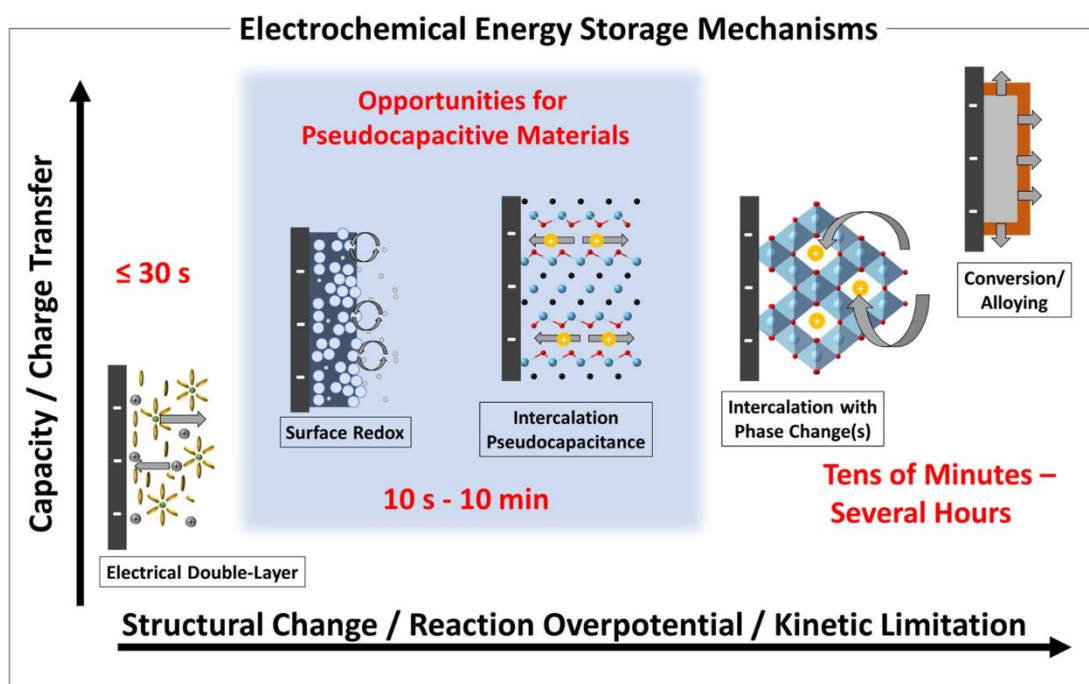
Figure 1-19 Schematic classification of pseudocapacitive energy storage mechanisms, Adapted from Ref [71]

Quantum capacitors

During the last few years, considerable efforts have been made mainly relying on the EDLCs and pseudocapacitance mechanisms. However, quantum capacitance, being one of the physical mechanisms giving rise to interfacial capacitance, is little exploited and not yet fully understood. The main difference between quantum capacitance compared with classical EDLCs and pseudocapacitance is the fact that there is no such thing as storage of charge alone and the charge of an electron is in contiguous. The traditional capacitance considering the component of electronic charge is quite different when there are only a few electrons. Only when the number of electrons is

large does the module of electronic charge stop exhibiting new features. When the size of the electrode material is below a couple of nanometers, the kinetic energy of quantum mechanically the stored electrons become dominant over the electrostatic stored energy. Xia *et al.*, and S. Ilani *et al.* reported that the quantum capacitance of graphene and carbon nanotubes might be the origin of the increased interfacial capacitance in some carbon-based electrodes.[72] Subsequently, Zhang *et al.*[73] and Song *et al.*[74] further explored this concept by introducing nitrogen or oxygen-containing (hydroxyl and epoxy) groups in graphene, which was found to be beneficial for the improvement of the quantum capacitance. Besides the aforementioned examples, the quantum capacitance mechanism has not been explored in supercapacitor electrode materials.

1.4.3 Aqueous Zinc-ion Batteries (ZIBs)

In 2021, the price of lithium carbonate, the mineral precursor of lithium batteries, skyrocketed 500% as a direct consequence of the demand boom for electric vehicles as well as the shortage of lithium, which has become critical raw material since 2020. Among the monovalent (Li^+, Na^+, and K^+) and multivalent metal-ion (Ca^{2+}, Mg^{2+}, and Al^{3+}) batteries, rechargeable aqueous zinc-ion batteries (ZIBs) represent the most promising alternative for large-

scale energy storage devices owing to their inherent high safety, environmental sustainability, and relatively low cost. [75-78] The main components of rechargeable aqueous ZIBs are exhibited in Figure 1-20, which consist of a Zn metal anode, cathode, an aqueous electrolyte, and separator.
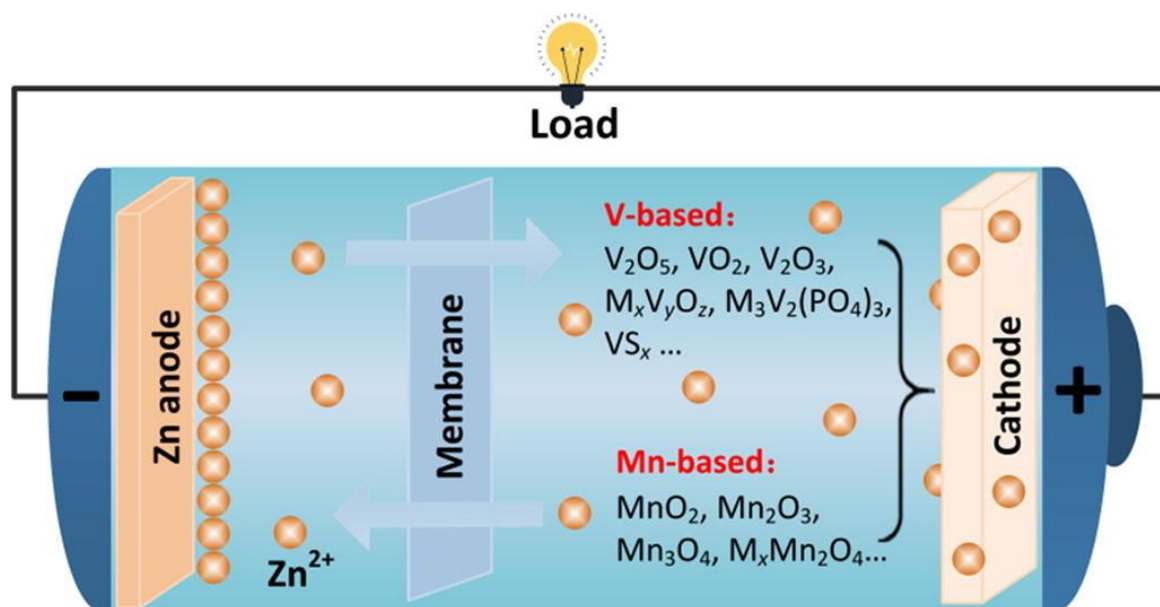
Figure 1-20 Schematic representative of aqueous ZIBs, Adapted from Ref [79]

The reaction mechanism of ZIBs in an aqueous solution seems to be complicated, and it is still under intense discussion.[80] In most aqueous ZIBs, the reaction mechanisms of ZIBs are mainly based on Zn^{2+} insertion/extraction, H^+/Zn^{2+} co-insertion/extraction, H_2O/Zn co-insertion/extraction, and chemical conversion reaction that occur at the metal zinc anode and zinc ion intercalation/de-intercalation reactions occur in the cathode material, deposition and dissolution reaction mechanism as shown in Figure 1-1 5.[76]
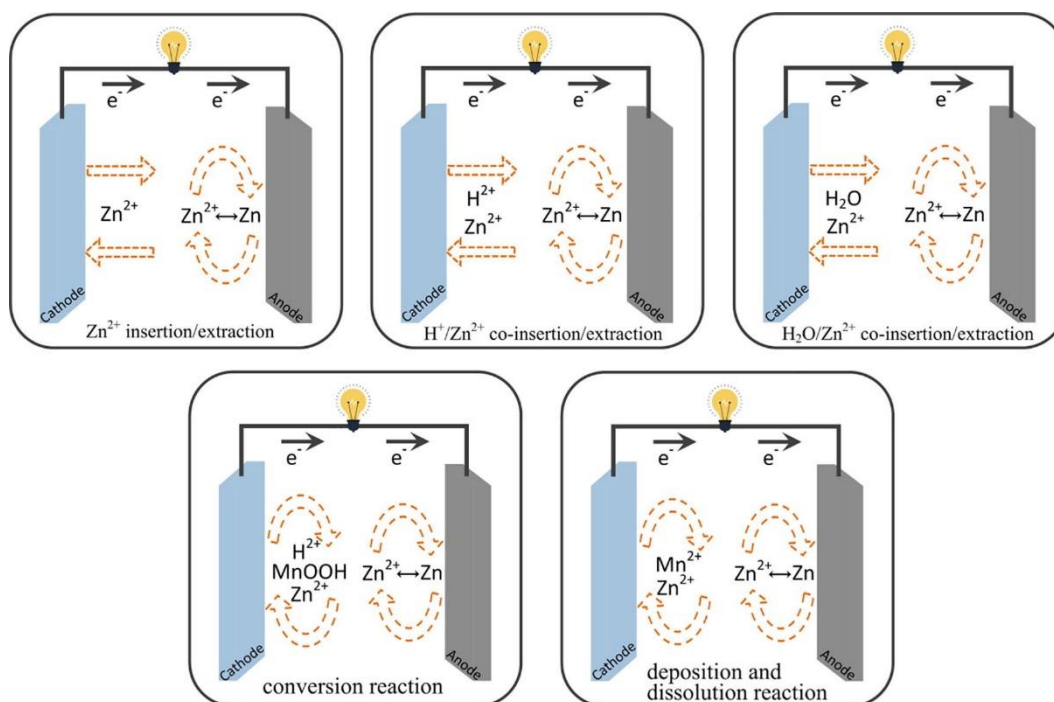
Figure 1-21 General classification and schematic diagram of energy storage mechanisms

of ZIBs, Adapted from Ref [79]

1.5 Aim of this Thesis

1.5.1 MOFs@COFs hybrids in supercapacitor application

The applications of MOFs in energy storage systems have recently emerged.[81-86] Unfortunately, the widespread use of MOFs as energy storage materials is hampered by their low specific capacitance, poor conductivity, and poor stability. For example, Diaz *et al*. reported for the first time based on MOF Co8-MOF-5 as SCs electrodes, which exhibited a relatively low gravimetric capacitive of 2 F g^{-1}.[87] Subsequently, numerous MOF-based SCs have been reported.[88-90] Furthermore, MOF-based SCs' electrodes frequently

exhibit low specific capacitance as a result of poor conductivity. In order to enhance MOF capacitance as SCs electrodes, MOFs have been incorporated into conductive materials, such as graphene,[91, 92] and conductive polymers.[93, 94] Yaghi *et al*. reported a series of different nanocrystal MOFs/graphene hybrids incorporated into solid-state SCs devices, finding a zirconium MOF with the exceptional high areal capacitance of 5.09 mF cm^{-2}.[95] More recently, MOFs@COFs hybrid structures have also been developed as a new type of multifunctional porous materials, which contain the structural traits and combine the merits of individual components and acquire the maximized performances in gas separation,[47, 56] (photo-)catalysis[52, 63, 96], aptasensors[59] and lithium storage[62]. However, except for the COF@Mn-MOF hybrid reported by Wang *et al*.[62] the use of MOFs @ COFs hybrid materials in energy storage applications remains largely unexplored.

The quantum capacitance as one of the physical mechanisms which give rise to the interfacial capacitance is not yet well understood. Noteworthy, Xia *et al*., and S. Ilani *et al*. reported that the quantum capacitance of graphene and carbon nanotubes might be the origin of the increased interfacial capacitance in some carbon-based electrodes.[72, 97] Subsequently, Zhang *et al*.[98] and Song *et al*.[74] further explored this concept by introducing nitrogen or oxygen-containing (hydroxyl and epoxy) groups in graphene, which was found to be

beneficial for the improvement of the quantum capacitance. Besides the aforementioned examples, the quantum capacitance mechanism has not been explored in supercapacitor electrode materials.

Lately, MOFs@COFs hybrid structures containing characteristics of both MOFs and COFs have been proposed as a new type of multifunctional porous materials exhibiting advantages of individual components, allowing harvesting the performance in gas separation,[56] (photo)catalysis,[52, 63] sensors,[59] bacterial inhibition[55] and lithium-ion batteries.[62] The number of reports dealing with MOFs@COFs hybrid porous materials has rapidly increased, most of which target at maximization of the advantages of pristine MOFs and COFs. For example, Fu *et al*. reported the COF@MOF (COF-300@ZIF-8) composite membranes, which displayed higher separation selectivity of H_2/CO_2 gas mixtures compared to the individual COF and MOF membranes.[56] Subsequently, various MOFs@COFs including NH_2-MIL-68-MOF@COF,[54] NH_2-UIO-66@COF-TpPa,[63] NH_2-MIL-125@COF-LZU1,[52] and UIO-66-NH_2@COF-TAPB-BTCA have been synthesized and successfully used in (photo)catalysis. However, except for Mn-MOF@COF[62] reported by Wang *et al*., and aza-MOF@COF-LZU1 reported by our group, the use of MOFs@COFs hybrid materials in energy storage applications remains largely unexplored.

1.5.2 COFs in aqueous zinc-ion batteries application

COFs have attracted wide attention among the energy-storage research community due to their intrinsically unique features including, structural diversity as a result of the tuneability of their well-defined chemical structures, reticular π-conjugated backbones, high porosity that allows continuous ion ($e.g.$, Zn^{2+}) diffusion, hence facilitating the access to the specific active sites, and large internal surface areas.[99, 100] Importantly, the use of electrochemically-active building blocks has proven to be the key to the realization of the next generation of high-performance electrode materials for energy storage applications.[101-103] Altogether, these features make COFs potentially promising cathode materials for rechargeable aqueous ZIBs. In 2019, Banerjee et $al.$, reported for the first time the use of a classical two-dimensional (2D)-COF HqTp as a cathode material for rechargeable aqueous ZIBs, delivering a specific capacity of 276.0 mAh g^{-1} at 0.125 A g^{-1}.[104] Other examples of COFs used as cathode materials in aqueous ZIBs exhibiting a high electrochemical performance include a 2D polyarylimide COF (capacity 92 mAh g^{-1} at 0.7 A g^{-1}) reported by Feng et $al.$,[105] an orthoquinone COF (225 mAh g^{-1} at 0.1 A g^{-1}) reported by Chen et $al.$,[106] and phenanthroline and quinone COF (247 and 344 mAh g^{-1} at 0.1 A g^{-1}) reported by Alshareef et $al.$[107, 108] To the best of our knowledge, all the electrochemically-active cathode materials in rechargeable aqueous ZIBs, not only based on COFs but also on

other organic materials including polymers (*e.g.*, PDA,[109] CLPy,[110]) and small organic molecules (*e.g.*, C4Q,[27] PQ-D,[111] DTT,[112] TABQ,[113] tetracholoro-1,4-benzoquinone,[114] phenothiazine,[115]), use carbonyl (C=O) moieties as electrochemically-active groups to reversibly coordinate Zn^{2+}.   However, the high solubility of organic carbonyl materials in aqueous electrolytes, as well as their low electronic conductivity and discharge potential represent critical drawbacks for their energy applications.[116, 117] In addition to the prevailing carbonyl derivatives, other electrochemically-active groups, including N-based bonds[118] and S-based bonds,[119] have gained considerable attention and provided enhanced electrochemical performance. Nitrogen and sulfur atoms exhibit a higher electronegativity (3.04 and 2.58, respectively) compared to that of carbon (2.55), and as a result, their addition to a carbon-based material's lattice improves not only its electrical conductivity but also the electrochemical. Thiadiazole derivatives, that contain both nitrogen and sulfur atoms have been used as cathode materials for rechargeable lithium batteries, exhibiting a dramatically improved performance[120] but, to the best of our knowledge, they have not been used as building blocks in COFs for energy applications.

1.6 References

1. Uemura, T.; Yanai, N.; Kitagawa, S., Polymerization reactions in porous coordination polymers. *Chemical Society Reviews* **2009,** *38* (5), 1228-1236.

2. Carrasco, S., Metal-Organic Frameworks for the Development of Biosensors: A Current Overview. *Biosensors* **2018,** *8* (4), 92.

3. Li, H.; Eddaoudi, M.; O'Keeffe, M.; Yaghi, O. M., Design and synthesis of an exceptionally stable and highly porous metal-organic framework. *Nature* **1999,** *402* (6759), 276-279.

4. Janiak, C.; Vieth, J. K., MOFs, MILs and more: concepts, properties and applications for porous coordination networks (PCNs). *New Journal of Chemistry* **2010,** *34* (11), 2366-2388.

5. Akporiaye, D. E.; Fjellvag, H.; Halvorsen, E. N.; Hustveit, J.; Karlsson, A.; Lillerud, K. P., The synthesis and structure solution of UIO-7, a new molecular sieve. *Chemical Communications* **1996,** (5), 601-602.

6. Gutiérrez-Serpa, A.; Pacheco-Fernández, I.; Pasán, J.; Pino, V., Metal-Organic Frameworks as Key Materials for Solid-Phase Microextraction Devices—A Review. *Separations* **2019,** *6* (4).

7. Sharanyakanth, P. S.; Radhakrishnan, M., Synthesis of metal-organic frameworks (MOFs) and its application in food packaging: A critical review. *Trends in Food Science & Technology* **2020,** *104*, 102-116.

8. Yaghi, O. M.; O'Keeffe, M.; Ockwig, N. W.; Chae, H. K.; Eddaoudi, M.; Kim, J., Reticular synthesis and the design of new materials. *Nature* **2003,** *423* (6941), 705-714.

9. Aakeröy, C. B.; Champness, N. R.; Janiak, C., Recent advances in crystal engineering. *CrystEngComm* **2010,** *12* (1), 22-43.

10. Noro, S.-i.; Kitaura, R.; Kondo, M.; Kitagawa, S.; Ishii, T.; Matsuzaka, H.; Yamashita, M., Framework Engineering by Anions and Porous Functionalities of Cu(II)/4,4'-bpy

Coordination Polymers. *Journal of the American Chemical Society* **2002,** *124* (11), 2568-2583.

11. Devic, T.; Serre, C., High valence 3p and transition metal based MOFs. *Chemical Society Reviews* **2014,** *43* (16), 6097-6115.

12. James, S. L., Metal-organic frameworks. *Chemical Society Reviews* **2003,** *32* (5), 276-288.

13. Furukawa, H.; Cordova, K. E.; O'Keeffe, M.; Yaghi, O. M., The Chemistry and Applications of Metal-Organic Frameworks. *Science* **2013,** *341* (6149), 1230444.

14. Côté Adrien, P.; Benin Annabelle, I.; Ockwig Nathan, W.; O'Keeffe, M.; Matzger Adam, J.; Yaghi Omar, M., Porous, Crystalline, Covalent Organic Frameworks. *Science* **2005,** *310* (5751), 1166-1170.

15. Feng, X.; Ding, X.; Jiang, D., Covalent organic frameworks. *Chemical Society Reviews* **2012,** *41* (18), 6010-6022.

16. Geng, K.; He, T.; Liu, R.; Dalapati, S.; Tan, K. T.; Li, Z.; Tao, S.; Gong, Y.; Jiang, Q.; Jiang, D., Covalent Organic Frameworks: Design, Synthesis, and Functions. *Chemical Reviews* **2020,** *120* (16), 8814-8933.

17. Chen, X.; Geng, K.; Liu, R.; Tan, K. T.; Gong, Y.; Li, Z.; Tao, S.; Jiang, Q.; Jiang, D., Covalent Organic Frameworks: Chemical Approaches to Designer Structures and Built-In Functions. *Angewandte Chemie International Edition* **2020,** *59* (13), 5050-5091.

18. Alahakoon, S. B.; Diwakara, S. D.; Thompson, C. M.; Smaldone, R. A., Supramolecular design in 2D covalent organic frameworks. *Chemical Society Reviews* **2020,** *49* (5), 1344-1356.

19. El-Kaderi Hani, M.; Hunt Joseph, R.; Mendoza-Cortés José, L.; Côté Adrien, P.; Taylor Robert, E.; O'Keeffe, M.; Yaghi Omar, M., Designed Synthesis of 3D Covalent Organic Frameworks. *Science* **2007,** *316* (5822), 268-272.

20. Côté, A. P.; Benin, A. I.; Ockwig, N. W.; O'Keeffe, M.; Matzger, A. J.; Yaghi, O. M., Porous, Crystalline, Covalent Organic Frameworks. *Science* **2005,** *310* (5751), 1166-1170.

21. Uribe-Romo, F. J.; Doonan, C. J.; Furukawa, H.; Oisaki, K.; Yaghi, O. M., Crystalline Covalent Organic Frameworks with Hydrazone Linkages. *Journal of the American Chemical Society* **2011,** *133* (30), 11478-11481.

22. Dalapati, S.; Jin, S.; Gao, J.; Xu, Y.; Nagai, A.; Jiang, D., An Azine-Linked Covalent Organic Framework. *Journal of the American Chemical Society* **2013,** *135* (46), 17310-17313.

23. Kandambeth, S.; Mallick, A.; Lukose, B.; Mane, M. V.; Heine, T.; Banerjee, R., Construction of Crystalline 2D Covalent Organic Frameworks with Remarkable Chemical (Acid/Base) Stability via a Combined Reversible and Irreversible Route. *Journal of the American Chemical Society* **2012,** *134* (48), 19524-19527.

24. Zhuang, X.; Zhao, W.; Zhang, F.; Cao, Y.; Liu, F.; Bi, S.; Feng, X., A two-dimensional conjugated polymer framework with fully sp2-bonded carbon skeleton. *Polymer Chemistry* **2016,** *7* (25), 4176-4181.

25. Bi, S.; Yang, C.; Zhang, W.; Xu, J.; Liu, L.; Wu, D.; Wang, X.; Han, Y.; Liang, Q.; Zhang, F., Two-dimensional semiconducting covalent organic frameworks via condensation at arylmethyl carbon atoms. *Nature Communications* **2019,** *10* (1), 2467.

26. Lyu, H.; Diercks, C. S.; Zhu, C.; Yaghi, O. M., Porous Crystalline Olefin-Linked Covalent Organic Frameworks. *Journal of the American Chemical Society* **2019,** *141* (17), 6848-6852.

27. Nagai, A.; Chen, X.; Feng, X.; Ding, X.; Guo, Z.; Jiang, D., A Squaraine-Linked Mesoporous Covalent Organic Framework. *Angewandte Chemie International Edition* **2013,** *52* (13), 3770-3774.

28. Guo, J.; Xu, Y.; Jin, S.; Chen, L.; Kaji, T.; Honsho, Y.; Addicoat, M. A.; Kim, J.; Saeki, A.; Ihee, H.; Seki, S.; Irle, S.; Hiramoto, M.; Gao, J.; Jiang, D., Conjugated organic framework with three-dimensionally ordered stable structure and delocalized π clouds. *Nature Communications* **2013,** *4* (1), 2736.

29. Li, H.; Pan, Q.; Ma, Y.; Guan, X.; Xue, M.; Fang, Q.; Yan, Y.; Valtchev, V.; Qiu, S., Three-Dimensional Covalent Organic Frameworks with Dual Linkages for Bifunctional

Cascade Catalysis. *Journal of the American Chemical Society* **2016,** *138* (44), 14783-14788.

30. Abuzeid, H. R.; El-Mahdy, A. F. M.; Kuo, S.-W., Covalent organic frameworks: Design principles, synthetic strategies, and diverse applications. *Giant* **2021,** *6*, 100054.

31. Diercks Christian, S.; Yaghi Omar, M., The atom, the molecule, and the covalent organic framework. *Science* **2017,** *355* (6328), eaal1585.

32. Sharma, R. K.; Yadav, P.; Yadav, M.; Gupta, R.; Rana, P.; Srivastava, A.; Zbořil, R.; Varma, R. S.; Antonietti, M.; Gawande, M. B., Recent development of covalent organic frameworks (COFs): synthesis and catalytic (organic-electro-photo) applications. *Materials Horizons* **2020,** *7* (2), 411-454.

33. Jin, S.; Furukawa, K.; Addicoat, M.; Chen, L.; Takahashi, S.; Irle, S.; Nakamura, T.; Jiang, D., Large pore donor-acceptor covalent organic frameworks. *Chemical Science* **2013,** *4* (12), 4505-4511.

34. Rowan, S. J.; Cantrill, S. J.; Cousins, G. R. L.; Sanders, J. K. M.; Stoddart, J. F., Dynamic Covalent Chemistry. *Angewandte Chemie International Edition* **2002,** *41* (6), 898-952.

35. Kandambeth, S.; Shinde, D. B.; Panda, M. K.; Lukose, B.; Heine, T.; Banerjee, R., Enhancement of Chemical Stability and Crystallinity in Porphyrin-Containing Covalent Organic Frameworks by Intramolecular Hydrogen Bonds. *Angewandte Chemie International Edition* **2013,** *52* (49), 13052-13056.

36. Xu, H.; Gao, J.; Jiang, D., Stable, crystalline, porous, covalent organic frameworks as a platform for chiral organocatalysts. *Nature Chemistry* **2015,** *7* (11), 905-912.

37. Du, Y.; Mao, K.; Kamakoti, P.; Wooler, B.; Cundy, S.; Li, Q.; Ravikovitch, P.; Calabro, D., The effects of pyridine on the structure of B-COFs and the underlying mechanism. *Journal of Materials Chemistry A* **2013,** *1* (42), 13171-13178.

38. Kuhn, P.; Antonietti, M.; Thomas, A., Porous, Covalent Triazine-Based Frameworks Prepared by Ionothermal Synthesis. *Angewandte Chemie International Edition* **2008,** *47* (18), 3450-3453.

39. Feng, X.; Chen, L.; Honsho, Y.; Saengsawang, O.; Liu, L.; Wang, L.; Saeki, A.; Irle, S.; Seki, S.; Dong, Y.; Jiang, D., An Ambipolar Conducting Covalent Organic Framework with Self-Sorted and Periodic Electron Donor-Acceptor Ordering. *Advanced Materials* **2012,** *24* (22), 3026-3031.

40. Cui, B.; Fu, G., Process of metal-organic framework (MOF)/covalent-organic framework (COF) hybrids-based derivatives and their applications on energy transfer and storage. *Nanoscale* **2022,** *14* (5), 1679-1699.

41. Wu, S.; Zhuang, G.; Wei, J.; Zhuang, Z.; Yu, Y., Shape control of core-shell MOF@MOF and derived MOF nanocages via ion modulation in a one-pot strategy. *Journal of Materials Chemistry A* **2018,** *6* (37), 18234-18241.

42. Peng, H.; Raya, J.; Richard, F.; Baaziz, W.; Ersen, O.; Ciesielski, A.; Samorì, P., Synthesis of Robust MOFs@COFs Porous Hybrid Materials via an Aza-Diels-Alder Reaction: Towards High-Performance Supercapacitor Materials. *Angewandte Chemie International Edition* **2020,** *59* (44), 19602-19609.

43. Guilong Lu, X. H. Y. L. G. Z. G. P. G. W., Covalently integrated core-shell MOF@COF hybrids as efficient visible-light-driven photocatalysts for selective oxidation of alcohols. *Journal of Energy Chemistry* **2020,** *43* (4), 8-15.

44. Winarta, J.; Shan, B.; McIntyre, S. M.; Ye, L.; Wang, C.; Liu, J.; Mu, B., A Decade of UIO-66 Research: A Historic Review of Dynamic Structure, Synthesis Mechanisms, and Characterization Techniques of an Archetypal Metal-Organic Framework. *Crystal Growth & Design* **2020,** *20* (2), 1347-1362.

45. Tang, H.-L.; Sun, X.-J.; Zhang, F.-M., Development of MOF-based heterostructures for photocatalytic hydrogen evolution. *Dalton Transactions* **2020,** *49* (35), 12136-12144.

46. Zheng, X.; Wang, L.; Pei, Q.; He, S.; Liu, S.; Xie, Z., Metal-Organic Framework@Porous Organic Polymer Nanocomposite for Photodynamic Therapy. *Chemistry of Materials* **2017,** *29* (5), 2374-2381.

47. Cheng, Y.; Ying, Y.; Zhai, L.; Liu, G.; Dong, J.; Wang, Y.; Christopher, M. P.; Long, S.; Wang, Y.; Zhao, D., Mixed matrix membranes containing MOF@COF hybrid fillers for efficient CO2/CH4 separation. *Journal of Membrane Science* **2019,** *573*, 97-106.

48. Qi, M.-H.; Gao, M.-L.; Liu, L.; Han, Z.-B., Robust Bifunctional Core-Shell MOF@POP Catalyst for One-Pot Tandem Reaction. *Inorganic Chemistry* **2018,** *57* (23), 14467-14470.

49. Wang, X.-Y.; Yin, H.-Q.; Yin, X.-B., MOF@COFs with Strong Multiemission for Differentiation and Ratiometric Fluorescence Detection. *ACS Applied Materials & Interfaces* **2020,** *12* (18), 20973-20981.

50. Chen, Y.; Yang, D.; Shi, B.; Dai, W.; Ren, H.; An, K.; Zhou, Z.; Zhao, Z.; Wang, W.; Jiang, Z., In situ construction of hydrazone-linked COF-based core-shell hetero-frameworks for enhanced photocatalytic hydrogen evolution. *Journal of Materials Chemistry A* **2020,** *8* (16), 7724-7732.

51. Zhu, Y.; Wang, W. D.; Sun, X.; Fan, M.; Hu, X.; Dong, Z., Palladium Nanoclusters Confined in MOF@COP as a Novel Nanoreactor for Catalytic Hydrogenation. *ACS Applied Materials & Interfaces* **2020,** *12* (6), 7285-7294.

52. Sun, D.; Jang, S.; Yim, S.-J.; Ye, L.; Kim, D.-P., Metal Doped Core-Shell Metal-Organic Frameworks@Covalent Organic Frameworks (MOFs@COFs) Hybrids as a Novel Photocatalytic Platform. *Advanced Functional Materials* **2018,** *28* (13), 1707110.

53. Sun, D.; Kim, D.-P., Hydrophobic MOFs@Metal Nanoparticles@COFs for Interfacially Confined Photocatalysis with High Efficiency. *ACS Applied Materials & Interfaces* **2020,** *12* (18), 20589-20595.

54. Peng, Y.; Zhao, M.; Chen, B.; Zhang, Z.; Huang, Y.; Dai, F.; Lai, Z.; Cui, X.; Tan, C.; Zhang, H., Hybridization of MOFs and COFs: A New Strategy for Construction of MOF@COF Core-Shell Hybrid Materials. *Advanced Materials* **2018,** *30* (3), 1705454.

55. Zhang, L.; Liu, Z.; Deng, Q.; Sang, Y.; Dong, K.; Ren, J.; Qu, X., Nature-Inspired Construction of MOF@COF Nanozyme with Active Sites in Tailored Microenvironment

and Pseudopodia-Like Surface for Enhanced Bacterial Inhibition. *Angewandte Chemie International Edition* **2021,** *60* (7), 3469-3474.

56. Fu, J.; Das, S.; Xing, G.; Ben, T.; Valtchev, V.; Qiu, S., Fabrication of COF-MOF Composite Membranes and Their Highly Selective Separation of H_2/CO_2. *Journal of the American Chemical Society* **2016,** *138* (24), 7673-7680.

57. Liu, X.; Hu, M.; Wang, M.; Song, Y.; Zhou, N.; He, L.; Zhang, Z., Novel nanoarchitecture of Co-MOF-on-TPN-COF hybrid: Ultralowly sensitive bioplatform of electrochemical aptasensor toward ampicillin. *Biosensors and Bioelectronics* **2019,** *123*, 59-68.

58. Gao, M.-L.; Qi, M.-H.; Liu, L.; Han, Z.-B., An exceptionally stable core-shell MOF/COF bifunctional catalyst for a highly efficient cascade deacetalization-Knoevenagel condensation reaction. *Chemical Communications* **2019,** *55* (45), 6377-6380.

59. Zhou, N.; Ma, Y.; Hu, B.; He, L.; Wang, S.; Zhang, Z.; Lu, S., Construction of Ce-MOF@COF hybrid nanostructure: Label-free aptasensor for the ultrasensitive detection of oxytetracycline residues in aqueous solution environments. *Biosensors and Bioelectronics* **2019,** *127*, 92-100.

60. Nguyen, H. L.; Gándara, F.; Furukawa, H.; Doan, T. L. H.; Cordova, K. E.; Yaghi, O. M., A Titanium-Organic Framework as an Exemplar of Combining the Chemistry of Metal and Covalent-Organic Frameworks. *Journal of the American Chemical Society* **2016,** *138* (13), 4330-4333.

61. Feng, L.; Wang, K.-Y.; Lv, X.-L.; Yan, T.-H.; Li, J.-R.; Zhou, H.-C., Modular Total Synthesis in Reticular Chemistry. *Journal of the American Chemical Society* **2020,** *142* (6), 3069-3076.

62. Sun, W.; Tang, X.; Yang, Q.; Xu, Y.; Wu, F.; Guo, S.; Zhang, Y.; Wu, M.; Wang, Y., Coordination-Induced Interlinked Covalent- and Metal-Organic-Framework Hybrids for Enhanced Lithium Storage. *Advanced materials* **2019,** *31* (37), 1903176.

63. Zhang, F.-M.; Sheng, J.-L.; Yang, Z.-D.; Sun, X.-J.; Tang, H.-L.; Lu, M.; Dong, H.; Shen, F.-C.; Liu, J.; Lan, Y.-Q., Rational Design of MOF/COF Hybrid Materials for

Photocatalytic H2 Evolution in the Presence of Sacrificial Electron Donors. *Angewandte Chemie International Edition* **2018,** *57* (37), 12106-12110.

64. Garzón-Tovar, L.; Pérez-Carvajal, J.; Yazdi, A.; Hernández-Muñoz, J.; Tarazona, P.; Imaz, I.; Zamora, F.; Maspoch, D., A MOF@COF Composite with Enhanced Uptake through Interfacial Pore Generation. *Angewandte Chemie International Edition* **2019,** *58* (28), 9512-9516.

65. Satpathy, S.; Das, S.; Bhattacharyya, B. K., How and where to use super-capacitors effectively, an integration of review of past and new characterization works on super-capacitors. *Journal of Energy Storage* **2020,** *27*, 101044.

66. Sharma, P.; Bhatti, T. S., A review on electrochemical double-layer capacitors. *Energy Conversion and Management* **2010,** *51* (12), 2901-2912.

67. Russell, J. C.; Posey, V. A.; Gray, J.; May, R.; Reed, D. A.; Zhang, H.; Marbella, L. E.; Steigerwald, M. L.; Yang, Y.; Roy, X.; Nuckolls, C.; Peurifoy, S. R., High-performance organic pseudocapacitors via molecular contortion. *Nature Materials* **2021,** *20* (8), 1136-1141.

68. Dröscher, S.; Roulleau, P.; Molitor, F.; Studerus, P.; Stampfer, C.; Ensslin, K.; Ihn, T., Quantum capacitance and density of states of graphene. *Applied Physics Letters* **2010,** *96* (15), 152104.

69. Najib, S.; Erdem, E., Current progress achieved in novel materials for supercapacitor electrodes: mini review. *Nanoscale Advances* **2019,** *1* (8), 2817-2827.

70. Liu, C.; Li, Q.; Wang, K., State-of-charge estimation and remaining useful life prediction of supercapacitors. *Renewable and Sustainable Energy Reviews* **2021,** *150*, 111408.

71. Fleischmann, S.; Mitchell, J. B.; Wang, R.; Zhan, C.; Jiang, D.-e.; Presser, V.; Augustyn, V., Pseudocapacitance: From Fundamental Understanding to High Power Energy Storage Materials. *Chemical Reviews* **2020,** *120* (14), 6738-6782.

72. Xia, J.; Chen, F.; Li, J.; Tao, N., Measurement of the quantum capacitance of graphene. *Nature Nanotechnology* **2009,** *4* (8), 505-509.

73. Zhang, L. L.; Zhao, X.; Ji, H.; Stoller, M. D.; Lai, L.; Murali, S.; McDonnell, S.; Cleveger, B.; Wallace, R. M.; Ruoff, R. S., Nitrogen doping of graphene and its effect on quantum capacitance, and a new insight on the enhanced capacitance of N-doped carbon. *Energy & Environmental Science* **2012,** *5* (11), 9618-9625.

74. Song, C.; Wang, J.; Meng, Z.; Hu, F.; Jian, X., Density Functional Theory Calculations of the Quantum Capacitance of Graphene Oxide as a Supercapacitor Electrode. *Chemphyschem* **2018,** *19* (13), 1579-1583.

75. Song, M.; Tan, H.; Chao, D.; Fan, H. J., Recent Advances in Zn-Ion Batteries. *Advanced Functional Materials* **2018,** *28* (41), 1802564.

76. Zhang, N.; Chen, X.; Yu, M.; Niu, Z.; Cheng, F.; Chen, J., Materials chemistry for rechargeable zinc-ion batteries. *Chemical Society Reviews* **2020,** *49* (13), 4203-4219.

77. Zhang, M.; Liang, R.; Or, T.; Deng, Y.-P.; Yu, A.; Chen, Z., Recent Progress on High-Performance Cathode Materials for Zinc-Ion Batteries. *Small Structures* **2021,** *2* (2), 2000064.

78. Ruan, P.; Liang, S.; Lu, B.; Fan, H. J.; Zhou, J., Design Strategies for High-Energy-Density Aqueous Zinc Batteries. *Angewandte Chemie International Edition* **2022,** *61* (17), e202200598.

79. Liu, N.; Li, B.; He, Z.; Dai, L.; Wang, H.; Wang, L., Recent advances and perspectives on vanadium- and manganese-based cathode materials for aqueous zinc ion batteries. *Journal of Energy Chemistry* **2021,** *59*, 134-159.

80. Fang, G.; Zhou, J.; Pan, A.; Liang, S., Recent Advances in Aqueous Zinc-Ion Batteries. *ACS Energy Letters* **2018,** *3* (10), 2480-2501.

81. Wei, S.; Xu, S.; Agrawral, A.; Choudhury, S.; Lu, Y.; Tu, Z.; Ma, L.; Archer, L. A., A stable room-temperature sodium-sulfur battery. *Nature communications* **2016,** *7*, 11722.

82. Peng, H.-J.; Hao, G.-X.; Chu, Z.-H.; Lin, J.; Lin, X.-M.; Cai, Y.-P., Mesoporous Mn3O4/C Microspheres Fabricated from MOF Template as Advanced Lithium-Ion Battery Anode. *Crystal Growth & Design* **2017,** *17* (11), 5881-5886.

83. Jerng, S. E.; Chang, B.; Shin, H.; Kim, H.; Lee, T.; Char, K.; Choi, J. W., Pyrazine-Linked 2D Covalent Organic Frameworks as Coating Material for High-Nickel Layered Oxide Cathodes in Lithium-Ion Batteries. *ACS Applied Materials & Interfaces* **2020**.

84. Jerng, S. E.; Chang, B.; Shin, H.; Kim, H.; Lee, T.; Char, K.; Choi, J. W., Pyrazine-Linked 2D Covalent Organic Frameworks as Coating Material for High-Nickel Layered Oxide Cathodes in Lithium-Ion Batteries. *ACS Applied Materials & Interfaces* **2020,** *12* (9), 10597-10606.

85. Hu, Y.; Goodeal, N.; Chen, Y.; Ganose, A. M.; Palgrave, R. G.; Bronstein, H.; Blunt, M. O., Probing the chemical structure of monolayer covalent-organic frameworks grown via Schiff-base condensation reactions. *Chemical communications* **2016,** *52* (64), 9941-4.

86. Sheberla, D.; Bachman, J. C.; Elias, J. S.; Sun, C.-J.; Shao-Horn, Y.; Dincă, M., Conductive MOF electrodes for stable supercapacitors with high areal capacitance. *Nature materials* **2016,** *16* (2), 220-224.

87. Díaz, R.; Orcajo, M. G.; Botas, J. A.; Calleja, G.; Palma, J., Co8-MOF-5 as electrode for supercapacitors. *Materials Letters* **2012,** *68*, 126-128.

88. Li, S.-L.; Xu, Q., Metal-organic frameworks as platforms for clean energy. *Energy & Environmental Science* **2013,** *6* (6), 1656-1683.

89. Wang, L.; Han, Y.; Feng, X.; Zhou, J.; Qi, P.; Wang, B., Metal-organic frameworks for energy storage: Batteries and supercapacitors. *Coordination Chemistry Reviews* **2016,** *307*, 361-381.

90. Wang, H.; Zhu, Q.-L.; Zou, R.; Xu, Q., Metal-Organic Frameworks for Energy Applications. *Chem* **2017,** *2* (1), 52-80.

91. Petit, C.; Bandosz, T. J., MOF-Graphite Oxide Composites: Combining the Uniqueness of Graphene Layers and Metal-Organic Frameworks. *Advanced Materials* **2009,** *21* (46), 4753-4757.

92. Qu, C.; Zhang, L.; Meng, W.; Liang, Z.; Zhu, B.; Dang, D.; Dai, S.; Zhao, B.; Tabassum, H.; Gao, S.; Zhang, H.; Guo, W.; Zhao, R.; Huang, X.; Liu, M.; Zou, R., MOF-

derived α-NiS nanorods on graphene as an electrode for high-energy-density supercapacitors. *Journal of Materials Chemistry A* **2018,** *6* (9), 4003-4012.

93. Lu, C.; Ben, T.; Xu, S.; Qiu, S., Electrochemical Synthesis of a Microporous Conductive Polymer Based on a Metal-Organic Framework Thin Film. *Angewandte Chemie International Edition* **2014,** *53* (25), 6454-6458.

94. Kalaj, M.; Bentz, K. C.; Ayala, S.; Palomba, J. M.; Barcus, K. S.; Katayama, Y.; Cohen, S. M., MOF-Polymer Hybrid Materials: From Simple Composites to Tailored Architectures. *Chemical reviews* **2020**.

95. Choi, K. M.; Jeong, H. M.; Park, J. H.; Zhang, Y.-B.; Kang, J. K.; Yaghi, O. M., Supercapacitors of Nanocrystalline Metal-Organic Frameworks. *ACS Nano* **2014,** *8* (7), 7451-7457.

96. Cai, M.; Li, Y.; Liu, Q.; Xue, Z.; Wang, H.; Fan, Y.; Zhu, K.; Ke, Z.; Su, C.-Y.; Li, G., One-Step Construction of Hydrophobic MOFs@COFs Core-Shell Composites for Heterogeneous Selective Catalysis. *Advanced Science* **2019,** *6* (8), 1802365.

97. Ilani, S.; Donev, L. A. K.; Kindermann, M.; McEuen, P. L., Measurement of the quantum capacitance of interacting electrons in carbon nanotubes. *Nature Physics* **2006,** *2* (10), 687-691.

98. Zhang, L. L.; Zhao, X.; Ji, H.; Stoller, M. D.; Lai, L.; Murali, S.; McDonnell, S.; Cleveger, B.; Wallace, R. M.; Ruoff, R. S., Nitrogen doping of graphene and its effect on quantum capacitance, and a new insight on the enhanced capacitance of N-doped carbon. *Energy & Environmental Science* **2012,** *5* (11).

99. Sun, T.; Xie, J.; Guo, W.; Li, D.-S.; Zhang, Q., Covalent-Organic Frameworks: Advanced Organic Electrode Materials for Rechargeable Batteries. *Advanced Energy Materials* **2020,** *10* (19), 1904199.

100. Zhang, K.; Kirlikovali, K. O.; Varma, R. S.; Jin, Z.; Jang, H. W.; Farha, O. K.; Shokouhimehr, M., Covalent Organic Frameworks: Emerging Organic Solid Materials for Energy and Electrochemical Applications. *ACS Applied Materials & Interfaces* **2020,** *12* (25), 27821-27852.

101. Cao, Y.; Wang, M.; Wang, H.; Han, C.; Pan, F.; Sun, J., Covalent Organic Framework for Rechargeable Batteries: Mechanisms and Properties of Ionic Conduction. *Advanced Energy Materials* **2022,** *12* (5), 2200057.

102. Shi, R.; Liu, L.; Lu, Y.; Wang, C.; Li, Y.; Li, L.; Yan, Z.; Chen, J., Nitrogen-rich covalent organic frameworks with multiple carbonyls for high-performance sodium batteries. *Nature Communications* **2020,** *11* (1), 178.

103. Kandambeth, S.; Kale, V. S.; Shekhah, O.; Alshareef, H. N.; Eddaoudi, M., 2D Covalent-Organic Framework Electrodes for Supercapacitors and Rechargeable Metal-Ion Batteries. *Advanced Energy Materials* **2022,** *12* (4), 2100177.

104. Khayum M, A.; Ghosh, M.; Vijayakumar, V.; Halder, A.; Nurhuda, M.; Kumar, S.; Addicoat, M.; Kurungot, S.; Banerjee, R., Zinc ion interactions in a two-dimensional covalent organic framework based aqueous zinc ion battery. *Chemical Science* **2019,** *10* (38), 8889-8894.

105. Yu, M.; Chandrasekhar, N.; Raghupathy, R. K. M.; Ly, K. H.; Zhang, H.; Dmitrieva, E.; Liang, C.; Lu, X.; Kühne, T. D.; Mirhosseini, H.; Weidinger, I. M.; Feng, X., A High-Rate Two-Dimensional Polyarylimide Covalent Organic Framework Anode for Aqueous Zn-Ion Energy Storage Devices. *Journal of the American Chemical Society* **2020,** *142* (46), 19570-19578.

106. Zheng, S.; Shi, D.; Yan, D.; Wang, Q.; Sun, T.; Ma, T.; Li, L.; He, D.; Tao, Z.; Chen, J., Orthoquinone-Based Covalent Organic Frameworks with Ordered Channel Structures for Ultrahigh Performance Aqueous Zinc-Organic Batteries. *Angewandte Chemie International Edition* **2022,** *61* (12), e202117511.

107. Wang, W.; Kale, V. S.; Cao, Z.; Kandambeth, S.; Zhang, W.; Ming, J.; Parvatkar, P. T.; Abou-Hamad, E.; Shekhah, O.; Cavallo, L.; Eddaoudi, M.; Alshareef, H. N., Phenanthroline Covalent Organic Framework Electrodes for High-Performance Zinc-Ion Supercapattery. *ACS Energy Letters* **2020,** *5* (7), 2256-2264.

108. Wang, W.; Kale, V. S.; Cao, Z.; Lei, Y.; Kandambeth, S.; Zou, G.; Zhu, Y.; Abouhamad, E.; Shekhah, O.; Cavallo, L.; Eddaoudi, M.; Alshareef, H. N., Molecular

Engineering of Covalent Organic Framework Cathodes for Enhanced Zinc-Ion Batteries. *Advanced Materials* **2021,** *33* (39), 2103617.

109. Yue, X.; Liu, H.; Liu, P., Polymer grafted on carbon nanotubes as a flexible cathode for aqueous zinc ion batteries. *Chemical Communications* **2019,** *55* (11), 1647-1650.

110. Zhang, C.; Ma, W.; Han, C.; Luo, L.-W.; Daniyar, A.; Xiang, S.; Wu, X.; Ji, X.; Jiang, J.-X., Tailoring the linking patterns of polypyrene cathodes for high-performance aqueous Zn dual-ion batteries. *Energy & Environmental Science* **2021,** *14* (1), 462-472.

111. Nam, K. W.; Kim, H.; Beldjoudi, Y.; Kwon, T.-w.; Kim, D. J.; Stoddart, J. F., Redox-Active Phenanthrenequinone Triangles in Aqueous Rechargeable Zinc Batteries. *Journal of the American Chemical Society* **2020,** *142* (5), 2541-2548.

112. Wang, Y.; Wang, C.; Ni, Z.; Gu, Y.; Wang, B.; Guo, Z.; Wang, Z.; Bin, D.; Ma, J.; Wang, Y., Binding Zinc Ions by Carboxyl Groups from Adjacent Molecules toward Long-Life Aqueous Zinc-Organic Batteries. *Advanced Materials* **2020,** *32* (16), 2000338.

113. Lin, Z.; Shi, H.-Y.; Lin, L.; Yang, X.; Wu, W.; Sun, X., A high capacity small molecule quinone cathode for rechargeable aqueous zinc-organic batteries. *Nature Communications* **2021,** *12* (1), 4424.

114. Kundu, D.; Oberholzer, P.; Glaros, C.; Bouzid, A.; Tervoort, E.; Pasquarello, A.; Niederberger, M., Organic Cathode for Aqueous Zn-Ion Batteries: Taming a Unique Phase Evolution toward Stable Electrochemical Cycling. *Chemistry of Materials* **2018,** *30* (11), 3874-3881.

115. Wang, N.; Guo, Z.; Ni, Z.; Xu, J.; Qiu, X.; Ma, J.; Wei, P.; Wang, Y., Molecular Tailoring of an n/p-type Phenothiazine Organic Scaffold for Zinc Batteries. *Angewandte Chemie International Edition* **2021,** *60* (38), 20826-20832.

116. Wang, H.-g.; Zhang, X.-b., Organic Carbonyl Compounds for Sodium-Ion Batteries: Recent Progress and Future Perspectives. *Chemistry European Journal* **2018,** *24* (69), 18235-18245.

117. An, S. Y.; Schon, T. B.; McAllister, B. T.; Seferos, D. S., Design strategies for organic carbonyl materials for energy storage: Small molecules, oligomers, polymers and supramolecular structures. *EcoMat* **2020,** *2* (4), e12055.

118. Xu, S.; Wang, G.; Biswal, B. P.; Addicoat, M.; Paasch, S.; Sheng, W.; Zhuang, X.; Brunner, E.; Heine, T.; Berger, R.; Feng, X., A Nitrogen-Rich 2D sp^2-Carbon-Linked Conjugated Polymer Framework as a High-Performance Cathode for Lithium-Ion Batteries. *Angewandte Chemie International Edition* **2019,** *58* (3), 849-853.

119. Shimizu, T.; Wang, H.; Matsumura, D.; Mitsuhara, K.; Ohta, T.; Yoshikawa, H., Porous Metal-Organic Frameworks Containing Reversible Disulfide Linkages as Cathode Materials for Lithium-Ion Batteries. *ChemSusChem* **2020,** *13* (9), 2256-2263.

120. Gao, J.; Lowe, M. A.; Conte, S.; Burkhardt, S. E.; Abruña, H. D., Poly(2,5-dimercapto-1,3,4-thiadiazole) as a Cathode for Rechargeable Lithium Batteries with Dramatically Improved Performance. *Chemistry European Journal* **2012,** *18* (27), 8521-8526.

Chapter 2   Experimental techniques

In this Chapter, the experimental techniques employed during the synthesis process of active materials described in this thesis (*i.e.,* MOF@COF and COF-TMT-BT) have been discussed. In addition, working principles of different characterization methods including FT-IR, XRD, SEM, Solid-state NMR, XPS, *etc*., have been discussed to provide an accurate and comprehensive understanding of these novel functional materials in supercapacitor and aqueous zinc-ion batteries application.

2.1 Chemicals and raw materials

All of the reagents and solvents used in this thesis were commercially available and used without further purification. Zinc foil (thickness of 100 µm), stainless steel gauze and coin cells cases were obtained from Alfa Aesar and S4R France, respectively. The nonwoven fabric membrane (NKK-MPF30AC-100) was purchased from Nippon Kodoshi Corporation (kochi, Japan). The Synthware glass of 15 mL pressure vessel with heavy wall and side port was purchased from FengTecEx GmbH company (Germany). 4,4′-(benzothiadiazole-4,7-diyl)dibenzaldehyde (BT) was prepared according to the previously reported procedure.[1]

2.2 Synthesis of active materials

2.2.1 Synthesis of MOFs and COFs

Synthesis of MOF UIO-66-NH$_2$: 2-aminoterephthalic acid (NH$_2$-BDC) (0.54 g, 3 mmol) and ZrCl$_4$ (0.5g, 2 mmol) were dissolved in 40 mL of DMF and sonicated for 30 minutes. Then, to the mixed solution it was added 1g PVP with additional 30 minutes sonication. The new mixed solution become transparent, and transferred it into a 100 mL round-bottom flask for the hydrothermal treatment at 120°C for 24h. After naturally cooling to room

temperature, the resultant suspension was centrifuged and washed with DMF, acetone and ethanol for three times, and then the result product was activated with anhydrous acetone for 3 days and dried at 120°C for 12 h in vacuum oven for further characterization and application. The results obtained with this system will be discussed in Chapter 3 and 4.

Synthesis of COF-TMT-BT: In a typical experiment, 2,4,6-trimethyl-1,3,5-triazine (TMT, 0.2 mmol, 24.6 mg), BT (0.3 mmol, 103.3 mg), mesitylene (3 mL), 1,4 -dioxane (1 mL), and acetonitrile (0.1 mL) were placed in a 15 mL pressure vessel with heavy wall and side port. The pressure vessel was charged with Argon by flowing the Argon gas for 5 min, then trifluoroacetic acid (0.8 mL) was added and sealed by screwing the cover tightly and heated at 150 °C for 3 days. The resulting precipitate was collected by centrifugation, subjected to Soxhlet extraction with methanol and tetrahydrofuran for 24 h for each solvent, and then dried at 80 °C under vacuum to produce the COF-TMT-BT. The results obtained with this system will be discussed in Chapter 5.
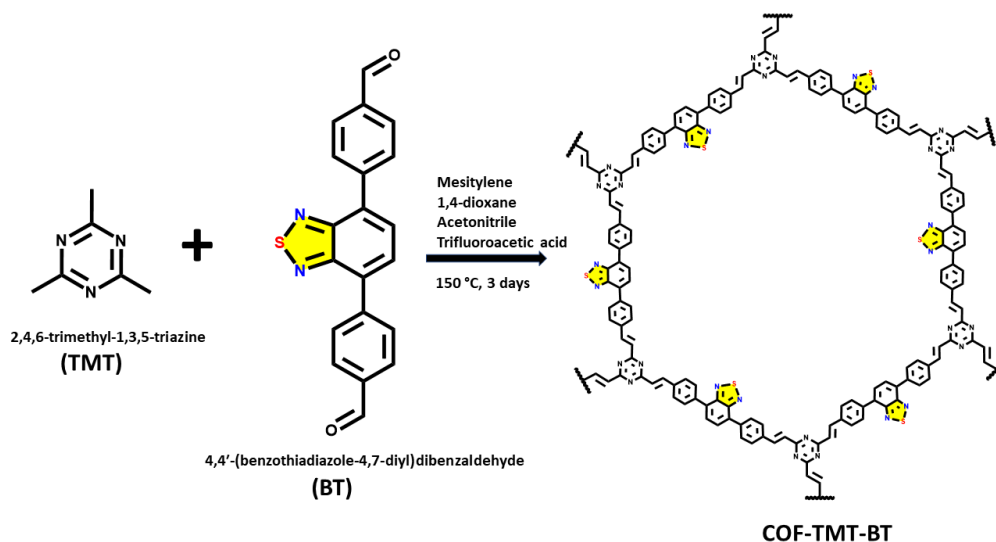
Figure 2-1 Illustration of the synthetic route of COF-TMT-BT.

Synthesis of COF-TMT-BP: The COF-TMT-BP was synthesized according to previous literature by Yaghi's group with a slight modification.[2] In a typical experiment, 2,4,6-trimethyl-1,3,5-triazine (TMT, 0.2 mmol, 24.6 mg), 4,4′-biphenyldicarbaldehyde (BP, 0.3 mmol, 85.8 mg), mesitylene (3 mL), 1,4 -dioxane (1 mL), and acetonitrile (0.1 mL) were placed in a 15 mL pressure vessel with heavy wall and side port. The pressure vessel was charged with Argon by flowing the Argon gas for 5 min, then adding trifluoroacetic acid (0.8 mL), then degassed through a vacuum pump for 5 min and heated at 150 °C for 3 days. The resulting precipitate was collected by centrifugation, subjected to Soxhlet extraction with methanol and tetrahydrofuran for 24 h for each solvent, and then dried at 100 °C under vacuum to produce the COF-TMT-BP. The results obtained with this system will be discussed in Chapter 5.
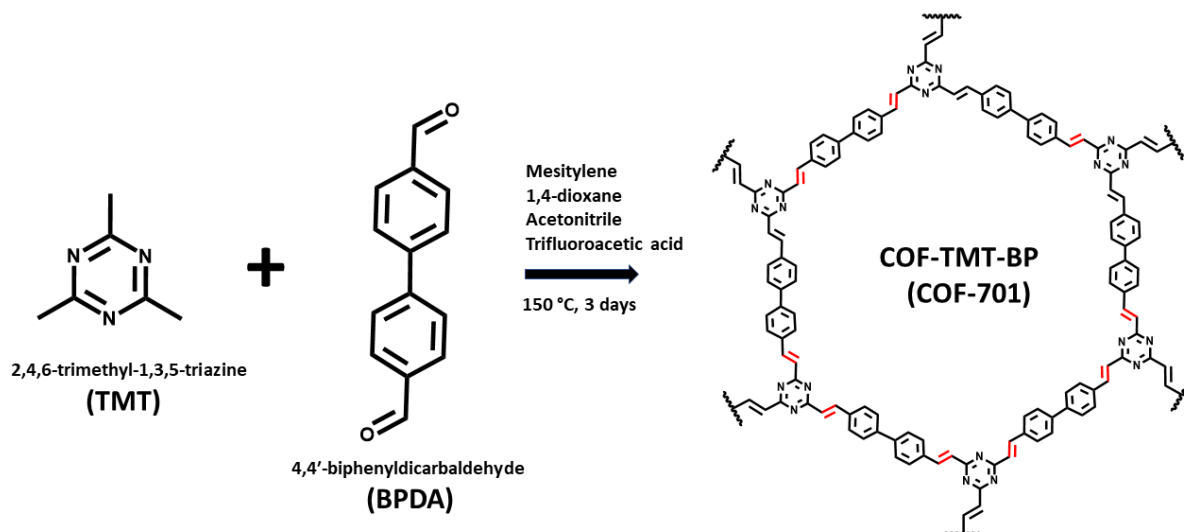
Figure 2-2 Schematic illustration for the synthesis of COF-TMT-BP.

Synthesis of COF-TAT-BT: The COF-TAT-BT was synthesized according to previous literature with a slight modification.[1] In a typical experiment, tris-(4-aminophenyl)triazine (TAT, 0.1 mmol, 35.4 mg), 4,4′-(benzothiadiazole-4,7-diyl)dibenzaldehyde (BT, 0.15 mmol, 51.7 mg), O-dichlorobenzene (1 mL) and n-butanol (5 mL), and acetic acid (0.6 mL) were placed in a 15 mL pressure vessel with heavy wall and side port. The pressure vessel was charged with Argon by flowing the Argon gas for 5 min, then freeze and degassed through a vacuum pump for 5 min and heated at 120 °C for 3 days. The resulting precipitates were collected by centrifugation, subjected to Soxhlet extraction with methanol and tetrahydrofuran for 24 h for each solvent, and then dried at 80 °C under vacuum to produce the COF-TAT-BT. The results obtained with this system will be discussed in Chapter 5.
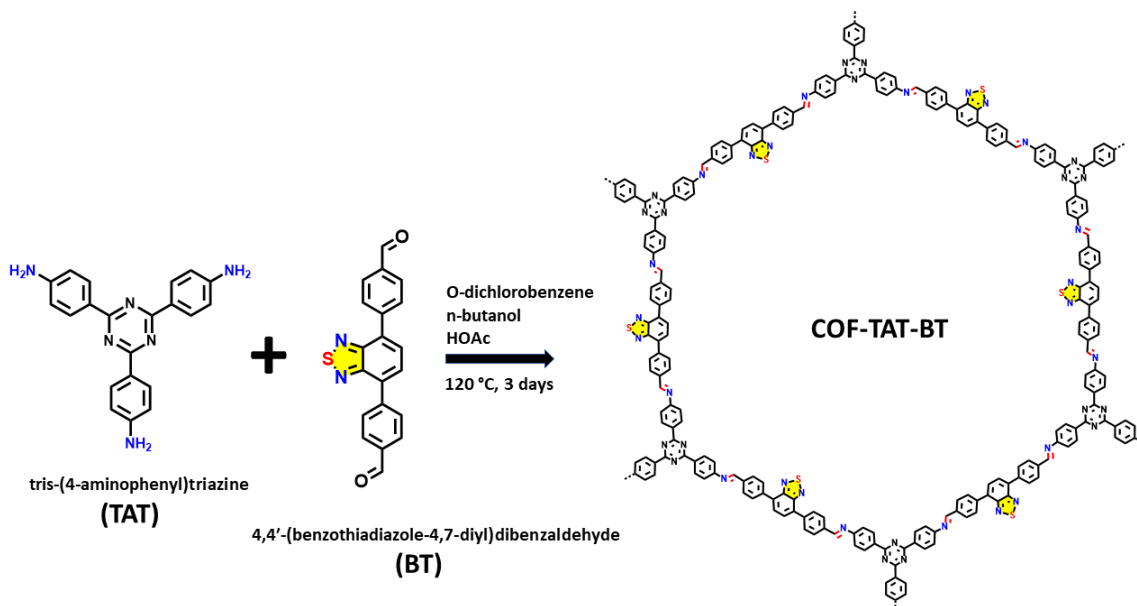
Figure 2-3 Schematic illustration for the synthesis of COF-TAT-BT.

2.2.2 Synthesis of MOF@COF hybrids porous materials

Synthesis of aza-MOF@COF: The synthetic route of the aza-MOF@COF is schematically illustrated in Figure 2-4. The aza-MOF@COF porous hybrid material was synthesised in three steps. MOF-UIO-66-NH$_2$ was reacted with 1,3,5-benzenetricarboxaldehyde (BTCA) and MOF-UIO-66(CHO) has been formed *via* condensation between amine groups of MOF-UIO-66-NH$_2$ and aldehyde moieties of BTCA. In the second step the COF layer has been grown on MOF-UIO-66 MOF by employing the condensation between the aldehydes present on the surface of the as-prepared MOF-UIO-66(CHO) and *p*-phenylenediamine. Finally, the PSM of MOF@COF-LZU1 has been accomplished by making use of aza-Diels-Alder reaction to obtain

65

aza-MOF@COF hybrid structure. In particular, aza-Diels-Alder reaction between aryl imine of MOF@COF-LZU1 and phenylacetylene resulted in successful conversion of the MOF@COF-LZU1 imine bridges into corresponding quinoline-linked aza-MOF@COF. The typically experimental details are: 60 mg of MOF UIO-66-NH$_2$ powders was suspended in 4 ml of 1,4-dioxane solution containing 16 mg of 1,3,5-Benzenetricarboxaldehyde. The mixture was sonicated for 30 min and heated at 80 °C for 2 h in oil bath with vigorously stirring. Subsequently, 0.4 ml of acetic acid (3 M) was gradually added to the suspension under stirring, during which the mixture solution becomes much brighter. 2 mL of 1,4-dioxane solution containing 16 mg p-Phenylenediamine was dropped into the above suspension in 20 min and continued stirring for 1 h. After that, the vial degassed through 3 freeze-pump-thaw cycles and vial were sealed and heated at 110 °C for 3 days. The resulted product was collected at 40 °C by centrifugation and washed with tetrahydrofuran, acetone and methanol, respectively and dried under vacuum to get the MOF@COF-LZU1. Then, MOF@COF-LZU1 (60 mg), phenylacetylene (120 μL, 1 mol), BF$_3$·OEt$_2$ (80 μL, 0.6 mmol), chloranil (120 mg, 0.45 mmol) and 20 mL of toluene were added to a 50 mL Schlenk tube. The tube was sealed and heated under N$_2$ at 110 °C in an oil bath. After 1-3 days, the mixture was cooled to room temperature and the precipitate was isolated *via* centrifugation. The reaction mixture was then washed with THF

66

and quenched with 20 mL saturated aqueous sodium bicarbonate. Subsequently, the solids were washed with THF using a Soxhlet extractor overnight and dried under vacuum. The results obtained with this system will be discussed in Chapter 3.
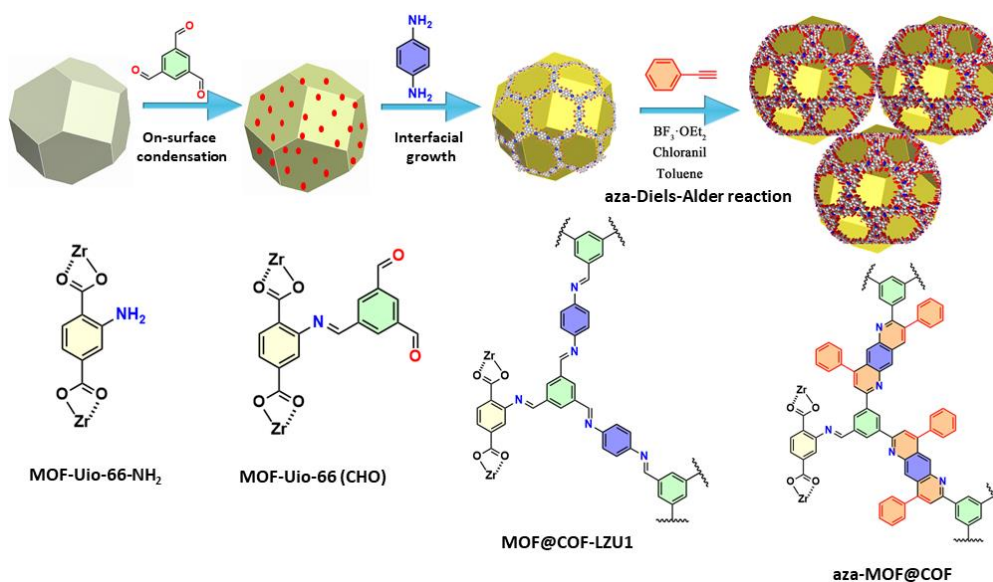

Figure 2-4 Schematic illustration of the synthetic route of aza-MOF@COF hybrid structure.

Synthesis of MOF@COF-TCNQ hybrid materials: The synthesis of MOF@COF-TCNQ is accomplished following the strategy illustrated in Figure 2-5 The MOF@COF-TCNQ hybrid material was synthesised in three steps. The first step relies on-surface condensation of the MOF-UIO-66-NH$_2$ with 1,3,5-triformylphloroglucinol (Tp) yielding MOF-UIO-66-NH$_2$ (Tp). In the second step the COF layer has been grown on MOF-UIO-66-NH$_2$ by employing the condensation between the Tp present on the surface of the as-prepared MOF-UIO-66-NH$_2$ (Tp) and p-phenylenediamine. In the third and

final step, the post-synthetic modification of MOF@COF has been accomplished by using liquid-phase infiltration of electron acceptors TCNQ to obtain MOF@COF-TCNQ hybrid materials. The typically experimental details: the MOF@COF hybrid porous material was prepared by adding 60 mg of MOF-UIO-66-NH$_2$ powder and 16 mg of 1,3,5-triformylphloroglucinol to 4 ml of 1,4-dioxane solution. The mixture was sonicated for 30 min and heated at 80 °C for 2 h in an oil bath and vigorously stirred. Then, 0.5 ml of acetic acid (3 M) was gradually added to the suspension under stirring, during which the mixture solution became brighter. 2 mL of a 1,4-dioxane solution containing 16 mg *p*-phenylenediamine was dropped into the above suspension in 20 min and continued stirring for 1 h. The vial was then degassed through 3 freeze-pump-thaw cycles and the vial was sealed and heated at 120 °C for 3 days. The resulting product was collected at 40 °C by means of centrifugation and rinsed with acetone, tetrahydrofuran, and methanol, respectively, and desiccated under vacuum. The as-prepared MOF@COF powders have been infiltrated with TCNQ by thermal annealing under vacuum (150 °C for 2 h) to eliminate coordinated H$_2$O molecules, then instantly transfer to a TCNQ saturated solution in CH$_2$Cl$_2$. The infiltrated MOF@COF samples were then rinsed with EtOH and CH$_2$Cl$_2$ solvent to eliminate excess of non-infiltrated TCNQ, which might be physisorbed on the outer surface of MOF@COF powder. Furthermore, samples have been processed in ambient conditions,

thus exposing the host-guest system to environmental amounts of solvent and moisture. The results obtained with this system will be discussed in Chapter 4.
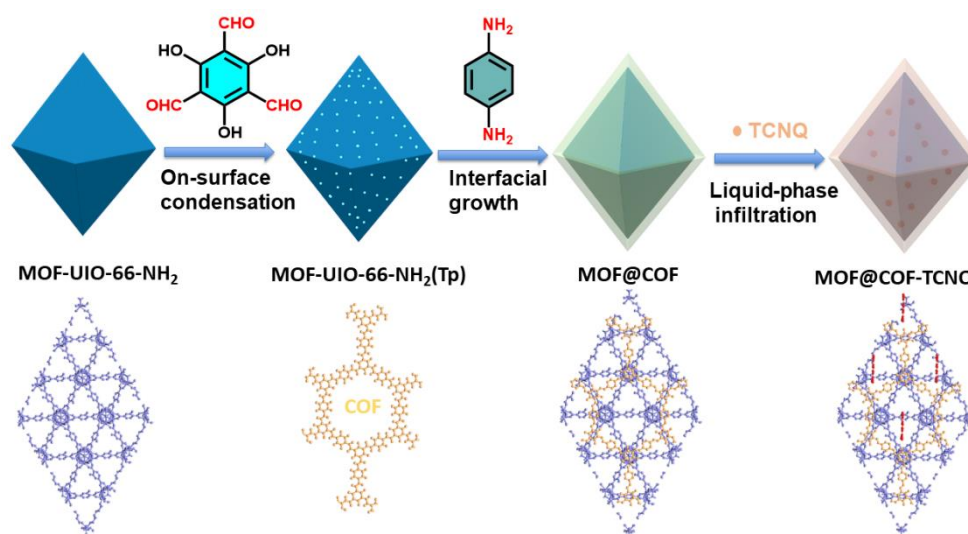

Figure 2-5 The schematic of synthesis route for MOF@COF-TCNQ hybrid materials.

2.3 Characterization techniques

The composition, structure, and texture properties of materials were investigated by X-ray powder diffraction (XRD) patterns (Bruker D8 X-ray diffractometer), Fourier transforms infrared (FT-IR) spectra were recorded using an FT-IR 4700 Fourier Transform Infrared Spectrometer (JASCO) equipped with ATR Diamond. Thermogravimetric analyses (TGA) decomposition curves are recorded in the range of 25-800 °C operating under a nitrogen atmosphere, with a thermal step of 10 °C/min on a Mettler Toledo TGA/SDTA851e system. The specific surface area was measured using a Micromeritics ASAP 2050 surface area and porosity analyzer. Prior to the BET

measurements, the samples were outgassed for 10 hours at 100 °C. Adsorption isotherms were calculated for nitrogen adsorption at 77 K and pressure up to 1 bar. Scanning Electron Microscopy (SEM) images were recorded with an FEI Quanta FEG 250 instrument S3 (FEI corporate, Hillsboro, Oregon, USA), X-ray Photoelectron Spectroscopy (Thermo Scientific K-alpha X-ray photoelectron spectrometer) which equipped with an aluminum X-ray source (energy 1.4866 keV) at a vacuum level of 10^{-8}-10^{-9} bar in the main chamber. The spot size of the X-ray beam was fixed at 400 μm. High-resolution transmission electron microscopy (HR-TEM) was performed on a JEOL 2100 F microscope working at 200 kV, equipped with a Cs probe corrector and a GATAN Tridiem imaging filter. The samples were prepared by depositing a drop of a dispersion containing graphene flakes on a TEM grid covered by a lacey carbon membrane. The as-prepared grids were kept overnight under a high vacuum to remove the eventual solvent residues and possible contaminants. MALDI-TOF mass spectrometry analysis was performed on a Bruker MicroflexLRF mass spectrometer in positive ions. All electrochemical measurements were carried out using an Autolab PGSTAT128N Potentiostat/Galvanostat instruments with a Metrohm Autolab DuoCoin Cell Holder (Metrohm AG).

2.3.1 Solid-state MAS NMR

The solid-state MAS NMR experiments in Chapter 4 were performed at room temperature on an AVANCE 750 MHz wide-bore spectrometer (BrukerTM) operating at a frequency of 750.12 MHz for ^{1}H and 188.5 MHz for ^{13}C. ^{1}H spectra were obtained by spinning all samples at 59.523 kHz in a triple resonance ^{1}H/^{13}C/^{15}N Ultra-Fast MAS probe (BrukerTM) designed for 1.3 mm o.d. zirconia rotors while ^{13}C spectra were recorded in a double resonance MAS probe (BrukerTM) allowing samples to be spun at 29.762 kHz after packing them inside 2.5 mm o.d. zirconia rotors (each type of rotors closed with vessel caps). To get undistorted lineshapes and filter out background probe signals a speed synchronized spin echo[1] was included inside the experimental pulse sequences for both nuclei. We should mention here that this kind of spin-echo (P90-τ-P180- τ) is possible for protons only because we are spinning fast enough to highly reduce the homonuclear dipolar interactions. Therefore ^{1}H spectra were directly acquired with this pulse scheme[3] with the following conditions: 2.75 μs and 5.5º s for P90° and P180° pulses, a spectral width of 59.523 kHz (also equal to the MAS speed) with 32768-time domain data points leading together to a spectral resolution of 3.63 Hz/pt. The echo time was set to 33.6 μs (2 rotation periods) and 16 scans were added separated by a 5 s recycle delay. Raw data were processed with a 20 Hz Lorentzian filter followed by Fourier transformation without zero filling.

All $^{13}C\{^1H\}$ CP/MAS spectra, including bidimensional spectra, were acquired accordingly to the polarization scheme designed for complete spectral editing in CP/MAS NMR[4] where the polarization inversion pulse was tuned to obtain as well as nonedited spectra (pulse width equal to zero) then edited. The latter polarisation inversion pulse was set to 55 µs as it was revealed to be optimal in maximizing Cq and CH_3 signals while keeping CH to null and CH_2 still negative. Hartmann-Hahn setup was for the n=1 condition with RF fields adjusted to 99.7 kHz for ^1H and 70 kHz for ^{13}C. Therefore the different pulse widths were used as follow for the different types of ^{13}C acquisitions after Hartmann-Hahn optimization; Cq edited: tcp (contact-time) = 5 ms, PIw (Polarization Inversion width)=55 µs; CH/CH_2 : tcp = 55 µs, Piw = 0 µs ; All ^{13}C (non-edited) : tcp = 500 µs or 5 ms, Piw = 0 µs. Spectra were acquired with a 29.06 Hz/pt resolution (4096 data points in the time domain and 59.523 kHz for the spectral width). Proton decoupling was obtained by using SPINAL-64[5] at a 90 kHz radiofrequency field, while the recycle time was set to 2 s. Prior to the FID acquisition, a rotation synchronized Hahn echo was inserted. Corresponding echo time was set to one rotation period (33,59 µs). 8192 scans were added leading to 6 hours of data accumulation per spectrum. A 100 Hz Lorentzian filter was applied before Fourier transform over 8192 points (zero filling by 4096 points). The chemical shift was given respective to tetramethysilane (TMS) using adamantane as a secondary

reference.[6]

The duration of the successive FSLG pulses in the 2D ^{1}H-^{13}C HETCOR with FSLG irradiation during the evolution time[7] was 3.57 μs and the magic-angle pulse length was 1.34 μs. Several 192 complex data points were acquired in the ^{1}H indirect dimension and for each t1 increment, 2048 scans were accumulated leading to a time resolution of 6.3361 ms for ^{1}H and 12.2880 ms for ^{13}C. Before Fourier transformation, a Lorentzian line broadening of 150 Hz was applied in the direct dimension while the proton dimension apodization was done with a 90° shifted squared sine-bell function, except in Figure 3-4 where a Gaussian deconvolution (-200 Hz) was applied in dimension F1 to separate the carboxy peaks. Spectral fitting was done with the TopSin 4.0 CSA fit subpackage, including ^{1}H. For MOF-UIO-66-NH$_2$ and COF-LZU1 proton chemical shifts were not adjusted but kept constant as they were directly given by the bidimensional experiments.

Assignment: ^{13}C/^{1}H HETCOR experiments were conducted in order to solve some discrepancies found in the literature that in turn may be misleading during spectral interpretation. To ensure proper assignments and structural insights bidimensional are interesting as they rely on spatial proximities by the nature of dipolar interaction between ^{1}H and ^{13}C. Moreover, tuning contact times from very short (ca 55μs) to longer (ca 500μs or more) may detect which proton is directly connected to its carbon and which are the ones remotely

spaced. For example, in Figure 3-5 the polarization pathways (blue arrows) are limited to the first case and directly provide CH connections while in the other cases (long contact times Figure 3-6, Figure 3-7, and brown trace in Figure 3-8) the additional polarization pathways (brown dotted arrows) gives valuable structural information and set or confirm assignments. It highlighted by the COOZr broad peak is the superimposition of two signal in 1D that appears here well separated and thereby assigned to the two different corresponding ^{13}C in the structure (Figure 3-6). Additionally, as some PVP residuals are present in MOF-UIO-66-NH$_2$, making the 1D spectra puzzling, the 2D map unambiguously reveals it's belonging to a different spin system (Figure 3-7). Note that due to the dipolar truncation phenomenon[6] CHs are only negligible polarized by other neighboring protons.

In order to decipher MOF@COF-LZU1 and aza-MOF@COF spectra, the same series of experiments (1D and 2D) were done upon COF-LZU1, as Figure 3-8 shows superimposition of CHs only detected HETCOR (blue trace) and Cq selective HETCOR (brown). Note that aza-MOF@COF is not given due to the lack of resolution, even in the 2D (not shown). Corresponding assignments in Figure 3-6 (C14 to C19) come from their most probable chemical shift given the structure. For instance, no other signals than CHs in the right small range are detected here and this is in good agreement with the proposed structure.

2.3.2 Fourier-transform infrared spectroscopy (FTIR)

FTIR is a useful tool to explore the infrared spectrum of adsorption or emission from solid, liquid, or gas. Especially, it can gather high-spectral-resolution signals over a wide spectral range. Therefore, it would offer significantly wider information than a dispersive spectrometer. In this thesis, we use the Thermo Scientific Nicolet iS50 FTIR Spectrometer as shown in Figure 2-6, which can utilize the permanently aligned sampling modules to acquire more information about solid active materials by utilizing ATR in both the mid and far-IR regions from 4000 to 400 cm^{-1}. In this work, MOF@COF hybrids, and COF-TMT-BT analyses of the selected FTIR regions corresponding to the 500−4000 cm^{-1} range were obtained to reveal the uniformity of the functional groups.
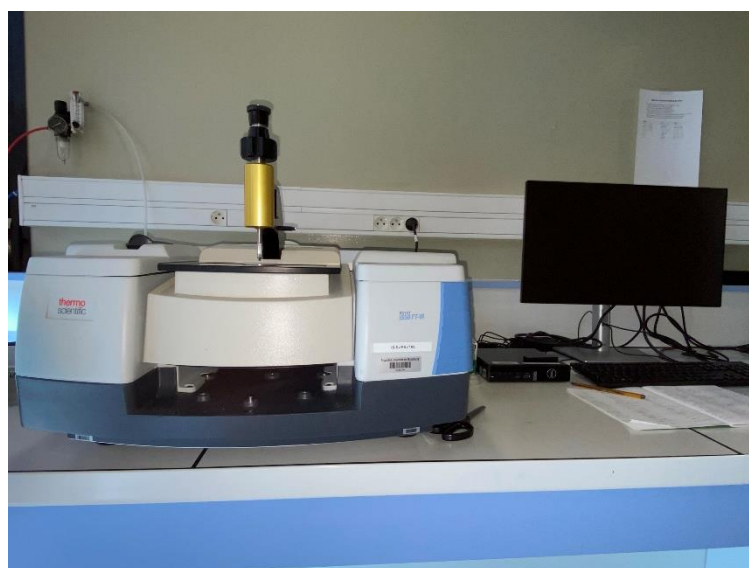
Figure 2-6 The optical image of Thermo Scientific Nicolet iS50 FTIR Spectrometer.

75

2.3.3 X-ray powder diffraction (XRD)

XRD is a facile and basic analytical technique mainly to investigate the crystal structures and phases of materials. There is a characteristic relationship between the wavelength and spacing of the crystal based on Bragg's law ($2d\sin\theta = n\lambda$) is employed to describe the diffraction from planes with spacing d, where θ is the angle of incidence with the lattice planes, d is the distance between lattice planes, n is any integer, and λ is the X-ray wavelength of the beam. In this thesis, A Bruker D8 ADVANCE with Cu Kα radiation ($\lambda = 1.5406$ Å) as shown in Figure 2-7 was hired to detect different MOFs@COFs and COF-TMT-BT powders. The powder materials are uniformly stacked on a disk holder, and the holder is placed on the axis of the diffractometer at an angle θ. The detector rotates around the diffractometer at the corresponding angle of 2θ. The current and working voltage was set at 40 kV and 40 mA, respectively.

Figure 2-7 The optical image of Bruker D8 ADVANCE.

2.3.4 Scanning electron microscopy (SEM)

SEM is one of the most commonly used for surface morphological characterization. Normally specimens are placed in a high vacuum chamber and irradiated with a focused beam of electrons. Other conditions such as low vacuum, wet conditions, cryogenic or elevated temperatures need specialized instruments to conduct the measurements. In this thesis, the morphology of

77

various MOFs@COFs hybrids and COF-TMT-BT powders materials was investigated with the field-emission scanning electron microscope FEI Quanta FEG 250 instrument S3 (FEI corporate, Hillsboro, Oregon, USA). For the preparation of powder samples, the powders would be directly pasted onto a pure silicon substrate with black conductive carbon tape or placed in the special cross-section holder.

2.3.5 X-ray Photoelectron Spectroscopy (XPS)

X-ray photoelectron spectroscopy (XPS) is a surface-sensitive quantitative spectroscopic technique that can provide information about the elemental composition, and chemical or electronic state of each element (except H and He) within the depth of ~10 nm. A X-rays beam with specific energy hits the material, ejecting electrons from the top surface of the material (0-10 nm) with a specific kinetic energy. Such info is outputted in the XPS spectrum. In this thesis, XPS was used to characterize the materials of the MOFs@COFs hybrid in Chapter 3 and Chapter 4 and COF-TMT-BT in Chapter 5. XPS analysis was performed with a Thermo Scientific K-Alpha X-ray photoelectron spectrometer. Details of the materials characterization are provided in the following chapters.

2.4 Electrochemical measurements

2.4.1 Electrochemical supercapacitor performance measurement

In this Thesis, three independent experimental chapters have been discussed to design supercapacitors and aqueous zinc-ion batteries in which novel post-synthetic modification MOFs@COFs hybrids and benzothiadiazole based olefin-linked COF-TMT-BT were used as active components. For the supercapacitor discussed in Chapter 3 and Chapter 4, all two-electrode symmetrical solid-state supercapacitors were fabricated in the same way according to the reported method.[21] Typically, MOF-UIO-66-NH$_2$ (70.0mg) was dispersed with 53 μL of oleic acid in 5.0 mL of hexane under ultrasonication for 3 h. After the mixture was separated from 1.0 mL of dispersion using a centrifuge (9000 rpm, 10 min), it was re-dispersed into 1.0 mL of a hexane solution containing 0.5 mg mL^{-1} of graphene (3.3 wt.% relative to MOF-UIO-66-NH$_2$). In the meantime, titanium substrates were cleaned with hypophosphorous acid (50 wt. % solution in water) for one hour after washing with acetone, ethanol, and water. The above dispersion solution was coated on the cleaned titanium substrates to give the 50 μm thickness of the electrode. Oleic acid was removed by immersing the electrode film in acetone, drying with nitrogen flow, and out-gassing at room temperature for 12 h. The electrode film was cut into several small slices (1.6 × 1.6 cm^2) before

assembling the cell. Two small slices were sandwiched with a separator (regenerated cellulose film, thickness 25 µm) in a coin-shaped cell and soaked with a 1 M solution of tetraethylammonium tetrafluoroborate($(C_2H_5)_4NBF_4$) in acetonitrile. The obtained two- and three-electrode symmetric solid-state supercapacitors as shown in Figure 2-8.
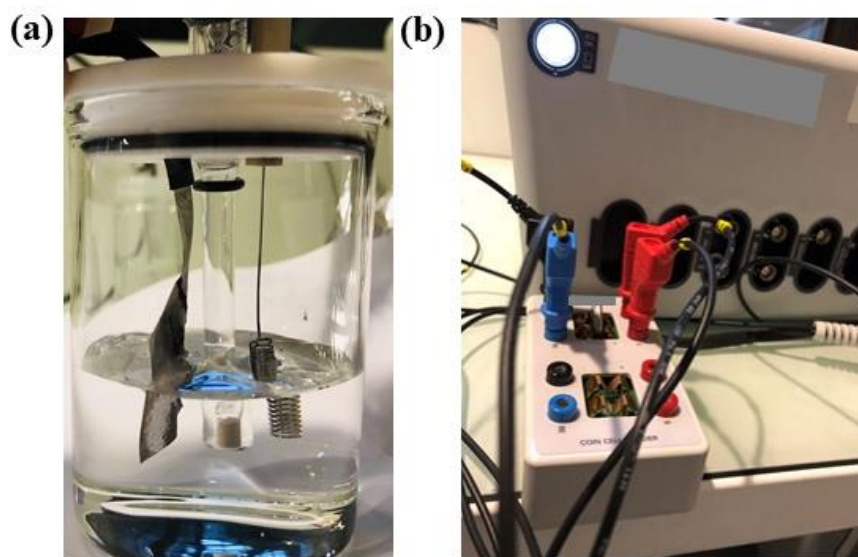

Figure 2-8 Supercapacitor device picture for (a) three electrode system, (b) two electrode cell system.

Areal capacitances (F cm^{-2}) were calculated from CV curves using Formula (1), where I (A) is the response current, ΔV (V) is the voltage window, v (mV S^{-1}) is the scan rate and S (cm^2) is the geometrical area of the electrode, stack capacitance changes the S (cm^2) to V (cm^3), the volumetric of the electrode (this includes a pair of the active material and Ti substrate, and the separator with electrolyte).

$$C = \frac{\int I \, dV}{v \, S \, \Delta V}$$
Formula (1)

2.4.2 Aqueous zinc-ion batteries performance measurement

For aqueous zinc-ion batteries discussed in Chapter 6, Zinc foil was directly used as an anode electrode after being polished with gauze and pouched into electrodes with a 12 mm diameter. The cathode electrode is composed of 70 wt% of COF-TMT-BT, 20 wt% of multi-walled carbon nanotubes (MWCNT), and 10 wt% of polytetrafluoroethylene (PTFE) as the binder. Ethanol solvent was added to the above mixture and then the mixture was coated on stainless steel gauze. The electrodes were dried in a vacuum oven at 80°C overnight. ZIBs were assembled with the electrolyte of 2 M $Zn(CF_3SO_3)_2$ aqueous solution, a non-woven separator MPF30AC as a separator, and a coin battery shell. For each electrode, the mass loading was 1.7 mg cm^{-2} and the weight ratio of 70 wt.% of active material.

The electrochemical performance of ZIBs was studied using cyclic voltammetry (CV), and electrochemical impedance spectroscopy (EIS) on Autolab PGSTAT128N Potentiostat / Galvanostat instruments with a Metrohm Autolab DuoCoin Cell Holder (Metrohm AG) at room temperature. CV was performed at scan rates of 0.1 - 100 mV s^{-1} in the voltage range between 0 and

1.6 V. EIS measurement was recorded with a frequency range of 0.01 Hz to 1 MHz. The galvanostatic charge-discharge (GCD) tests were carried out on Neware Battery Tester (BTS-4008T-5V/10mA, Neware Technology Company, Guangdong, China). GCD curves were tested at current densities ranging from 0.1 to 5 A g^{-1}.

The energy density E and power density P:

$$E = \int V \times I dt / m$$

$$P = \frac{E}{t}$$

in which V is average discharge voltage, m is COF-TMT-BT electrode mass. The accurate value is obtained from the integral computation given by the analyzing software of the testing instrument.

2.5 References

1. Wang, G.-B.; Li, S.; Yan, C.-X.; Lin, Q.-Q.; Zhu, F.-C.; Geng, Y.; Dong, Y.-B., A benzothiadiazole-based covalent organic framework for highly efficient visible-light driven hydrogen evolution. *Chemical Communications* **2020,** *56* (83), 12612-12615.

2. Lyu, H.; Diercks, C. S.; Zhu, C.; Yaghi, O. M., Porous Crystalline Olefin-Linked Covalent Organic Frameworks. *Journal of the American Chemical Society* **2019,** *141* (17), 6848-6852.

3. Hahn, E. L., Spin Echoes. *Physical Review* **1950,** *80* (4), 580-594.

4. Wu, X. L.; Zilm, K. W., Complete Spectral Editing in CPMAS NMR. *Journal of Magnetic Resonance, Series A* **1993,** *102* (2), 205-213.

5. Fung, B. M.; Khitrin, A. K.; Ermolaev, K., An Improved Broadband Decoupling Sequence for Liquid Crystals and Solids. *Journal of Magnetic Resonance* **2000,** *142* (1), 97-101.

6. Morcombe, C. R.; Zilm, K. W., Chemical shift referencing in MAS solid state NMR. *Journal of Magnetic Resonance* **2003,** *162* (2), 479-486.

7. van Rossum, B. J.; Förster, H.; de Groot, H. J. M., High-Field and High-Speed CP-MAS13C NMR Heteronuclear Dipolar-Correlation Spectroscopy of Solids with Frequency-Switched Lee-Goldburg Homonuclear Decoupling. *Journal of Magnetic Resonance* **1997,** *124* (2), 516-519.

8. Choi, K. M.; Jeong, H. M.; Park, J. H.; Zhang, Y.-B.; Kang, J. K.; Yaghi, O. M., Supercapacitors of Nanocrystalline Metal-Organic Frameworks. *ACS Nano* **2014,** *8* (7), 7451-7457.

Chapter 3 Synthesis of robust MOFs@COFs porous hybrid materials *via* Aza-Diels-Alder reaction: towards high performance supercapacitor

In this Chapter, we discuss an unprecedented use of aza-Diels-Alder cycloaddition reaction as post-synthetic modification of MOF@COF-LZU1, to generate aza-MOFs@COFs hybrid porous materials with extended π-delocalization. As a proof-of-concept, the obtained aza-MOFs@COFs are used as an electrode in supercapacitors displaying a specific capacitance of 20.35 μF cm^{-2} and high volumetric energy density of 1.16 F cm^{-3}. Our approach of post-synthetic modification of MOFs@COFs hybrids implements rational design for the synthesis of functional porous materials and expands the plethora of promising application of MOFs@COFs hybrid porous materials in energy storage applications. The Solid-state NMR analysis has been done in the collaboration with Dr. Jésus Raya, and the HR-TEM images were collected by Dr. Walid Baaziz, and the XPS spectra were collected by Dr. Fanny Richard from the University of Strasbourg, France.

3.1 Introduction

Though a vast number of SCs' electrode materials have been reported to date, carbon nanomaterials attracted great attention due to their physicochemical and electrochemical properties. In particular, activated carbons and metal oxides have an important role to increase the overall performance of SCs. However, their irregular morphologies, wide pore size distributions and low energy density cannot keep pace with increasing higher energy storage requirements.[1, 2] Three-dimensional architectures have allured remarkable attention for SCs applications owing to their highly accessible surface area, low density, structural interconnectivity (micro-, meso- and macro-interconnected pores). Therefore, the use of porous scaffolds such as MOFs and COFs can benefit especially in terms of specific surface area, presence of pores with controllable size and effective charge transport. Yet, the aforementioned drawbacks of those materials have to be overcome. A key strategy for overcoming the problem of low energy density is the use of new synthetic paths or the post-synthetic modification (PSM) of MOFs@COFs hybrid porous materials toward improved electrochemical SCs electrodes.

3.2 Results and Discussion

In this Chapter, we have developed a novel aza-MOF@COF hybrid electrode for supercapacitors through the formation of MOF@COF followed by aza-Diels-Alder cycloaddition. The synthetic route of the aza-MOF@COF has been discussed in experimental Chapter 2. The multiscale characterization of MOF-UIO-66-NH$_2$, MOF@COF-LZU1 and aza-MOF@COF structures have been carried out using different experimental techniques (detailed information has been discussed in experimental Chapter 2). The obtained MOF-UIO-66-NH$_2$, MOF@COF-LZU1, and aza-MOF@COF porous materials were used as electrodes in symmetric solid-state supercapacitors. MOF-UIO-66-NH$_2$, MOF@COF-LZU1 and aza-MOF@COF based electrodes were constructed into a coin-shaped cell capacitor and soaked with 1 M solution of tetraethylammonium tetrafluoroborate ($(C_2H_5)_4NBF_4$) in acetonitrile. After the coin-shaped cell was sealed, cyclic voltammetry (CV) was measured in a relatively wide scan range from 10 to 1000 mv s^{-1} with the potential values swept in a range of the cut-off values ($0 \leq E \leq 2.7$ V) as shown in Figure 3-1, which is typically used to calculate the capacitance performance (including the role played by a pair of active materials and substrate, and separator)[3]
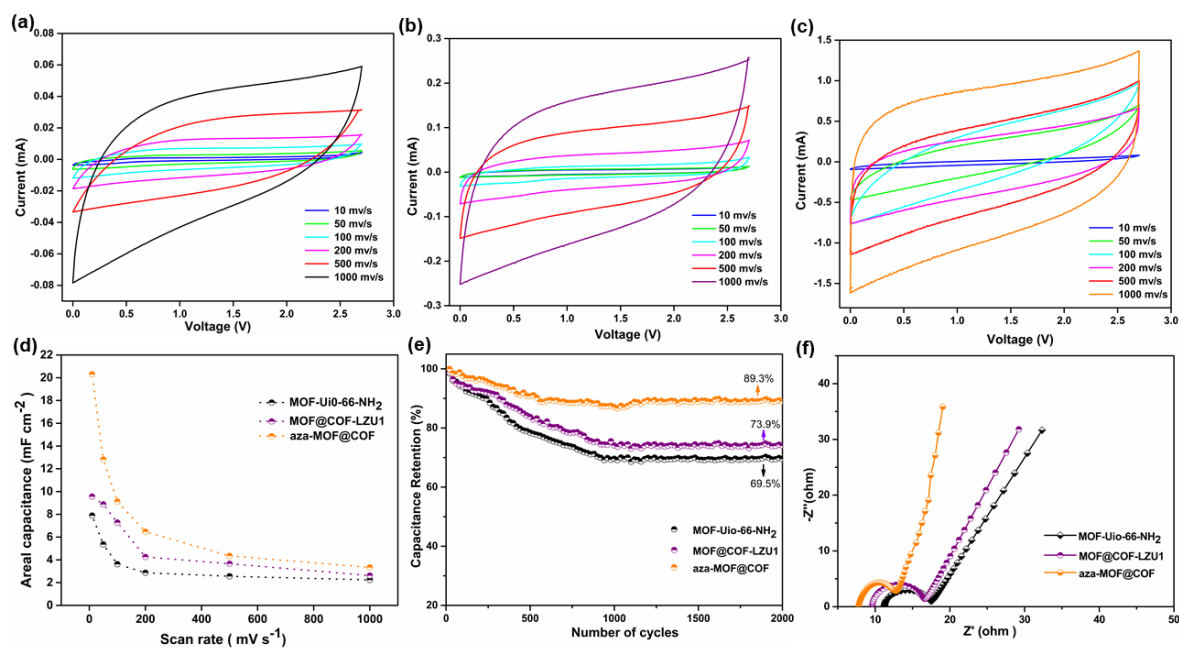
Figure 3-1 Cyclic voltammetry curve of a) MOF-UIO-66-NH$_2$, b) MOF@COF-LZU1, c) aza-MOF@COF, d) areal capacitance, e) capacitance retention, f) Nyquist electrochemical impedance spectra.

The CV curves of the aza-MOF@COF-based electrode display a more rectangular shape and higher current values compared with MOF-UIO66-NH$_2$ and MOF@COF-LZU1, confirming the improved electrochemical stability and capacitance.[4-6] Specific capacitance calculated from the CV curves at different scan rates and charge/discharge profiles in Figure 3-2 to Figure 3-4 was used to evaluate the charge storage capacity of the supercapacitors.
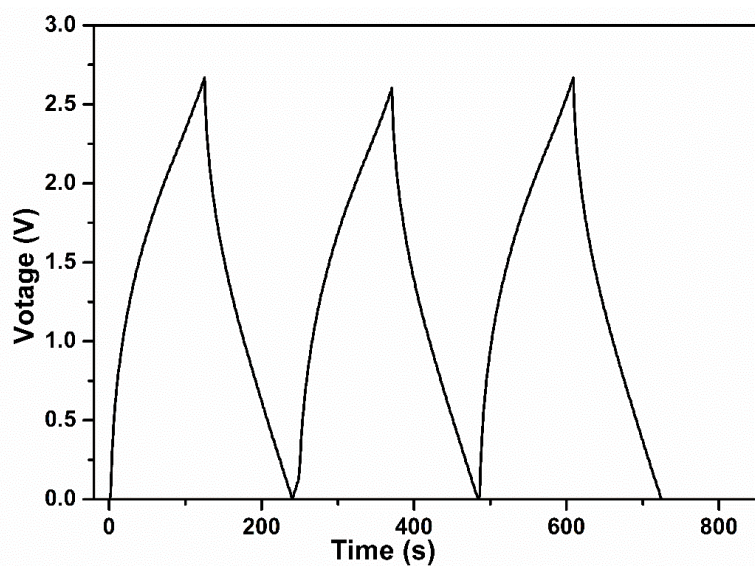
Figure 3-2 Charge/discharge profile at 0.2 A cm^{-2} for MOF-UIO-66-NH$_2$.
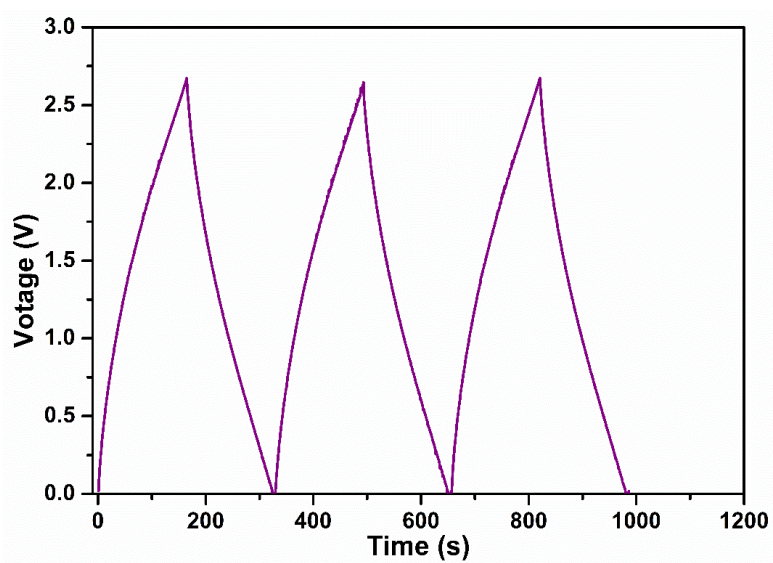
Figure 3-3 Charge/discharge profile at 0.2 A cm^{-2} for MOF@COF-LZU1.
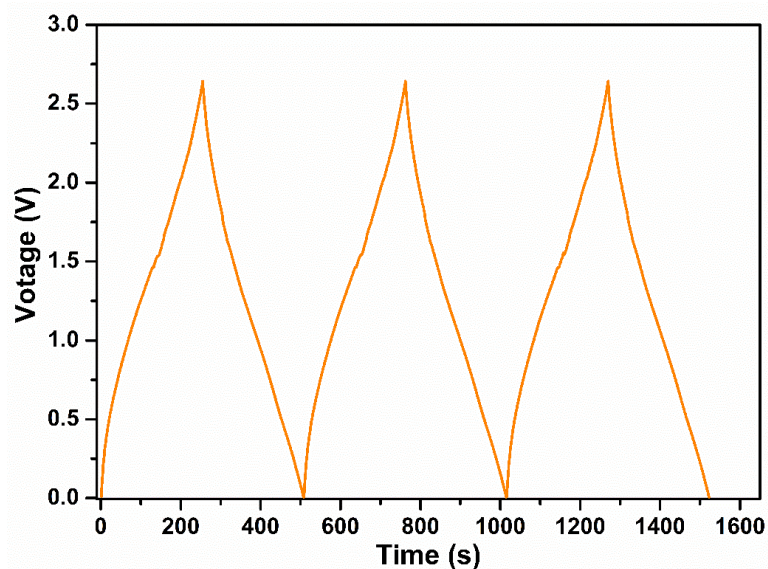
Figure 3-4 Charge/discharge profile at 0.2 A cm^{-2} for aza-MOF@COF.

The areal capacitance of MOF-UIO-66-NH$_2$, MOF@COF-LZU1 and aza-MOF@COF were estimated as 7.89, 9.56 and 20.35 mF cm$_{areal}^{-2}$, respectively (Figure 3-1d). The corresponding stack capacitance was calculated as 0.45, 0.55 and 1.16 F cm$_{stack}^{-3}$, respectively. The measured capacitance of aza-MOF@COF is twice as high as that of pristine MOF-UIO66-NH$_2$ and MOF@COF-LZU1 materials. Noteworthy, such capacitance is over 11 and 17 times higher than those of activated carbon (0.788 mF cm$_{areal}^{-2}$ and 0.100 F cm$_{stack}^{-3}$) and graphene (0.515 mF cm$_{areal}^{-2}$ and 0.065 F cm$_{stack}^{-3}$), and much higher than some literature reported so far (Tables 3-1). Furthermore, the aza-MOF@COF cell exhibits good cycling stability with a capacitance retention of 89.3% compared with MOF-UIO-66-NH$_2$ (69.5%) and MOF@COF-LZU1 (73.9%) after 2000 cycles performed at a current density

of 0.2 mA cm^{-2} (Figure 3-1e). The excellent supercapacitor performances of aza-MOF@COF are attributed to the extended π-delocalization in the hybrid structure and decreased pore size (from ~1 nm to ~0.7 nm) which is closer to the electrolyte ions (The diameter of $(C_2H_5)_4^+$ and NBF_4^- ions in the electrolyte is 0.68 and 0.33 nm, respectively[7]) and result in an anomalous increase in supercapacitor devices.[7-9] To get more insight into the anomalous capacitance increase, electrochemical impedance spectroscopy (EIS) was carried out between 10^{-1} and 10^6 Hz to evaluate the internal resistances for the charge transfer process of the samples, as shown in Figure 3-1, a relatively small semicircle in the high-frequency region represents the dominant resistive nature of the supercapacitor system consisting of electrode/electrolyte/current-collector, the beginning of the semicircle line represent the resistance (Rs) of the electrolyte in contact with the current collector and electrode materials, the termination of the semicircle line represents the internal resistance (Rp) of the electrode materials, the diameter of the semicircle (Rp-Rs) is equal to the equivalent series resistance (ESR), the calculation results for MOF-UIO66-NH$_2$, MOF@COF-LZU1 and aza-MOF@COF are 6.85, 6.39 and 4.84 Ω cm^{-1}, respectively. The ESR results confirm that the PSM of MOF@COF-LZU1 results in increased electrical conductivity, what's more, the second segment of the aza-MOF@COF EIS curves display a steeper slope which highlights increased ion permeation into

the electrode material concerning MOF-UIO66-NH$_2$, MOF@COF-LZU1.

Table 3-1. Performance comparison of this work and other capacitor materials based on symmetric solid-state supercapacitors.

Type	Electrode materials	stack capacitance (F cm^{-3})	areal capacitance (mF cm^{-2})	Ref
Activated carbon (ACs)	Commercial ACs	20.3-80	0.006-0.014	Science 2006, 313, 1760.Wiley Interdiscip. Rev. Energy Environ. 2014, 3,424.
	Chemosynthetic ACs		0.005-0.046	Carbon 2001, 39, 937
Carbon nanotubes (CNTs)	Multi-walled CNTs	15-25		J. Power Sources 1999, 84, 126.
	C-MWCNTs	95.3	0.06	Bull. Chem. Soc. Jpn. 1999, 72, 2563.
	Pitch-derived carbon fiber	90	0.013	J. Electrochem. Soc. 2000, 147, 38.
Graphene	Graphene		0.064	J. Phys. Chem. C 2009, 113, 13103.
	Microwave exfoliated GO	60	0.007	Science 2011, 332, 1537.
	3D graphene-based materials	80	0.006	Sci. Rep. 2013, 3, 1408.
MOF	Ni-HAB	760	3700	Nat. Mater. 2016, 16, 220.
	MOF-5	0.043	0.341	
	HKUST-1	0.296	2.334	ACS Nano 2014, 8, 7451.
	ZIF-8	0.034	0.268	
	nMOF-867	0.64	5.09	
COF	CT-Dq1Da1Tp		8.5	ACS Appl. Mater. Interfaces 2018, 10, 28139
	CT-DqTp		12	
	e-JUC-510	1.02	4.17	Advance Materials2020, 32, 1907289
	e-JUC-511	5.32(W cm^{-3})	5.46	
	e-JUC-512	4.08(W cm^{-3})	5.85	
MOF@COF	**MOF-UIO-66-NH$_2$**	**0.45**	**7.89**	
	MOF@COF-LZU1	**0.55**	**9.56**	**This work**
	aza-MOF@COF	**1.16**	**20.35**	

3.3 Characterization

3.3.1 PXRD spectra of MOF-UIO-66-NH₂, MOF@COF-LZU1 and aza-MOF@COF

The structure of the MOF-UIO-66-NH$_2$ was firstly investigated by powder X-ray diffraction (PXRD) analysis as shown in Figure 3-5, the patterns of as-synthesized MOF-UIO-66-NH$_2$ matched well with the previously reported results,[10] highlighting that the use of PVP doesn't influence the reaction itself, yet improves the dispersibility of MOF-UIO-66-NH$_2$. As shown in Figure 3-6, the crystallinity of synthesized compounds was further elucidated using PXRD analysis. In comparison to the pristine simulated pattern of MOF-UIO-66-NH$_2$ and COF-LZU1, the PXRD pattern of MOF@COF-LZU1 and aza-MOF@COF are in good agreement demonstrating a similarly high level of crystallinity. The insignificant shift of (100) peak in the aza-MOF@COF sample indicates the preservation of a high crystalline framework, which could be potentially affected during the imine-to-quinoline linkage transformation.
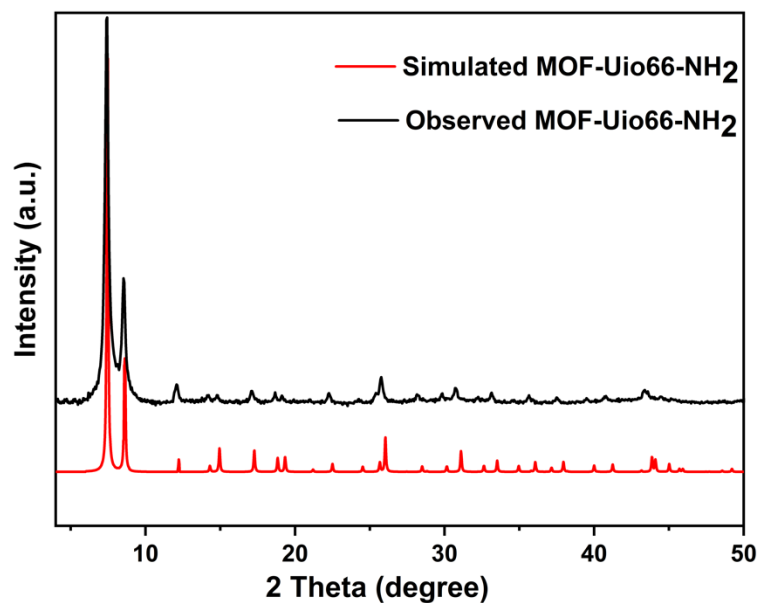
Figure 3-5 The PXRD patterns of MOF-UIO66-NH$_2$
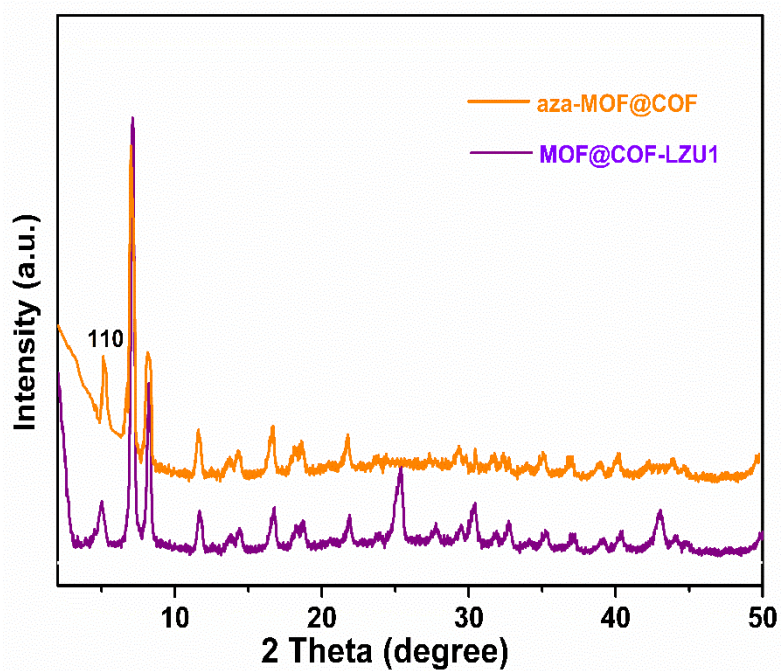
Figure 3-6 The PXRD patterns of MOF@COF-LZU1 and aza-MOF@COF hybrid materials.

3.3.2 FT-IR spectra of MOF-UIO-66-NH₂, MOF@COF-LZU1 and aza-MOF@COF

The successful growth of COF-LZU1 onto MOF-UIO-66-NH$_2$ and corresponding conversion into quinoline-linked aza-MOF@COF upon addition of phenylacetylene into MOF@COF-LZU1 hybrid materials were then characterized by and Fourier transforms infrared (FT-IR) spectroscopy. The comparison of FT-IR spectra of aza-MOF@COF with MOF-UIO-66-NH$_2$ and MOF@COF-LZU1 (Figure 3-7 and Figure 3-8) revealed the presence of a new broad cluster of peaks at ~1600 cm^{-1}. Within this cluster characteristic peaks at 1541 and 1580 cm^{-1} can be identified and ascribed to the formation of quinolyl species,[11] what's more, the blue shift of the C-C=N-C stretch from 1232 to 1256 cm^{-1} unambiguously demonstrated the formation of aromatic quinoline core after the reaction.[12] Aza-Diels-Alder reaction between aryl imines and aryl alkynes allows the conversion of COF-LZU1 imine linkers in MOF@COF-LZU1 into corresponding quinoline-linked aza-MOF@COF. However, because of the steric hindrance between MOF-UIO-66-NH$_2$ and COF-LZU1, the imine-to-quinoline conversion is not quantitative as evidenced by the presence of there are still some C=N imine bonds that cannot be modified by the aza-Diels-Alder reaction and the broad cluster of peaks of quinoline overlaps with C=N imine stretch between two monomers.
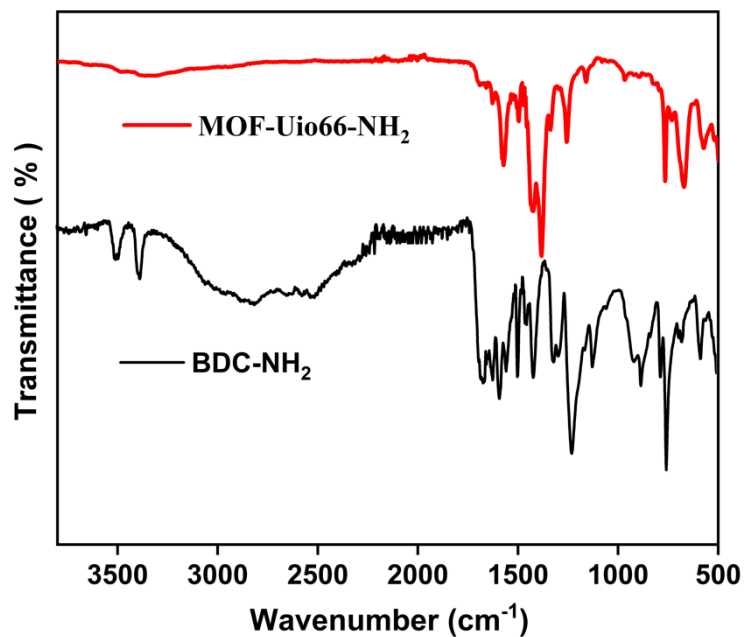
94

Figure 3-7 The FT-IR spectra of MOF-UIO-66-NH$_2$ and organic ligand 2-aminoterephthalate.
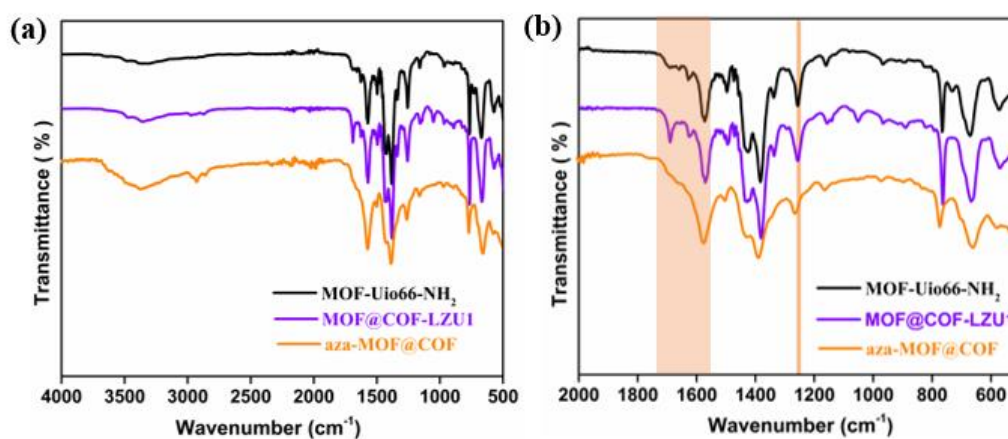

Figure 3-8 a-b) FTIR and magnified spectra of MOF-UIO-66-NH$_2$, MOF@COF-LZU1 and aza-MOF@COF.

3.3.3 Solid-state NMR structural analysis of MOF-UIO-66-NH₂, MOF@COF-LZU1 and aza-MOF@COF

The solid-state NMR shreds of evidence for structural analysis of such materials are usually obtained based on classical mono-dimensional ^{1}H to ^{13}C Cross Polarization Magic Angle Spinning experiments (CP/MAS)[13-15] and discussions rely exclusively on isotropic chemical shifts measurements that give structural information at nucleus level. Unlike in solution and even with improved sample crystallinity ^{13}C resonances are rather broad in the solid-state, they easily overlap. It may render assignments quite difficult, leading in turn to misinterpretation, especially in the case of MOFs and COFs where quaternary and CH chemical shifts are piled up in the same small, crowded zone (ca 110 to 160 ppm). In order to solve this issue, we also performed more advanced experiments like ^{13}C spectral edition[16], ^{1}H Ultra-Fast MAS Direct Polarisation (^{1}H DP/MAS) and $^{1}H/^{13}C$ Frequency Shifted Lee-Goldburg HETCOR ($^{1}H/^{13}C$ FSLG HETCOR)[17-21]. The latter allows for the detection of spatial proximities between ^{1}H and ^{13}C and may be tuned to select short internuclear distances like CH to remoter quaternaries. Moreover, in addition to its enhanced resolution for mono-dimensional spectra, it may separate spin-systems belonging to different molecules and proves useful when residual reagents also overlap peaks of interest as exhibited in Figure 3-9 to Figure 3-12.
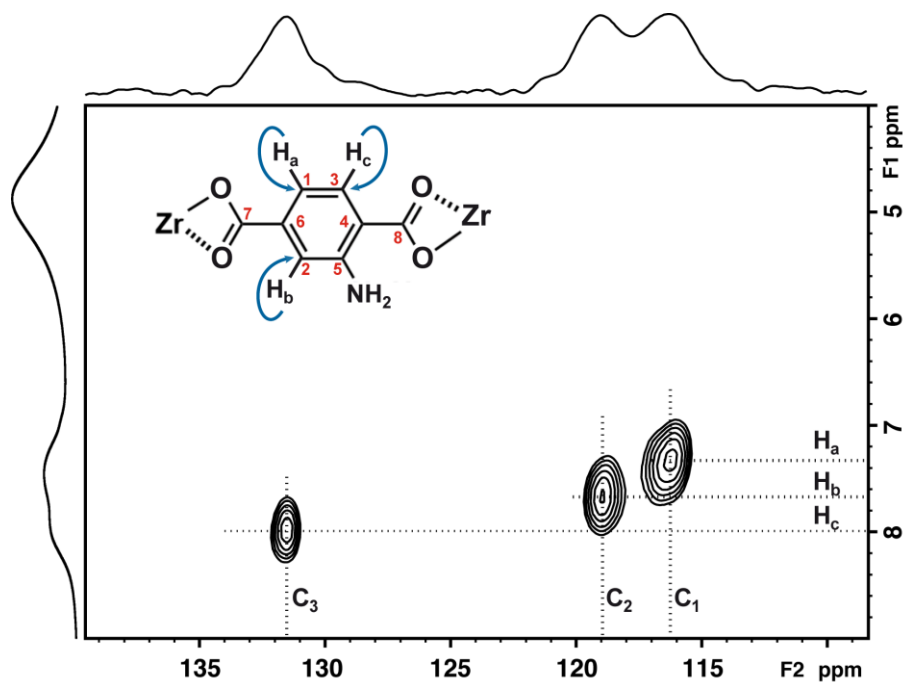
Figure 3-9. 2D FSLG ^{1}H-^{13}C HETCOR of MOF-UIO-66-NH$_2$. Contact time=55 µs. Only one bond C-H pairs are detected. Blue arrows schematize the polarization pathway from proton to carbon (top trace: projection, left trace: direct ultra-fast MAS ^{1}H spectrum).
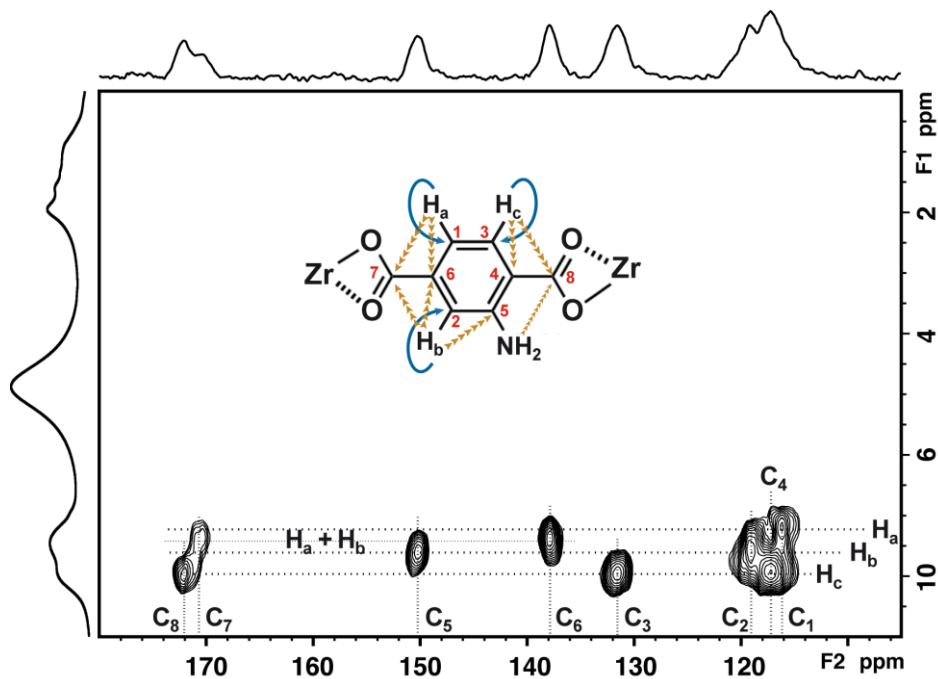
Figure 3-10 2D FSLG ^{1}H-^{13}C HETCOR of MOF-UIO-66-NH$_2$. Contact time=5 ms, unselective. Cq is polarized by their neighboring protons, depicted by brown dotted arrows (spin diffusion pathway is not represented). ^{1}H dimension is apodized by a gaussian function to deconvolute the two COO peaks. C$_7$ and C$_6$ are remotely polarized by both H$_a$ and H$_b$ leading to superimposition in the ^{1}H dimension (top trace: projection, left trace: direct ultra-fast MAS ^{1}H spectrum).
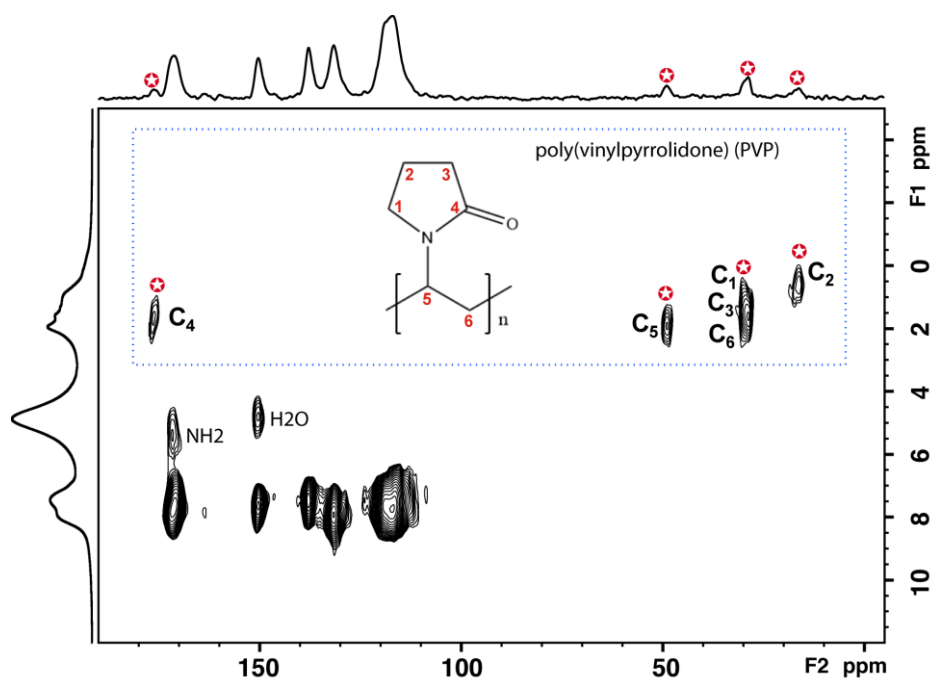
Figure 3-11 The same as Figure 3-9 at lower contour levels. Residual PVP peaks are visible and identified. C4 is unambiguously assigned to PVP and not to MOF-UIO-66-NH$_2$. (top trace: projection, left trace: direct ultra-fast MAS ^{1}H spectrum).
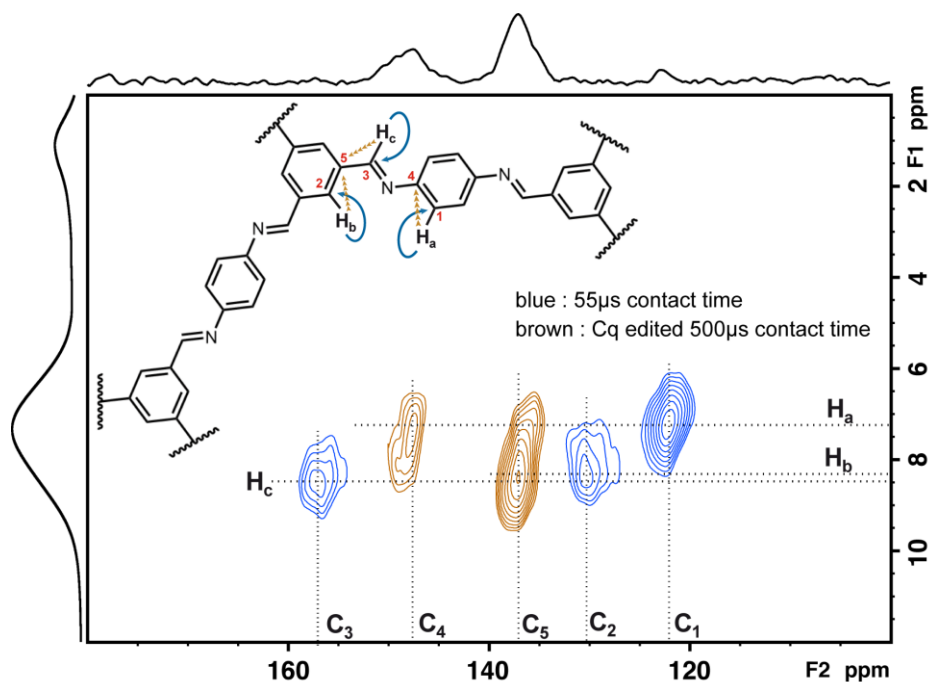
Figure 3-12 Superimposition of 2D HETCORs on COF-LZU1. 55 µs contact time (blue, only CHs detected) and 5 ms contact time Cq-CH$_3$ edited (brown, only Cq here). (top trace: projection, left trace: direct ultra-fast MAS ^{1}H spectrum).

99

Based on the above 2D NMR analysis results, we can obtain a possible complete assignment as shown in Figure 3-13 on both proton and carbon sides which gives strong evidence for reaction completion.
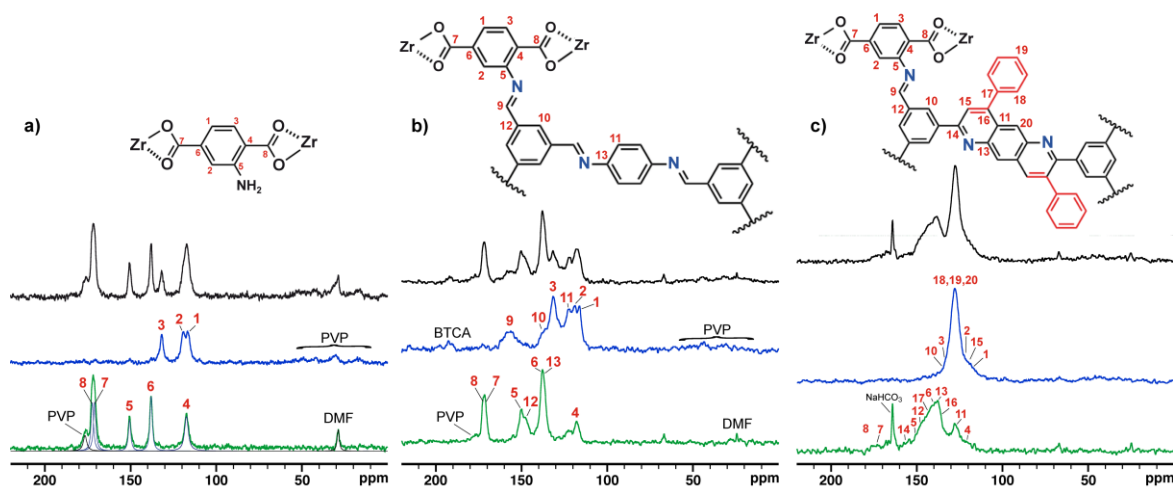

Figure 3-13 ^{13}C solid-state NMR series of MOF-UIO-66-NH$_2$ (a), MOF@COF-LZU1 (b) and aza-MOF@COF (c). Bottom (green) : Edited CP/MAS (only Cq and CH$_3$ detected); Middle (blue) : short contact time (55µs) CP/MAS (selects CHs and CH$_2$) ; top (black) : long contact time (5ms) regular CP/MAS spectrum (all carbons there). CSA fitting of Edited CP/MAS MOF-UIO-66-NH$_2$ (dark blue and black) in Cq/CH$_3$ spectrum to show overlapped components in carboxylic peaks, Omitted on the other traces for clarity.

An attentive examination of MOF-UIO-66-NH$_2$ and COF-LZU1 substructures of MOF@COF-LZU1 indicates that the latter ^{13}C spectra shouldn't differ significantly from individual ones from MOF-UIO-66-NH$_2$ and COF-LZU1 alone. As chemical shifts are essentially due to electronic surrounding at the nucleus level and as there aren't any or very few changes on any carbon site from MOF@COF-LZU1 relative to MOF-UIO-66-NH$_2$ and

COF-LZU1, it is natural to observe no changes between spectra from MOF@COF-LZU1 versus the sum of MOF-UIO-66-NH$_2$ and COF-LZU1as exhibited in Figure 3-14.
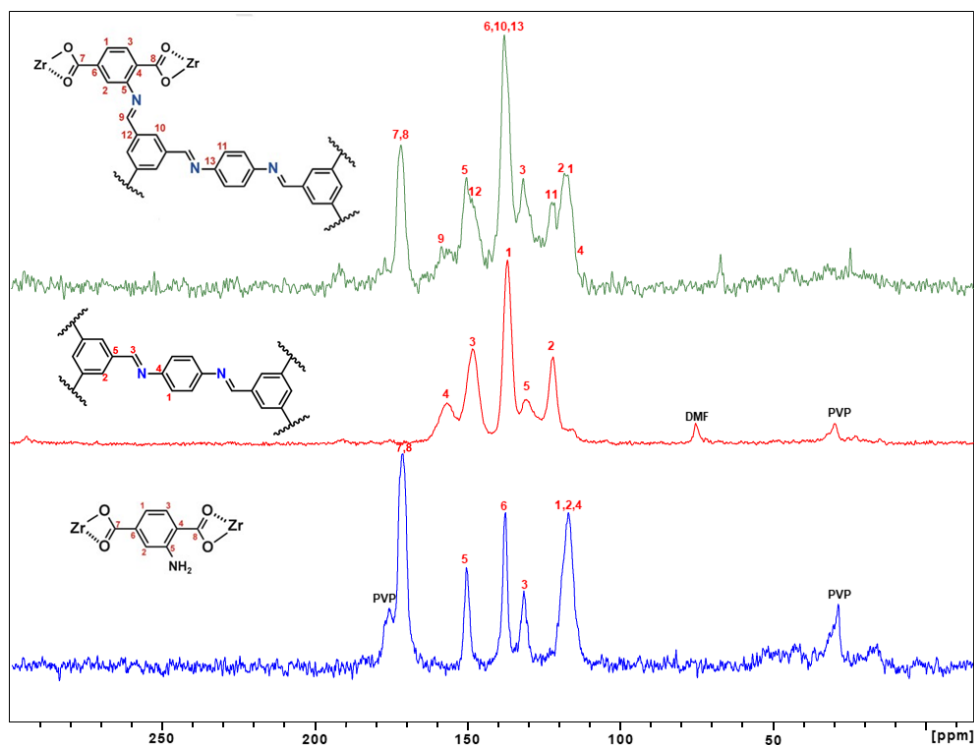

Figure 3-14 Superimposition of ^{13}C CP/MAS NMR spectrum of the blue line for MOF-UIO-66-NH$_2$, red wine for COF-LZU1 and green line for MOF@COF-LZU1.

On the other hand, ^{1}H ultra-fast MAS at speeds up to 60 kHz can achieve provide the resolution needed to gain more details. Indeed, the only site experiencing a drastic change is the NH$_2$: it should completely disappear from the MOF@COF-LZU1 ^{1}H spectrum with reaction completion. In the MOF-UIO-66-NH$_2$ ^{1}H spectrum, a broad and intense peak located at ca 5 ppm is ascribed to overlapped NH$_2$+water while there isn't any in COF and a smaller

101

one remains in MOF@COF-LZU1 at 4.8 ppm (Figure 3-15). Given the fact that, unlike ^{13}C CP/MAS, ^{1}H DP/MAS spectra are quantitative it was possible to deconvolve them in order to get relative intensities of each signal of interest, mainly the CHs and NH$_2$/H$_2$O. When in MOF-UIO-66-NH$_2$ the NH$_2$/H$_2$O signal integrates to 7.8 for 3 CHs in MOF@COF-LZU1 it gives 5.8 for the same 3 CHs in its MOF-UIO-66-NH$_2$ sub-spectrum. Within the experimental error, it appears clearly that the NH$_2$ has quite completely disappeared and thus been quite totally converted in C-N=C. Hence the remaining huge peak at 4.8 ppm may be ascribed to be only water. The difference in areas corresponds to the loss of 2 protons when passing from MOF-UIO-66-NH$_2$ to MOF@COF-LZU1, indicating total conversion of NH$_2$ in the imine bridge. CH Chemical shifts were not fitted as they were got directly from ^{1}H/^{13}C 2D experiments.
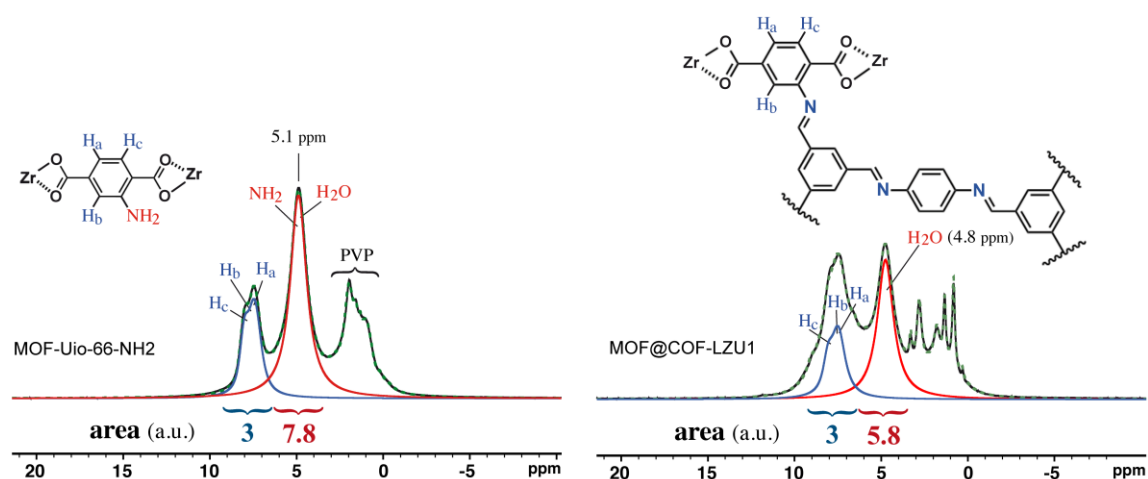
Figure 3-15 Ultra-Fast MAS ^{1}H NMR of MOF-UIO-66-NH$_2$ (left) and MOF@COF-LZU1 (right). For the sake of clarity, only CHs and NH$_2$/H$_2$O components are shown. Black: experimental, dotted green: calculated spectrum, blue: sum of fitted CHs, red: H$_2$O+NH$_2$ or H$_2$O.

Finally, the imine to quinoline conversion in aza-MOF@COF is evidenced in Figure 3-16 where quite no signal is detected anymore within the 150-160 ppm range in the CH-edited ^{13}C spectrum. Signals reappear in the Cq/CH$_3$ edited one, clearly showing rather an efficient transformation of C=N imine (CH at 157 ppm) in 2-quinolyl carbon (157 ppm also). Anyway, some residual signal in the baseline is indicative of residual imine (-C=N) presence in a very low amount.
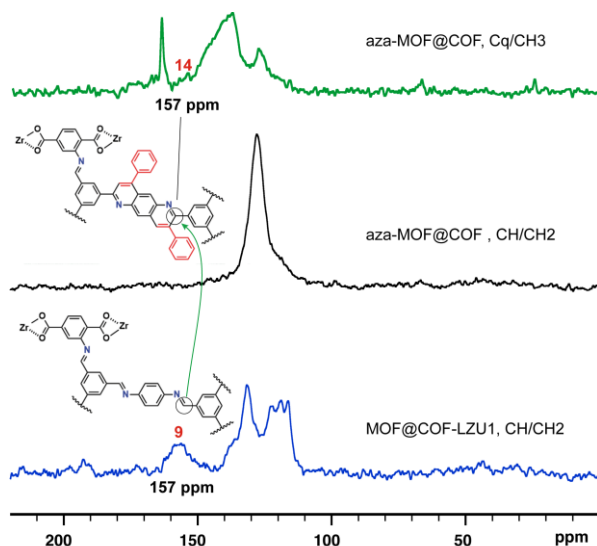
Figure 3-16 Bottom (blue): CH/CH$_2$ selected ^{13}C CP/MAS NMR spectrum of MOF@COF-LZU1, with a focus on imine CH located at 157 ppm (see fig. 2 for labeling). Middle (black): aza-MOF-COF CH/CH$_2$ selective ^{13}C CP/MAS spectrum, where no more imine CH is present. Top (green): aza-MOF-COF Cq/CH$_3$ selective ^{13}C CP/MAS spectrum. 2-quinolyl carbon signal at 157 ppm is detected.

3.3.4 XPS spectra of MOF-UIO-66-NH$_2$, MOF@COF-LZU1 and aza-MOF@COF

To gain more insight into the nature of nitrogen species in aza-MOF@COF and the conversion from imine to quinoline, we performed the X-ray photoelectron spectroscope (XPS) of the electronic state of the N element. The analysis of N1s spectra of MOF-UIO-66-NH$_2$ revealed the presence of a peak at 399.5 eV corresponding to the primary amine species. As previously observed, a negligible peak at 401.6 eV can be assigned to -NH

groups of the organic linkers in pure UIO-66-NH$_2$ nanocrystals (Figure 3-17a).[22, 23] Compared with pristine MOF-UIO-66-NH$_2$, MOF@COF-LZU1 only shows binding energy at 399.2 eV, indicating the formation of imine bonds(Figure 3-18b). Upon PSM, a fraction of the N1s is shifted to higher binding energies ~399.7 eV, corresponding to the C=N in quinoline moieties (Figure 3-18c).[24]
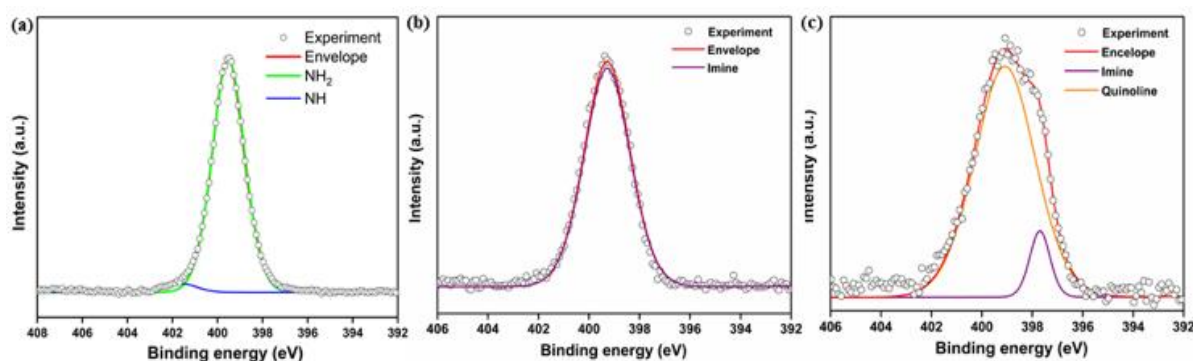

Figure 3-17 The N1s XPS spectra of a) MOF-UIO-66-NH$_2$, b) MOF@COF-LZU1, c) aza-MOF@COF

In addition, as shown in Figure 3-18, the C1s XPS spectra of aza-MOF@COF compared with MOF-UIO-66-NH$_2$ and MOF@COF-LZU1, showing an apparent π-π* satellite peak, which was contributed by the extended delocalized π electrons from induced phenylacetylene aromatic ring.[25]
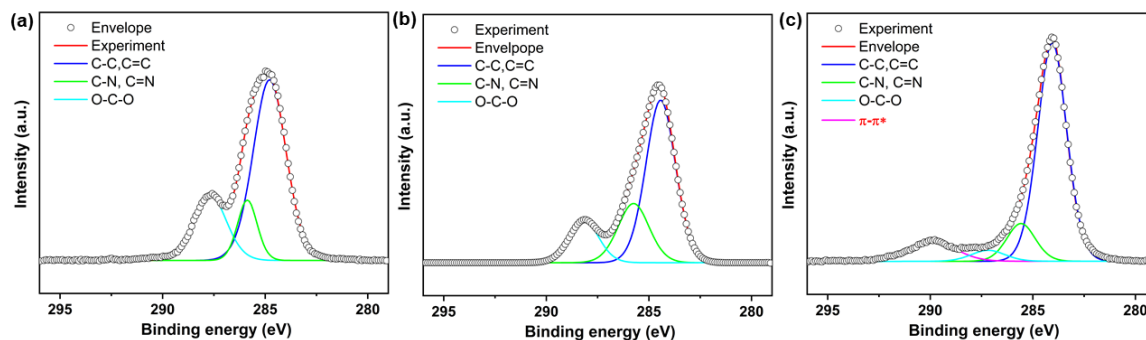
Figure 3-18 The C1s XPS spectra of (a)MOF-UIO-66-NH$_2$, (b) MOF@COF-LZU1 and (c)aza-MOF@COF.

3.3.5 SEM and TEM images of MOF-UIO-66-NH$_2$, MOF@COF-LZU1 and aza-MOF@COF

The morphologies of the as-synthesized MOF-UIO-66-NH$_2$, MOF@COF-LZU1 and aza-MOF@COF were characterized by field-emission scanning electron microscopy (FS-SEM) and high-resolution transmission electron microscope (HR-TEM). MOF-UIO-66-NH$_2$ nanoparticles shown in Figure 3-19 exhibit an octahedral shape with a smooth surface and an average diameter of ~200 nm. After the surface modification with COF, the MOF@COF-LZU1 nanoparticles maintain the morphology with an increased averaged diameter of ~220 nm as shown in Figure 3-19d. Noteworthy, after PSM the surface of aza-MOF@COF nanoparticles becomes rougher and a slight increase of the diameter has been monitored (~230 nm, Figure 3-19g). The HR-TEM images of MOF@COF-LZU1 nanoparticles

illustrated in Figure 3-19f reveal an obvious layer lattice for COF-LZU1 at the edge of pristine MOF-UIO-66-NH$_2$ around 20 nm, which is consistent with the increased nanoparticle average diameter. It is worth mentioning that after the surface PSM with aza-Diels-Alder reaction, the aza-MOF@COF nanoparticles showed apparent drawbacks in the COF-LZU1 lattice layer and a relatively short lattice layer in Figure 3-19i, which can be ascribed to the induced quinolyl moieties.
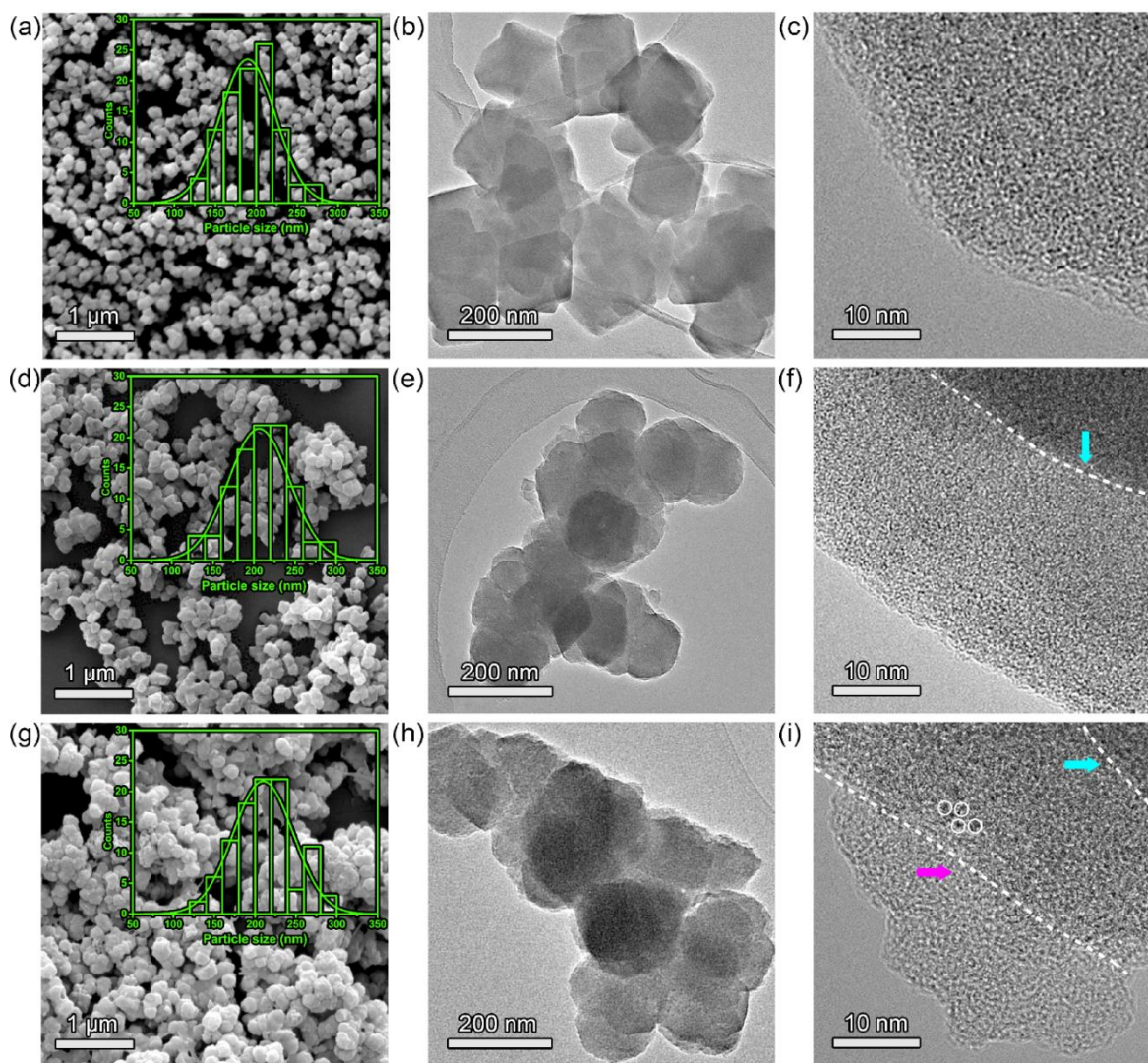
Figure 3-19 The SEM images (insert is particle size distribution), TEM and HRTEM of a-c) MOF-Uio-66-NH$_2$, d-f) MOF@COF-LZU1and g-i) aza-MOF@COF.

3.3.5 TGA and BET analysis of MOF-UIO-66-NH₂, MOF@COF-LZU1 and aza-MOF@COF

As shown in Figure 3-21, thermogravimetric analyses (TGA) reveal the aza-MOF@COF has a higher decomposition onset temperature compared to MOF-UIO-66-NH$_2$ and MOF@COF-LZU1, indicating higher thermal stability of aza-MOF@COF.
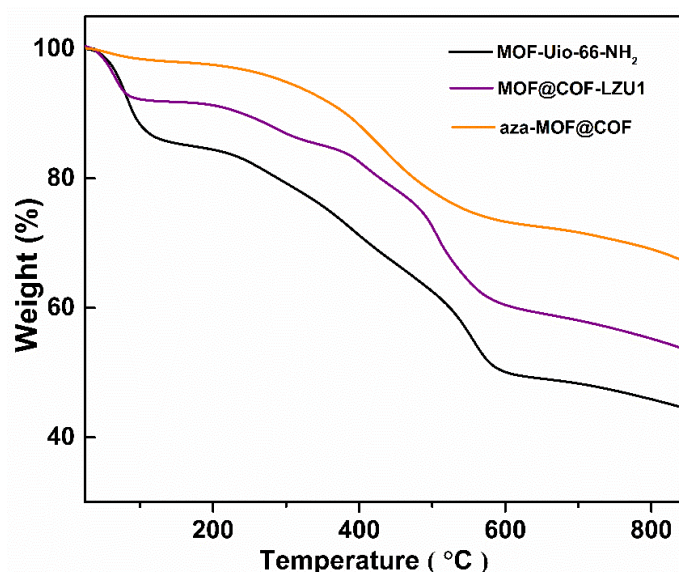

Figure 3-20 The TGA curves of MOF-UIO-66-NH$_2$, MOF@COF-LZU1 and aza-MOF@COF.

As shown in Figure 3-21 and 3-22, the N$_2$ adsorption and desorption isotherms of Brunauer-Emmett-Teller (BET) revealed the surface areas of 585, 428 and 365 m^2 g^{-1} for MOF-UIO-66-NH$_2$, MOF@COF-LZU1 and aza-MOF@COF, respectively. Pore size distribution analysis showed an increase of pore sizes from 0.6 nm to 1.1 nm upon growing COF layer on MOF-UIO-

109

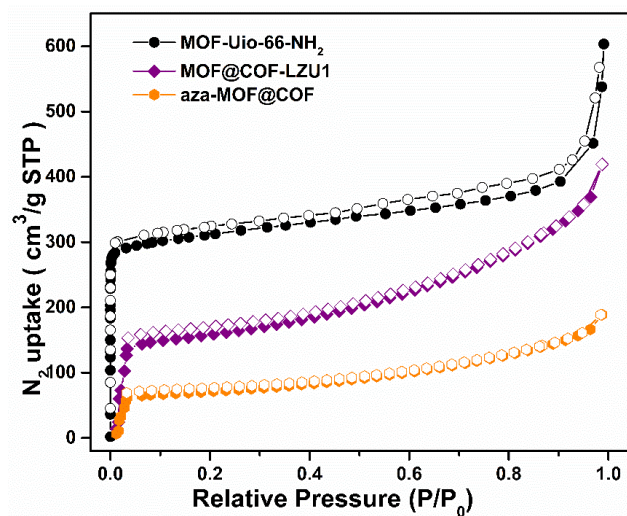66-NH$_2$ and a slight reduction to ca. 0.7 nm after PSM and aza-MOF@COF

formation.

Figure 3-21 The N$_2$ adsorption and desorption isotherms curves of MOF-UIO-66-NH$_2$, MOF@COF-LZU1 and aza-MOF@COF.
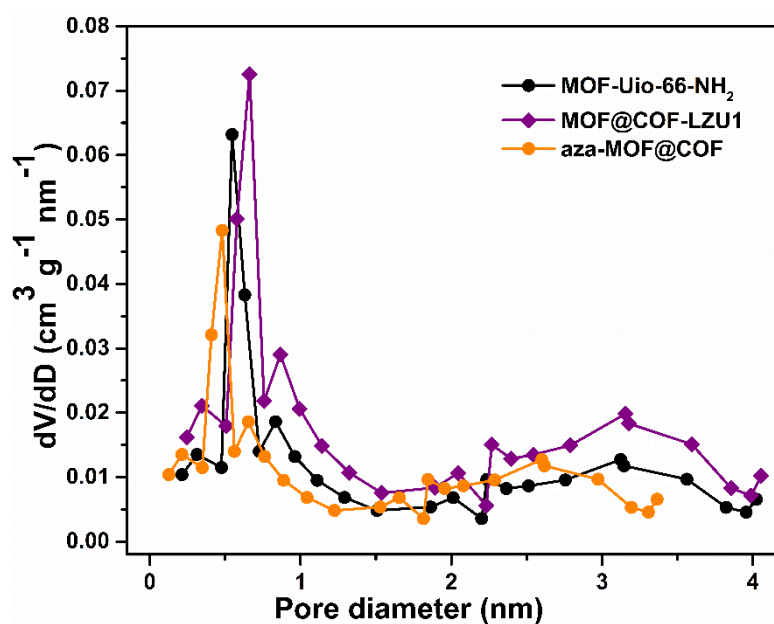

Figure 3-22 The Pore size distribution of MOF-UIO-66-NH$_2$, MOF@COF-LZU1 and aza-MOF@COF.

110

3.4 Conclusions

In summary, we have synthesized a new functional porous material aza-MOF@COF by introducing quinoline moieties *via* post-synthetic modification employing aza-Diels-Alder cycloaddition into imine-linked MOF@COF hybrid porous materials. The obtained aza-MOF@COF hybrid not only retains a highly crystalline nature and porosity but also displays superior capacitor performance in the energy storage system. As a *proof-of-concept* application in supercapacitor devices, the aza-MOF@COF device exhibits a high specific capacitance of 20.35 $\mu F\ cm^{-2}$ and an exceptional stack capacitance of 1.16 $F\ cm^{-3}$, which exceeds most of the previously reported state-of-the-art MOFs@COFs hybrid materials. Our approach of PSM of MOFs@COFs hybrids implement rational design for the synthesis of functional porous materials and expands the plethora of promising application of MOFs@COFs hybrid porous materials in energy storage applications.

3.5 References

1.   Zhang, L. L.; Zhao, X. S., Carbon-based materials as supercapacitor electrodes. *Chemical Society reviews* **2009,** *38* (9), 2520-2531.

2.   Salunkhe, R. R.; Kaneti, Y. V.; Yamauchi, Y., Metal-Organic Framework-Derived Nanoporous Metal Oxides toward Supercapacitor Applications: Progress and Prospects. *ACS Nano* **2017,** *11* (6), 5293-5308.

3.   Gogotsi, Y.; Simon, P., True Performance Metrics in Electrochemical Energy Storage. *Science* **2011,** *334* (6058), 917.

4.   Raymundo-Piñero, E.; Cadek, M.; Béguin, F., Tuning Carbon Materials for Supercapacitors by Direct Pyrolysis of Seaweeds. *Advanced Functional Materials* **2009,** *19* (7), 1032-1039.

5.   Feng, X.; Liang, Y.; Zhi, L.; Thomas, A.; Wu, D.; Lieberwirth, I.; Kolb, U.; Müllen, K., Synthesis of Microporous Carbon Nanofibers and Nanotubes from Conjugated Polymer Network and Evaluation in Electrochemical Capacitor. *Advanced Functional Materials* **2009,** *19* (13), 2125-2129.

6.   Kou, Y.; Xu, Y.; Guo, Z.; Jiang, D., Supercapacitive energy storage and electric power supply using an aza-fused pi-conjugated microporous framework. *Angewandte Chemie* **2011,** *50* (37), 8753-7.

7.   Chmiola, J.; Yushin, G.; Gogotsi, Y.; Portet, C.; Simon, P.; Taberna, P. L., Anomalous Increase in Carbon Capacitance at Pore Sizes Less Than 1 Nanometer. *Science* **2006,** *313* (5794), 1760.

8.   Largeot, C.; Portet, C.; Chmiola, J.; Taberna, P.-L.; Gogotsi, Y.; Simon, P., Relation between the Ion Size and Pore Size for an Electric Double-Layer Capacitor. *Journal of the American Chemical Society* **2008,** *130* (9), 2730-2731.

9.   Segalini, J.; Iwama, E.; Taberna, P.-L.; Gogotsi, Y.; Simon, P., Steric effects in adsorption of ions from mixed electrolytes into microporous carbon. *Electrochemistry Communications* **2012,** *15* (1), 63-65.

10. Zhang, F.-M.; Sheng, J.-L.; Yang, Z.-D.; Sun, X.-J.; Tang, H.-L.; Lu, M.; Dong, H.; Shen, F.-C.; Liu, J.; Lan, Y.-Q., Rational Design of MOF/COF Hybrid Materials for Photocatalytic H2 Evolution in the Presence of Sacrificial Electron Donors. *Angewandte Chemie International Edition* **2018,** *57* (37), 12106-12110.

11. Shindoh, N.; Tokuyama, H.; Takemoto, Y.; Takasu, K., Auto-Tandem Catalysis in the Synthesis of Substituted Quinolines from Aldimines and Electron-Rich Olefins: Cascade Povarov-Hydrogen-Transfer Reaction. *The Journal of Organic Chemistry* **2008,** *73* (19), 7451-7456.

12. Dibble, D. J.; Umerani, M. J.; Mazaheripour, A.; Park, Y. S.; Ziller, J. W.; Gorodetsky, A. A., An Aza-Diels-Alder Route to Polyquinolines. *Macromolecules* **2015,** *48* (3), 557-561.

13. Jia, X.; Liu, C.; Neale, Z. G.; Yang, J.; Cao, G., Active Materials for Aqueous Zinc Ion Batteries: Synthesis, Crystal Structure, Morphology, and Electrochemistry. *Chemical Reviews* **2020,** *120* (15), 7795-7866.

14. Meyet, C. E.; Larsen, C. H., One-Step Catalytic Synthesis of Alkyl-Substituted Quinolines. *The journal of Organic chemistry***2014,** *79*, 9835-9841.

15. Zhang, F.-M.; Sheng, J.-L.; Yang, Z.-D.; Sun, X.-J.; Tang, H.-L.; Lu, M.; Dong, H.; Shen, F.-C.; Liu, J.; Lan, Y.-Q., Rational Design of MOF/COF Hybrid Materials for Photocatalytic H2 Evolution in the Presence of Sacrificial Electron Donors. *Angewandte Chemie International Edition*   **2018,** *57*, 12106-12110.

16. Wu, X. L.; Zilm, K. W., Complete Spectral Editing in CPMAS NMR. *Journal of Magnetic resonance* **1993,** *102* (2), 205-213.

17. Le Brech, Y.; Delmotte, L.; Raya, J.; Brosse, N.; Gadiou, R.; Dufour, A., High Resolution Solid State 2D NMR Analysis of Biomass and Biochar. *Analytical Chemistry* **2015,** *87* (2), 843-847.

18. Ortiz, G.; Chaplais, G.; Paillaud, J.-L.; Nouali, H.; Patarin, J.; Raya, J.; Marichal, C., New Insights into the Hydrogen Bond Network in Al-MIL-53 and Ga-MIL-53. *Journal of Physical Chemistry C* **2014,** *118* (38), 22021-22029.

19. Rossum, B.-J. v.; Förster, H.; Groot, H. J. M. D., High-Field and High-Speed CP-MAS 13C NMR Heteronuclear Dipolar-Correlation Spectroscopy of Solids with Frequency Switched Lee-Goldburg Homonuclear Decoupling. *Journal of Magnetic Resonance***1996,** *124*, 516-519.

20. Vacchi, I. A.; Spinato, C.; Raya, J.; Bianco, A.; Menard-Moyon, C., Chemical reactivity of graphene oxide towards amines elucidated by solid-state NMR. *Nanoscale* **2016,** *8* (28), 13714-13721.

21. Xue, X. Y.; Kanzaki, M., Proton Distribution and Hydrogen Bonding in Crystalline and Glassy Hydrous Silicates and Related Inorganic Materials : Insights from High-Resolution Solid-State Nuclear Magnetic Resonance Spectroscopy. *Journal of the American Ceramic Society***2009,** *92* (12), 2803-2830.

22. Xu, J.; He, S.; Zhang, H.; Huang, J.; Lin, H.; Wang, X.; Long, J., Layered metal-organic framework/graphene nanoarchitectures for organic photosynthesis under visible light. *Journal of Materials Chemistry A* **2015,** *3* (48), 24261-24271.

23. Sun, D.; Jang, S.; Yim, S.-J.; Ye, L.; Kim, D.-P., Metal Doped Core-Shell Metal-Organic Frameworks@Covalent Organic Frameworks (MOFs@COFs) Hybrids as a Novel Photocatalytic Platform. *Advanced Functional Materials* **2018,** *28* (13), 1707110.

24. Gammon, W. J.; Kraft, O.; Reilly, A. C.; Holloway, B. C., Experimental comparison of N(1s) X-ray photoelectron spectroscopy binding energies of hard and elastic amorphous carbon nitride films with reference organic compounds. *Carbon* **2003,** *41* (10), 1917-1923.

25. Gardella, J. A.; Ferguson, S. A.; Chin, R. L., π *- π Shakeup Satellites for the Analysis of Structure and Bonding in Aromatic Polymers by X-Ray Photoelectron Spectroscopy. *Applied Spectroscopy* **1986,** *40* (2), 224-232.

Chapter 4 Quantum Capacitance through Molecular Infiltration of 7,7,8,8-Tetracyanoquinodimethane in Metal-Organic Framework/Covalent Organic Framework Hybrids

Inspired by the post-synthetic modification of MOF@COF hybrids and their application in supercapacitors (Chapter 3), in this Chapter, we design and synthesize a MOF@COF-TCNQ hybrid, with TCNQ active moieties incorporated in the pores of MOF@COF. As a proof-of-concept, MOF@COF-TCNQ has been employed as active material in supercapacitors. Electrochemical energy storage analysis revealed outstanding supercapacitor performance with a specific areal capacitance of 78.36 mF cm^{-2} and a high stack volumetric energy density of 4.46 F cm^{-3}. DFT calculations result strongly indicate that the high capacitance of MOF@COF-TCNQ has a quantum capacitance origin. Our approach to post-synthetic modification of MOF@COF hybrids by using liquid-phase infiltration with redox-active molecules offers new insights into the rational design of functional porous materials and opens new perspectives for increasing the electronic density of states and capacitance of MOF@COF hybrids. The DFT simulations has been done in the collaboration with Senhe Huang and Dr. Diana Tranca under the

supervision of Prof. Xiaodong Zhuang from Shanghai Jiao Tong University, Shanghai, China.

4.1 Introduction

To unravel the potential of MOFs@COFs in energy storage applications, an alternative approach is to use the MOF or COF pores as platforms for modulating the electrical transport properties. Since Talin *et al*. report the first approach to tuning electrical conductivity in MOFs by incorporating the redox-active 7,7,8,8-tetracyanoquinodimethane (TCNQ) in the pores of Cu_3BTC_2 (also known as HKUST-1; BTC= 1,3,5-benzenetricarboxylate).[1] A series of structural and computational studies were undertaken to investigate the role played by the electron-acceptor guest TCNQ in the electron-donor host MOFs or COFs.[2-6] Noteworthy, Feng *et al*. have demonstrated the electronic doping of MOF with TCNQ by employing $TCNQ@Cu_3(BTC)_2$ as an active material micro-supercapacitors.[7] The infiltration of TCNQ into MOFs@COFs and their application in energy storage is still unexplored, thus far, we envisioned that infiltrating TCNQ into the MOFs@COFs hybrid pores would harness their performance as a supercapacitor electrode.

In this Chapter, we synthesized a novel MOF@COF-TCNQ hybrid through a liquid-phase infiltration of TCNQ into the MOF@COF pore

channels. The obtained MOF@COF-TCNQ hybrid exhibits a high specific areal capacitance of 78.36 mF cm^{-2} and an exceptional stack capacitance of 4.46 F cm^{-3}. Moreover, we introduce the concept of quantum capacitance to MOF@COF hybrids for the first time by combining the experimental results with DFT calculations.

4.2 Results and Discussion

In this Chapter, we have synthesized a novel MOF@COF-TCNQ hybrid through a liquid-phase infiltration of TCNQ into the MOF@COF pore channels. The synthesis of MOF@COF-TCNQ has been discussed in experimental Chapter 2. The multiscale characterization of MOF-UIO-66-NH$_2$, MOF@COF and MOF@COF-TCNQ structures has been carried out using different experimental techniques (detailed information has been discussed in Experimental Chapter 2). The obtained MOF-UIO-66-NH$_2$, MOF@COF and MOF@COF-TCNQ porous materials were used as electrodes in both two- and three-electrode symmetric solid-state supercapacitors. The MOF-UIO-66-NH$_2$, MOF@COF, and MOF@COF-TCNQ-based electrodes were first tested in a three-electrode system in a 1M solution of H$_2$SO$_4$, and cyclic voltammetry (CV) was measured in a relatively wide scan range from 10 to 1000 mV s^{-1} with the potential values swept in a

range of the cut-off values (0≤E≤0.8), which is typically used to calculate the capacitance performance (including the role played by a pair of active materials and substrate, and separator).[8]
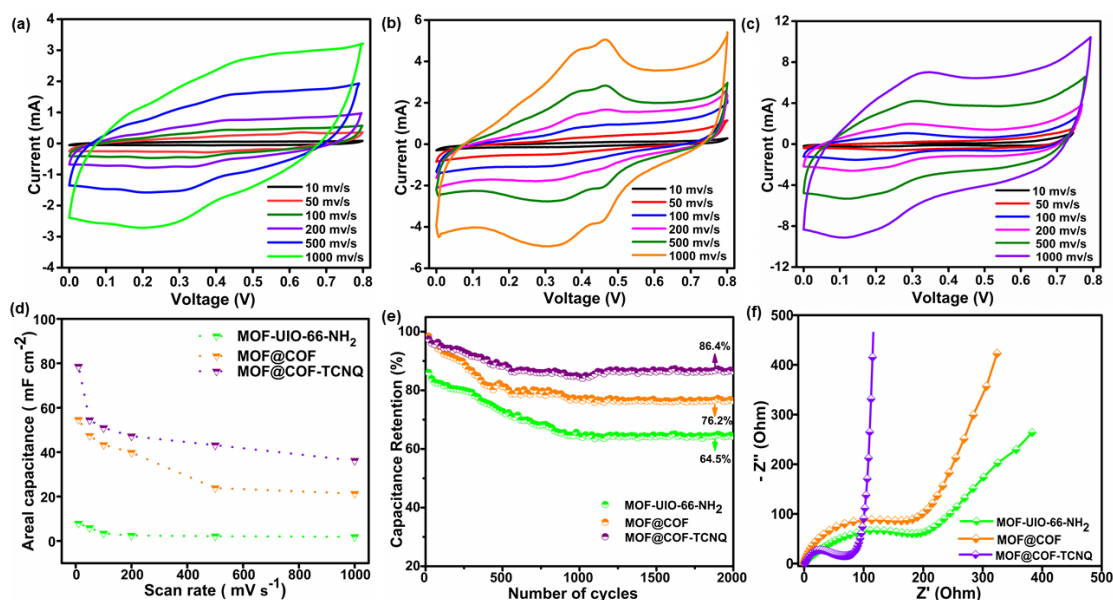

Figure 4-1 CV curves of a) MOF-UIO-66-NH₂, b) MOF@COF, c) MOF@COF-TCNQ, d) areal capacitance, e) capacitance retention, and f) Nyquist electrochemical impedance spectra.

As shown in Figure 4-1 a-c, the CV curves of the MOF@COF-based electrode display an evident pair of redox peaks compared with MOF-UIO-66-NH₂, indicating that there is a redox reaction in MOF@COF, and the obtained capacitance consisted of both pseudo-capacitance and electric double-layer capacitance. The position of the redox peak didn't shift when the scanning rate was increased, it indicates that electron transfer between electrolyte and the MOF@COF electrode is rapid and reversible.[9]

MOF@COF-TCNQ based electrode showed a more rectangular shape and higher current values compared with MOF@COF, confirming the improved electrochemical stability and capacitance.[10, 11] The specific capacitance calculated from the CV curves at different scan rates and charge/discharge profiles as exhibited in Figure 4-2, Figure 4-3 and Figure 4-4, which was used to evaluate the charge storage capacitance at different current densities of the supercapacitors.
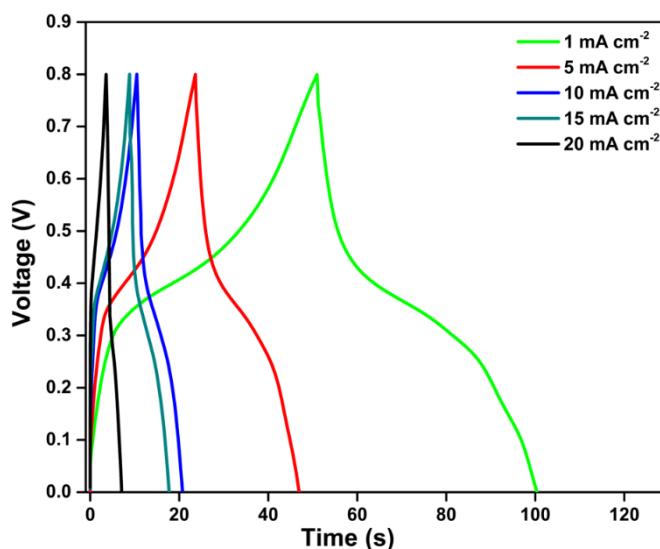

Figure 4-2 Charge/discharge profile of MOF-UIO-66-NH$_2$ at different current densities from 1 mA cm^{-2} to 20 mA cm^{-2}.
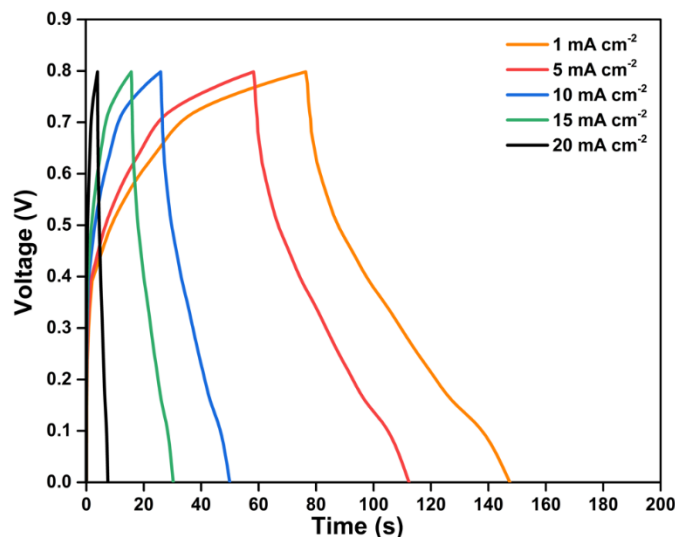
Figure 4-3 Charge/discharge profile of MOF@COF at different current densities from 1 mA cm^{-2} to 20 mA cm^{-2}.
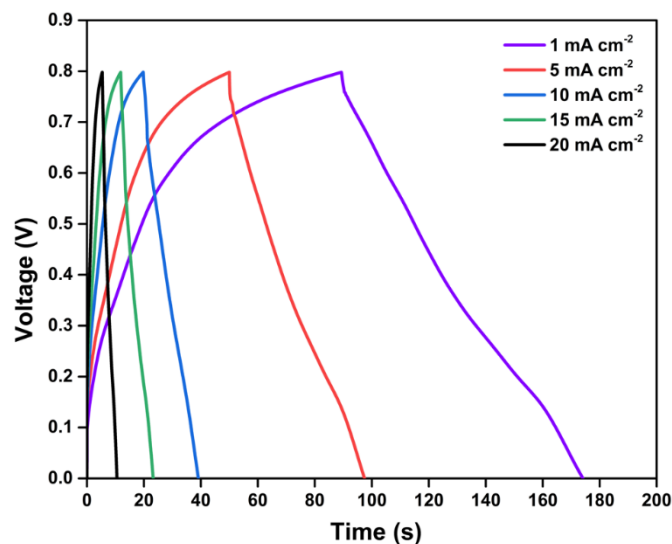

Figure 4-4 Charge/discharge profile of MOF@COF-TCNQ at different current densities from 1 mA cm^{-2} to 20 mA cm^{-2}.

The areal capacitance of MOF-UIO-66-NH$_2$, MOF@COF and MOF@COF-TCNQ were estimated as 8.21, 54.02 and 78.36 mF cm^{-2}, respectively (Figure 4-1d). The corresponding stack capacitance was calculated as 0.46, 3.12 and 4.46 F cm^{-3}, respectively. The measured

capacitance of MOF@COF-TCNQ is twice as high as that of pristine MOF-UIO-66-NH$_2$ and MOF@COF. Noteworthy, such capacitance is also higher than those of activated carbon, and graphene and much higher than some previously reported systems as shown in Table 4-1.

Table 4-1 Performance comparison of this work and other MOFs and COFs based symmetric solid-state supercapacitors.

Type	Electrode materials	volumetric capacitance (F cm^{-3})	areal capacitance (mF cm^{-2})	Ref
MOF	MOF-5	0.043	0.341	ACS Nano 2014, 8, 7451.
	HKUST-1	0.296	2.334	
	ZIF-8	0.034	0.268	
	nMOF-867	0.64	5.09	
	Ni-MOF	4.18	23.12	J. Mater. Chem. A, 2016, 4, 19078-19085
	HAB-MOF		20	Nat.Energy 2018,3,30-36
	Co-MOF	1.7	4	Chem. Commun. 2018, 54, 10499--10502
	c-MOF Ni$_2$[CuPc(NH)$_8$]		18.9	Adv.Funct.Mater.2020,30,2002664
	3D bulk MOF	8.7	28.3	Chem. Eng. Sci. 2021,413,127520.
COF	CT-Dq1Da1Tp		8.5	ACS Appl. Mater. Interfaces 2018, 10, 28139
	CT-DqTp		12	
	g-C$_{34}$N$_6$-COF	7.3	15.2	Angewandte Chemie International Edition 2019, 58,12065 -12069
	e-JUC-510	1.02	4.17	Advance Materials2020, 32, 1907289
	e-JUC-511		5.46	
	e-JUC-512		5.85	
	COF-5		15.3	Carbon 2021, 184, 418-425
	COF-316-1		2.5	
	COF-316		18.9	Adv. Funct. Mater. 2021,31,2010306
MOF@COF	**MOF-UIO-66-NH$_2$**	**0.46**	**8.21**	**This work**
	MOF@COF	**3.12**	**54.02**	
	MOF@COF-TCNQ	**4.46**	**78.36**	

Furthermore, the MOF@COF-TCNQ cell exhibits good cycling stability with a capacitance retention of 86.4% compared with MOF-UIO-66-

NH_2(64.5%) and MOF@COF (76.2%) after 2000 cycles performed at a current density of 0.2 A cm^{-2} (Figure 4-1e). The excellent capacitance of MOF@COF-TCNQ can be attributed to the uniform pores that facilitate the diffusion of ions and the redox behavior of doped β-keto-enamine linked COF on MOF which can provide extra pseudocapacitance. On the other hand, the highly crystalline structure and well-defined pores provide channels, allowing fast transport of ions, and the redox-active TCNQ embedded in the framework of MOF@COF ensures the fast transfer of electrons during the charge-discharge process in the supercapacitor devices.

Electrochemical impedance spectroscopy (EIS) was carried out between 10^{-1} and 10^5 Hz to evaluate the internal resistance for the charge transfer process of the samples. As shown in Figure 4-1f, a relatively small semicircle in the high-frequency region represents the dominant resistive nature of the supercapacitor system consisting of an electrode/electrolyte/current collector. The beginning of the semicircle line represents the resistance (R_s) of the electrolyte in contact with the current collector and electrode materials, and the termination of the semicircle line represents the internal resistance (R_p) of the electrode materials. The diameter of the semicircle (R_p-R_s) is equal to the equivalent series resistance (ESR),[29] the simulation ESR results of MOF-UIO-66-NH_2, MOF@COF and MOF@COF-TCNQ are 212.6, 185.2 and 74.5 Ω cm^{-1} respectively. The ESR

results confirm that the infiltrating TCNQ into MOF@COF results in increased electrical conductivity in MOF@COF hybrid porous materials. To further test the effect of TCNQ doping, a two-electrode symmetrical supercapacitor cell was constructed using MOF-UIO-66-NH$_2$, MOF@COF, and MOF@COF-TCNQ as the electrodes and an aprotic electrolyte 1M tetraethylammonium tetrafluoroborate (TEABF$_4$) in acetonitrile (AN) as electrolyte. The two-electrode cell yielded similar capacitance enhancements for TCNQ-doped MOF@COF-TCNQ electrodes when tested in aprotic electrolytes (Figure 4-5). These results prompted us to try to understand the mechanism(s) for the increase in capacitance by TCNQ doping of MOF@COF.
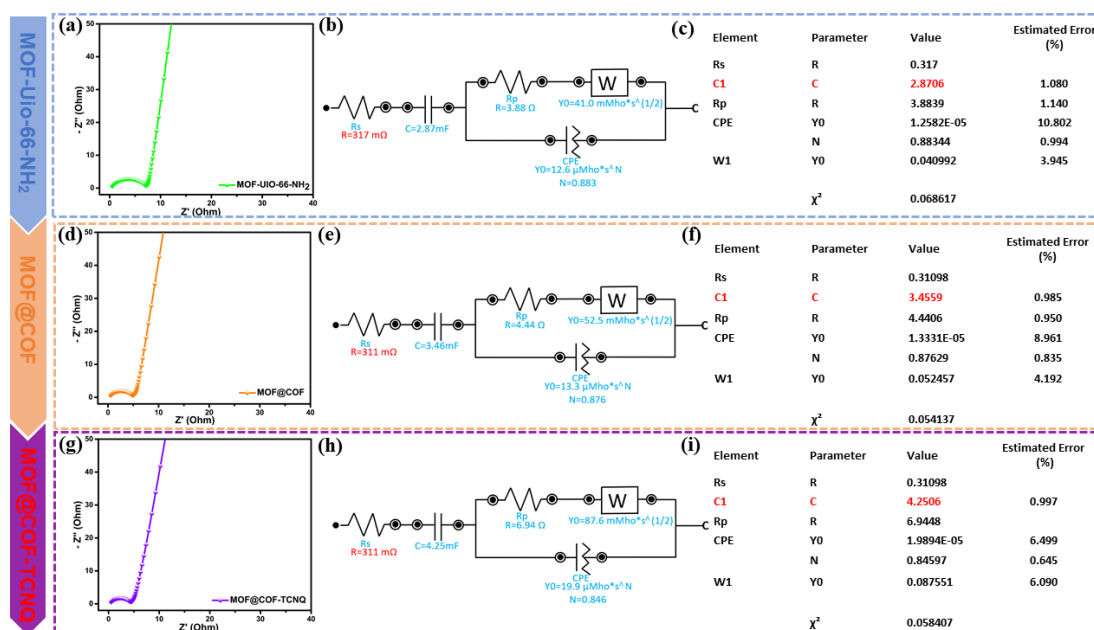

Figure 4-5 Nyquist electrochemical impedance spectra of (a) MOF-UIO-66-NH$_2$, (d) MOF@COF, (g) MOF@COF-TCNQ; Equivalent circuits for the EIS measurement of (b) MOF-UIO-66-NH$_2$, (e) MOF@COF (h) MOF@COF-TCNQ; Circuit parameters for the EIS measurement of (c) MOF-UIO-66-NH$_2$, (f) MOF@COF, (i) MOF@COF-TCNQ.

Noteworthy, to explore the content of TCNQ for the contribution to supercapacitors performance, we mixed the TCNQ with MOF@COF to construct supercapacitor devices, and the devices were short-circuited because the mixed TCNQ moieties can cross over the separator into the electrolyte.

4.3 Characterization

4.3.1 PXRD spectra of MOF-UIO-66-NH₂, MOF@COF and MOF@COF-TCNQ

The structure of the MOF-UIO-66-NH$_2$ has been discussed in Chapter 3, and MOF@COF and MOF@COF-TCNQ were investigated by powder X-ray diffraction (PXRD) analysis and Fourier transform infrared (FTIR) spectroscopy. The patterns of as-synthesized MOF-UIO-66-NH$_2$ are in good accordance with the previously reported results[13] and the successful growth of COF-TpPa onto MOF-UIO-66-NH$_2$ and corresponding conversion onto MOF@COF-TCNQ upon liquid-phase infiltration of TCNQ into MOF@COF hybrid materials were characterized by several analytical methods. The presence of a new characteristic diffraction peak at 4.7°, originating from the (100) plane of COF-TpPa (Figure 4-8), confirmed the formation of COF-TpPa on the MOF@COF.[14] Note that the PXRD patterns of the as-synthesized MOF@COF after infiltrated with TCNQ remained unchanged, which proves

that the MOF@COF crystalline structure was unaffected by the infiltration process.
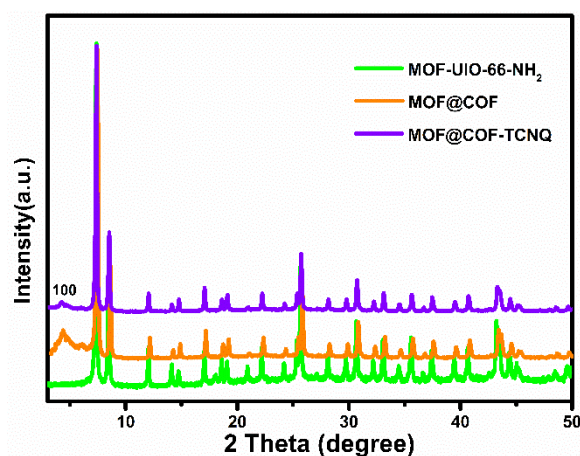

Figure 4-6 XRD patterns of MOF-UIO-66-NH$_2$, MOF@COF, and MOF@COF-TCNQ.

On the other hand, major differences in PXRD patterns of MOF-UIO-66-NH$_2$ were observed after integration of TCNQ as shown in Figure 4-7a, and were accompanied by a drastic color change from pale yellow to dark green (Figure 4-7b). Such observations confirmed the superior stability of MOF@COF structure over MOF-UIO-66-NH$_2$ during the infiltration process.
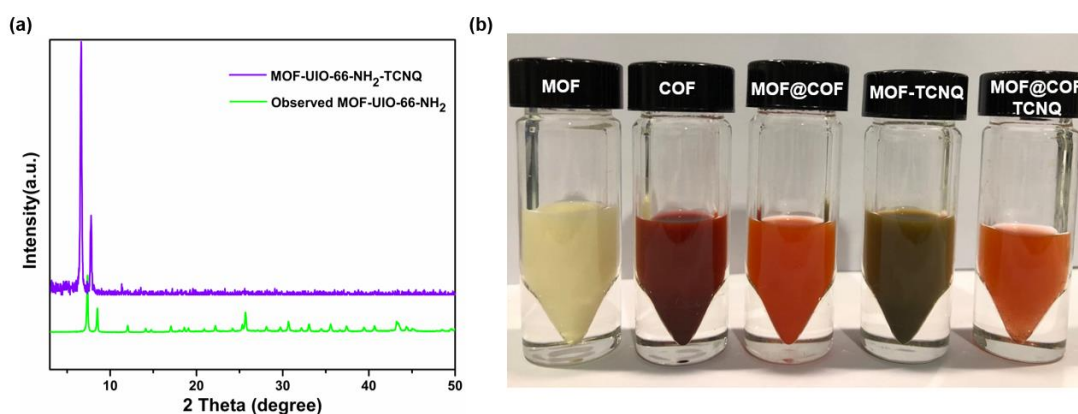

Figure 4-7 (a) The PXRD patterns of MOF-UIO-66-NH$_2$ after infiltration of TCNQ. (b) Optical image of all the synthesized materials.

4.3.2 FT-IR and UV-vis absorption spectra of MOF-UIO-66-NH2, MOF@COF and MOF@COF-TCNQ

The comparison of FTIR spectra of MOF@COF-TCNQ with MOF-UIO-66-NH$_2$ and MOF@COF revealed a presence of a new band at about 2212 cm^{-1}, which is attributed to the nitrile stretch (C≡N) vibration of TCNQ (Figure 4-8a).[15] The UV-vis absorption spectroscopy of MOF@COF-TCNQ compared with MOF-UIO-66-NH$_2$ and MOF@COF showed a broad red-shift, demonstrating that the infiltrated TCNQ is more effective in transmitting π conjugation over the MOF@COF skeleton than the pristine MOF-UIO-66-NH$_2$ (Figure 4-8b).[16]
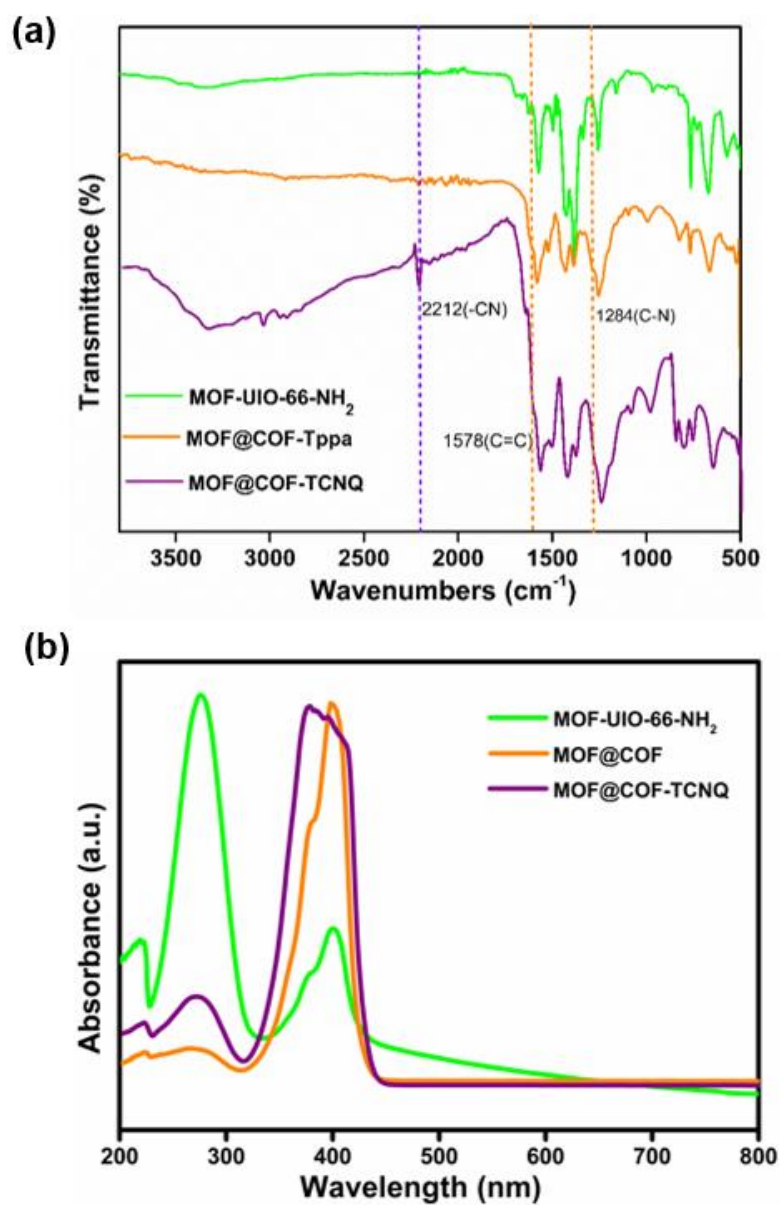
Figure 4-8 (a) The FT-IR spectra of MOF-UIO-66-NH$_2$ after infiltration of TCNQ. (b) UV-vis absorption spectra of MOF-UIO-66-NH$_2$, MOF@COF, and MOF@COF-TCNQ.

4.3.3 XPS spectra of MOF-UIO-66-NH₂, MOF@COF and MOF@COF-TCNQ

The electronic state of the N element was studied by X-ray photoelectron spectroscopy (XPS) to gain more insights into the nature of nitrogen species in MOF@COF-TCNQ after infiltrating TCNQ. As shown in Figure 4-9, the analysis of N 1s spectra of MOF-UIO-66-NH₂ revealed the presence of a peak at 399.5 eV corresponding to the primary amine (-NH₂) species. As previously observed, a negligible peak at 401.6 eV can be assigned to -NH groups of the organic linkers in pure UIO-66-NH₂ nanocrystals.[17,18] When compared to pristine MOF-UIO-66-NH₂, MOF@COF shows two new peaks at binding energies of 400.08 eV and 403.34 eV, indicating the formation of enamine (C-NH-C) bond and π-π* satellite peak, being in line with previous reports.[19] Upon post-synthetic modification of infiltrating TCNQ, a fraction of N1s appeared at higher binding energies, *i.e.*, 400.4 eV (Figure 4-9c), corresponding to the nitrile (-C≡N) in TCNQ moieties.[20]
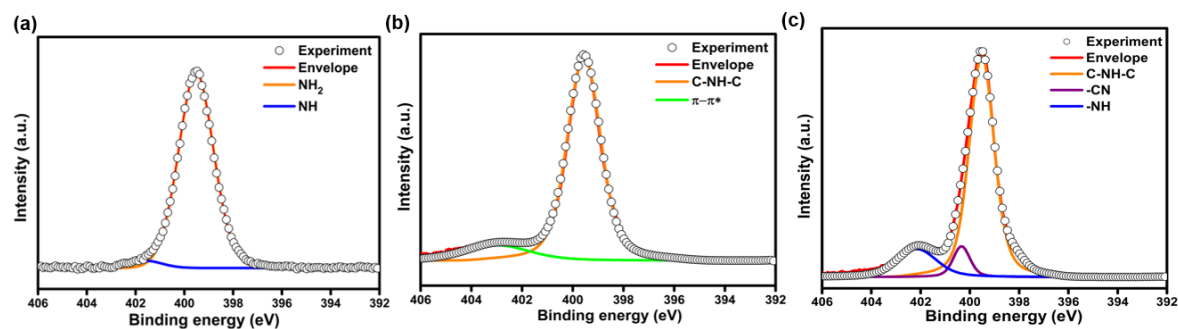

Figure 4-9 XPS spectra of (a) MOF-UIO-66-NH₂, (b) MOF@COF (c) MOF@COF-TCNQ.

What's more, the high-resolution C1s spectra depicted in Figure 4-10 also display a peak of -C≡N groups, which is following the previous literature report,[21] and serves as further evidence for the presence of TCNQ in the doped MOF@COF.
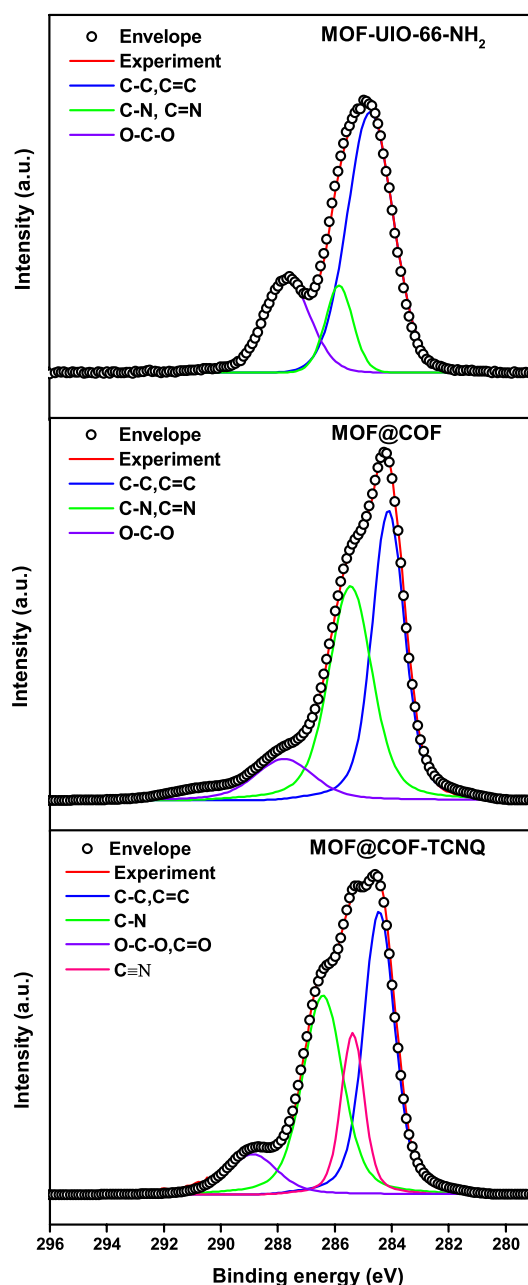

Figure 4-10 The XPS spectra of C1s for MOF-UIO-66-NH$_2$, MOF@COF and MOF@COF-TCNQ, respectively.

4.3.4 MALDI-TOF mass spectra of MOF-UIO-66-NH$_2$, MOF@COF and MOF@COF-TCNQ

The chemical composition of MOF@COF and the content of the infiltrated TCNQ were further investigated by matrix-assisted laser desorption/ionization-time-of-flight (MALDI-TOF) mass spectra as shown in Figure 4-11, the MALDI-TOF mass spectra did not show any chemical changes that could be expected from the infiltration of TCNQ into MOF@COF.
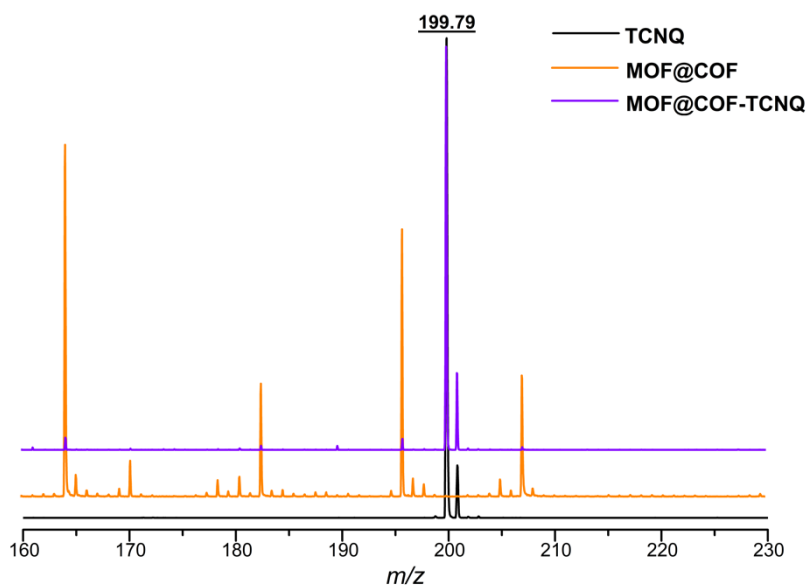

Figure 4-11 The matrix-assisted laser desorption/ionization-time-of-flight (MALDI-TOF) mass spectra of TCNQ, MOF@COF and MOF@COF-TCNQ.

4.3.5 TGA and BET analysis of MOF-UIO-66-NH$_2$, MOF@COF and MOF@COF-TCNQ

As shown in Figure 4-12, the thermogravimetric analysis (TGA) and differential scanning calorimetry (DSC) spectra revealed ca. 19% mass loss below 150 °C attributed to the removal of the solvent molecules adsorbed inside the pores of pristine MOF-UIO-66-NH$_2$. After coating of MOF-UIO-66-NH$_2$ with COF and subsequent infiltration with TCNQ, the amounts of solvent molecules were found to be much lower and amounted to ca.11% and ca. 8% for MOF@COF and MOF@COF-TCNQ, respectively. The main mass loss observed in the temperature range 150 and 700 °C corresponds to the degradation of the framework and thermal decomposition of TCNQ (280-500 °C),[22] which is determined to be ca. 42 %, 53 % and 59% for MOF-UIO-66-NH$_2$, MOF@COF and MOF@COF-TCNQ, respectively. Based on such observations, we could roughly estimate the content of TCNQ in MOF@COF-TCNQ, which amounts to 6%.
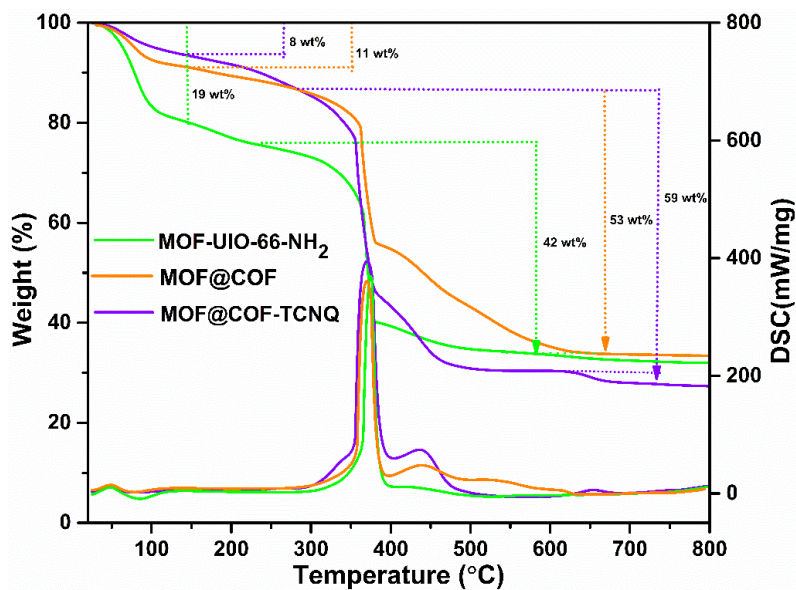
Figure 4-12 The TGA and DSC curve of MOF-UIO-66-NH$_2$, MOF@COF and MOF@COF-TCNQ.

To probe the porosity we performed N$_2$ adsorption and desorption isotherms experiments. As expected, a decrease in Brunauer-Emmett-Teller (BET) surface areas is observed, from 526 m^2 g^{-1} for MOF@COF to 265 m^2 g^{-1} for MOF@COF-TCNQ, compared with pristine MOF-UIO-66-NH$_2$ about 585 m^2 g^{-1} as exhibited in Figure 4-13.
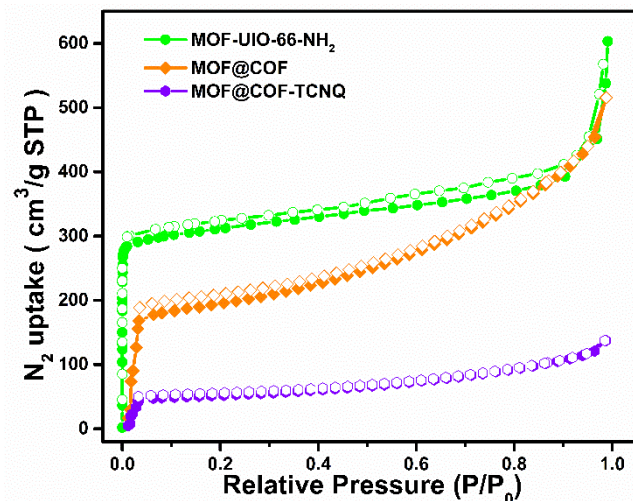
Figure 4-13 The BET surface area of MOF-UIO-66-NH$_2$, MOF@COF and MOF@COF-TCNQ.

Pore size distribution analysis revealed an increase of pore sizes from 0.6 nm to 1.6 nm upon growing COF layer on MOF-UIO-66-NH$_2$ and a slight reduction to ca. 0.9 nm after infiltrating of TCNQ (Figure 4-14), which provides additional evidence for the incorporation of the TCNQ molecules into the MOF@COF framework.
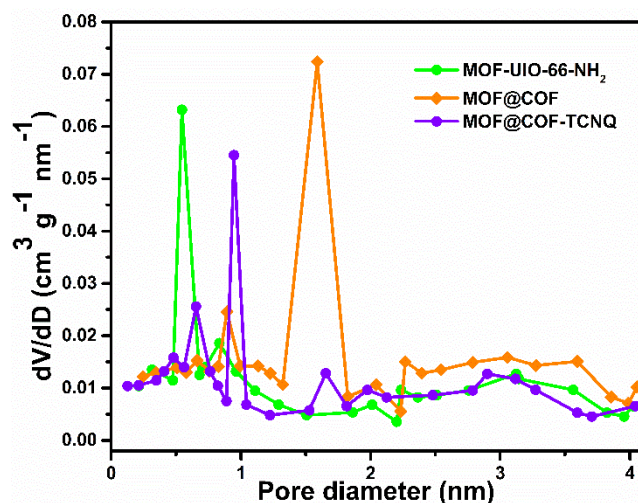

Figure 4-14 The pore size distribution of MOF-UIO-66-NH$_2$, MOF@COF and MOF@COF-TCNQ.

4.3.6 SEM and TEM images of MOF-UIO-66-NH2, MOF@COF and MOF@COF-TCNQ

The morphologies of the as-synthesized MOF-UIO-66-NH$_2$, MOF@COF and MOF@COF-TCNQ were characterized by field-emission scanning electron microscopy (FS-SEM) and high-resolution transmission electron microscope (HR-TEM). MOF-UIO-66-NH$_2$ particles shown in Figure 4-15 exhibit octahedral shapes with smooth surfaces and an average diameter of ~200 nm. After the surface modification with COF, the MOF@COF particles maintain the morphology with an increased averaged diameter of ~220 nm as shown in Figure 4-15d. Noteworthy, after infiltrating with the TCNQ, the surface of MOF@COF-TCNQ particles becomes rougher and a slight increase of the particles' diameter has been monitored (~230 nm, Figure 4-15g). The HR-TEM images of MOF@COF particles illustrated in Figure 4-15f reveal the presence of layer lattice for COF-TpPa at the edge of pristine MOF-UIO-66-NH$_2$, which was estimated at around 20 nm, being consistent with the increased nanoparticle average diameter. It is worth mentioning that after the infiltrating of TCNQ, the MOF@COF-TCNQ particles showed apparent drawbacks in the COF-TpPa lattice layer in Figure 4-15i, which can be ascribed to the induced TCNQ moieties.
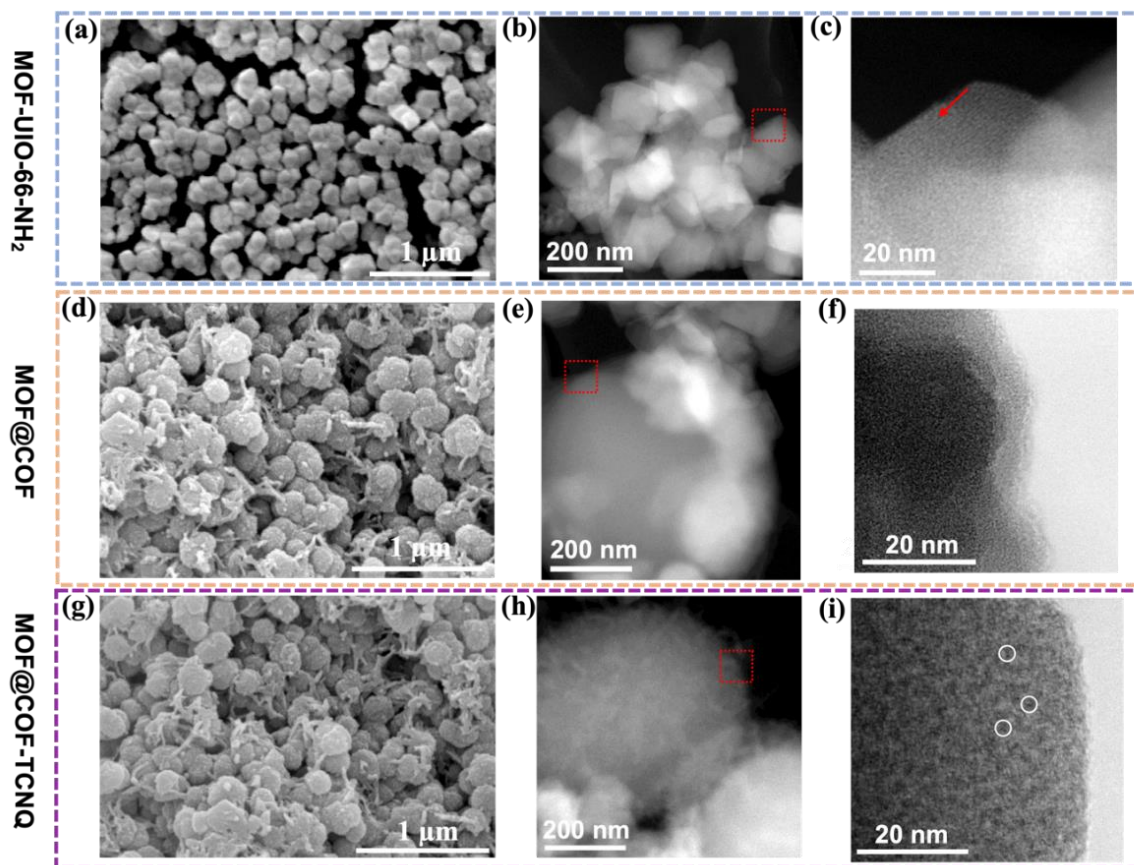
Figure 4-15 The SEM images, TEM, and HR-TEM of (a)-(c) of MOF-UIO-66-NH₂, (d)-(f) MOF@COF, and (g)-(i) MOF@COF-TCNQ.

4.3.7 Density Functional Theory (DFT) Calculations of MOF-UIO-66-NH₂, MOF@COF and MOF@COF-TCNQ

Density functional theory (DFT) calculations were performed by using the Vienna *ab* initio simulation package (VASP)[23] with the projector-augmented wave (PAW)[24] method. All calculations were based on the same generalized gradient approximation (GGA) method with Perdew-Burke-Ernzerhof (PBE)[25] functional for the exchange-correlation term. The plane

wave cutoff was set to 400 eV. The Brillouin zone integration was carried out with a 1×1×1 Monkhorst-Pack k-point grid in structure optimization and electronic properties simulations. The convergence of energy and forces were set to $5×10^{-5}$ eV and 0.01 eV $Å^{-1}$, respectively.

To gain more insight into the significant capacitance increase of MOF@COF after infiltration with TCNQ molecules, we performed DFT calculations and investigated the electronic properties and quantum capacitance, which are conducive to increasing the total electrochemical performances. As previously reported, the total capacity of the supercapacitors can be considered as a series combination of double-layer capacitance and quantum capacitance when there is no consideration of pseudocapacitance. The quantum capacitance was calculated based on the electronic structure of electrodes, specifically the electronic density of states (DOS) near the Fermi level.[26,27] Therefore, we first built and optimized the models of MOF-UIO-NH$_2$-66, MOF-UIO-NH$_2$-66-NH$_2$ and COF-TpPa, then calculated their partial densities of states (PDOS) and local densities of states (LDOS), respectively (Figure 4-16 and Figure 4-17).
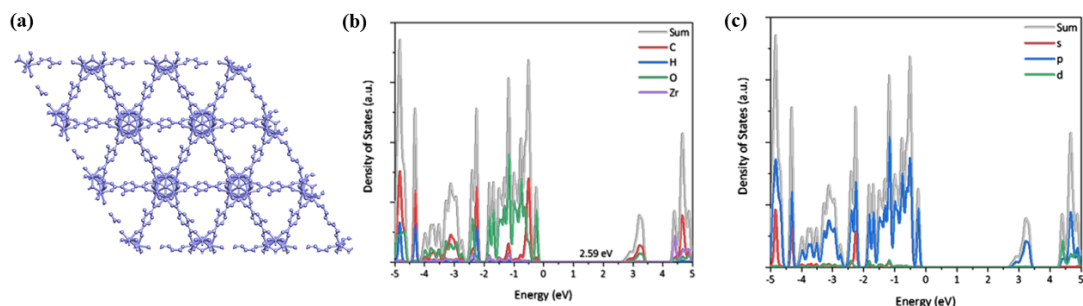
Figure 4-16 (a) Simulated model structure of 3D-MOF-UIO-66-NH$_2$. Color code: Zr, purple; C, gray; N, blue; O, red; H, white. Partial H atoms are omitted for clarity. (b) Simulated LDOS of C, H, N, O and Zr in 3D-MOF-UIO-66-NH$_2$; (c) Simulated PDOS of s, p and d orbitals in 3D-MOF-UIO-66-NH$_2$.
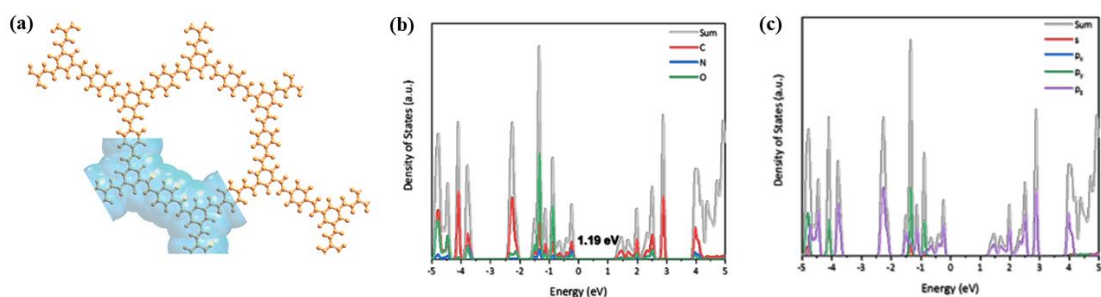

Figure 4-17 (a) Top view and side view of simulated 2D-COF-Tppa structure. Color code: C, gray; O, red; N, blue. H atoms are omitted for clarity; (b) Top view and side view of surface area (blue ground) in 2D-COF-Tppa unit cell. (c) Simulated LDOS of C, N and O in 2D-COF-Tppa. (d) Simulated PDOS of s, p$_x$, p$_y$ and p$_z$ orbitals in 2D-COF-Tppa.

Based on PDOS and LDOS analyses of the MOF-UIO-NH$_2$-66, MOF-UIO-NH$_2$-66-NH$_2$ and COF-TpPa, we calculated the theoretical surface areas of MOF-UIO-66-NH$_2$ monolayer (Figure 4-18a). The heterostructure of MOF@COF was also built based on the MOF-UIO-66-NH$_2$ monolayer and COF-TpPa structure (Figure 4-18c and 4-18d). Further, we simulated the

138

MOF@COF-TCNQ structure by adding the TCNQ molecules in the pores of COF-TpPa to simulate the TCNQ incorporated MOF@COF-TCNQ hybrid materials.
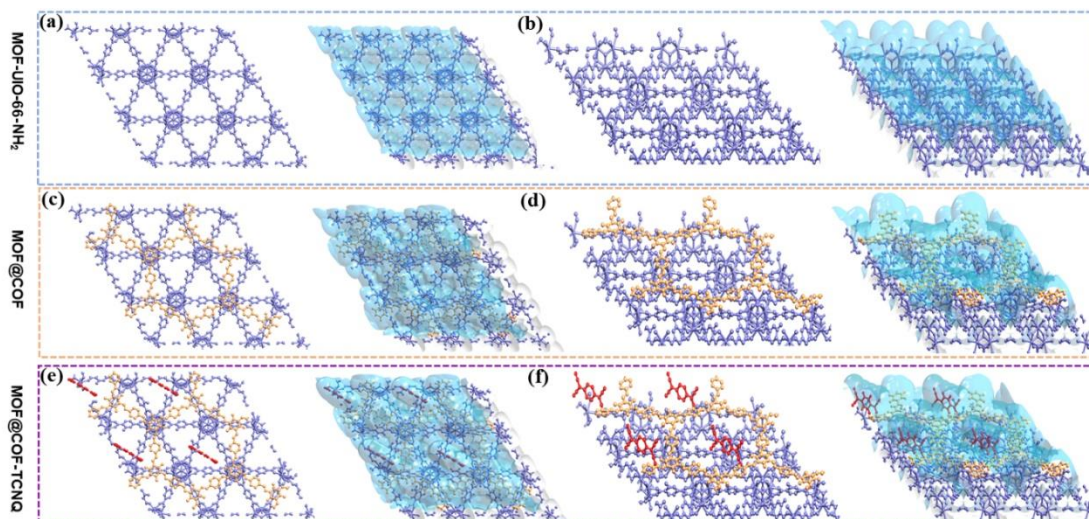

Figure 4-18 Top view and side view of model structures and iso-surfaces of (a-b) MOF-UIO-66-NH$_2$-monolayer structure; (c-d) MOF@COF structure; (e-f) MOF@COF-TCNQ structure. H atoms are omitted for clarity.

The DOS of MOF-UIO-66-NH$_2$-monolayer, MOF@COF heterostructure and MOF@COF-TCNQ were investigated to calculate their quantum capacitance (Figure 4-18a). The quantum capacitance (C$_Q$) can be obtained from the density of states from the equation[42]:

$$C_Q = \frac{e^2}{S/2} \int_{-\infty}^{+\infty} D(E) F_T (E - \mu) dE$$

where μ represents the electrochemical potential, $D(E)$ is the electron density of states, and $F_T(E)$ is the thermal broadening function [$=(4kT)^{-1}\text{sech}^2(E/2kT)$], in our case, $T = 300K$, E is the relative energy for the Fermi level E_F, e is the

elementary charge,[29] and S is the calculated surface area (Table 4-2).

Table 4-2 The surface area of MOF-UIO-66-NH$_2$-monolayer, COF-Tppa, MOF@COF, MOF@COF-TCNQ~1%, MOF@COF-TCNQ~2%, MOF@COF-TCNQ~3%, MOF@COF-TCNQ~5%.

Structures	Surface area (Å^2)
MOF-UIO-66-NH$_2$	5468.30
COF-Tppa	811.28
MOF@COF	5622.88
MOF@COF-TCNQ~1%	5664.13
MOF@COF-TCNQ~2%	5739.49
MOF@COF-TCNQ~3%	5805.94

The calculated quantum capacitance results demonstrate that MOF-UIO-66-NH$_2$-monolayer exhibits a maximum value of 86 µF cm^{-2} compared with COF-TpPa of 67 µF cm^{-2}. The quantum capacitance of the MOF@COF heterostructure was found to be 26 µF cm^{-2} lower than MOF-UIO-66-NH$_2$-monolayer. However, after doping with TCNQ (~5 wt%, to be consistent with the experiment results) molecules into MOF@COF, The MOF@COF-TCNQ deliver obvious increased C$_Q$ with a maximum value of 218 µF cm^{-2} (Figure 4-21b).
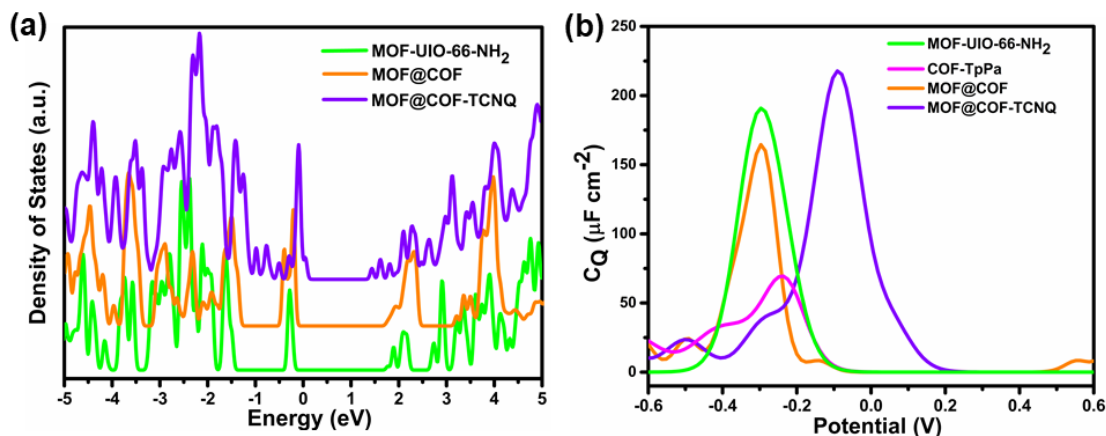
Figure 4-19 (a) The calculated density of states (DOS) of MOF-UIO-66-NH$_2$, MOF@COF, MOF@COF-TCNQ~5%. (b) Calculated potential-dependent quantum capacitances.

To further probe the effect of TCNQ content with C$_Q$ on MOF@COF hybrid materials. We also considered different contents of TCNQ into MOF@COF heterostructure, and then calculated the DOS and C$_Q$ for MOF@COF-TCNQ~1% (Figure 4-20), MOF@COF-TCNQ~2% (Figure 4-21) and MOF@COF-TCNQ~3% (Figure 4-22). It was further found that the calculated C$_Q$ results are closely related to the TCNQ concentration.

Figure 4-20 (a) Top view and side view of simulated MOF@COF-TCNQ~1% structure. H atoms are omitted for clarity; (b) Top view and side view of surface area in MOF@COF-TCNQ~1%. (c) Simulated DOS of MOF@COF-TCNQ~1%. (d) The simulated quantum capacitance of MOF@COF-TCNQ~1%.

Figure 4-21 (a) Top view and side view of simulated MOF@COF-TCNQ~2% structure. H atoms are omitted for clarity; (b) Top view and side view of surface area in MOF@COF-TCNQ~2%. (c) Simulated DOS of MOF@COF-TCNQ~2%. (d) The simulated quantum capacitance of MOF@COF-TCNQ~2%.
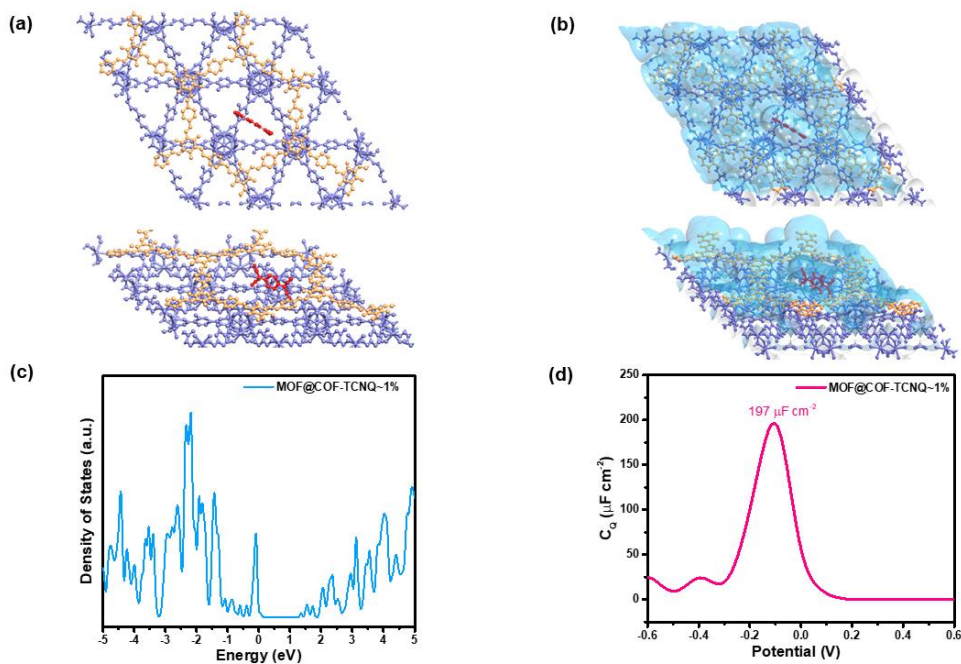
142
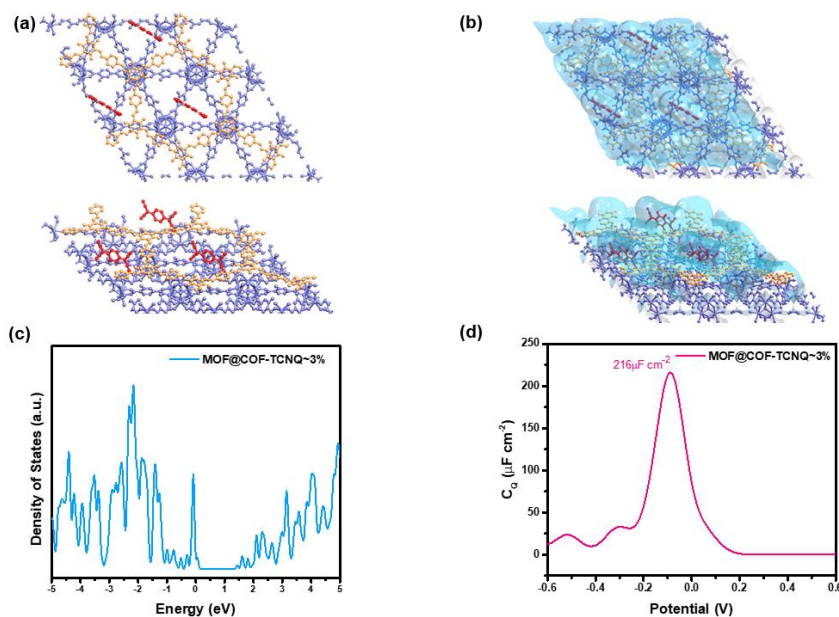
Figure 4-22 (a) Top view and side view of simulated MOF@COF-TCNQ~3% structure. H atoms are omitted for clarity; (b) Top view and side view of surface area in MOF@COF-TCNQ~3%. (c) Simulated DOS of MOF@COF-TCNQ~3%. (d) The simulated quantum capacitance of MOF@COF-TCNQ~3%.
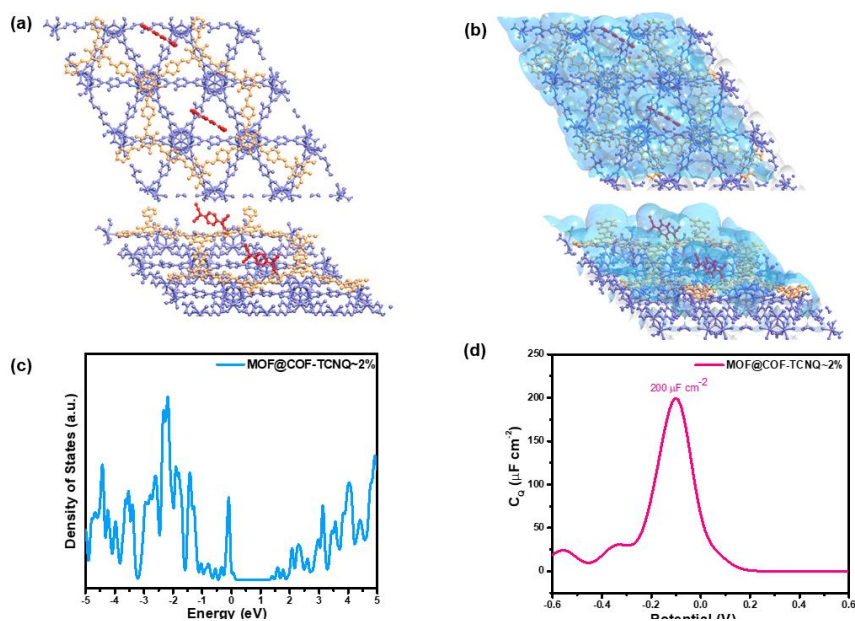
4.4 Conclusions

In this Chapter, we have synthesized a new hybrid material MOF@COF-TCNQ *via* liquid-phase infiltration of TCNQ molecules into MOF@COF hybrid porous material. The obtained MOF@COF-TCNQ hybrid exhibits a high specific areal capacitance of 78.36 mF cm^{-2}, and an exceptional stack capacitance of 4.46 F cm^{-3}, which exceeds most of the previously reported state-of-the-art MOFs@COFs hybrid materials. Combined with the experimental and theoretical DFT results, the superior performance of

143

MOF@COF-TCNQ can not only be credited with the favorable synergistic effects in what follows: (i) the uniform pores that facilitate the diffusion of ions and the redox behavior of doped β-keto-enamine linked COF on MOF which can provide extra pseudocapacitance; (ii) the highly crystalline structure and well-defined pores provide channels, allowing fast transport of ions; (iii) the redox-active TCNQ embedded in the framework of MOF@COF ensure the fast transfer of electrons during the charge-discharge process in the supercapacitor devices, but also for the improved quantum capacitance after the infiltration of TCNQ molecules into MOF@COF hybrid frameworks. Our approach to post-synthetic modification of MOFs@COFs hybrids implements rational design for the synthesis of high-performance supercapacitor materials and provides an effective way to increase the electrical DOS and C_Q of MOF@COF hybrid materials.

4.5 References

1.   Talin, A. A.; Centrone, A.; Ford, A. C.; Foster, M. E.; Stavila, V.; Haney, P.; Kinney, R. A.; Szalai, V.; El Gabaly, F.; Yoon, H. P.; Léonard, F.; Allendorf, M. D., Tunable Electrical Conductivity in Metal-Organic Framework Thin-Film Devices. *Science* **2014,** *343* (6166), 66.

2.   Schneider, C.; Ukaj, D.; Koerver, R.; Talin, A. A.; Kieslich, G.; Pujari, S. P.; Zuilhof, H.; Janek, J.; Allendorf, M. D.; Fischer, R. A., High electrical conductivity and high porosity in a Guest@MOF material: evidence of TCNQ ordering within Cu_3BTC_2 micropores. *Chemical Science* **2018,** *9* (37), 7405-7412.

3.   Usov, P. M.; Jiang, H.; Chevreau, H.; Peterson, V. K.; Leong, C. F.; D'Alessandro, D. M., Guest-Host Complexes of TCNQ and TCNE with $Cu_3(1,3,5$-benzenetricarboxylate$)_2$. *The Journal of Physical Chemistry C* **2017,** *121* (47), 26330-26339.

4.   Nie, X.; Kulkarni, A.; Sholl, D. S., Computational Prediction of Metal Organic Frameworks Suitable for Molecular Infiltration as a Route to Development of Conductive Materials. *The Journal of Physical Chemistry Letters* **2015,** *6* (9), 1586-1591.

5.   Bláha, M.; Valeš, V.; Bastl, Z.; Kalbáč, M.; Shiozawa, H., Host-Guest Interactions in Metal-Organic Frameworks Doped with Acceptor Molecules as Revealed by Resonance Raman Spectroscopy. *The Journal of Physical Chemistry C* **2020,** *124* (44), 24245-24250.

6.   Leith, G. A.; Rice, A. M.; Yarbrough, B. J.; Berseneva, A. A.; Ly, R. T.; Buck Iii, C. N.; Chusov, D.; Brandt, A. J.; Chen, D. A.; Lamm, B. W.; Stefik, M.; Stephenson, K. S.; Smith, M. D.; Vannucci, A. K.; Pellechia, P. J.; Garashchuk, S.; Shustova, N. B., A Dual Threat: Redox-Activity and Electronic Structures of Well-Defined Donor-Acceptor Fulleretic Covalent-Organic Materials. *Angewandte Chemie International Edition* **2020,** *59* (15), 6000-6006.

7.   He, Y.; Yang, S.; Fu, Y.; Wang, F.; Ma, J.; Wang, G.; Chen, G.; Wang, M.; Dong, R.; Zhang, P.; Feng, X., Electronic Doping of Metal-Organic Frameworks for High-Performance Flexible Micro-Supercapacitors. *Small Structures* **2020,** *n/a* (n/a), 2000095.

8.   Gogotsi, Y.; Simon, P., True Performance Metrics in Electrochemical Energy Storage. *Science* **2011,** *334* (6058), 917.

9.   Xu, F.; Xu, H.; Chen, X.; Wu, D.; Wu, Y.; Liu, H.; Gu, C.; Fu, R.; Jiang, D., Radical Covalent Organic Frameworks: A General Strategy to Immobilize Open-Accessible Polyradicals for High-Performance Capacitive Energy Storage. *Angewandte Chemie International Edition* **2015,** *54* (23), 6814-6818.

10. Raymundo-Piñero, E.; Cadek, M.; Béguin, F., Tuning Carbon Materials for Supercapacitors by Direct Pyrolysis of Seaweeds. *Advanced Functional Materials* **2009,** *19* (7), 1032-1039.

11. Kou, Y.; Xu, Y.; Guo, Z.; Jiang, D., Supercapacitive Energy Storage and Electric Power Supply Using an Aza-Fused π-Conjugated Microporous Framework. *Angewandte Chemie International Edition* **2011,** *50* (37), 8753-8757.

12. Zhang, S.; Pan, N., Supercapacitors Performance Evaluation. *Advanced Energy Materials* **2015,** *5* (6), 1401401.

13. Zhang, F.-M.; Sheng, J.-L.; Yang, Z.-D.; Sun, X.-J.; Tang, H.-L.; Lu, M.; Dong, H.; Shen, F.-C.; Liu, J.; Lan, Y.-Q., Rational Design of MOF/COF Hybrid Materials for Photocatalytic H2 Evolution in the Presence of Sacrificial Electron Donors. *Angewandte Chemie International Edition* **2018,** *57* (37), 12106-12110.

14. Kandambeth, S.; Mallick, A.; Lukose, B.; Mane, M. V.; Heine, T.; Banerjee, R., Construction of Crystalline 2D Covalent Organic Frameworks with Remarkable Chemical (Acid/Base) Stability via a Combined Reversible and Irreversible Route. *Journal of the American Chemical Society* **2012,** *134* (48), 19524-19527.

15. Pal, S.; Maiti, S.; Maiti, U. N.; Chattopadhyay, K. K., Scalable approach for the realization of garland shaped 3D assembly of CuTCNQ nanorods: an efficient electron emitter. *Journal of Materials Chemistry C* **2014,** *2* (20), 4005-4011.

16. Jin, E.; Asada, M.; Xu, Q.; Dalapati, S.; Addicoat, M. A.; Brady, M. A.; Xu, H.; Nakamura, T.; Heine, T.; Chen, Q.; Jiang, D., Two-dimensional sp^2 carbon-conjugated covalent organic frameworks. *Science* **2017,** *357* (6352), 673.

17. Sun, D.; Jang, S.; Yim, S.-J.; Ye, L.; Kim, D.-P., Metal Doped Core-Shell Metal-Organic Frameworks@Covalent Organic Frameworks (MOFs@COFs) Hybrids as a Novel Photocatalytic Platform. *Advanced Functional Materials* **2018,** *28* (13), 1707110.

18. Xu, J.; He, S.; Zhang, H.; Huang, J.; Lin, H.; Wang, X.; Long, J., Layered metal-organic framework/graphene nanoarchitectures for organic photosynthesis under visible light. *Journal of Materials Chemistry A* **2015,** *3* (48), 24261-24271.

19. Yao, Y.-H.; Li, J.; Zhang, H.; Tang, H.-L.; Fang, L.; Niu, G.-D.; Sun, X.-J.; Zhang, F.-M., Facile synthesis of a covalently connected rGO-COF hybrid material by in situ reaction for enhanced visible-light induced photocatalytic H_2 evolution. *Journal of Materials Chemistry A* **2020,** *8* (18), 8949-8956.

20. Capitán, M. J.; Álvarez, J.; Navio, C., Study of the electronic structure of electron accepting cyano-films: TCNQ versus TCNE. *Physical Chemistry Chemical Physics* **2018,** *20* (15), 10450-10459.

21. Son, S.-B.; Gao, T.; Harvey, S. P.; Steirer, K. X.; Stokes, A.; Norman, A.; Wang, C.; Cresce, A.; Xu, K.; Ban, C., An artificial interphase enables reversible magnesium chemistry in carbonate electrolytes. *Nature Chemistry* **2018,** *10* (5), 532-539.

22. Bonnet, S.; Forano, C.; Besse, J.-P., Intercalation of Tetracyanoquinodimethane in [Zn-Al] Layered Double Hydroxide. *Materials Research Bulletin* **1998,** *33* (5), 783-788.

23. Kresse, G.; Furthmüller, J., Efficient iterative schemes for ab initio total-energy calculations using a plane-wave basis set. *Physical Review B* **1996,** *54* (16), 11169-11186.

24. Blöchl, P. E., Projector augmented-wave method. *Physical Review B* **1994,** *50* (24), 17953-17979.

25. Perdew, J. P.; Burke, K.; Ernzerhof, M., Generalized Gradient Approximation Made Simple. *Physical Review Letters* **1996,** *77* (18), 3865-3868.

26. Zhan, C.; Lian, C.; Zhang, Y.; Thompson, M. W.; Xie, Y.; Wu, J.; Kent, P. R. C.; Cummings, P. T.; Jiang, D.-e.; Wesolowski, D. J., Computational Insights into Materials and Interfaces for Capacitive Energy Storage. *Advanced Science* **2017,** *4* (7), 1700059.

27. Mousavi-Khoshdel, M.; Targholi, E.; Momeni, M. J., First-Principles Calculation of Quantum Capacitance of Codoped Graphenes as Supercapacitor Electrodes. *The Journal of Physical Chemistry C* **2015,** *119* (47), 26290-26295.

28. Paek, E.; Pak, A. J.; Hwang, G. S., A Computational Study of the Interfacial Structure and Capacitance of Graphene in [BMIM][PF$_6$] Ionic Liquid. *Journal of The Electrochemical Society* **2012,** *160* (1), A1-A10.

29. Paek, E.; Pak, A. J.; Kweon, K. E.; Hwang, G. S., On the Origin of the Enhanced Supercapacitor Performance of Nitrogen-Doped Graphene. *The Journal of Physical Chemistry C* **2013,** *117* (11), 5610-5616.

Chapter 5 Benzothiadiazole Functionalized Two-Dimensional Olefin-Linked Covalent Organic Framework as Novel Active Sites for Aqueous Zinc-ion Energy Storage Devices

In this Chapter, we design and synthesize a novel olefin-linked COF through the aldol condensation between 2,4,6-trimethyl-1,3,5-triazine (TMT) and 4,4′-(benzothiadiazole-4,7-diyl)dibenzaldehyde (BT), COF-TMT-BT, where benzothiadiazole units are explored as novel electrochemically-active groups. COF-TMT-BT exhibits an outstanding Zn^{2+} storage capability, delivering a capacity of 283.5 mAh g^{-1} at a current density of 0.1 A g^{-1}. The computational and experimental analysis provide further evidence that the benzothiadiazole units are the electrochemically-active sites for Zn^{2+} coordination not only in olefin (C=C) but also in imine (C=N) linked COF electrodes. This work paves the way towards the rational design of advanced benzothiadiazole-based COF materials for Zn^{2+} storage energy storage devices. The DFT simulations has been done in the collaboration with Senhe Huang, the Solid-state NMR analysis was made by Dr. Dawid Pakulski, the XPS spectra were recorded by Dr. Fanny Richard from the University of Strasbourg, France.

5.1 Introduction

In this Chapter, we report a novel benzothiadiazole-functionalized olefin-linked COF generated *via* the aldol condensation of 2,4,6-trimethyl-1,3,5-triazine (TMT) and 4,4-(benzothiadiazole-4,7-diyl)dibenzaldehyde (BT), (COF-TMT-BT). An aqueous ZIB was assembled, in which COF-TMT-BT and Zn foil were used as cathode and anode, respectively, while an aqueous solution containing zinc trifluoromethanesulfonate ($Zn(CF_3SO_3)_2$) served as electrolyte. Density functional theory (DFT) simulations together with experimental findings revealed that the benzothiadiazole units are the electrochemically-active sites for Zn^{2+} storage. COF-TMT-BT-based ZIB displayed a specific capacity of 283.5 mAh g^{-1} at a current density of 0.1 A g^{-1} as well as an outstanding maximum energy density of 219.6 Wh kg^{-1} and power densities of 23.2 kW kg^{-1}, which, according to our knowledge, are superior to most of the reported COFs cathodes and another organic or inorganic electrode materials to date. Moreover, we also showed the superior electrochemical performance for aqueous ZIBs of other imine-linked COF by using benzothiadiazole as electrochemically-active units in its structure. This research not only highlights the importance of the rational design of novel electrochemically active COFs but also offers an efficient strategy to construct high-performance cathodes for aqueous ZIBs.

150

5.2 Results and Discussion

In this Chapter, we have synthesized a novel benzothiadiazole-functionalized olefin-linked COF generated *via* the aldol condensation of 2,4,6-trimethyl-1,3,5-triazine (TMT) and 4,4 ' -(benzothiadiazole-4,7-diyl)dibenzaldehyde (BT), (COF-TMT-BT). The synthesis of COF-TMT-BT has been discussed in experimental Chapter 2. The multiscale characterization of COF-TMT-BT structures has been carried out using different experimental techniques (detailed information has been discussed in Experimental chapter 2). The electrochemical performance of COF TMT-BT for Zn^{2+}storage is assessed in a two-electrode system by assembling a COF TMT-BT cathode with a Zn foil anode and 2 M zinctrifluoromethanesulfonate $(Zn (CF_3SO_3)_2)$ aqueous electrolyte as shown in Figure 5-1a. The cyclic voltammograms (CVs) of the first five cycles at 5 mV s^{-1} in the potential range of 0.5-1.6 V *vs* Zn^{2+}/Zn are displayed in Figure 5-2b. A pair of redox peaks at 1.31 and 1.12 V indicates the reversible insertion/extraction process of Zn^{2+}in the COF structures. Importantly, the peak positions remain almost unchanged during the successive cycling except for the peak currents that gradually increase due to the activation of the COF TMT-BT cathode.
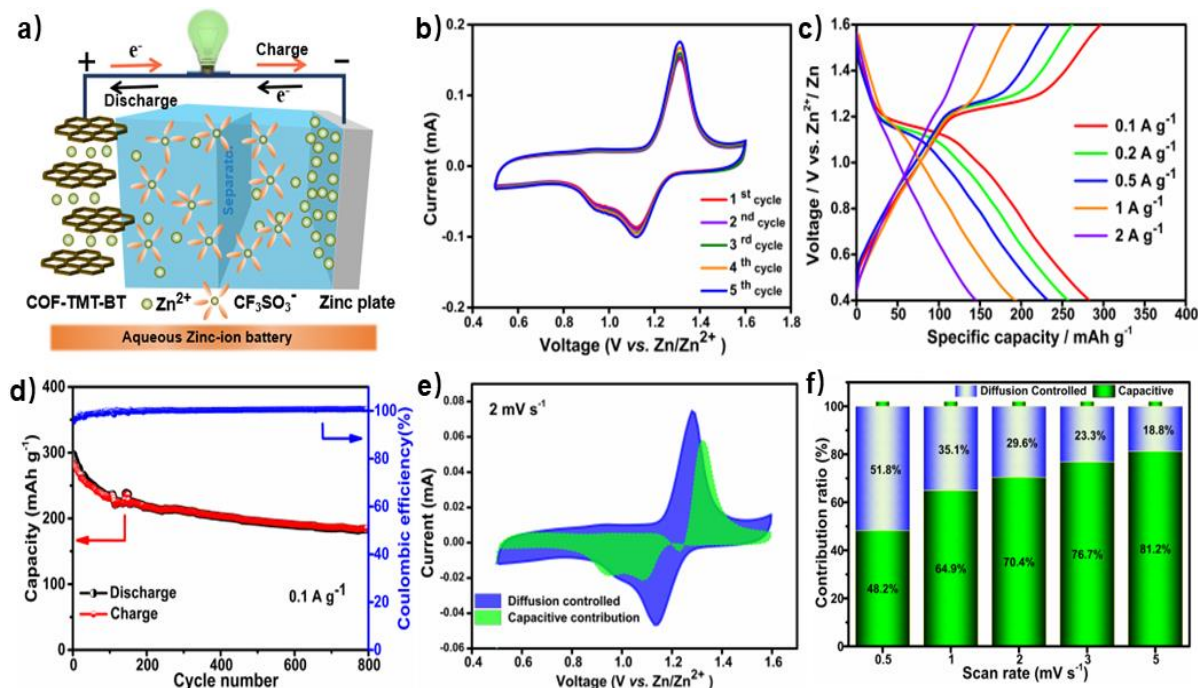
Figure 5-1. a) Schematic of COF-TMT-BT//Zn(CF₃SO₃)₂//Zn energy storage system. used as an electrolyte, b) CV curves of COF-TMT-BT at 5 mV s⁻¹ during 5 cycles, c) GCD profiles for COF-TMT-BT electrodes at various current densities, d) long-term cycling performance at 0.1 A g⁻¹, e) the comparison of CV curves for the capacitive contribution and diffusion-controlled fraction at 2 mV s⁻¹, f) capacitive contribution of the COF- TMT-BT electrode at different scan rates.

The galvanostatic charge-discharge (GCD) profiles of COF-TMT-BT (Figure 5-1c) in the adopted potential window reveal a high capacity of 283.5, 261.2, 232.6, 210.4, 184.7 mAh g⁻¹ at a current density of 0.1, 0.2, 0.5, 1, 2 A g⁻¹, respectively, which are superior to most of the reported COFs cathodes and another organic or inorganic electrode materials in aqueous ZIBs as exhibited in Table 5-1.

Table 5-1. The gravimetric capacity of our COF-TMT-BT electrode compared to recently reported COFs and other reported cathode materials for aqueous Zn^{2+} energy storage.

Material type	Electrode	Electrolyte	Voltage (V)	Current density / A g^{-1}	Capacity / mA g^{-1}	Ref
Inorganic compounds	ZMO/C	3M Zn(CF$_3$SO$_3$)$_2$	0.8-1.9	0.5	150	1
				0.2	72	
	H$_2$V$_3$O$_8$ nanowire	3M Zn(CF$_3$SO$_3$)$_2$	0.2-1.6	0.5	279	2
				5	155	
	HfO$_2$-coated ZVO	1M ZnSO$_4$	0.2-1.8	0.1	215	3
				3	88	
	Mesoporous carbon spheres	2M ZnSO$_4$	0.2-1.8	0.1	174.7	4
				5	108.7	
	ZMO@Ti3C2Tx	1M ZnSO$_4$ 0.05M MnSO$_4$	0.8-1.8	0.2	150	5
				4	84.5	
Organic compounds	C4Q	3M Zn(CF$_3$SO$_3$)$_2$	0.2-1.8	0.25	220	6
				1	172	
	Tetrachloro-1,4 benzoquinone	1 M Zn(CF$_3$SO$_3$)$_2$	0.8-1.4	0.217	118	7
	PQ-D	3M Zn(CF$_3$SO$_3$)$_2$	0.25-1.6	0.03	225	8
				0.15	210	
	DTT	2M ZnSO$_4$	0.3-1.4	0.2	175	9
				2	99	
	Phenothiazine	2M ZnSO$_4$	0.5-1.7	0.04	188.24	10
				0.1	145.56	
COFs	PI-COF	2M ZnSO$_4$	0.9-0	0.7	92	11
	PA-COF	1M ZnSO4	0.2-1.6	0.1	247	12
				5	93	
	HqTp	3M ZnSO$_4$	0.2-1.8	0.125	276	13
				3.75	85	
	HA-COF	2M ZnSO$_4$	0.2-1.6	0.1	339	14
				5	170	
	Tp-PTO-COF	2M ZnSO$_4$	0.4-1.5	0.2	301.4	15
				5	192.8	
	COF-TMT-BT	**2M Zn(CF$_3$SO$_3$)$_2$**	**0.5-1.6**	**0.1**	**283.5**	**This work**
				2	**184.7**	

Noteworthy, we observe a voltage plateau at 1.27 V using a significantly low current density (*i.e.*, between 0.1 and 0.5 A g^{-1}) for the first time in organic compounds (including small organic molecules, COFs, and polymers), which is vital for its practical application. The rate capability of COF-TMT-BT is analyzed at different current densities as shown in Figure 5-2. When the current density decreases from 2 to 0.1 A g^{-1}, the specific capacity of 272.6 mAh g^{-1} is fully recovered, indicating an excellent rate capability.
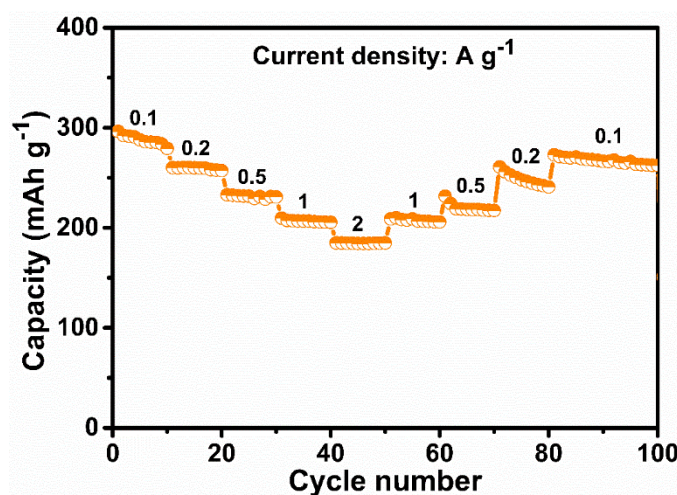

Figure 5-2. The rate performance of COF-TMT-BT cathode in the current range of 0.1-2 A g^{-1}.

The long-term cycling test (Figure 5-1d) shows the high cyclability of COF-TMT-BT electrodes at a current density of 0.1 A g^{-1}, which can retain a 186.8 mAh g^{-1} specific capacity value after 800 cycles. Moreover, the coulombic efficiency of the COF-TMT-BT cells is well maintained to 99.6% throughout the 800 charge-discharge cycles. Remarkably, COF-TMT-BT-

based electrodes deliver an outstanding maximum energy density of 219.6 Wh kg^{-1} and power densities of 23.2 kW kg^{-1} (based on a mass loading of 1.7 mg cm^{-2} and the weight ratio of 70 wt.% of active material).

To gain insight into the electrochemical kinetic aspects of COF-TMT-BT cathodes, CV tests at scan rates ranging from 0.5 to 5 mV s^{-1} are conducted as exhibited in Figure 5-3.
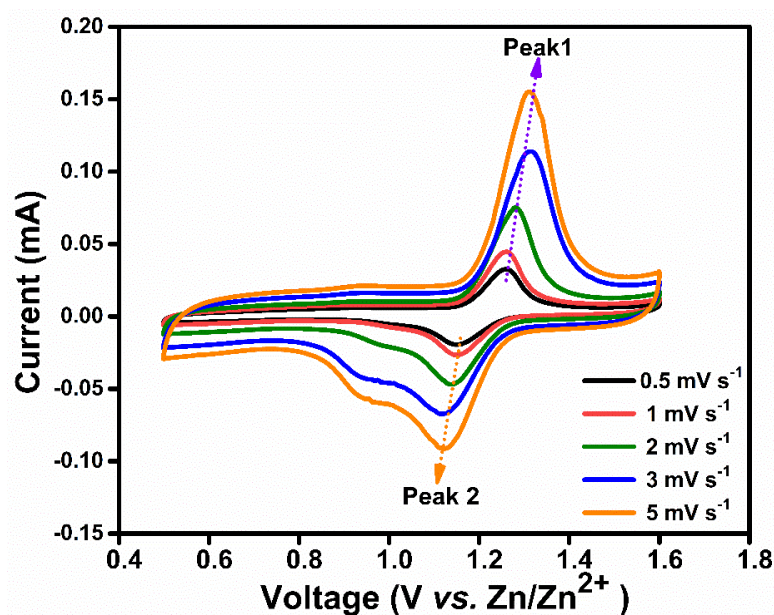

Figure 5-3. The CV curves of COF-TMT-BT cathode at multiple scan rates from 0.5 to 5 mV s^{-1}.

The CV curves only exhibit a small peak shift within the scan rate of 0.5-5 mV s^{-1}, indicating excellent electrochemical reversibility. The electrochemical kinetics COF-TMT-BT are investigated by exploiting the procedure proposed by Wu *et al*., according to the equation: $I = av^b$, where i represents current density, v refers to scan rate, a and b are variable

parameters.[16, 17] It is well-established that when the b-value is closer to 0.5 means a diffusion-controlled process, while the b-value is closer to 1 indicating a capacitive-controlled process in the charge storage mechanism. The b-value of COF-TMT-BT cathodes calculated from the slope of log (i) - log(v) curves in Figure 5-4 are 0.71 and 0.76, which indicates the Zn^{2+} storage mechanism of the COF-TMT-BT cathodes is dominated by a capacitive contribution. To further quantify the capacitive (k_1v) and diffusion-controlled contribution ($k_2v^{0.5}$) from the CV curves at different scan rates, the following equation can be used: $i = k_1v + k_2v^{0.5}$, where k_1 and k_2 are constants parameters.[18]
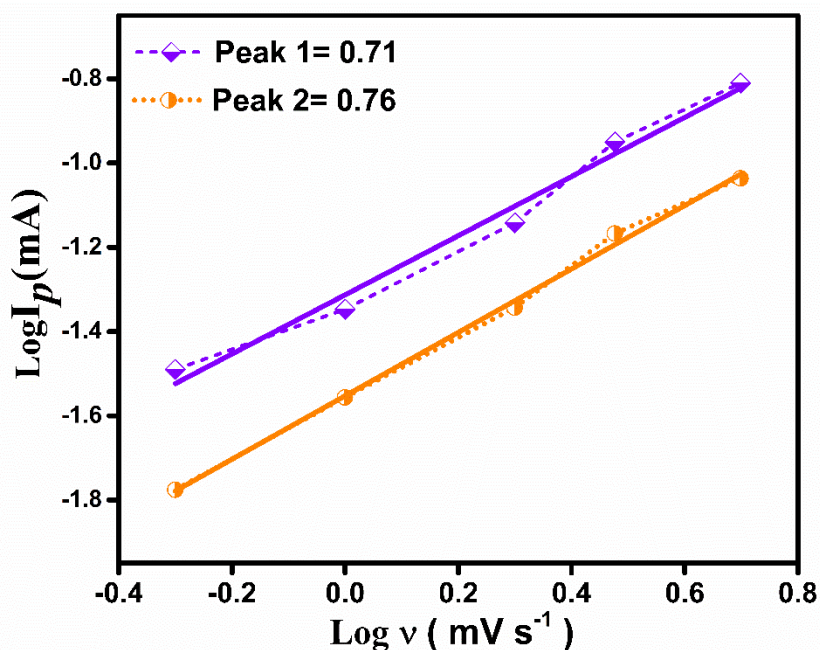

Figure 5-4 The linear fits of I log vs log v plots to calculate b values according to the equation of $i = av^b$ for COF-TMT-BT cathode.

As shown in Figure 5-5, the capacitive contribution to the charge storage mechanism for the COF-TMT-BT cathodes is the highest (81.2%) at the highest scan rate (5 mV s^{-1}). The capacitive contribution gradually decreases (76.7, 70.4, 64.9 and 48.2%) at lower scan rates (3, 2 ,1 and 0.5 mV s^{-1}, respectively) (Figure 5-2e-f and Figure 5-6). Thus, the coexistence of capacitive and diffusion-controlled charge storage mechanisms confirms the pseudocapacitive nature of COF-TMT-BT materials which is highly beneficial for energy storage.[19-23]
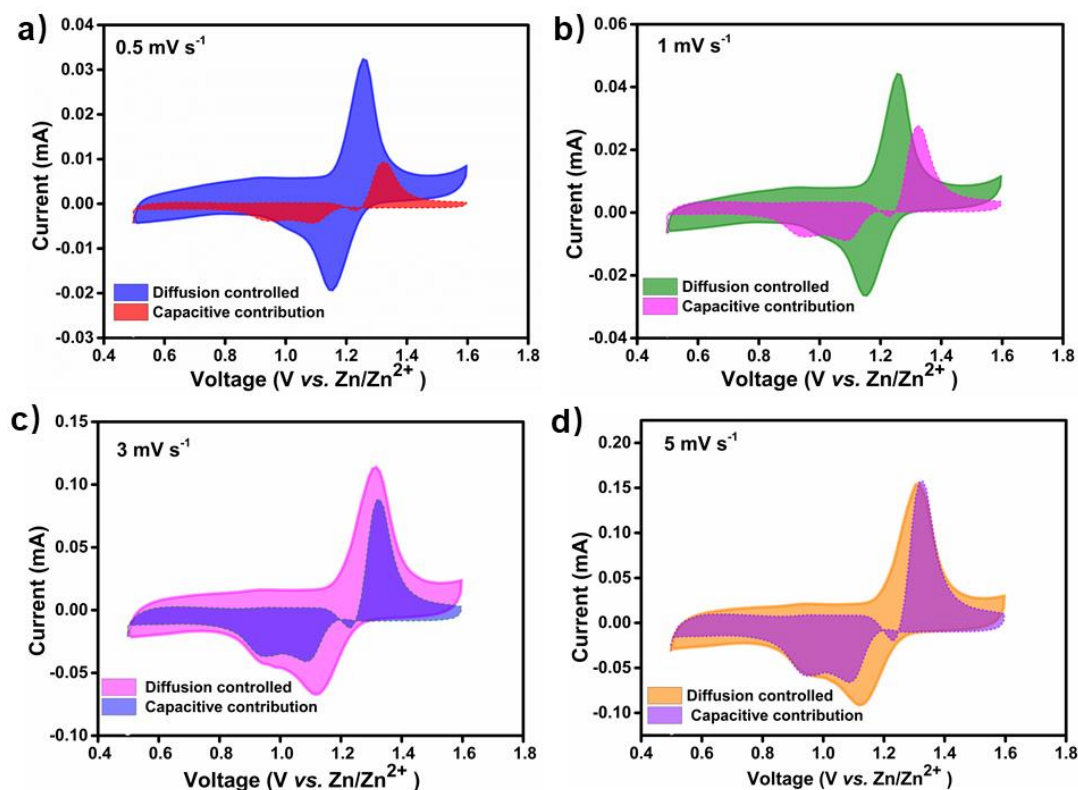

Figure 5-5. The comparison of the capacitive contribution and the diffusion-controlled charge storage mechanism of COF-TMT-BT cathode at different scan rates: a) 0.5 mV s^{-1}; b) 1 mV s^{-1};   c) 3 mV s^{-1}; d) 5 mV s^{-1}.

157

To further confirm that the benzothiadiazole units play a key role in the Zn^{2+} storage, we performed a control experiment where we synthesized a similar olefin-linked COF without benzothiadiazole moieties (*i.e.*, the BT monomer is replaced by 4,4'-biphenyldicarbaldehyde (BP)), COF- TMT-BP, and we assess its electrochemical performance as cathode material in aqueous ZIBs as shown in Figure 5-6. The CV test results of the COF-TMT-BP cathode do not exhibit obvious oxidation and reduction peaks in the same potential range of COF-TMT-BT, indicating no chemisorption of Zn^{2+}. We finally extended the use benzothiadiazole units as electrochemically-active sites in Zn^{2+} energy storage for the fabrication of other COFs with different linkages. Therefore, a benzothiadiazole-based imine-linked COF is synthesized through a Schiff-base reaction of tris-(4-aminophenyl)triazine (TAT) and BT monomer under solvothermal conditions (the synthesis details can be found in the Experimental chapter 2), COF-TAT-BT. Interestingly, the CV analysis of the COF-TMT-BP cathode displays a clear oxidation and reduction peak, which confirms once again that the benzothiadiazole units are the electrochemically active sites in imine-linked COF for aqueous ZIBs.
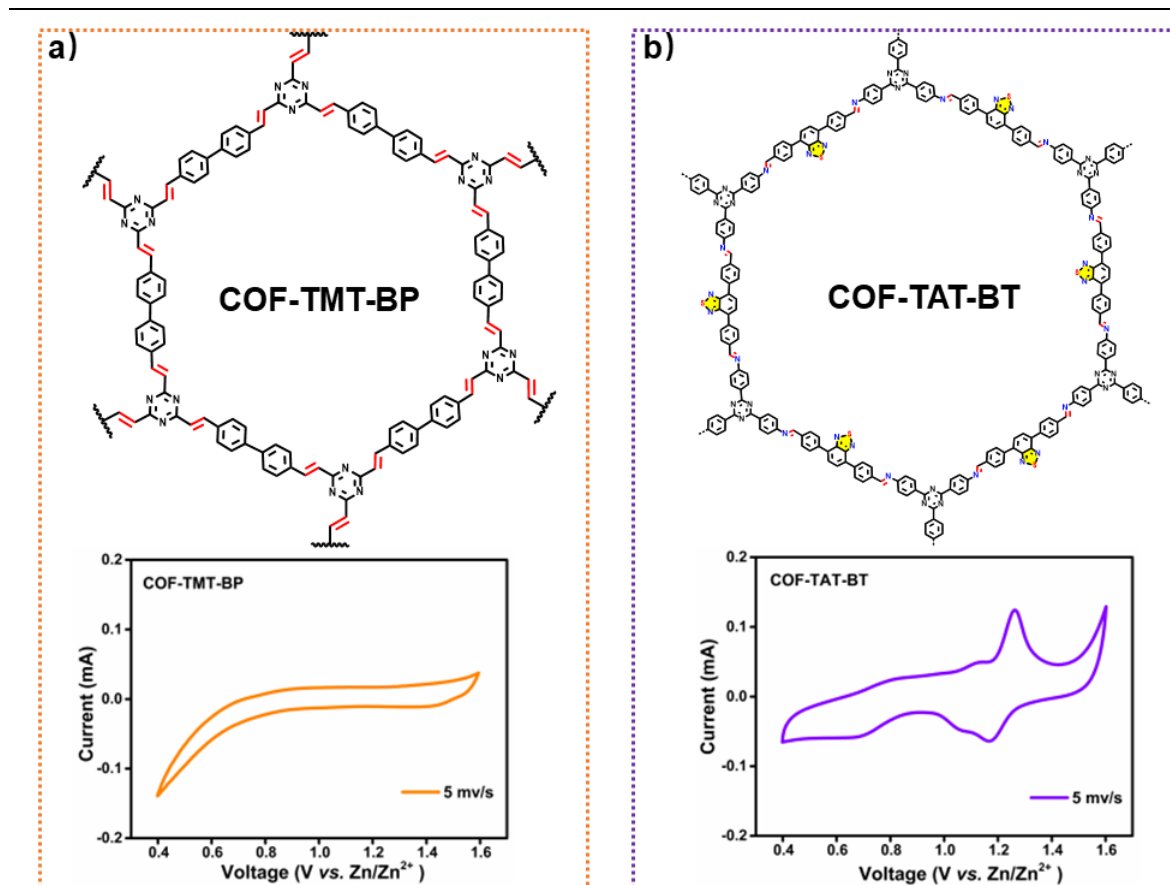
Figure 5-6. Chemical structure and corresponding CV in aqueous ZIBs for a) COF-TMT-BP. b) COF-TAT-BT.

5.3 Characterization

5.3.1 PXRD spectra and structure simulation of COF-TMT-BT

As shown in Figure 5-7, the powder X-ray diffraction (PXRD) pattern of COF-TMT-BT reveals that the COF-TMT-BT structure is crystalline, and the pattern matches more precisely with the simulated PXRD of the aligned AA stacked model (Figure 5-8) in space group of hexagonal $P6_3/m$ as compared with AB stacked model (Figures 5-9 and 5-10). The full profile

159

Pawley refinement of the model against the experimental pattern yields a unit cell of a = b = 37.6 Å, c = 3.7 Å, α = β = 90°, γ = 120° with good agreement factors of R_{wp}=3.93% and R_p=3.08% (Table 5-2).
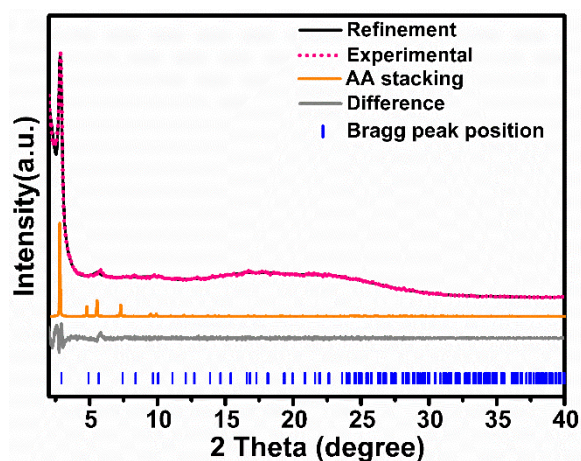

Figure 5-7. PXRD pattern fitting of COF-TMT-BT with Pawley refinement and simulated AA-stacking patterns.
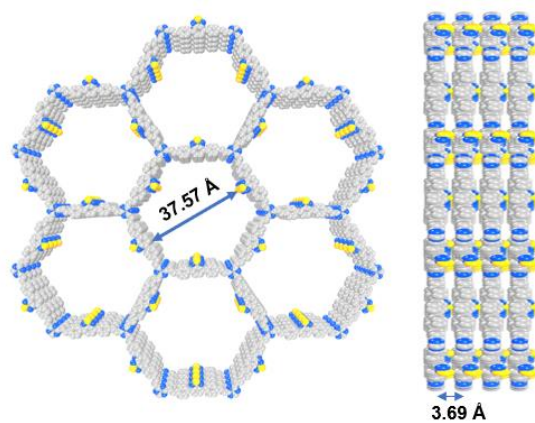

Figure 5-8. top and side view of the AA eclipsed model
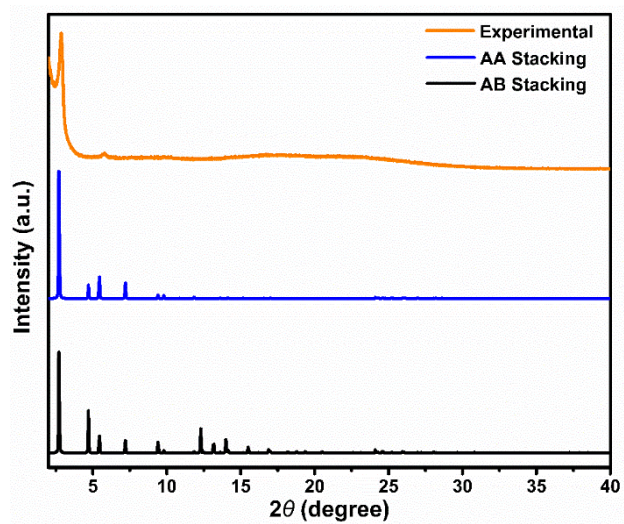
160

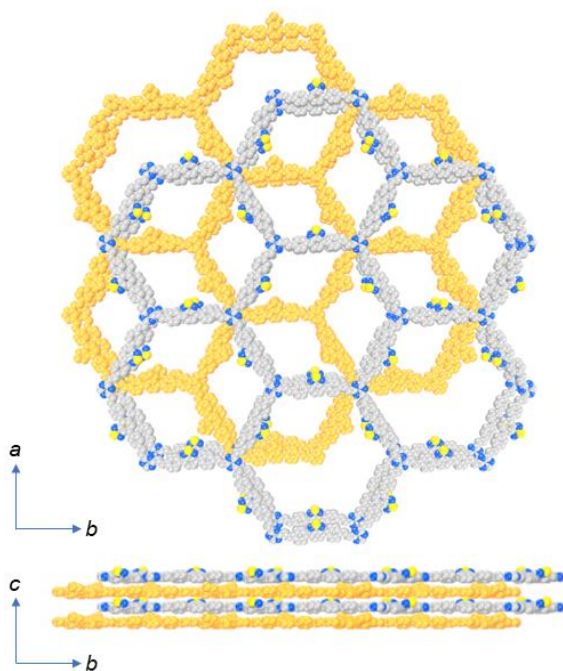**Figure 5-9.** Experimental PXRD pattern of COF-TMT-BT and the simulated PXRD patterns for AA and AB stacking models.

Figure 5-10. Top view and side view of COF-TMT-BT with AB stacking mode, hydrogen atoms are omitted for clarity.

161

Table 5-2. Fractional Atomic Coordinates of Structure Model of COF-TMT-BT with Staggered (AA) Stacking Mode, Resulting from Pawley Refinement.

Hexagonal , $P6_3/m$

a = b = 37.5653Å, c = 3.6887 Å

α = β = 90°, γ = 120°

Atom	X	y	z
N1	0.62477	0.30664	0.51626
N2	0.69336	0.31813	0.51625
N3	0.68187	0.37523	0.51626
N4	0.30778	0.68322	0.53888
N5	0.31678	0.62456	0.53891
N6	0.37543	0.69221	0.53887
N7	0.58642	0.04349	0.76995
N8	0.9565	0.54292	0.76995
N9	0.45708	0.41358	0.76996
N10	0.55312	0.96671	0.76254
N11	0.03329	0.58642	0.76253
N12	0.41358	0.44688	0.76252
C1	0.64112	0.3477	0.51641
C2	0.6523	0.29343	0.51642
C3	0.70658	0.35888	0.51642
C4	0.63714	0.24938	0.51002
C5	0.75062	0.38776	0.51003
C6	0.61224	0.36286	0.51002
C7	0.59695	0.22082	0.54131
C8	0.77918	0.37612	0.54132
C9	0.62388	0.40306	0.54132
C10	0.57966	0.17657	0.53168
C11	0.82343	0.40309	0.5317
C12	0.59691	0.42035	0.5317
C13	0.53881	0.1508	0.6457
C14	0.8492	0.38802	0.64571
C15	0.61199	0.46119	0.64571
C16	0.52143	0.10836	0.64771
C17	0.89164	0.41307	0.64771
C18	0.58693	0.47857	0.64771
C19	0.54413	0.08988	0.53426
C20	0.91012	0.45425	0.53428
C21	0.54575	0.45587	0.53428

C22	0.58479	0.1155	0.41429
C23	0.8845	0.4693	0.41431
C24	0.53071	0.41521	0.41431
C25	0.602	0.15782	0.4115
C26	0.84218	0.44417	0.4115
C27	0.55583	0.398	0.41151
C28	0.52533	0.04496	0.53471
C29	0.95504	0.48037	0.53472
C30	0.51963	0.47467	0.53473
C31	0.48465	0.01914	0.43442
C32	0.98085	0.4655	0.43442
C33	0.5345	0.51535	0.43444
C34	0.46585	0.97587	0.43106
C35	0.02413	0.48998	0.43105
C36	0.51002	0.53415	0.43107
C37	0.48627	0.95498	0.52676
C38	0.04502	0.53129	0.52674
C39	0.46871	0.51373	0.52675
C40	0.52809	0.98025	0.6376
C41	0.01974	0.54783	0.63759
C42	0.45217	0.47191	0.63759
C43	0.54741	0.02481	0.64183
C44	0.97519	0.5226	0.64183
C45	0.4774	0.45259	0.64183
C46	0.4659	0.90994	0.5188
C47	0.09006	0.55596	0.51879
C48	0.44404	0.5341	0.51879
C49	0.42471	0.88608	0.63178
C50	0.11391	0.53862	0.63177
C51	0.46138	0.5753	0.63177
C52	0.40481	0.84354	0.62703
C53	0.15646	0.56127	0.62704
C54	0.43873	0.59519	0.62704
C55	0.42526	0.82285	0.50715
C56	0.17715	0.60242	0.50719
C57	0.39759	0.57474	0.5072
C58	0.46642	0.84684	0.39421
C59	0.15316	0.61958	0.39424
C60	0.38042	0.53357	0.39425
C61	0.48648	0.88948	0.39923
C62	0.11052	0.597	0.39923

163

C63	0.403	0.51352	0.39925
C64	0.40603	0.77838	0.50067
C65	0.22162	0.62765	0.50073
C66	0.37235	0.59397	0.50074
C67	0.36561	0.75108	0.54263
C68	0.24892	0.61453	0.54269
C69	0.38547	0.63439	0.54271
C70	0.34897	0.70677	0.53833
C71	0.29323	0.64221	0.53838
C72	0.35779	0.65102	0.53836
H1	0.66097	0.24105	0.48258
H2	0.75896	0.41993	0.48257
H3	0.58008	0.33903	0.4826
H4	0.57546	0.2321	0.58303
H5	0.7679	0.34336	0.58303
H6	0.65665	0.42454	0.58301
H7	0.52109	0.16472	0.74216
H8	0.83528	0.35637	0.74215
H9	0.64363	0.47891	0.74213
H10	0.49019	0.08909	0.74863
H11	0.91091	0.4011	0.74863
H12	0.5989	0.50981	0.74864
H13	0.6023	0.10166	0.31297
H14	0.89834	0.50064	0.31299
H15	0.49936	0.39771	0.31298
H16	0.63308	0.17685	0.30698
H17	0.82315	0.45623	0.30698
H18	0.54377	0.36692	0.30696
H19	0.46675	0.03303	0.34236
H20	0.96697	0.43372	0.34237
H21	0.56628	0.53325	0.34237
H22	0.43416	0.95801	0.33678
H23	0.04198	0.47615	0.33676
H24	0.52386	0.56584	0.33679
H25	0.40878	0.90147	0.73779
H26	0.09853	0.50731	0.73777
H27	0.49269	0.59122	0.73777
H28	0.37341	0.82594	0.72858
H29	0.17405	0.54747	0.7286
H30	0.45253	0.62659	0.72861
H31	0.48258	0.83132	0.2968

H32	0.16867	0.65126	0.29682
H33	0.34874	0.51741	0.29683
H34	0.51803	0.90731	0.30378
H35	0.09269	0.61072	0.30377
H36	0.38928	0.48197	0.30378
H37	0.42627	0.76572	0.45348
H38	0.23428	0.66055	0.45355
H39	0.33945	0.57373	0.45357
H40	0.34273	0.7606	0.5764
H41	0.2394	0.58213	0.57646
H42	0.41787	0.65728	0.57645
S1	0.59599	0.0072	0.86797
S2	0.9928	0.58878	0.86797
S3	0.41121	0.40401	0.86796

5.3.2 FT-IR spectra of COF-TMT-BT

The olefin linkage of COF-TMT-BT can be unambiguously confirmed by Fourier transform infrared (FT-IR) spectroscopy as shown in Figure 5-11. The FT-IR spectrum of COF-TMT-BT displays a characteristic peak at 1626 cm^{-1}, which belongs to the C=C stretching of the formed olefin linkage, and it is not present in the starting monomers TMT or BT. In addition, the characteristic peak at 1686 cm^{-1} of the C=O stretching in BT is extensively attenuated in COF-TMT-BT, indicating the successful aldol condensation.
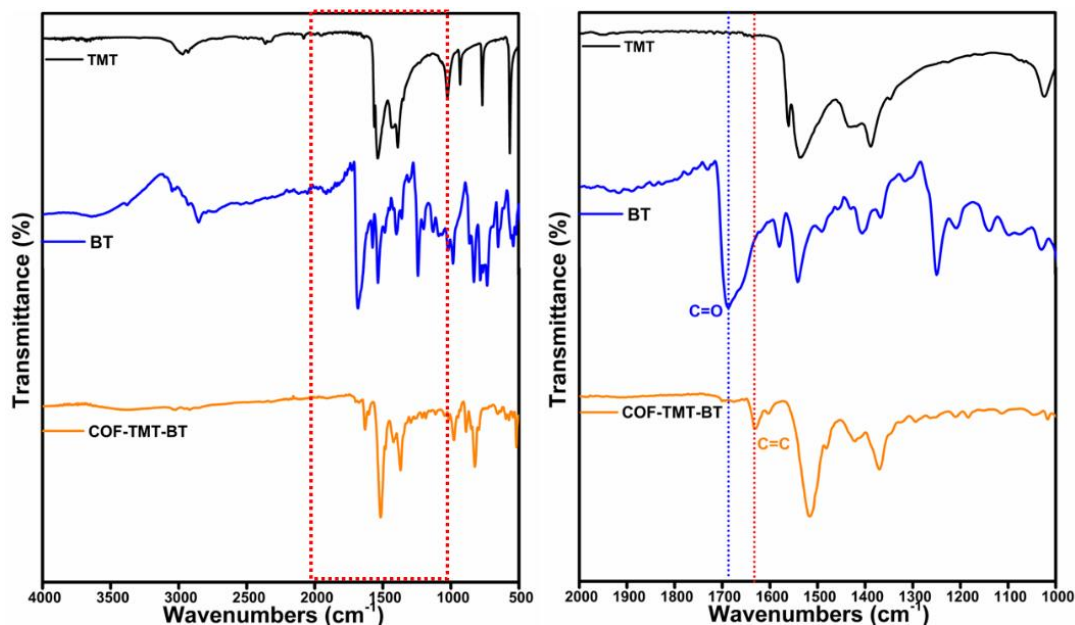
Figure 5-11. FT-IR spectra of COF-TMT-BT (orange curves) compared with TMT (black curves) and BT (blue curves) monomers.

5.3.3 Solid-state NMR spectroscopy of COF-TMT-BT

The solid-state structural analysis of COFs is then analyzed by edited solid-state (SS) ^{13}C cross-polarization magic angle spinning (CP-MAS) nuclear magnetic resonance (NMR) spectroscopy.[24,25]   In the unlabeled COF-TMT-BT (Figure 5-12, blue spectrum), the clear and unambiguous assignment of the alkene carbon peaks is not possible due to overlapped signals of aromatic and olefinic carbons of the backbone of the structure. Therefore, more advanced experiments of edited ^{13}C CP-MAS NMR spectral,[42] which provided more precise assignments of matching expected chemical shifts to the expected moieties are performed. The observed signals located at δ ~ 142 and 135 ppm can be uniquely attributed to the aromatic carbon signals of
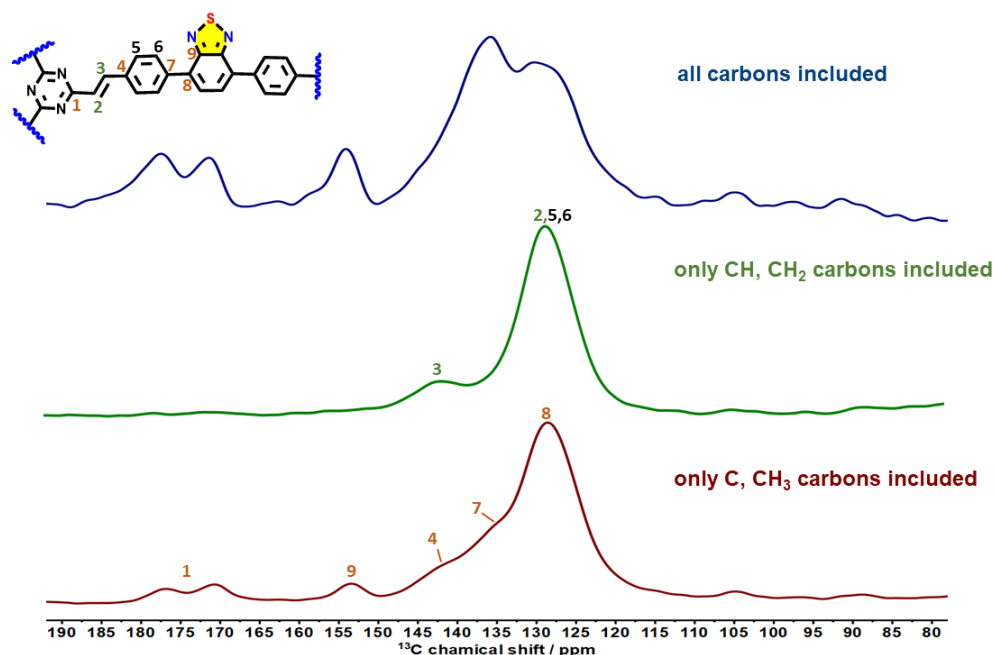
166

vinylene (-CH=CH-).

Figure 5-12. Edited solid-state ^{13}C NMR spectra of COF-TMT-BT.

The chemical shift signal of the labeled BT aldehyde starting material is observed at around 192 ppm and it is largely attenuated in COF TMT-BT as shown in Figure 5-13. Moreover, the COF-TMT-BT surprisingly reveals two distinct aromatic triazine carbon (C_1) signals at $\delta \sim 170$ and ~ 176 ppm which is in good agreement with the reported ^{13}C NMR spectrum of 2,4,6-triamino-1,3,5-triazine (melamine). The different hydrogen-bonding environment results in two chemically diverse carbon atoms and hence in two different signals in the ^{13}C NMR spectrum.[27]
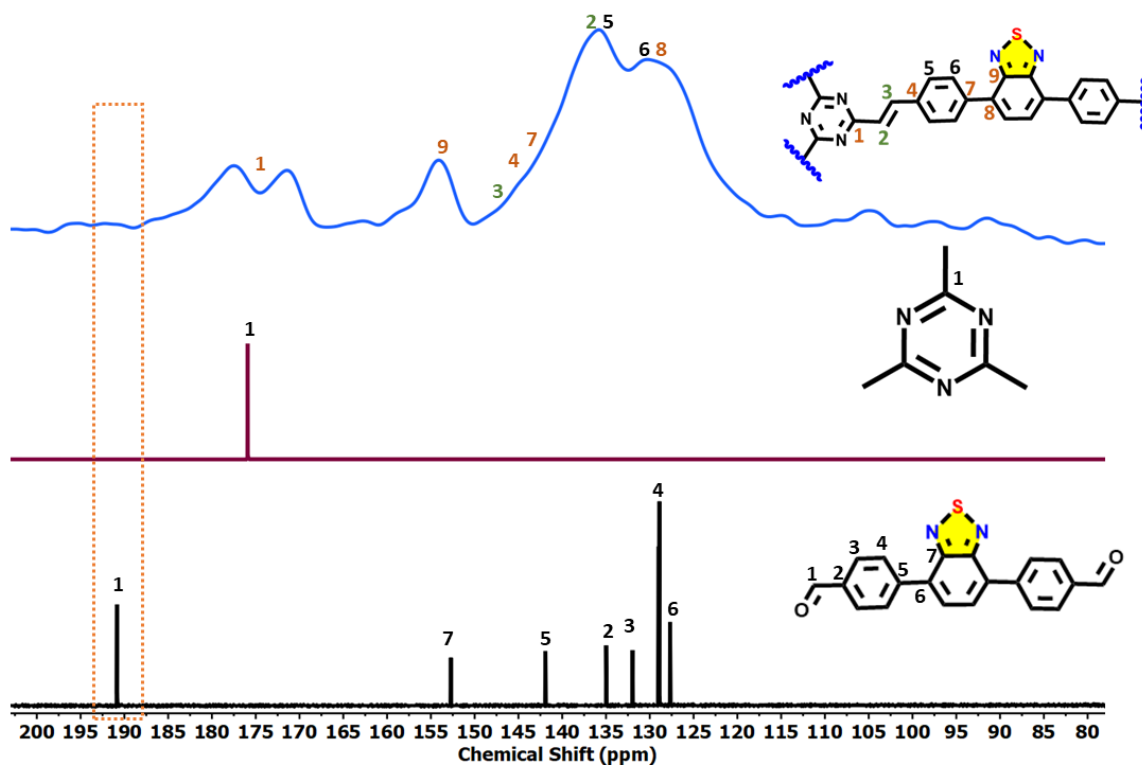
Figure 5-13. Solid-state ^{13}C CP-MAS NMR of labeled COF-TMT-BT(blue), and ^{13}C-labeled TMT (purple) and BT (black) monomers for comparison.

5.3.4 XPS spectroscopy of COF-TMT-BT

To gain more insights into the electronic states of sulfur and nitrogen heteroatoms of benzothiadiazole units, X-ray photoelectron spectroscopy (XPS) is then performed, confirming the presence of C1s, S2p, and N1s electronic states in COF-TMT-BT as shown in Figure 5-14.
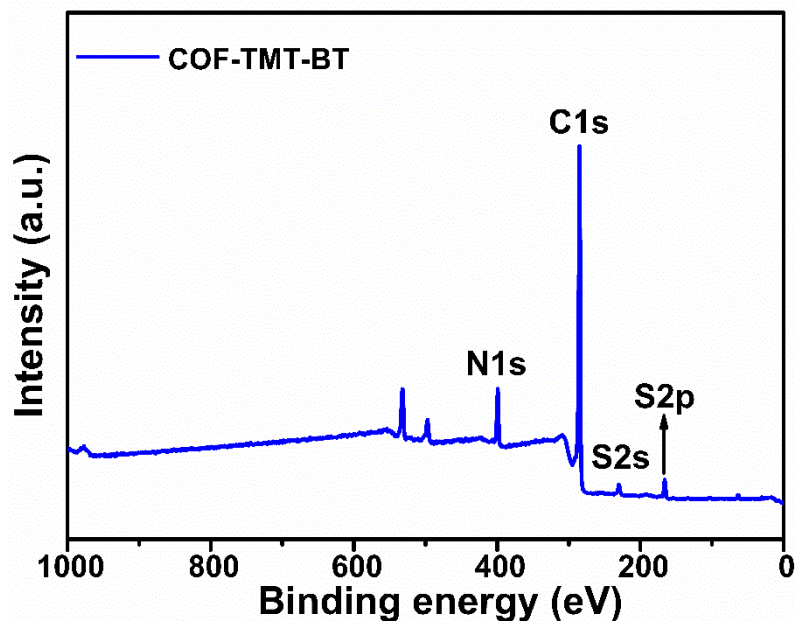
Figure 5-14. XPS survey spectrum of COF-TMT-BT.

The C1s spectrum of the COF-TMT-BT in Figure 5-15 shows the presence of three distinctive peaks, located at 284.5 eV, 285.7 eV, and 286.7 eV, and can be attributed to C-C, C-H (*e.g.*, -CH=CH- chains) and C=N bonding in the benzothiadiazole units, respectively.[32,33]
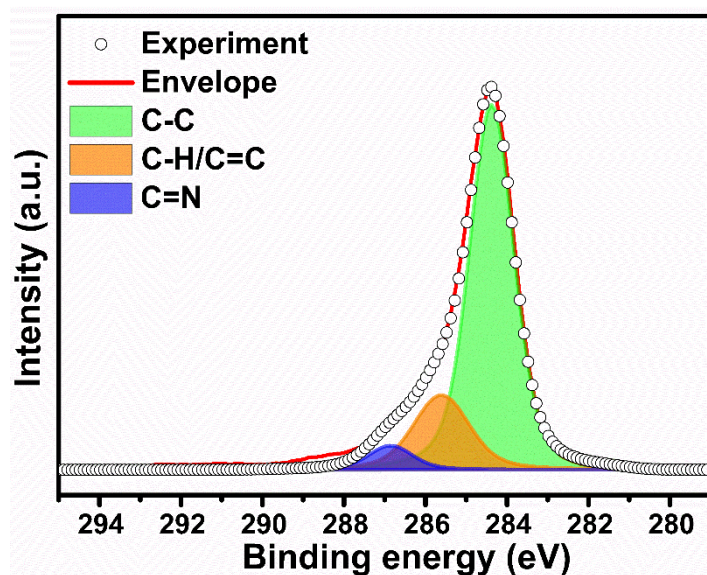

Figure 5-15. High-resolution XPS spectra of COF-TMT-BT for C1s.

169

The N1s spectrum of the COF-TMT-BT in Figure 5-16 shows two different N signals which come from two different locations within the repeat unit (one in the triazine unit and the other in the benzothiadiazole unit), the peak at 399.1 eV originates from the pyridinic-N in benzothiadiazole unit,[30, 31] and the other peak at higher binding energy (at 400.5 eV) can be ascribed to the pyrrolic-N core levels in triazine moiety.[32, 33]
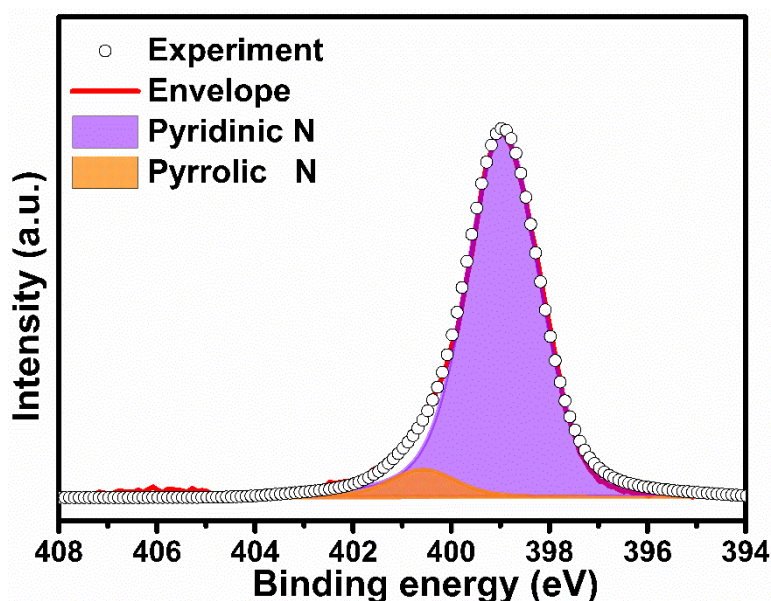

Figure 5-16. High-resolution XPS spectra of COF-TMT-BT for N1s.

The high-resolution XPS spectra of S2p in Figure 5-22 exhibit a peak at ~165.2 eV along with a shoulder peak at ~166.4 eV assigned to the benzothiadiazole $S2p_{3/2}$ and $S2p_{1/2}$, respectively.[34, 35] All the experimental findings from the XPS analysis of COF-TMT-BT are in good agreement with the previous FT-IR and ^{13}C CP-MAS NMR analysis, which further verify the olefin linkage formation and benzothiadiazole moiety in our COF framework.
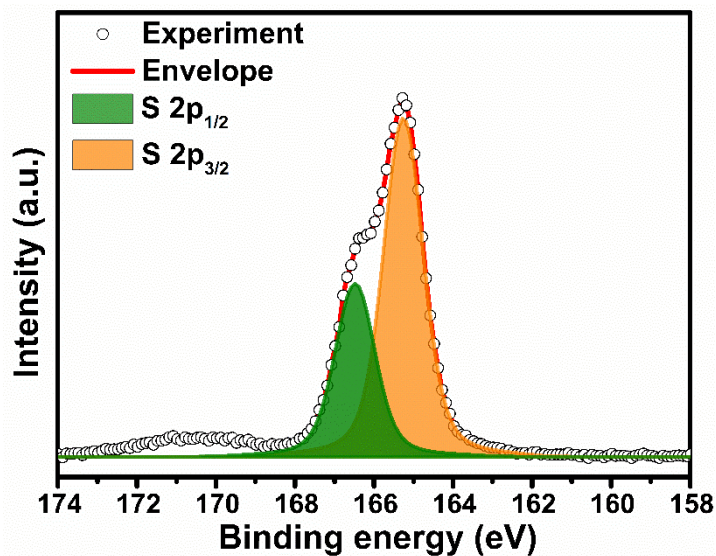
Figure 5-17. High-resolution XPS spectra of COF-TMT-BT for S2p.

To shed more light onto the charge storage mechanism of Zn^{2+} from the benzothiadiazole electrochemically active units, XPS analysis is performed in the pristine, discharged, and charged state of COF-TMT-BT cathodes as shown in Figures 5-18.
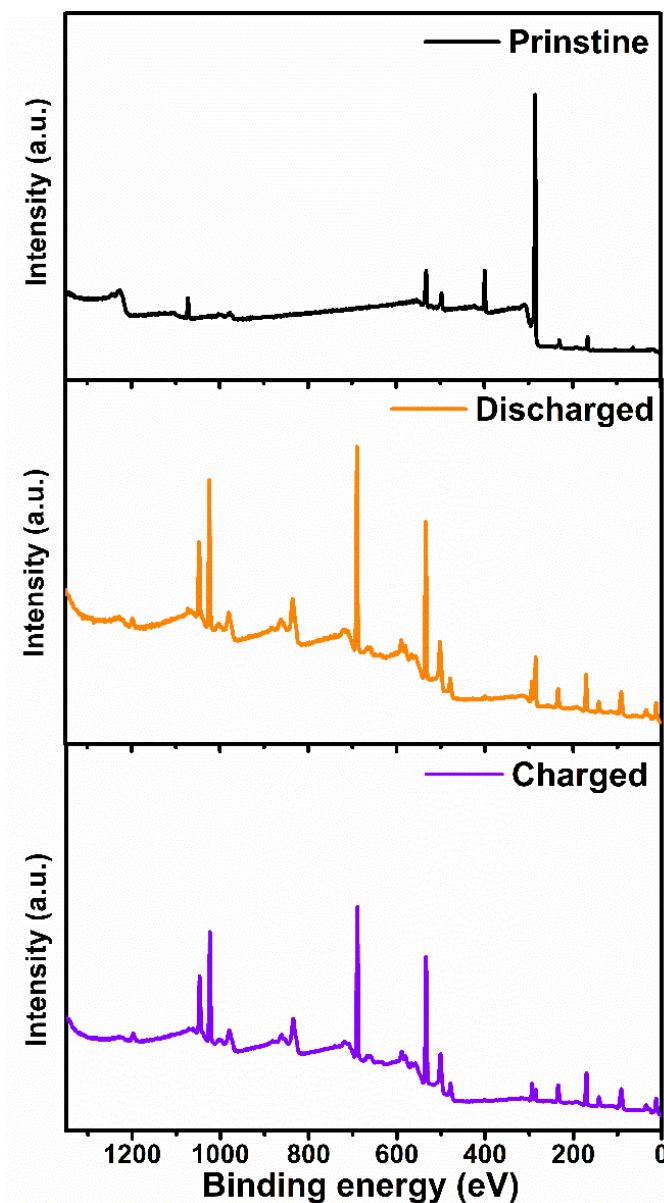
Figure 5-18. XPS survey spectra of pristine charged and discharged COF-TMT-BT cathode.

In the pristine electrodes, the observed signals of $S2p_{1/2}$ 165.2 eV, and $S2p_{3/2}$ 166.5 eV are ascribed to benzothiadiazole sulfur as exhibited in Figures 5-19. During the discharging process, Zn^{2+} is moved from the Zn anode to the COF-TMT-BT cathode and bound to the S atoms from the benzothiadiazole

units forming the S-Zn-S coordination bond between the successive COF-TMT-BT layers. This complex formation results in the chemical shift to the higher binding energy of S2p$_{1/2}$* 169.8 eV, and S2p$_{3/2}$* 171.0 eV in COF-TMT-BT cathodes. On the contrary, during the charging process, the Zn^{2+} dissociates from the COF-TMT-BT cathode and returns to be deposited on the Zn anode. As a result, the intensity of S2p$_{1/2}$* 169.8 eV, and S2p$_{3/2}$* 171.0 eV peaks diminishes by half as compared to the discharged state, which can be further verified by the lower intensity of the XPS peaks of Zn^{2+}(Figure 5-20),
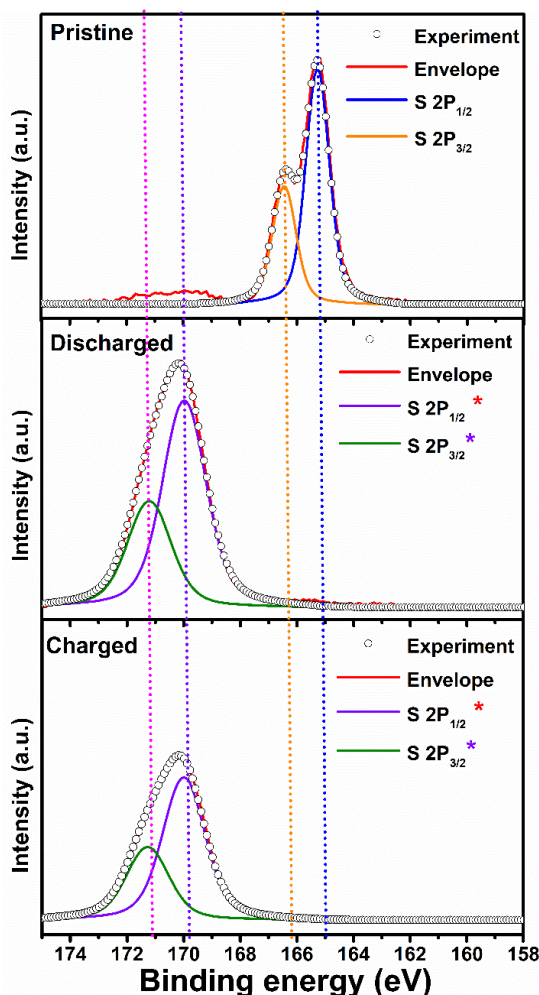

Figure 5-19. XPS analysis of sulfur in benzothiadiazole moieties of COF-TMT-BT cathodes in pristine, charged, and discharged state.
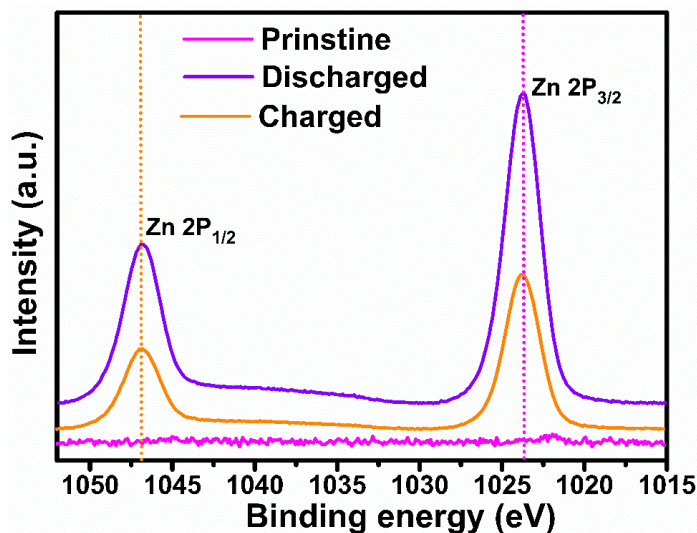
Figure 5-20. XPS analysis of Zn^{2+} in pristine charged and discharged COF-TMT-BT cathodes.

5.3.5 SEM and TEM images of COF-TMT-BT

The morphology of COF-TMT-BT is investigated by field-emission scanning electron (FE-SEM) and it reveals the presence of spherical nanoparticles with a diameter of ~500 nm. Furthermore, transmission electron microscope (TEM) and energy-dispersive spectroscopy (EDS) elemental mapping images confirm the homogeneous nature of the COF-TMT-BT spherical structures with a uniform distribution of C, N, and S elements (Figure 5-21).
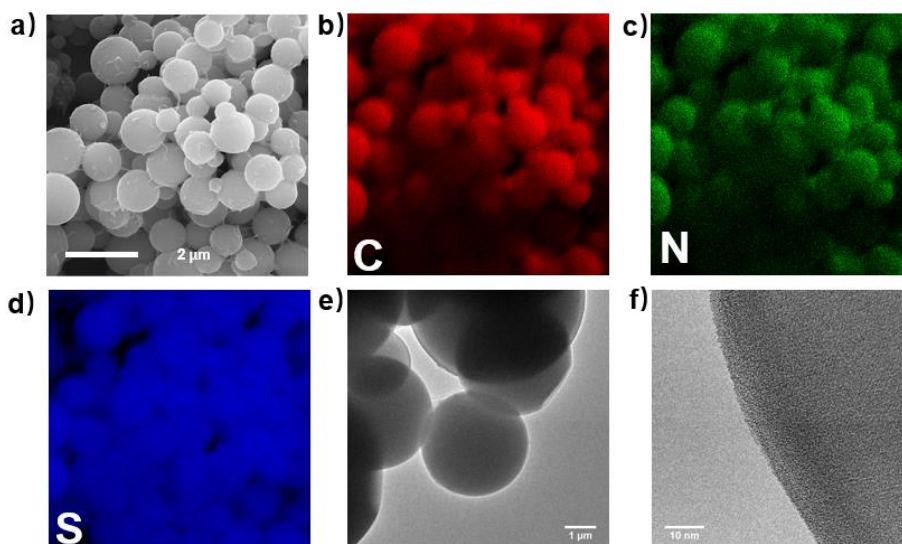
Figure 5-21. FE-SEM image and corresponding elemental mapping analysis of C (red), N (green), S (blue) and TEM images of COF-TMT-BT.

In addition, the energy-dispersive X-ray spectroscopy (EDS) analysis was also used to explore the COF-TMT-BT cathode at the pristine electrode and after 800 cycles as shown in Figure 5-22 and Figure 5-23, which further prove that during the discharging process, Zn^{2+} is moved from the Zn anode to the COF-TMT-BT cathode.
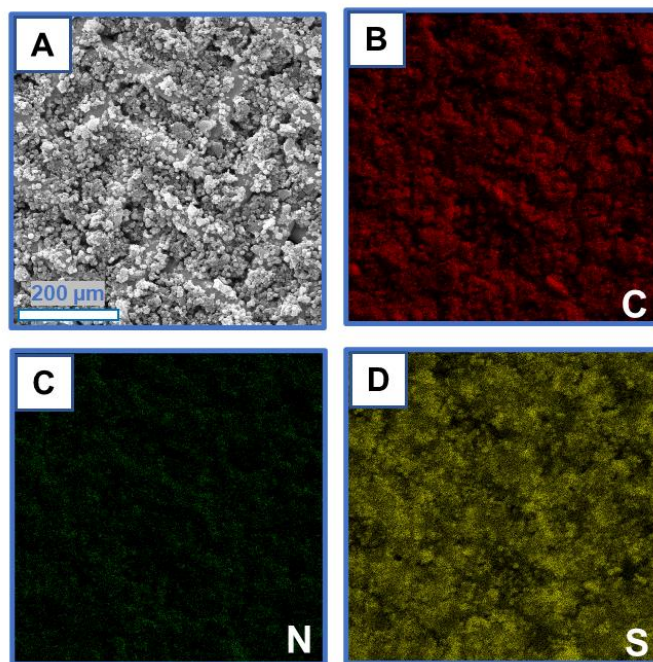
Figure 5-22. EDS analysis results of COF-TMT-BT cathode pristine electrode. a) SEM image, b) EDS map of C, c) EDS map of N, d) EDS map of S.
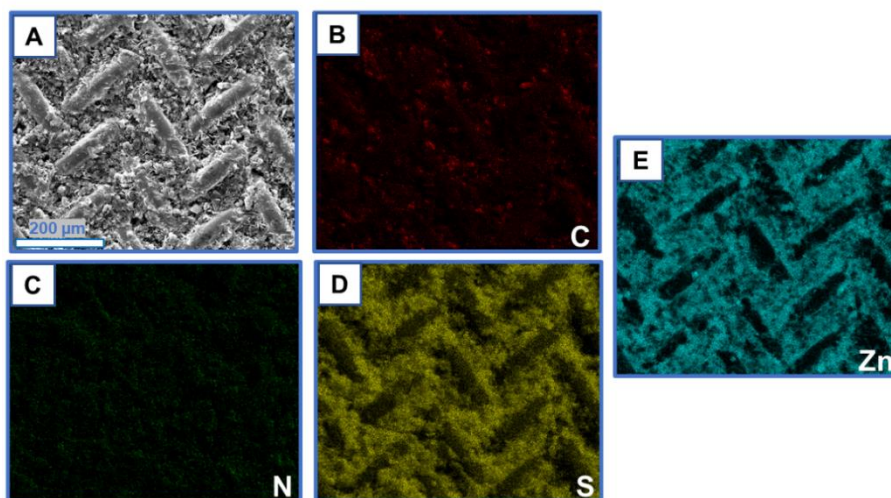

Figure 5-23. EDS analysis results of COF-TMT-BT cathode after 800 charge/discharge cycles. a) SEM image, b) EDS map of C, c) EDS map of N, d) EDS map of S, e) EDS map of Zn.

It is worth mentioning that the SEM morphology of COF-TMT-BT cathodes after 800 cycles does not show any obvious change except for the surface doping of a Zn layer, which could indicate their high stability during the charge-discharge process as shown in Figure5-24.
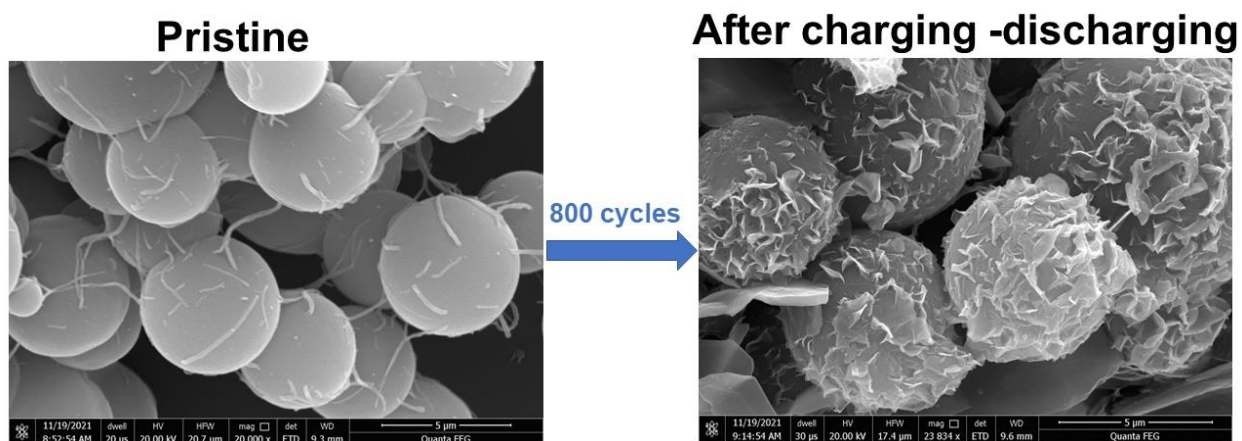

Figure 5-24. The comparison SEM images of pristine and after 800 charge/discharge cycles of COF-TMT-BT cathode.

5.3.6 TGA and BET analysis of COF-TMT-BT

The structural stability of COF-TMT-BT is evaluated by thermogravimetric analysis (TGA) and differential scanning calorimetry (DSC) analysis, which reveal high thermal stability up to 450 °C as displayed in Figure 5-29.
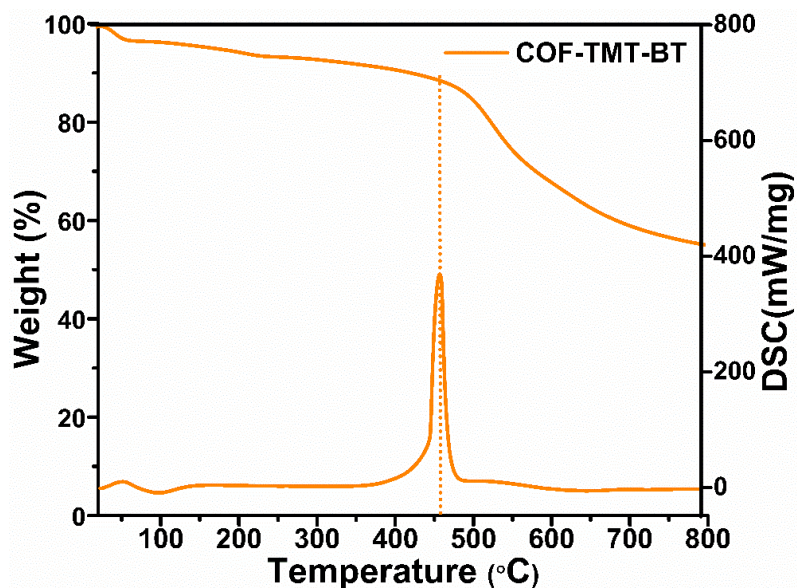
Figure 5-25. The thermogravimetric analysis (TGA) and differential scanning calorimetry (DSC) curves of COF-TMT-BT.

Furthermore, the porosity and the calculated Brunauer-Emmett-Teller (BET) surface area of COF-TMT-BT are evaluated by N_2 adsorption-desorption isotherms at 77 k as shown in Figure 5-30. As portrayed in Figure 5-26 COF-TMT-BT exhibits a typical type-Ⅱ adsorption isotherm along with a high surface area of 342.5 m^2 g^{-1}. The pore size distribution (Figure 5-27) shows the dominance of micropores of less than 5 nm, in good agreement with the average pore size value of 3.5 nm calculated by non-local density functional theory in Figure 5-8.

Figure 5-26. BET surface area of COF-TMT-BT.

Figure 5-27. Pore size distribution of COF-TMT-BT.

5.3.7 Density Functional Theory (DFT) Calculations of COF-TMT-BT

Density functional theory (DFT) calculations are performed to simulate the atomic configuration evolution of the COF-TMT-BT cathode during the
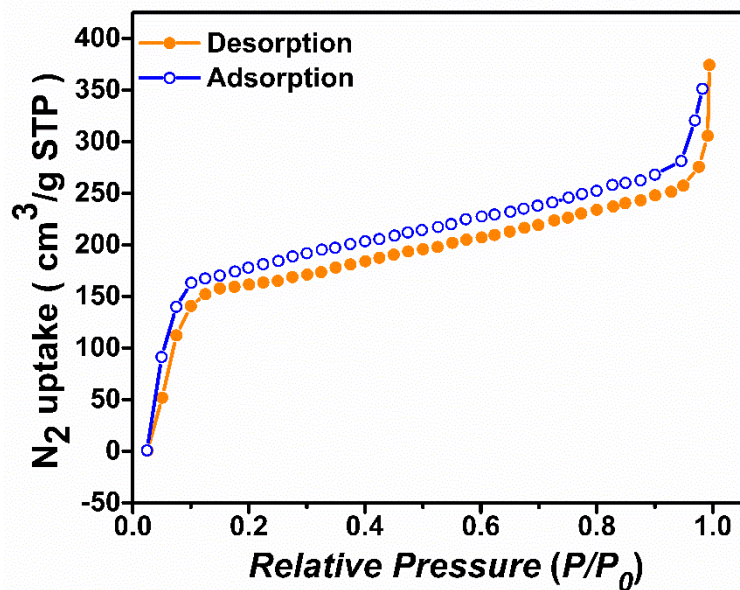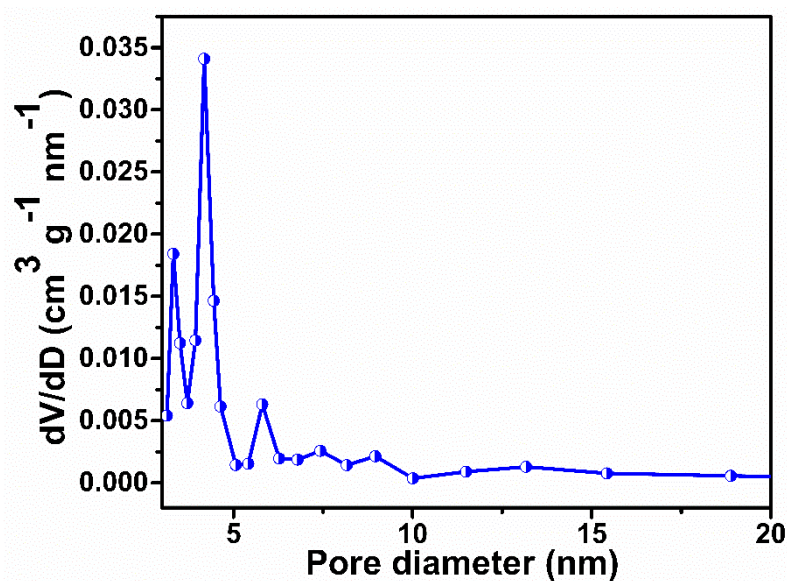
179

Zn^{2+} storage process. DFT calculations have been performed using the Vienna ab initio simulation package (VASP) with the projector-augmented wave (PAW) method. All calculations were based on the same generalized gradient approximation (GGA) method with Perdew-Burke-Ernzerhof (PBE) functional for the exchange-correlation term. The plane wave cutoff was set to 520 eV. The Brillouin zone integration was carried out with 1×1×3 and 3×3×9 Monkhorst-Pack k-point grid in structure optimization and electronic properties simulations, respectively. The convergence of energy and forces were set to $5×10^{-5}$ eV and 0.01 eV $Å^{-1}$, respectively. Electronic properties calculations (HOMO-LUMO and electrostatic potential) of the repetitive unit were performed using the Gaussian 09 program. The obtained structures were used for the final optimization using 6-31G(d) basis sets. The results obtained with B3LYP/6-31G(d) method were used throughout the discussion. The molecule's electronic structure plays a vital role in determining its redox properties and therefore the structure in Figure 5-28 is considered a repetitive unit for the calculations.[36]
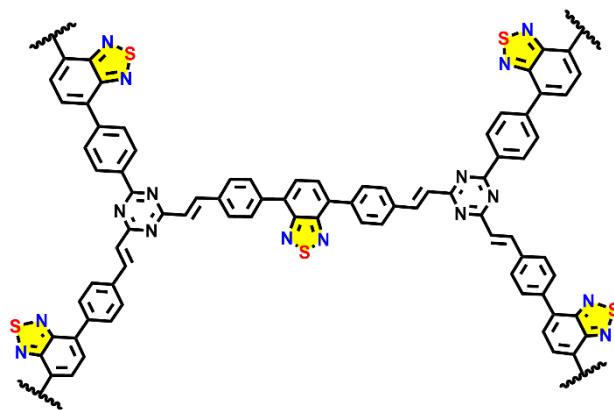
Figure 5-28. The repetitive units of COF-TMT-BT for DFT computation.

The simulated projected density of states (PDOS) and band structures are first calculated to elucidate the origin of the interactions from the perspective of the electronic structures. As shown in Figures 5-29 a and b, the monolayer of COF-TMT-BT possesses a narrowed indirect bandgap of 1.77 eV, which is reduced to 1.11 eV in the multilayer structure. The narrowing of the bandgap reveals an enhanced excitation of charge carriers to the conduction band. The energy levels of the LUMO and the highest occupied crystal orbital (HOMO) are used to study the redox properties of the COF-TMT-BT materials (Figure 5-29c). The HOMO orbital of the COF-TMT-BT unit is primarily distributed on the benzothiadiazole moieties without a continuous overlap, and also for the LUMO orbital, the electron cloud is mainly located around the benzothiadiazole units, demonstrating that the benzothiadiazole units possess theoretical good electron affinities and high reduction potential.[9, 37, 38] The electrostatic potential surface is further

simulated to expose the electrochemically active sites for cation chelation. As shown in Figure 5-29d, the electronegativity of COF-TMT-BT is located around the orange region near the corner nitrogen of the two neighboring triazine cores. Besides, the electronegative region unit spreads over the entire boundary within the COF-TMT-BT molecular plane, which indicates the possible active sites for ion accommodation in the COF-TMT-BT. The binding energies (BE) of COF-TMT-BT after the redox reaction with Zn^{2+} are calculated at the B3LYP/6-31+G(d) method using three possible model compounds (Figure 29e).[15,39,40] The optimized structures of Zn_X@COF-TMT-BT (X=2, 4, 6) and the average binding energy needed for each Zn^{2+} are exhibited in Figure 5-29e, based on the minimum energy principle. The Zn_6@COF-TMT-BT model shows the most stable configuration after the Zn^{2+} uptake. According to these DFT theoretical calculation results and some previous reports,[41, 42] we propose the following electrochemical mechanism of COF-TMT-BT during the reversible process of Zn^{2+} ion insertion/extraction: COF-TMT-BT stores charges *via* an ion-coordination process where each Zn^{2+} binds with the S atoms from the benzothiadiazole units to form S-Zn-S bond in the successive COF-TMT-BT layers.
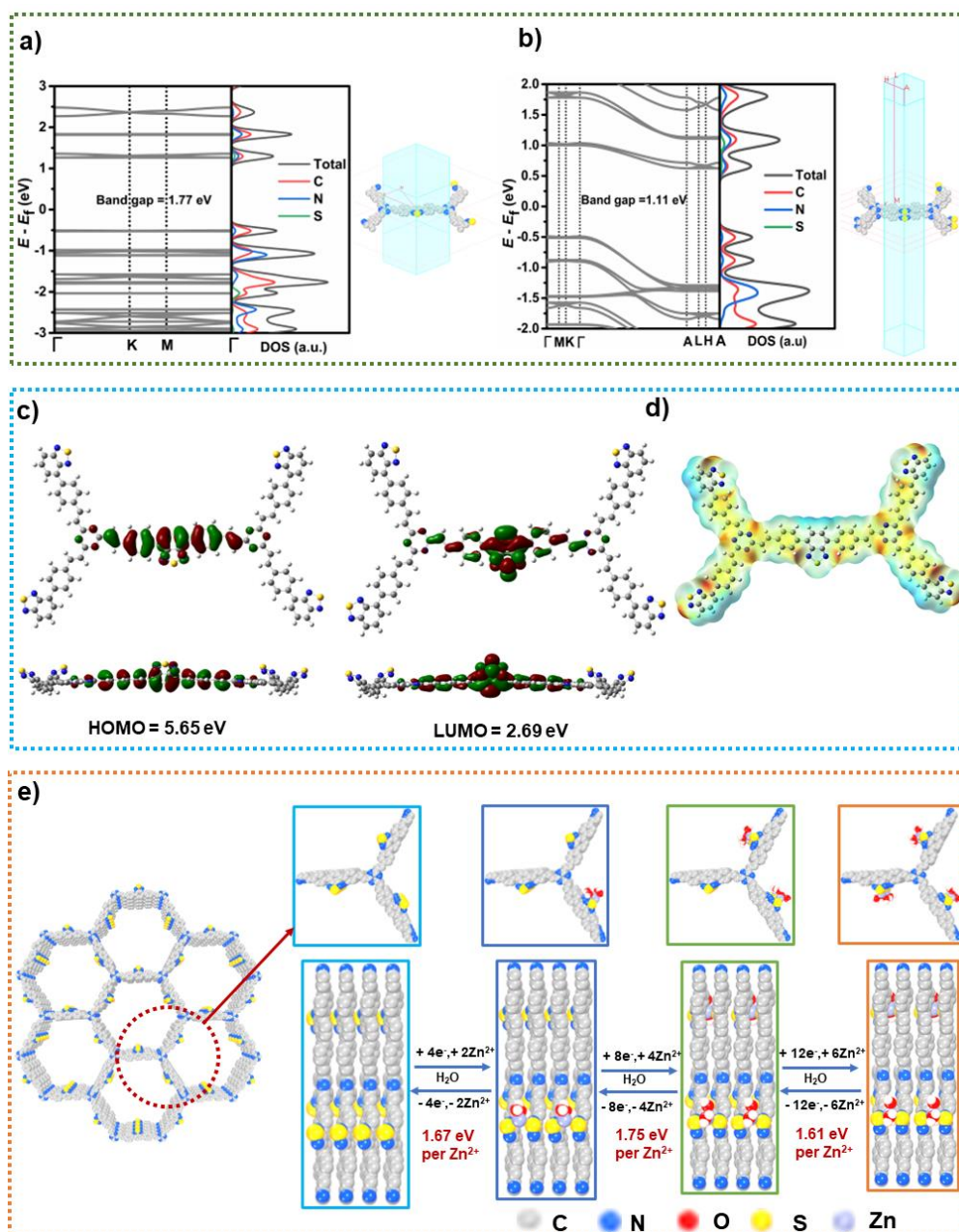
Figure 5-29. a) Simulated band structure and PDOS of a monolayer COF-TMT-BT with corresponding first Brillouin zone and high symmetry K-points. Γ (0, 0, 0); K (-1/3, 2/3, 0); M (0, 0.5, 0). b) Simulated band structure and PDOS of COF-TMT-BT multilayers with corresponding first Brillouin zone and high symmetry K-points. Γ (0, 0, 0); K (-1/3, 2/3, 0); M (0, 0.5, 0); A (0, 0, 0.5); H (-1/3, 2/3, 0.5); L (0, 0.5, 0.5). c) HOMO and LUMO orbitals of COF-TMT-BDTA repetitive unit. d) Electrostatic potential surface of COF-TMT-BT repetitive units. e) Binding energy for COF-TMT-BDTA at each zincation stage (H atom deleted for clarity).

5.4 Conclusions

In summary, in this chapter we are reported a study on the relationship between the electrochemically-active benzothiadiazole units and performance in aqueous ZIBs by designing and synthesizing a new olefin-linked 2D-COF. The as-synthesized COF-TMT-BT delivered a high capacity of 283.5 mAh g^{-1} at a current density of 0.1 A g^{-1} and an outstanding maximum energy and power densities of 219.6 Wh kg^{-1}, 23.2 kW kg^{-1}, respectively, which are superior to most of the reported COFs and another organic or inorganic cathodes materials for aqueous ZIBs. The experimental results together with the theoretical DFT calculations indicated that the highly electronegative pyridinic/pyrrolic N dopants in the COF-TMT-BT framework reduce the binding energy between benzothiadiazole group and Zn^{2+} by inducing charge delocalization of the benzothiadiazole group, hence promoting the formation of S-Zn-S bonds in the successive COF-TMT-BT layers. Furthermore, we extended the use of electrochemically-active benzothiadiazole units to an imine-linked COF. We believe that our new benzothiadiazole functionalized 2D olefin-linked COF-TMT-BT not only paves the way for the further rational design of benzothiadiazole-based COF electrodes but also broadens the applications of COFs in aqueous ZIBs.

5.5 References

1.   Zhang, N.; Cheng, F.; Liu, Y.; Zhao, Q.; Lei, K.; Chen, C.; Liu, X.; Chen, J., Cation-Deficient Spinel $ZnMn_2O_4$ Cathode in $Zn(CF_3SO_3)_2$ Electrolyte for Rechargeable Aqueous Zn-Ion Battery. *Journal of the American Chemical Society* **2016,** *138* (39), 12894-12901.

2.   He, P.; Quan, Y.; Xu, X.; Yan, M.; Yang, W.; An, Q.; He, L.; Mai, L., High-Performance Aqueous Zinc-Ion Battery Based on Layered H2V3O8 Nanowire Cathode. *Small* **2017,** *13* (47), 1702551.

3.   Guo, J.; Ming, J.; Lei, Y.; Zhang, W.; Xia, C.; Cui, Y.; Alshareef, H. N., Artificial Solid Electrolyte Interphase for Suppressing Surface Reactions and Cathode Dissolution in Aqueous Zinc Ion Batteries. *ACS Energy Letters* **2019,** *4* (12), 2776-2781.

4.   Liu, P.; Liu, W.; Huang, Y.; Li, P.; Yan, J.; Liu, K., Mesoporous hollow carbon spheres boosted, integrated high performance aqueous Zn-Ion energy storage. *Energy Storage Materials* **2020,** *25*, 858-865.

5.   Shi, M.; Wang, B.; Shen, Y.; Jiang, J.; Zhu, W.; Su, Y.; Narayanasamy, M.; Angaiah, S.; Yan, C.; Peng, Q., 3D assembly of MXene-stabilized spinel $ZnMn_2O_4$ for highly durable aqueous zinc-ion batteries. *Chemical Engineering Journal* **2020,** *399*, 125627.

6.   Zhao, Q.; Huang, W.; Luo, Z.; Liu, L.; Lu, Y.; Li, Y.; Li, L.; Hu, J.; Ma, H.; Chen, J., High-capacity aqueous zinc batteries using sustainable quinone electrodes. *Science Advances* **2018,** *4* (3), eaao1761.

7.   Kundu, D.; Oberholzer, P.; Glaros, C.; Bouzid, A.; Tervoort, E.; Pasquarello, A.; Niederberger, M., Organic Cathode for Aqueous Zn-Ion Batteries: Taming a Unique Phase Evolution toward Stable Electrochemical Cycling. *Chemistry of Materials* **2018,** *30* (11), 3874-3881.

8.   Nam, K. W.; Kim, H.; Beldjoudi, Y.; Kwon, T.-w.; Kim, D. J.; Stoddart, J. F., Redox-Active Phenanthrenequinone Triangles in Aqueous Rechargeable Zinc Batteries. *Journal of the American Chemical Society* **2020,** *142* (5), 2541-2548.

9. Wang, Y.; Wang, C.; Ni, Z.; Gu, Y.; Wang, B.; Guo, Z.; Wang, Z.; Bin, D.; Ma, J.; Wang, Y., Binding Zinc Ions by Carboxyl Groups from Adjacent Molecules toward Long-Life Aqueous Zinc-Organic Batteries. *Advanced Materials* **2020,** *32* (16), 2000338.

10. Wang, N.; Guo, Z.; Ni, Z.; Xu, J.; Qiu, X.; Ma, J.; Wei, P.; Wang, Y., Molecular Tailoring of an n/p-type Phenothiazine Organic Scaffold for Zinc Batteries. *Angewandte Chemie International Edition* **2021,** *60* (38), 20826-20832.

11. Yu, M.; Chandrasekhar, N.; Raghupathy, R. K. M.; Ly, K. H.; Zhang, H.; Dmitrieva, E.; Liang, C.; Lu, X.; Kühne, T. D.; Mirhosseini, H.; Weidinger, I. M.; Feng, X., A High-Rate Two-Dimensional Polyarylimide Covalent Organic Framework Anode for Aqueous Zn-Ion Energy Storage Devices. *Journal of the American Chemical Society* **2020,** *142* (46), 19570-19578.

12. Wang, W.; Kale, V. S.; Cao, Z.; Kandambeth, S.; Zhang, W.; Ming, J.; Parvatkar, P. T.; Abou-Hamad, E.; Shekhah, O.; Cavallo, L.; Eddaoudi, M.; Alshareef, H. N., Phenanthroline Covalent Organic Framework Electrodes for High-Performance Zinc-Ion Supercapattery. *ACS Energy Letters* **2020,** *5* (7), 2256-2264.

13. Khayum M, A.; Ghosh, M.; Vijayakumar, V.; Halder, A.; Nurhuda, M.; Kumar, S.; Addicoat, M.; Kurungot, S.; Banerjee, R., Zinc-ion interactions in a two-dimensional covalent organic framework based aqueous zinc ion battery. *Chemical Science* **2019,** *10* (38), 8889-8894.

14. Wang, W.; Kale, V. S.; Cao, Z.; Lei, Y.; Kandambeth, S.; Zou, G.; Zhu, Y.; Abouhamad, E.; Shekhah, O.; Cavallo, L.; Eddaoudi, M.; Alshareef, H. N., Molecular Engineering of Covalent Organic Framework Cathodes for Enhanced Zinc-Ion Batteries. *Advanced Materials* **2021,** *33* (39), 2103617.

15. Ma, D.; Zhao, H.; Cao, F.; Zhao, H.; Li, J.; Wang, L.; Liu, K., A carbonyl-rich covalent organic framework as a high-performance cathode material for aqueous rechargeable zinc-ion batteries. *Chemical Science* **2022,** *13* (8), 2385-2390.

16. Wang, J.; Polleux, J.; Lim, J.; Dunn, B., Pseudocapacitive Contributions to Electrochemical Energy Storage in TiO_2 (Anatase) Nanoparticles. *The Journal of Physical Chemistry C* **2007,** *111* (40), 14925-14931.

17. Jin, Y.; Zou, L.; Liu, L.; Engelhard, M. H.; Patel, R. L.; Nie, Z.; Han, K. S.; Shao, Y.; Wang, C.; Zhu, J.; Pan, H.; Liu, J., Joint Charge Storage for High-Rate Aqueous Zinc-Manganese Dioxide Batteries. *Advance Materials* **2019,** *31* (29), 1900567.

18. Kim, H.-S.; Cook, J. B.; Lin, H.; Ko, Jesse S.; Tolbert, Sarah H.; Ozolins, V.; Dunn, B., Oxygen vacancies enhance pseudocapacitive charge storage properties of MoO_3-x. *Nature Materials* **2017,** *16* (4), 454-460.

19. Shi, H.-Y.; Ye, Y.-J.; Liu, K.; Song, Y.; Sun, X., A Long-Cycle-Life Self-Doped Polyaniline Cathode for Rechargeable Aqueous Zinc Batteries. *Angewandte Chemie International Edition* **2018,** *57* (50), 16359-16363.

20. Yue, X.; Liu, H.; Liu, P., Polymer grafted on carbon nanotubes as a flexible cathode for aqueous zinc ion batteries. *Chemical Communications* **2019,** *55* (11), 1647-1650.

21. Wang, N.; Dong, X.; Wang, B.; Guo, Z.; Wang, Z.; Wang, R.; Qiu, X.; Wang, Y., Zinc-Organic Battery with a Wide Operation-Temperature Window from -70 to 150 °C. *Angewandte Chemie International Edition* **2020,** *59* (34), 14577-14583.

22. Tie, Z.; Niu, Z., Design Strategies for High-Performance Aqueous Zn/Organic Batteries. *Angewandte Chemie International Edition* **2020,** *59* (48), 21293-21303.

23. Tie, Z.; Liu, L.; Deng, S.; Zhao, D.; Niu, Z., Proton Insertion Chemistry of a Zinc-Organic Battery. *Angewandte Chemie International Edition* **2020,** *59* (12), 4920-4924.

24. Yuan, C.; Fu, S.; Yang, K.; Hou, B.; Liu, Y.; Jiang, J.; Cui, Y., Crystalline C-C and C=C Bond-Linked Chiral Covalent Organic Frameworks. *Journal of the American Chemical Society* **2021,** *143* (1), 369-381.

25. Lyu, H.; Diercks, C. S.; Zhu, C.; Yaghi, O. M., Porous Crystalline Olefin-Linked Covalent Organic Frameworks. *Journal of the American Chemical Society* **2019,** *141* (17), 6848-6852.

26. Wu, X. L.; Zilm, K. W., Complete Spectral Editing in CPMAS NMR. *Journal of Magnetic Resonance, Series A* **1993,** *102* (2), 205-213.

27. Jürgens, B.; Irran, E.; Senker, J.; Kroll, P.; Müller, H.; Schnick, W., Melem (2,5,8-Triamino-tri-s-triazine), an Important Intermediate during Condensation of Melamine Rings to Graphitic Carbon Nitride: Synthesis, Structure Determination by X-ray Powder Diffractometry, Solid-State NMR, and Theoretical Studies. *Journal of the American Chemical Society* **2003,** *125* (34), 10288-10300.

28. Mohd Yusoff, A. R. b.; Kim, H. P.; Jang, J., High performance organic photovoltaics with zinc oxide and graphene oxide buffer layers. *Nanoscale* **2014,** *6* (3), 1537-1544.

29. Mohammadnezhad, M.; Aïssa, B.; Harnagea, C.; Rosei, F., Hybrid PCDTBT:PCBM:Graphene-Nanoplatelet Photoabsorbers. *Journal of The Electrochemical Society* **2020,** *167* (13), 136504.

30. Jha, P.; Koiry, S. P.; Saxena, V.; Veerender, P.; Gusain, A.; Chauhan, A. K.; Debnath, A. K.; Aswal, D. K.; Gupta, S. K., Air-stability and bending properties of flexible organic field-effect transistors based on poly[N-9-heptadecanyl-2,7-carbazole-alt-5,5-(4,7-di-2-thienyl-2,1,3-benzothiadiazole)]. *Organic Electronics* **2013,** *14* (10), 2635-2644.

31. Cho, S.; Seo, J. H.; Park, S. H.; Beaupré, S.; Leclerc, M.; Heeger, A. J., A Thermally Stable Semiconducting Polymer. *Advance Materials***2010,** *22* (11), 1253-1257.

32. Osadchii, D. Y.; Olivos-Suarez, A. I.; Bavykina, A. V.; Gascon, J., Revisiting Nitrogen Species in Covalent Triazine Frameworks. *Langmuir* **2017,** *33* (50), 14278-14285.

33. Xue, R.; Gou, H.; Zhang, L.; Liu, Y.; Rao, H.; Zhao, G., A new squaraine-triazine based covalent organic polymer as an electrode material with long life and high performance for supercapacitors. *New Journal of Chemistry* **2021,** *45* (2), 679-684.

34. Castner, D. G.; Hinds, K.; Grainger, D. W., X-ray Photoelectron Spectroscopy Sulfur 2p Study of Organic Thiol and Disulfide Binding Interactions with Gold Surfaces. *Langmuir* **1996,** *12* (21), 5083-5086.

35. Kim, J.-S.; Ho, P. K. H.; Murphy, C. E.; Friend, R. H., Phase Separation in Polyfluorene-Based Conjugated Polymer Blends: Lateral and Vertical Analysis of Blend Spin-Cast Thin Films. *Macromolecules* **2004,** *37* (8), 2861-2871.

36. Bachman, J. C.; Kavian, R.; Graham, D. J.; Kim, D. Y.; Noda, S.; Nocera, D. G.; Shao-Horn, Y.; Lee, S. W., Electrochemical polymerization of pyrene derivatives on functionalized carbon nanotubes for pseudocapacitive electrodes. *Nature Communications* **2015,** *6* (1), 7040.

37. Peng, C.; Ning, G.-H.; Su, J.; Zhong, G.; Tang, W.; Tian, B.; Su, C.; Yu, D.; Zu, L.; Yang, J.; Ng, M.-F.; Hu, Y.-S.; Yang, Y.; Armand, M.; Loh, K. P., Reversible multi-electron redox chemistry of π-conjugated N-containing heteroaromatic molecule-based organic cathodes. *Nature Energy* **2017,** *2* (7), 17074.

38. Cui, C.; Ji, X.; Wang, P.-F.; Xu, G.-L.; Chen, L.; Chen, J.; Kim, H.; Ren, Y.; Chen, F.; Yang, C.; Fan, X.; Luo, C.; Amine, K.; Wang, C., Integrating Multiredox Centers into One Framework for High-Performance Organic Li-Ion Battery Cathodes. *ACS Energy Letters* **2020,** *5* (1), 224-231.

39. Rassolov, V. A.; Pople, J. A.; Ratner, M. A.; Windus, T. L., 6-31G* basis set for atoms K through Zn. *The Journal of Chemical Physics* **1998,** *109* (4), 1223-1229.

40. Kim, K. C.; Liu, T.; Lee, S. W.; Jang, S. S., First-Principles Density Functional Theory Modeling of Li Binding: Thermodynamics and Redox Properties of Quinone Derivatives for Lithium-Ion Batteries. *Journal of the American Chemical Society* **2016,** *138* (7), 2374-2382.

41. Liang, Y.; Jing, Y.; Gheytani, S.; Lee, K.-Y.; Liu, P.; Facchetti, A.; Yao, Y., Universal quinone electrodes for long cycle life aqueous rechargeable batteries. *Nature Materials* **2017,** *16* (8), 841-848.

42. Guo, Z.; Ma, Y.; Dong, X.; Huang, J.; Wang, Y.; Xia, Y., An Environmentally Friendly and Flexible Aqueous Zinc Battery Using an Organic Cathode. *Angewandte Chemie International Edition* **2018,** *57* (36), 11737-11741.

189

Chapter 6 Conclusions and Future perspectives

6.1 Conclusions

This PhD Thesis addresses the ever-increasing demand for the novel electrode of MOF@COF-based hybrid porous materials for high performance supercapacitors and innovative olefin-linked benzothiadiazole-based COF-TMT-BT as novel active sites for aqueous zinc-ion batteries. The main conclusions of this PhD Thesis are presented in three sections based on the research findings discussed in each chapter in more detail.

i) The first research project discussed in Chapter 3 has been devoted to the design of a robust aza-MOF@COF hybrid porous material *via* aza-Diels-Alder cycloaddition driven post-synthetic modification of MOF@COF. The obtained aza-MOF@COF hybrid not only retains a highly crystalline nature with extended π-delocalization but also displays superior capacitor performance in energy storage systems thanks to its high robustness. As a *proof-of-concep*t application in supercapacitor devices, the aza-MOF@COF device exhibits a high specific capacitance of 20.35 μF cm^{-2} and an exceptional stack capacitance of 1.16 F cm^{-3}, which exceeds most of the previously reported state-of-the-art MOFs@COFs hybrid materials. Our approach to

post-synthetic modification of MOFs@COFs hybrids implements rational design for the synthesis of robust, functional porous materials and expands the plethora of promising application of MOFs@COFs hybrid porous materials in energy storage applications.

ii)   The second research project presented in Chapter 4 targets the design of MOF@COF-TCNQ through the infiltration of redox-active TCNQ molecules into the pores of MOF@COF, which improves the characteristics of the latter thereby attaining high-performance in energy storage devices. Density functional theory (DFT) calculations were employed to guide the design of a MOF@COF-TCNQ hybrid with the TCNQ functional units incorporated in the pores of MOF@COF. To demonstrate the potential application of our hybrids, the as-synthesized MOF@COF-TCNQ hybrid has been employed as active material in supercapacitors. Electrochemical energy storage analysis revealed outstanding supercapacitor performance as evidenced by a specific areal capacitance of 78.36 mF cm^{-2} and a high stack volumetric energy density of 4.46 F cm^{-3}, with capacitance retention of 86.4% after 2000 cycles completed at 0.2 A cm^{-2}. DFT calculations result strongly indicate that the high capacitance of MOF@COF-TCNQ has a quantum capacitance origin. Our liquid-phase infiltration protocol of MOF@COF hybrids with redox-active molecules represents an efficacious approach to designing functional porous hybrids.

iii) The third research project discussed in Chapter 5 deals with the design of novel olefin-linked COF through the aldol condensation between 2,4,6-trimethyl-1,3,5-triazine (TMT) and 4,4′-(benzothiadiazole-4,7-diyl)dibenzaldehyde (BT), COF-TMT-BT, where benzothiadiazole units are explored as novel electrochemically-active groups. COF-TMT-BT exhibits an outstanding Zn^{2+} storage capability, delivering a capacity of 283.5 mAh g^{-1} at a current density of 0.1 A g^{-1}. The computational and experimental analysis further verify that the benzothiadiazole units are the electrochemically-active sites for Zn^{2+} coordination not only in olefin (C=C) but also on imine (C=N) linked COF electrodes. This work paves the way for the rational design of advanced benzothiadiazole-based COF materials for Zn^{2+} storage energy storage devices.

6.2 Future Perspectives

Despite considerable achievements during last years and in particular those discussed in this Thesis, some challenges still need to be addressed. In particular, the increase of the specific capacitance of MOF@COF hybrids for practical application and finding novel electrochemically-active groups of COFs with high performance in aqueous ZIBs as well as ion storage mechanisms. Several directions can be identified that require further improvements in the future:

i) Innovative nanocomposite MOF@COF hybrids materials: Combining/doping different materials into the pores of MOF@COF hybrids porous materials to design innovative nanocomposite is a vital approach for further development of MOF@COF hybrids with high capacitive supercapacitors performance in the future. Nanocomposite materials can have a synergistic effect by enhancing specific surface area, inducing porosity, facilitating electron and ion conduction, improving cycling stability, increasing wettability of electrodes, providing short/diffusion path lengths for electrons and metal-ions leading to faster energy transfer kinetics, creating more efficient interfaces between electrolytes and electrodes, increasing active sites, resulting fast charge-discharge and providing extra pseudocapacitance even at high current densities. As a result, the obtained MOF@COF with nanocomposite hybrids can overcome the shortcoming of the individual substances and incorporate the advantages of all constituents of the nanocomposite materials.

ii) Optimizing pore-size properties of MOF@COF-based electrode materials: According to some studies, pore engineering by adjusting the pore size of electrode materials with the ion size of electrolyte would improve the overall performance of supercapacitors devices. However, the pore engineering of MOF@COF-based electrode materials is still limited because of a suitable post-synthetic modification method. To address this issue, more

fundamental experiments are still required to fully understand the relationship of pore size in MOF@COF hybrids in the energy storage field.

iii) Designing novel MOF or COF-based electrodes which contain more and more active sites that would be able to undergo redox reactions and interact with the active sites of electrode materials, thereby exhibiting pseudocapacitance contributions. For this purpose, the innovative MOF or COF-based electrode should contain different functional groups in the building blocks, bearing multifunctional groups.

iv) Even though the high energy density of the MOF or COF-based energy storage devices was achieved, they are still far from real practical applications. There is plenty of room to explore new electrode composites for supercapacitors and aqueous ZIBs. At the same time, in this thesis, we only investigated the electrochemical performance of two MOF@COF hybrids and one new olefin-linked COFs. In future works, it will be of interest to investigate low-cost high-performance novel COFs-based electrode materials and explore their electrochemical performance to construct hybrid batteries with higher energy and power densities, moreover, the strategies for improving the performance of COFs electrodes should be demonstrated in full cells for practical applications.

Statement of Work

All the experimental data analysis presented in this Thesis was carried out by the author (Haijun PENG) except for the following:

In Chapter 3, the solid-state NMR analysis was made by Dr. Jésus Raya; the HR-TEM images were recorded by Dr. Walid Baaziz, and the XPS spectra were recorded by Dr. Fanny Richard from the University of Strasbourg, France.

In Chapter 4, the DFT simulations were carried out by Senhe Huang and Dr. Diana Tranca under the supervision of Prof. Xiaodong Zhuang from the School of Chemistry and Chemical Engineering, Shanghai Jiao Tong University, Shanghai, China.

In Chapter 5, the Solid-state NMR analysis was made by Dr. Dawid Pakulski from the Adam Mickiewicz University in Poznań, Poland; and the XPS spectra were recorded by Dr. Fanny Richard from the University of Strasbourg, France.

All the images displayed in this thesis were designed by the author (Haijun Peng), and all the original projects reported in this thesis were designed and developed by Haijun Peng, Dr. Artur Ciesielski, and Prof. Paolo Samorì.

Acknowledgments

I would like to firstly thank my Ph.D. supervisor, Prof. Paolo Samorì for accepting me as a Ph.D. student in his group, and for his valuable guidance during my Ph.D. I appreciate the opportunity of working in such an outstanding research environment.

I also would like to express my highest gratitude to my Ph.D. co-supervisor Dr. Artur Ciesielski. He was always willing to give me abundant discussions, his curiosity about science, rich knowledge, efficiency and hard-working attitude, responsibility, and love for family.

Very special thanks to Dr. Daniel Iglesias, Dr. Hanlin Wang, Dr. Haipeng Guo, Dr. Ye Wang, Dr. Verónica Montes Garcia, Dr. Yifan Yao, and Dr. Yuda Zhao Dr. Haixin Qiu, and Dr. Can Wang for many fruitful discussions and patience in answering my questions. Interacting with them broadened my knowledge and stimulated my new ideas. They are my models of excellent young researchers. Besides, Dr. Changbo Huang, Dr. Chun Ma, Dr. Zhaoyang

Liu, Feng Luo, Bin Han, Yusheng Chen, Pietro, Nicholas, Luca, and all remaining team members who worked in the Nanochemistry lab and helped me in every aspect of lab chores.

Last but not least, I would like to thank my parents, my wife, and my brother who have always been my strongest supporters. Despite the geographical distance, our family has always been connected by love.

Haijun PENG

彭海军

List of Publications

1. **Haijun Peng,** Yongxiang Zheng, Cyril Antheaume, Paolo Samorì, Artur Ciesielski, "Novel thiophene-based donor-acceptor scaffolds as cathodes for rechargeable aqueous zinc-ion hybrid supercapacitors", *Chem. Commun.*, 2022, *58*, 6689-6692.

   DOI: https://doi.org/10.1039/D2CC02021A

2. **Haijun Peng**, Senhe Huang, Diana Tranca, Fanny Richard, Walid Baaziz, Xiaodong Zhuang, Paolo Samorì, Artur Ciesielski,

   "Quantum Capacitance through Molecular Infiltration of 7, 7, 8, 8-Tetracyanoquinodimethane in Metal-Organic Framework/Covalent Organic Framework Hybrids" *ACS Nano*, 2021, 15, 18580-18589.

   DOI: https://doi.org/10.1021/acsnano.1c09146

3. **Haijun Peng**, Jésus Raya, Fanny Richard, Walid Baaziz, Ovidiu Ersen, Artur Ciesielski, Paolo Samorì "Synthesis of Robust MOFs@COFs Porous Hybrid Materials via an Aza-Diels-Alder Reaction: Towards High-Performance Supercapacitor Materials", *Angewandte Chemie International Edition* , **2020**, *59*, 19602-19609.

   DOI: https://doi.org/10.1002/anie.202008408

4. Luca Cusin, **Haijun Peng**, Artur Ciesielski, Paolo Samorì" Chemical conversion and locking of the imine linkage: enhancing the functionality of covalent organic frameworks", *Angewandte Chemie International Edition* 2021, 60(26), 14236-14250.

   DOI: https://doi.org/10.1002/anie.202016667

5. Hanlin Wang, Ye Wang, Zhenjie Ni, Nicholas Turetta, Sai Manoj Gali, **Haijun Peng**, Yifan Yao, Yusheng Chen, Iwona Janica, David Beljonne, Wenping Hu, Artur Ciesielski, Paolo Samorì, "2D MXene-Molecular Hybrid Additive for High‑Performance Ambipolar Polymer Field‑Effect Transistors and Logic Gates" *Adv. Mater.*, 2021, 33 (20), 2008215.

   DOI: https://doi.org/10.1002/adma.202008215

6. Yifan Yao, Qi Ou, Kuidong Wang, **Haijun Peng,** Feier Fang, Yumeng Shi, Ye Wang, Daniel Iglesias Asperilla, Zhigang Shuai, Paolo Samorì "Supramolecular engineering of charge transfer in wide bandgap organic semiconductors with enhanced visible-to-NIR photoresponse", *Nat. Comm.,* 2021, 12(1), 3667.

   DOI: https://doi.org/10.1038/s41467-021-23914-2

List of Presentations

1. Haijun Peng, Jesus Raya, Fanny Richard,Walid Baaziz, Ovidiu Ersen, Artur Ciesielski and Paolo Samorì, Chem2Dmat 2021, Bologna, Italy, 03-09 Septembre 2021. Poster

Haijun PENG

Cadre organique métallique/ Cadre organique covalent dans les applications de stockage d'énergie

Résumé

Cette thèse se étudie principalement sur la conception et la fabrication de nouvelles électrodes par la synthèse de nouveaux matériaux hybrides MOFs@COFs et par l'exploration de nouveaux COFs bidimensionnels (2D) liés à des oléfines (C=C) pour des dispositifs de supercondensateurs et de batteries zinc-ion, respectivement. L'ingénierie des pores des hybrides MOFs@COFs par des méthodes post-synthétiques *via* une cycloaddition aza-Diels-Alder et une infiltration en phase liquide du 7,7,8,8-tétracyanoquinodiméthane (TCNQ) redox-actif est la nouveauté majeure des deux premiers projets de recherche de cette thèse. Dans le dernier projet, un nouveau COF-TMT-BT 2D lié à une oléfine par condensation Aldol a été utilisé pour fabriquer des batteries zinc-ion aqueuses, qui ont révélé de nouveaux sites électrochimiquement actifs d'unités benzothiadiazole et d'excellentes densités d'énergie/puissance, supérieures à la plupart des cathodes COFs rapportées et à d'autres matériaux d'électrode organiques ou inorganiques.

Mots clés: cadre organique métallique, cadres organiques covalents, modification post-synthétique, supercondensateurs, batteries zinc-ion aqueuses.

Résumé en Anglais

This thesis mainly studies the design and fabrication of novel electrodes *via* the synthesis of new metal-organic frameworks and covalent organic frameworks (MOFs@COFs) hybrid materials and by exploring new olefin-linked (C=C) two-dimensional (2D) COFs for supercapacitor and aqueous zinc-ion battery devices, respectively. Pore engineering of MOFs@COFs hybrids through post-synthetic methods *via* aza-Diels-Alder cycloaddition and liquid-phase infiltration of redox-active 7,7,8,8-tetracyanoquinodimethane (TCNQ) is the main novelty of the first two research projects in this thesis. n the last project, a new olefin-linked 2D COF-TMT-BT through Aldol condensation has been utilized to fabricate aqueous zinc-ion batteries, which exhibited novel electrochemically-active sites of benzothiadiazole units and excellent energy/power densities that are superior to most of the reported COFs cathodes and another organic or inorganic electrode materials.

Keywords: metal-organic frameworks, covalent organic frameworks, post-synthetic modification, supercapacitors, aqueous zinc-ion batteries.